

Optical cavities defined by SU-8 photoresist on photonic crystal waveguides



Stephen A. Lennon

Linacre College

University of Oxford

A thesis submitted for the degree of

Doctor of Philosophy

Trinity Term 2019

Optical cavities defined by SU-8 photoresist on photonic crystal waveguides

Stephen A. Lennon

Linacre College

Thesis submitted for the degree of Doctor of Philosophy

Trinity Term 2019

Abstract

A novel photonic crystal (PhC) cavity design is presented, for which the location of the cavity mode is determined by laser patterning of SU-8 – a commercially-available negative photoresist – on top of a conventionally-fabricated PhC waveguide. This method aims towards the goal of achieving deterministic coupling between a self-assembled InGaAs/GaAs quantum dot (QD) and a PhC cavity mode using *in situ* all-optical techniques. The experimental and theoretical work presented in this thesis focus on developing the technique to a stage at which it is ready for this intended application. The devices are designed to operate at a wavelength $\lambda_0 \sim 1.3\mu\text{m}$ to be suitable for integration with telecommunications systems using commercially available optical fibres.

Finite-difference time-domain (FDTD) simulations are performed to investigate key attributes of the SU-8 PhC cavities, which are believed to operate via a mode gap confinement mechanism, due to an alteration of the modes supported by the PhC waveguide beneath the SU-8 structure. Real devices are fabricated with high yields (generally exceeding 80%) and characterised predominantly using micro-photoluminescence (μPL) mapping techniques. The viability of the design is first demonstrated experimentally for cavities defined by exposing a disk of SU-8 on the waveguide, which yields fundamental cavity modes with a quality factor (Q) in the range 2300–7400 and a predicted mode volume $V_0 \sim 1.44(\lambda_0/n)^3$. The Q of the cavity mode is found to be critically depend upon the thickness of the SU-8: in general, a thickness of $\sim 100\text{nm}$ or less is preferable for optimal Q factors.

An improved cavity design is devised which defines the cavity by a strip of SU-8 written perpendicular to the PhC waveguide. Higher Q factors up to 8700 are measured from fabricated devices and analysis suggests that cavity parameters are achieved which would be suitable for observing the strong coupling regime with a QD. The increase in Q factor is attributed primarily to the less stringent alignment requirements of the SU-8 strip cavity design. An investigation is also conducted into the effects of altering the width of the SU-8 strip, which allows the Q to be increased beyond 10^4 and also enables some control over λ_0 . However, it is expected that these results are ultimately limited by e-beam fabrication imperfections of the PhC waveguides.

Finally, coupled cavities (known as photonic molecules) formed from two SU-8 strips written on the same waveguide are investigated through FDTD simulations and experiments. It is shown that the coupling strength between the two cavities can be tuned by controlling the separation between them. The coupled supermodes of the system are characterised and the coupling strength is estimated from measurements of the coupling-induced mode splitting and delocalization of the modes. Confocal μPL measurements are used to explicitly show optical coupling between two cavities.

Publications

- *Photonic molecules defined by SU-8 photoresist strips on a photonic crystal waveguide*
Stephen A. Lennon, Frederic S.F. Brossard, Luke P. Nuttall, Jiang Wu, Jonathan Griffiths and Robert A. Taylor, Optics Express **26**, 32332–32345 (2018).
- *Optical fabrication and characterisation of SU-8 disk photonic waveguide heterostructure cavities*
Luke P. Nuttall, Frederic S.F. Brossard, Stephen A. Lennon, Benjamin P.L. Reid, Jiang Wu, Jonathan Griffiths and Robert A. Taylor, Optics Express **25**, 24615–24622 (2017).
- *Room-temperature InP/InGaAs nano-ridge lasers grown on Si and emitting at telecom bands*
Yu Han, Wai Kit Ng, Chao Ma, Qiang Li, Si Zhu, Christopher C.S. Chan, Kar Wei Ng, Stephen A. Lennon, Robert A. Taylor, Kam Sing Wong and Kei May Lau, Optica **5**, 918–923 (2018).

Acknowledgements

First and foremost, I would like to thank my supervisor, Robert Taylor for his support and guidance throughout my time in Oxford. His mentorship and positive, supportive attitude have been invaluable to driving the project forward to where it is today. Robert has always been available to help with my work, whether he was drawing on his vast knowledge of physics to provide insights into complex technical problems, providing vital feedback on experimental results and analysis, or using his wealth of experience to provide assistance in the lab. I have greatly enjoyed my time as a member of his group and have learned a great deal about physics, experimental techniques and good wine. This thesis would not have been possible without his supervision.

I would also like to extend my gratitude towards the colleagues I have worked with, both within Robert's group and through wider collaboration. I would like to thank Luke Nuttall and Benjamin Reid for welcoming me into the group and teaching me key experimental skills. Luke performed a significant amount of preliminary work for the SU-8 cavity project, including optimisation of the processes involved, which can be found in his thesis [1]. I worked closely with Luke on the initial SU-8 disk cavity experiments, which are covered in chapter 4 of this thesis. The AFM measurements and μ PL measurements in this chapter were divided between us. Luke additionally provided extremely helpful advice and assistance on FDTD simulations and coding – some of the code used for data analysis in this project is based on Python code written by Luke. He also wrote much of the LabVIEW code used to control the μ PL mapping system, which I then added to.

I owe gratitude to our collaborators Fred Brossard at Hitachi Cambridge Laboratory and Jonathan Griffiths at the Cavendish Laboratory, who performed the e-beam lithography and etching processes on the PhC samples studied in this work. Fred engaged in numerous theoretical discussions of the SU-8 cavity devices, providing useful advice and valuable feedback on my results. Fred also performed FDTD simulations on the SU-8 disk cavities, which are presented in chapter 4. His FDTD results and advice were incredibly helpful for learning to perform my own FDTD simulations. I would also like to thank Jiang Wu from University College London and Ed Clarke from the University of Sheffield, who grew the QD samples for this project.

In the Physics Department, I would like to thank Robin Nicholas for generously allowing us to use his AFM for sample characterisation and Ian Walmsley for kindly lending us a single photon detector for time-resolved measurements. I am also grateful to Helen Chrzanowski for helping us to characterise the detector. I would like to thank Paul Pattinson for the use of his cleanroom facilities and Robert Storey, Kieran McCall and Tony Hickman for reliably supplying liquid helium for experiments. My gratitude goes to Rick Makin for his work at the thin film facility to fabricate a custom-designed beam splitter and to Ghassan Yassin for use of his 5000 \times optical microscope.

In addition to those already mentioned, I would like to thank the other members of – and visitors to – the Taylor group, including Tim Puchtler, Tong Wang, Claudius Kocher, Guanhua Ying, Vitaly Osokin, Youngsin Park, Mo Li and Chris Chan for their stimulating discussions about physics and their good company. Tim and Claudius in particular were always willing to lend a hand in the lab or help solve a problem. I would also like to thank Niall McGroarty, who, during his brief time in the group, assisted with FDTD simulations.

I would like to thank the Engineering and Physical Sciences Research Council for providing the funding to make this research possible and Linacre College for also providing financial aid towards

living and conference expenses. In particular I am grateful to Jane Hoverd, the senior tutor, who has been kind and understanding throughout the process and has endeavoured to provide the support I needed.

Finally, I would like to express my warmest gratitude to my friends and family, without whom I would not be where I am today. The friends that I've made in Oxford have made my time here a joy. In particular I'd like to thank Sean, Glenn, Hannah, Claire, Gavin, Laura and all of the Linacre College bar staff for all of the great times that we have shared. Working at the college bar was a key part of my Oxford experience, which provided both an amazing social experience and additional financial support to see the DPhil through. It was also where I met my girlfriend Megan, to whom I am sincerely grateful for her unwavering support and encouragement, especially during the difficult final stages of the DPhil. I would also like to extend my deepest gratitude to my parents, Tony and Clare, for their patience and unyielding support throughout my time in Oxford. This thesis would not have been possible without their support through the highs and lows of the DPhil.

Contents

| | |
|--|-------------|
| Contents | vi |
| List of abbreviations | viii |
| 1 Introduction | 1 |
| 2 Finite-difference time-domain simulations of photonic crystal microcavities | 4 |
| 2.1 Introduction to photonic crystals | 4 |
| 2.2 The FDTD method | 6 |
| 2.3 Photonic band structure of a photonic crystal slab | 13 |
| 2.4 FDTD simulation of a photonic crystal cavity | 23 |
| 2.5 Photonic crystal waveguides and mode gap cavities | 35 |
| 2.6 The SU-8 strip cavity | 47 |
| 2.7 Summary | 60 |
| 3 Overview of cavity quantum electrodynamics and experimental techniques | 62 |
| 3.1 Single photon sources | 62 |
| 3.2 Self-assembled In(Ga)As/GaAs quantum dots | 65 |
| 3.3 CQED with quantum dot-microcavity systems | 72 |
| 3.4 Literature review | 78 |
| 3.5 The SU-8 cavity-writing technique | 85 |
| 3.6 Requirements for strong coupling | 88 |
| 3.7 Sample details | 92 |
| 3.8 Experimental apparatus | 93 |
| 3.9 Summary | 101 |

| | | |
|----------|--|------------|
| 4 | SU-8 disk cavities | 102 |
| 4.1 | FDTD simulations of SU-8 disk cavities | 102 |
| 4.2 | Fabrication and characterisation of SU-8 disk cavities | 104 |
| 4.3 | Varying the disk diameter | 113 |
| 4.4 | Summary | 116 |
| 5 | SU-8 strip cavities | 117 |
| 5.1 | Limitations of the SU-8 disk cavity design | 117 |
| 5.2 | Simulating the SU-8 strip cavity performance | 121 |
| 5.3 | SU-8 strip cavities: experimental results | 128 |
| 5.4 | Varying the strip width: simulation results | 145 |
| 5.5 | Varying the strip width: experimental results | 152 |
| 5.6 | Summary | 169 |
| 6 | SU-8 strip photonic molecules | 171 |
| 6.1 | Introduction to photonic molecules | 171 |
| 6.2 | FDTD simulations of SU-8 strip photonic molecules | 182 |
| 6.3 | Fabrication and characterisation of SU-8 strip PMs | 197 |
| 6.4 | Confocal measurements of SU-8 strip PMs | 210 |
| 6.5 | Summary | 217 |
| 7 | Conclusion | 221 |
| | Appendices | 225 |
| A | Exposure dose calibration summary | 225 |
| | Bibliography | 227 |

List of abbreviations

| | | |
|--------------|-------|---|
| AFM | | Atomic force microscope |
| AS | | Anti-symmetric |
| BS | | Beam splitter |
| CB | | Conduction band |
| CQED | | Cavity quantum electrodynamics |
| CW | | Continuous wave |
| DBR | | Distributed Bragg reflector |
| FDTD | | Finite-difference time-domain |
| FWHM | | Full width at half maximum |
| GS | | Ground state |
| HBT | | Hanbury Brown and Twiss |
| HOM | | Hong-Ou-Mandel |
| IPA | | Isopropyl alcohol |
| IRF | | Instrument response function |
| MBE | | Molecular beam epitaxy |
| ML | | Monolayers |
| PBS | | Polarising beam splitter |
| PGMEA | | Propylene glycol monomethyl ether acetate |
| PhC | | Photonic crystal |
| PM | | Photonic molecule |
| PML | | Perfectly matched layer |
| PMMA | | Poly(methyl methacrylate) |

| | |
|--------------------|--|
| QD | Quantum dot |
| S | Symmetric |
| SEM | Scanning electron microscope |
| SK | Stranski-Krastanov |
| SPC | Single photon counter |
| SPDC | Spontaneous parametric down-conversion |
| SPS | Single photon source |
| TCSPC | Time correlated single photon counting |
| TE | Transverse-electric |
| TM | Transverse-magnetic |
| TRPL | Time-resolved photoluminescence |
| VB | Valence band |
| WL | Wetting layer |
| WMLD | Width-modulated line defect |
| μPL | Micro-photoluminescence |

Introduction

Quantum technologies which exploit coherent quantum mechanical phenomena, such as in quantum information processing and quantum communication protocols, are expected to pave the way to a new generation of devices which significantly outperform their classical counterparts. For example, quantum computers show promise to simulate quantum systems and perform certain operations much more efficiently than a conventional computer [2]. Likewise, quantum key distribution protocols can guarantee secure sharing of cryptographic keys using methods that are not possible via classical means [3, 4]. Many possible candidates are currently being explored as potential hardware for quantum technology [5]. Among these are systems which employ single photons as qubits, which have been used to successfully demonstrate simple quantum logic gates and algorithms [6, 7, 8, 9], in addition to quantum key distribution [10, 11, 12, 13], in a laboratory environment. Such applications often rely on light sources with the ability to emit exactly one photon on demand. This has driven the development of single photon sources (SPSs), which have seen significant advances in recent years – particularly in solid state media incorporating self-assembled semiconductor quantum dots (QDs) [14]. Such devices typically rely on light-matter coupling between a single QD and an optical microcavity structure, which enables efficient generation and collection of single photons [15, 16, 17] by exploiting the effects of cavity quantum electrodynamics (CQED) [18].

One of the main barriers to scaling SPSs based on coupled QD-microcavity structures to larger systems and real-world applications is the difficulty of reproducibly fabricating such devices. Precise spatial alignment, typically on the scale of tens of nanometres, is required between a single QD and the microcavity in order for photons emitted by the QD to couple efficiently to a cavity

mode [19, 20]. Unfortunately, the self-assembled growth mechanism typically results in QDs located at random positions with a distribution of sizes [21, 22], which makes overlapping a single QD with a cavity mode a significant technical challenge. Further to this, spectral resonance must be achieved between an optical transition of the QD and a cavity mode, which is complicated by random variation of the emission wavelength between individual QDs, due to their size distribution. The randomness of these factors makes deterministic fabrication of a coupled self-assembled QD-microcavity system particularly difficult; the development of techniques which facilitate the necessary levels of precision is currently an area of active research [20, 23, 24, 25, 26, 27, 28]. The work of this thesis comprises the development, characterisation and optimisation of a novel cavity fabrication method, which is designed for the purpose of deterministic coupling to a single self-assembled semiconductor QD, with the ultimate goal of deterministic fabrication of SPSs which operate at telecommunications wavelengths. The success of this technique holds the potential for scalable fabrication of on-demand SPSs, which would be compatible with commercially-available optical fibres – a necessity if single-photon-based technologies such as quantum key distribution are to be operated over the long distances required for practical applications.

This thesis focuses on long wavelength ($\sim 1.3\mu\text{m}$) self-assembled InGaAs QDs [29, 30, 31] embedded in photonic crystal (PhC) cavity devices: a type of structure with a periodic refractive index that can exploit a photonic band gap to confine light to cavity modes on a scale similar to its wavelength [32, 33, 34]. We employ a novel cavity design which is created using all-optical techniques to pattern SU-8 photoresist (a commercially available, negative photoresist [35]) on top of a conventionally-fabricated PhC waveguide [36, 37]. A cavity mode is created in the waveguide, localized at the position of the SU-8, enabling deterministic placement of the cavity mode. The advantage of this technique is that the exposure process applied to set the cavity position can be performed *in-situ* using micro-photoluminescence (μPL) experimental apparatus, which can be used in conjunction with μPL measurements to visualize the embedded QDs. The technique therefore holds the potential for deterministic coupling between a cavity and self-assembled QD, by first locating a single, randomly positioned QD in the PhC waveguide using μPL techniques, then proceeding to pattern an SU-8-defined cavity at this position. The work performed during this project aimed to develop this novel SU-8 cavity fabrication technique up to the point at which it is ready for this intended application.

The thesis begins in Ch. 2 by covering the fundamental physics of 2D PhC slab devices, using finite-difference time-domain (FDTD) techniques as a tool to examine their properties. Simulations of

well-established PhC cavity and waveguide structures are first performed to demonstrate their favourable properties and verify the validity of the FDTD results. Initial simulations are then presented of the novel SU-8 defined cavity structure as a proof of concept, which is expanded upon in the chapters that follow.

In Ch. 3, a summary of CQED effects, in addition to QD properties and growth methods, are presented. The state of the field is examined with respect to achieving cavity-QD coupling and single photon sources, including an analysis of the requirements to achieve the strong coupling regime. Finally, we present the experimental apparatus and techniques relevant to the project, especially for experimental implementation of the SU-8 defined cavity. This mostly consists of μ PL techniques performed at cryogenic temperatures.

Chapters 4, 5 and 6 focus on the experimental implementation of the SU-8 cavity, presenting experimental results complemented by additional FDTD simulation results. Characterisation of the fabricated structures is performed predominantly using high resolution μ PL mapping measurements and AFM scanning techniques. Ch. 4 covers the first successful implementation of the SU-8-defined cavity: the simplest cavity design, which involves exposing a disk of SU-8 on top of the PhC waveguide. Ch. 5 aims to improve upon the cavity design, replacing the SU-8 disk with an SU-8 strip running perpendicular to the waveguide, which is patterned using a moving laser spot. This design circumvents alignment issues which limit the performance of the original SU-8 disk cavity design and enables high quality factor cavity modes to be more reliably manufactured. Measurements of these cavities also include time-resolved photoluminescence techniques. The latter part of Ch. 5 seeks to optimise the cavity design further by altering the SU-8 strip dimensions.

The final experimental chapter – Ch. 6 – investigates optical coupling between two SU-8 strip cavities patterned onto the same PhC waveguide. This system is commonly referred to as a photonic molecule (PM) [38], owing to similarities between the coupled optical modes and the electron orbitals of diatomic molecules. The fundamental physics of PMs and the state of research into this topic are summarised. FDTD simulation results of PMs formed from two coupled SU-8 strip cavities are presented, followed by successful experimental realisation of the structures. Coupling between the two cavities is characterised using similar μ PL methods to chapters 4 and 5, in addition to confocal measurement techniques.

2

Finite-difference time-domain simulations of photonic crystal microcavities

2.1 Introduction to photonic crystals

A photonic crystal (PhC) is a structure which, in analogy to the periodic electric potential of a conventional crystal lattice, has a periodic refractive index in one or more dimensions. One of the simplest and most well-known examples of a PhC is the distributed Bragg reflector (DBR), which is a one-dimensional PhC consisting of alternating layers of two dielectric materials with different refractive indices, n_1 and n_2 [see Fig. 2.1(a)]. When the thickness of the layers, d_1 and d_2 of the two materials respectively, is selected so that the optical path lengths are equal ($n_1 d_1 = n_2 d_2$), then light with a wavelength close to $\lambda_0/4 = n_1 d_1 = n_2 d_2$ (where λ_0 is the wavelength of the light in vacuum) will destructively interfere. This destructive interference suppresses propagation of the light through the structure and, in the case of an ideal infinite 1D structure, is able to completely prohibit transmission. This is the simplest example of a photonic band gap: a range of frequencies of light for which propagation through the PhC is forbidden, analogous to the concept of an electronic band gap in a conventional crystal lattice. More details about the DBR can be found in Ch. 4 of Ref. [39].

For the case of a DBR, the photonic band gap is useful because frequencies in the photonic band gap are reflected, enabling the DBR to act as a high reflectivity mirror. A similar concept can also

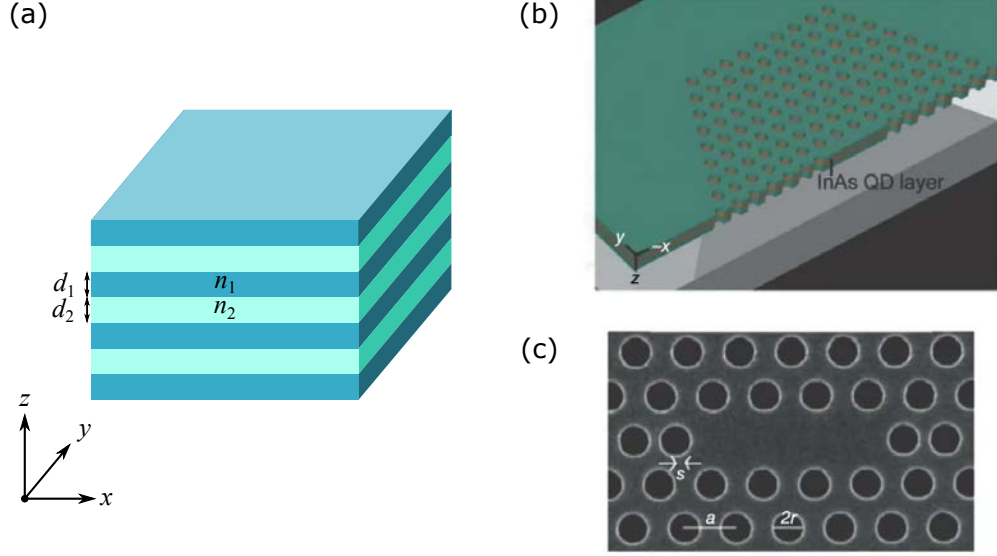


Figure 2.1: Examples of PhCs with periodicity in one and two dimensions. (a) Schematic diagram of a 1D PhC: a stack of alternating layers of material. (b) Schematic diagram of a 2D PhC cavity, formed by etching a periodic array of air holes into a thin slab. An optically-active layer of QDs can be embedded in the centre of the slab. (c) Scanning electron microscope (SEM) image of a 2D PhC fabricated in GaAs. Figs. (b) and (c) are taken from Ref. [19].

be applied to PhCs with periodicity in two or three dimensions, which can be engineered to exhibit a photonic band gap in a 2D plane [40, 41] or in all three spatial dimensions, respectively [42, 43]. By exploiting the photonic band gap in more than one dimension, light can be confined to high quality factor, small mode volume cavity modes [44, 45, 46, 47], which are ideal for light matter coupling experiments (see Ch. 3). This project focuses on 2D PhC slab structures defined by a periodic array of air holes in a thin slab of dielectric material [see Figs. 2.1(b) and 2.1(c), which show a 2D PhC slab cavity from Ref. [19]], which have seen much interest due to their ease of fabrication and excellent performance for making optical cavities [32, 33, 34, 48].

In this chapter, photonic devices based on 2D hole-in-slab PhCs are introduced and characterised using finite-difference time-domain (FDTD) simulation techniques. The FDTD method and simulation methodology are detailed, which are then applied to various PhC structures. Simulation results including photonic band structures and cavity mode parameters are presented, which provide an insight into the optical properties of the devices. Finally, a novel hybrid cavity incorporating SU-8 negative photoresist on top of a 2D PhC slab is introduced, which forms the basis of the rest of the work in the thesis.

2.2 The FDTD method

The finite-difference time-domain (FDTD) simulation method is a powerful tool for the modelling of optical devices with wavelength-scale features, such as micropillar DBRs and PhC cavities. The technique computes the time-domain evolution of electromagnetic fields injected into a structure (by a source, such as an electric or magnetic dipole) according to a finite difference approximation of Maxwell's equations. By tracking the fields and their Fourier transform, vital information such as quality factors (Q) and mode volumes of cavity modes or photonic band structures of PhCs can be extracted from FDTD simulations, making them an invaluable tool in the design and optimisation of PhC microcavities. FDTD simulations in this work were performed using Lumerical FDTD Solutions software from Lumerical Inc. [49], which applies a variant of the standard FDTD algorithm detailed in section 2.2.1.

2.2.1 The FDTD algorithm

The most commonly used algorithm for performing FDTD simulations was initially proposed by K. Yee [50], which we cover the principle of here. First, we consider Maxwell's equations in an isotropic medium with no free charges or currents:

$$\begin{aligned} \nabla \cdot [\epsilon(\mathbf{r})\mathbf{E}(\mathbf{r}, t)] &= 0, & \nabla \times \mathbf{E}(\mathbf{r}, t) &= -\mu(\mathbf{r})\frac{\partial \mathbf{H}(\mathbf{r}, t)}{\partial t}, \\ \nabla \cdot [\mu(\mathbf{r})\mathbf{H}(\mathbf{r}, t)] &= 0, & \nabla \times \mathbf{H}(\mathbf{r}, t) &= \epsilon(\mathbf{r})\frac{\partial \mathbf{E}(\mathbf{r}, t)}{\partial t}, \end{aligned} \tag{2.1}$$

where $\epsilon(\mathbf{r})$ and $\mu(\mathbf{r})$ are the permittivity and permeability of the medium, respectively, at position \mathbf{r} . Evidently, the time evolution of the fields is encapsulated by the two curl equations, which we wish to apply a finite-difference approach to. In Yee's algorithm, the fields are propagated in discrete time steps, Δt , using a "leapfrog" approach: the \mathbf{E} field is updated at integer time steps, $n\Delta t$, and the \mathbf{H} field is updated at half-integer time steps, $(n + 1/2)\Delta t$. The fields are therefore updated according to

$$\mathbf{E}^{n+1}(\mathbf{r}) = \mathbf{E}^n(\mathbf{r}) + \frac{\Delta t}{\epsilon(\mathbf{r})} \nabla \times \mathbf{H}^{n+\frac{1}{2}}(\mathbf{r}), \quad (2.2)$$

$$\mathbf{H}^{n+\frac{1}{2}}(\mathbf{r}) = \mathbf{H}^{n-\frac{1}{2}}(\mathbf{r}) - \frac{\Delta t}{\mu(\mathbf{r})} \nabla \times \mathbf{E}^n(\mathbf{r}), \quad (2.3)$$

where, for example, \mathbf{E}^n represents the value of \mathbf{E} recorded at time step n . A finite difference approach is also required in the spatial domain, in order to calculate the curl of the fields. The two curl equations from 2.1 can be divided up to give 6 equations, one to govern the time-dependence of each field component:

$$\begin{aligned} \frac{\partial H_x}{\partial t} &= -\frac{1}{\mu} \left(\frac{\partial E_z}{\partial y} - \frac{\partial E_y}{\partial z} \right), & \frac{\partial E_x}{\partial t} &= \frac{1}{\epsilon} \left(\frac{\partial H_z}{\partial y} - \frac{\partial H_y}{\partial z} \right), \\ \frac{\partial H_y}{\partial t} &= -\frac{1}{\mu} \left(\frac{\partial E_x}{\partial z} - \frac{\partial E_z}{\partial x} \right), & \frac{\partial E_y}{\partial t} &= \frac{1}{\epsilon} \left(\frac{\partial H_x}{\partial z} - \frac{\partial H_z}{\partial x} \right), \\ \frac{\partial H_z}{\partial t} &= -\frac{1}{\mu} \left(\frac{\partial E_y}{\partial x} - \frac{\partial E_x}{\partial y} \right), & \frac{\partial E_z}{\partial t} &= \frac{1}{\epsilon} \left(\frac{\partial H_y}{\partial x} - \frac{\partial H_x}{\partial y} \right), \end{aligned} \quad (2.4)$$

and so a finite-difference approximation can be made to update the field components from these 6 equations. The novelty of Yee's FDTD algorithm was to devise a particular lattice geometry which allows an efficient and effective finite-difference approach to evolving the fields. Space is divided up into cells, often referred to as Yee cells, of dimensions $\Delta x \times \Delta y \times \Delta z$, which record individual field components at specific locations, as shown in Fig. 2.2. Many Yee cells build up a simulation mesh in which the \mathbf{E} and \mathbf{H} field components are recorded at interlaced positions, so that a given field component can be calculated from the relevant components half a cell spacing away. This allows a finite difference approach to the 6 equations (2.4) to be applied in order to update each field component. If we use the indices (i, j, k) to represent the position $(i\Delta x, j\Delta y, k\Delta z)$, then two examples of updating the E_x and H_x field components via the finite-difference approach are:

$$\begin{aligned}
 E_x^{n+1}(i+1/2, j, k) &= E_x^n(i+1/2, j, k) \\
 &+ \frac{\Delta t}{\epsilon \Delta y} \left[H_z^{n+1/2}(i+1/2, j+1/2, k) - H_z^{n+1/2}(i+1/2, j-1/2, k) \right] \\
 &- \frac{\Delta t}{\epsilon \Delta z} \left[H_y^{n+1/2}(i+1/2, j, k+1/2) - H_y^{n+1/2}(i+1/2, j, k-1/2) \right], \\
 & \\
 H_x^{n+1/2}(i, j+1/2, k+1/2) &= H_x^{n-1/2}(i, j+1/2, k+1/2) \\
 &+ \frac{\Delta t}{\mu \Delta z} \left[E_y^n(i, j+1/2, k+1) - E_y^n(i, j+1/2, k) \right] \\
 &- \frac{\Delta t}{\mu \Delta y} \left[E_z^n(i, j+1, k+1/2) - E_z^n(i, j, k+1/2) \right].
 \end{aligned} \tag{2.5}$$

A similar approach can be applied to the other 4 field components; more details about the FDTD algorithm, including expressions for the other field components, can be found in the textbook by Taflov and Hagness [51].

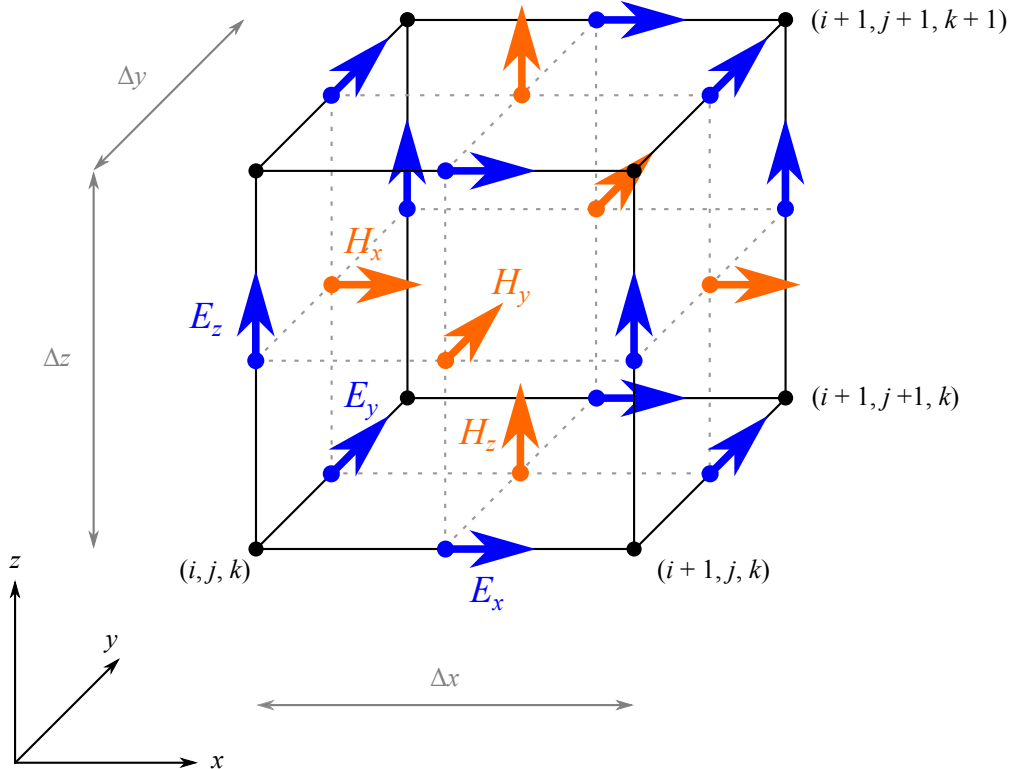


Figure 2.2: The Yee cell used to construct the simulation mesh for FDTD simulations, which records field components at specific points.

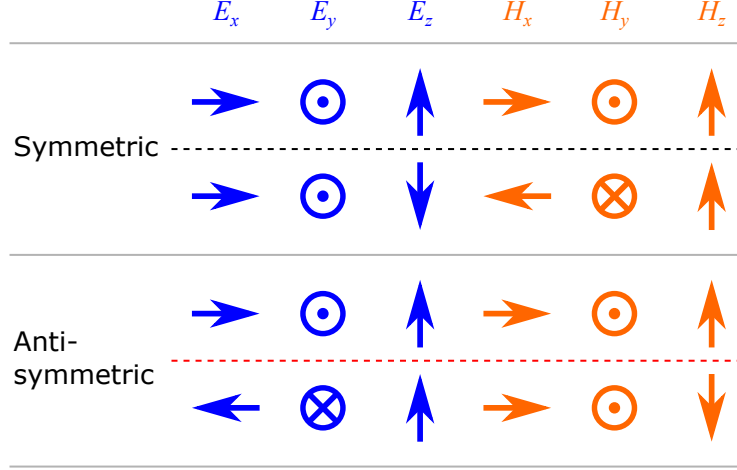


Figure 2.3: Transformation of the \mathbf{E} and \mathbf{H} field components under symmetric (black dashes) and anti-symmetric (red dashes) reflection about a z -plane of symmetry.

2.2.2 Symmetry

Symmetry plays a key role in the physics of PhCs, and can be exploited in FDTD simulations to select for certain modes, in addition to reducing the computational requirements. If we consider a structure with reflection symmetry about the plane $z = 0$, the fields can either transform symmetrically or anti-symmetrically about the plane of symmetry. A rigorous mathematical proof of this can be found in the textbook by Joannopoulos *et al.* [39](Ch. 3, pp. 37–39). The appropriate transformations of the \mathbf{E} and \mathbf{H} field components under symmetric (S) and anti-symmetric (AS) reflection about $z = 0$ are shown in Fig. 2.3. Note that as \mathbf{H} is a pseudovector, its components transform inversely to the \mathbf{E} field components.

The S and AS reflection rules have far-reaching consequences for the modes supported by a structure with reflection symmetry about $z = 0$, such as the 2D PhCs that are of interest in this project (see Fig. 2.5, for example). As the fields cannot be discontinuous, certain field components are constrained to be zero in the plane of symmetry. A mode with S symmetry about $z = 0$ must have $H_x = 0$, $H_y = 0$ and $E_z = 0$ at $z = 0$, whereas a mode with AS symmetry must have $E_x = 0$, $E_y = 0$ and $H_z = 0$ at $z = 0$. Thus, due to z -symmetry, a mode can either be transverse-electric (TE) polarised at $z = 0$, with only E_x , E_y and H_z components in the plane of symmetry, or transverse-magnetic (TM) polarised at $z = 0$, with only H_x , H_y and E_z components in this plane. If the structure extends infinitely in z , then it possesses reflection symmetry about any choice of z -plane. As a result, each mode is restricted to being either solely TE or solely TM polarised. The TE and TM modes are completely orthogonal, which prevents interaction between them, and is

crucial to the operation of a 2D PhC, which typically possesses a photonic band gap for either TE or TM modes, and not both (see Ch. 8 of the textbook by Joannopoulos *et al.* [39]).

In the case of a finite PhC slab with z -symmetry, such as the one examined in section 2.3.4, the reflection symmetry only applies at the centre of the slab (which we choose as $z = 0$) and the modes are only restricted to TE and TM polarisation in this plane. However, away from $z = 0$, it is possible for the modes to still possess predominantly TE or TM field components, accordingly, due to field continuity. The modes are then described as TE-like and TM-like, possessing mostly orthogonal components to each other, which enables PhC slabs of finite thickness to operate with a photonic band gap for TE-like or TM-like modes only.

In FDTD simulations, S or AS symmetry conditions can be applied, which copy the fields under the corresponding reflection transformation in a given plane. This not only cuts the computational time by half per symmetry plane (particularly important for FDTD simulations, which are highly demanding computationally), but allows us to select for certain modes that we wish to focus on. For example, by applying an S or AS symmetry condition at $z = 0$, TE/TE-like or TM/TM-like modes can be selected for, respectively. Similarly, symmetry of the structure can be exploited by applying S or AS symmetry conditions at the $x = 0$ or $y = 0$ planes. However, care must be taken when applying symmetry conditions, in order to prevent non-physical results. Both the structure and the sources must possess the reflection symmetry, so the source must be chosen carefully. In this work, an electric or magnetic dipole source is used with an appropriate orientation that obeys the symmetry conditions. More details about the application of symmetry conditions to PhC cavity simulations are provided in section 2.4.1.

2.2.3 Boundary conditions

Boundary conditions are required at the edges of the FDTD simulation mesh, which can either be used to emulate the effects of the surrounding media, or as a tool to simulate periodic structures. Two types of boundary conditions are used in this work, the first of which is the perfectly matched layer (PML) boundary condition. A PML refers to an artificial layer of material, usually placed at the edge of the simulation region, which is designed to absorb incident electromagnetic fields with minimal reflections [52]. PML boundary conditions are used to model open boundaries, as if the media at the edges of the simulation mesh extend beyond the simulation boundaries. PML boundaries were typically applied in this work when modelling any device with a finite extent, so

that electromagnetic radiation propagating away from the device was not reflected at the simulation edges. This provides a good match to the physical situation of the real PhC slab devices, for which the surrounding air/vacuum and substrate extend much further than the dimensions of the simulation mesh. The default settings of the Lumerical FDTD Solutions software were used to configure the PML boundary conditions: a PML thickness of 8 cells.

Where PML boundary conditions were used around a structure, so-called “padding” regions were also inserted: regions of uniform cladding or substrate, which prevent the PML boundaries from interacting undesirably with evanescent fields in the structure. Unless stated otherwise, the thickness of each padding region was $\lambda_0/2$, where λ_0 is the wavelength of the cavity mode in air. A thickness of $\lambda_0/2$ was chosen based on the general rule that the PML boundaries should be situated at least half of the longest wavelength (of the simulated electromagnetic fields) away from the structure [52].

Boundary conditions can also be used as a tool to simulate infinitely repeating structures, by applying periodic boundary conditions at the edges of the simulation region. This is relevant to the photonic band structure simulations performed for the PhC structures in this work, which make use of Bloch boundary conditions – a special type of periodic boundary condition. The application and function of the Bloch boundary condition is explained in section 2.3.2, where it is applied in photonic band structure calculations.

2.2.4 Resolution

The Lumerical FDTD Solutions software includes functionality for an automatically-generated, non-uniform simulation mesh. The size of the Yee cells is allowed to vary across the simulation volume, which enables structures to be simulated with optimal computational speed and accuracy. A finer mesh (optimal accuracy) can be applied in regions of the structure where fine details in the geometry and interactions of the fields are expected to be critical, whereas a coarser mesh (optimal speed) can be used away from these areas, where the interactions of the fields are less important. In the simulations performed, a mesh override region is applied over the PhC slab, which forces each Yee cell to be identical, with cell dimensions set by the user. The rest of the simulation mesh is non-uniform and set by the software’s algorithms.

For a PhC slab defined in the x - y plane, centred at $z = 0$, with a thickness z_{slab} [see Figs. 2.5(a) and 2.7], the mesh override region is set between $-z_{\text{slab}}/2$ and $z_{\text{slab}}/2$ in z , and set to cover the

extent of the periodic pattern of the PhC in the x - y plane (excluding the padding regions). We choose not to use cubic Yee cells, so that the mesh can better fit the simulated structure. To ensure that the mesh provides a good fit, we apply the constraints that the mesh must follow the same periodicity as the PhC lattice in x and y , and there must be an integer number of cells across the z -extent of the slab. Three mesh resolution parameters, ρ_x , ρ_y , and ρ_z are defined; ρ_x and ρ_y correspond to the number of cells per period of the PhC lattice in the x and y directions, respectively. Therefore, in the override region:

$$\Delta x = a_x / \rho_x, \quad \Delta y = a_y / \rho_y, \quad (2.6)$$

where a_x and a_y are the period of the PhC lattice in the x and y direction. The definition of ρ_z is slightly more complicated: if we consider a situation in which we set $\rho_x = \rho_y = \rho_z$, then intuitively we wish to have mesh cells with $\Delta x \approx \Delta y \approx \Delta z$, except for the constraints discussed previously. For the structures considered, z_{slab} is considerably smaller than a_x and a_y , so if we chose the seemingly obvious definition $\Delta z = z_{\text{slab}} / \rho_z$, then a mesh with $\rho_x = \rho_y = \rho_z$ would not have $\Delta x \approx \Delta y \approx \Delta z$. Instead, it is useful to define Δz relative to a_x or a_y – we choose to define it relative to a_y because it is smaller than a_x for the structures simulated. We therefore wish to define a relation between Δz and ρ_z so that $\Delta z \approx a_y / \rho_z$, but which also assures an integer number of cells across the z extent of the slab. These conditions are met using the definition:

$$\Delta z = z_{\text{slab}} \left[\text{ceil} \left(\frac{\rho_z z_{\text{slab}}}{a_y} \right) \right]^{-1}, \quad (2.7)$$

where ceil is the ceiling function, which rounds a non-integer argument up to the nearest integer. Using this definition, setting $\rho_x = \rho_y = \rho_z$ yields a mesh with $\Delta x \approx \Delta y \approx \Delta z$, as desired. The rest of the simulation mesh, away from the override region, is non-uniform and determined via the software’s algorithms. The cells gradually increase in size the further from the override region they are, reaching a typical maximum size of $30 \text{ nm} \times 30 \text{ nm} \times 90 \text{ nm}$ at the furthest point from the structures simulated (with $a = 340 \text{ nm}$). In addition to automatic meshing, Lumerical FDTD Solutions applies proprietary “Conformal Mesh Technology” [53], which accounts for sub-cell structural variations through application of integral forms of Maxwell’s equations near structure boundaries, to improve simulation accuracy.

The temporal resolution of the FDTD simulation is automatically handled by Lumerical FDTD

Solutions, based on the time stability condition:

$$C_f < \frac{n_{\min}}{\sqrt{d}}, \quad C_f = \frac{c\Delta t}{\delta}, \quad (2.8)$$

where C_f is the Courant factor, n_{\min} is the minimum refractive index in the simulation, d is the number of spatial dimensions and δ is the smallest cell dimension in the entire simulation mesh. This stability criterion is derived from the maximum propagation speed of fields in the simulation volume [54](Ch. 3, pp. 163–164), and puts a theoretical maximum, Δt_{\max} , on the time step:

$$\Delta t_{\max} = \frac{n_{\min}\delta}{c\sqrt{d}}. \quad (2.9)$$

In the simulations performed in this work, the time step was set to $\Delta t = 0.99\Delta t_{\max}$ – the default for the software.

2.3 Photonic band structure of a photonic crystal slab

In this section, the photonic band structure of a hexagonal hole-in-slab PhC is simulated using FDTD methods. This PhC structure forms the basis of the nano-scale optical devices studied in this work. We first review the properties of hexagonal lattices and the corresponding reciprocal lattice, followed by the general method of performing band structure calculations using FDTD simulations. Finally, the technique is applied to calculate the band structure of the hexagonal PhC slab relevant to this work, first as a simplified 2D structure and then as a full 3D PhC slab.

2.3.1 The hexagonal lattice

To calculate the band structure of a hexagonal PhC slab, we first need to identify the unit cell of the real lattice and the first Brillouin zone of the corresponding reciprocal lattice. We consider a slab of GaAs with a hexagonal lattice of circular air holes etched into it (with lattice constant a), as shown in Fig. 2.4(a). A choice of unit cell and primitive lattice vectors, \mathbf{a}_1 and \mathbf{a}_2 , is shown. The primitive vectors are given by

$$\mathbf{a}_1 = a \left(\frac{1}{2}, \frac{\sqrt{3}}{2} \right), \quad \mathbf{a}_2 = a \left(-\frac{1}{2}, \frac{\sqrt{3}}{2} \right), \quad (2.10)$$

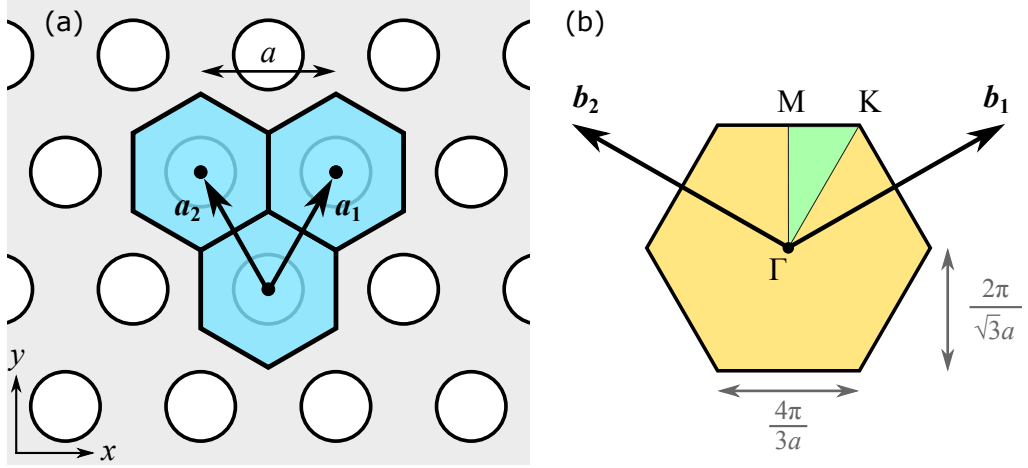


Figure 2.4: 2D hexagonal hole-in-slab PhC and the corresponding first Brillouin zone. (a) Schematic representation of the PhC slab: a hexagonal array of air holes (white), with lattice constant a , is etched into a GaAs slab (grey). A choice of unit cell is shown in blue (3 are shown), in addition to two choices of primitive lattice vector, \mathbf{a}_1 and \mathbf{a}_2 . (b) First Brillouin zone of the corresponding reciprocal lattice, with two choices of primitive lattice vector, \mathbf{b}_1 and \mathbf{b}_2 , shown. Annotations Γ , M and K indicate high-symmetry points.

and as the hexagonal lattice is a Bravais lattice, any lattice point can be obtained by an integer combination of these vectors.

Analogous to the Bloch wavefunctions of electrons in a crystal lattice, the periodic refractive index of the PhC gives rise to Bloch modes of the form

$$\mathbf{E}_{\mathbf{k}}(\mathbf{r}) = e^{i\mathbf{k} \cdot \mathbf{r}} \mathbf{u}_{\mathbf{k}}(\mathbf{r}), \quad (2.11)$$

$$\mathbf{u}_{\mathbf{k}}(\mathbf{r}) = \mathbf{u}_{\mathbf{k}}(\mathbf{r} + \mathbf{R}), \quad (2.12)$$

where $\mathbf{E}_{\mathbf{k}}(\mathbf{r})$ is the electric field of the Bloch mode with wave vector \mathbf{k} and $\mathbf{u}_{\mathbf{k}}(\mathbf{r})$ is the periodic component of the Bloch mode with the same periodicity as the lattice. The lattice vector, \mathbf{R} , is a discrete combination of primitive lattice vectors, which always corresponds to a point in the lattice. In general, for a 3D Bravais lattice, the lattice vector is defined by

$$\mathbf{R} = n_1 \mathbf{a}_1 + n_2 \mathbf{a}_2 + n_3 \mathbf{a}_3, \quad (2.13)$$

where n_i are integers and \mathbf{a}_i are the primitive lattice vectors. A useful concept when working with a Bravais lattice is its reciprocal lattice, which represents its Fourier transform and is itself a Bravais lattice. An important consequence of the periodicity of the lattice is that the Bloch modes within the same band with a \mathbf{k} vector that differs by a reciprocal lattice vector, \mathbf{G} , are identical:

$$\mathbf{E}_{n,\mathbf{k}} = \mathbf{E}_{n,\mathbf{k}+\mathbf{G}}, \quad (2.14)$$

$$\mathbf{G} = m_1 \mathbf{b}_1 + m_2 \mathbf{b}_2 + m_3 \mathbf{b}_3, \quad (2.15)$$

where n denotes the band index, m_i are integers and \mathbf{b}_i are the primitive reciprocal lattice vectors. As a result of this, the band structure can be fully described by \mathbf{k} vectors in the first Brillouin zone, which is the unit cell of the reciprocal lattice. To find the first Brillouin zone, we first find the primitive vectors of the reciprocal lattice. In general, the primitive vectors of a 3D reciprocal lattice are given by:

$$\mathbf{b}_1 = \frac{2\pi (\mathbf{a}_2 \times \mathbf{a}_3)}{\mathbf{a}_1 \cdot (\mathbf{a}_2 \times \mathbf{a}_3)}, \quad \mathbf{b}_2 = \frac{2\pi (\mathbf{a}_3 \times \mathbf{a}_1)}{\mathbf{a}_1 \cdot (\mathbf{a}_2 \times \mathbf{a}_3)}, \quad \mathbf{b}_3 = \frac{2\pi (\mathbf{a}_1 \times \mathbf{a}_2)}{\mathbf{a}_1 \cdot (\mathbf{a}_2 \times \mathbf{a}_3)}. \quad (2.16)$$

As the PhC is a 2D lattice, which can be considered homogeneous in the z -direction, we are free to choose $\mathbf{a}_3 = (0, 0, 1)$, the unit vector in the z -direction. Therefore, for the 2D hexagonal reciprocal lattice, two possible choices of primitive vector are:

$$\mathbf{b}_1 = b \left(\frac{\sqrt{3}}{2}, \frac{1}{2} \right), \quad \mathbf{b}_2 = b \left(-\frac{\sqrt{3}}{2}, \frac{1}{2} \right), \quad (2.17)$$

$$b = \frac{4\pi}{\sqrt{3}a},$$

where b is the lattice constant of the reciprocal lattice. The first Brillouin zone of the reciprocal lattice, in addition to these two choices of primitive vector, are shown in Fig. 2.4(b). It is evident that the reciprocal lattice is another hexagonal lattice, rotated by 30° . In the band structure simulations that follow in this chapter, we wish to calculate the allowed frequencies of the Bloch modes for \mathbf{k} vectors within the first Brillouin zone. Specifically, \mathbf{k} are chosen along the directions of the high symmetry points Γ , M and K, labelled on the Brillouin zone. More details about the reciprocal lattice and the Brillouin zone can be found in the appendices of the textbook by Joannopoulos *et al.* [39].

2.3.2 Applying the FDTD method

Simulating the photonic band structure of a PhC using the FDTD method requires the Bloch modes to be excited and measured. We wish to obtain the frequencies, $\omega(\mathbf{k})$ at which the Bloch modes are permitted for each value of \mathbf{k} within the first Brillouin zone (as this completely characterises the band structure). This is achieved with the FDTD method by performing multiple simulations – each one for a different \mathbf{k} – and measuring the frequency response, for example by using multiple dipole sources to excite the Bloch modes. A unit cell of the PhC is simulated with periodic Bloch boundary conditions enforced at the boundaries of the cell, which replicates an infinitely repeating structure through which the modes can propagate. The Bloch boundary conditions apply a phase correction to the fields at the edges of the simulation region according to the wave vector, \mathbf{k} , assigned to the simulation. For example, Bloch boundaries at x_{\min} and x_{\max} , the minimum and maximum bounds of the simulation in the x dimension, perform the operations:

$$\mathbf{E}(x_{\min}, y, z) = e^{-ia_x k_x} \mathbf{E}(x_{\max}, y, z) \quad (2.18)$$

$$\mathbf{E}(x_{\max}, y, z) = e^{ia_x k_x} \mathbf{E}(x_{\min}, y, z), \quad (2.19)$$

where a_x is the width of the unit cell in the x dimension and k_x is the x component of \mathbf{k} . Similar logic applies for y and z Bloch boundaries and for the magnetic field. These conditions are necessary to correctly conserve the phase of the simulated Bloch modes, which would not be the case if the field was simply duplicated at the boundaries.

In the band structure calculations that follow in this chapter, simulations are run using multiple dipole sources with principally random phase and orientation (apart from constraints due to symmetry) to excite the Bloch modes. The resulting electric field is monitored in the time domain at multiple randomly selected positions and the frequency response at each location is obtained from the Fourier transform of the temporal signal. To calculate the allowed frequencies of the Bloch modes, the spectra from all of the locations are summed together and peak fitting is performed on the resulting spectrum. This is performed for multiple \mathbf{k} vectors within the first Brillouin zone and the results are compiled to give the band structure, such as the one shown in Fig. 2.6. The band structure calculation method detailed here was adapted from examples included with the Lumerical FDTD Solutions software.

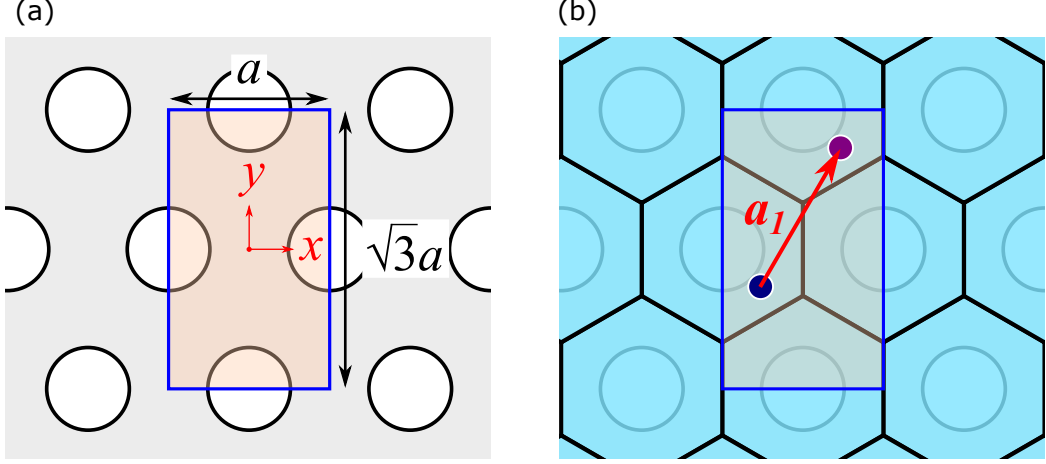


Figure 2.5: Schematics of the FDTD simulation region used to calculate the band structure of the 2D hexagonal PhC. (a) The choice of supercell used as the simulation region (shaded orange), with Bloch boundaries shown in blue. (b) Schematic diagram demonstrating the 4 unit cells of the hexagonal lattice intersected by the supercell. A dipole positioned at the blue point must be duplicated and offset by primitive lattice vector \mathbf{a}_1 (purple point) to ensure that all unit cells of the hexagonal lattice are excited identically. A phase correction must also be applied.

2.3.3 Band structure of a 2D hexagonal photonic crystal

We first simulate the PhC in two dimensions only, which can be considered as extending infinitely in the z -direction. In this case, the modes of the PhC are pure TE and TM modes, which are orthogonal. Hole-in-slab PhCs generally exhibit a band gap for TE modes (whereas dielectric rods surrounded by air generally exhibit a TM mode gap), so we calculate the TE band structure of the PhC.

We simulate a slab of GaAs, with refractive index $n_{\text{slab}} = 3.33$ at cryogenic temperatures [55], with a hexagonal lattice of circular holes etched into it, containing air or vacuum (refractive index 1). A lattice constant of $a = 340 \text{ nm}$ and a hole radius of $r = 0.27a$ were chosen, based on favourable parameters for PhC-based cavities presented in the literature [19, 34, 56, 57] and also on target cavity mode wavelengths close to $1.3 \mu\text{m}$ in the experimentally-realised devices.

The simulation region for the band structure calculation is shown in Fig. 2.5(a), which spans a distance a in the x -direction and $\sqrt{3}a$ in the y -direction. Bloch boundary conditions are applied to the edges of the simulation region, as discussed in section 2.3.2. As the unit cell of the hexagonal PhC lattice is not square or rectangular, it is not possible to simulate only one unit cell in the simulation region, which must fit the rectangular Yee cells of the FDTD method. Instead, we simulate a rectangular supercell, which contains multiple unit cells [as shown in Fig. 2.5(b)]. The supercell chosen is just one possible choice.

When simulating a supercell, care must be taken not to introduce artificial band folding to the band structure by incorrectly treating the supercell as the unit cell. We must ensure that each unit cell of the structure is excited identically, with a phase correction applied according to the Bloch wave vector. It can be seen in Fig. 2.5(b) that the supercell intersects 4 unit cells, and contains 2 complete unit cells in total. For a given position within the supercell, there is only one other position inside the supercell that corresponds to the same point in the unit cell. This is illustrated by the blue and purple points in Fig. 2.5(b) - all other equivalent positions in the unit cell lie outside of the supercell. Therefore, in order to excite each unit cell identically, a dipole source placed in the simulation region was duplicated (including its phase and orientation) at the equivalent unit cell position by offsetting it by the primitive lattice vector \mathbf{a}_1 (as long as this new position was also inside the simulation region). Additionally, a phase correction, $\Delta\phi = \mathbf{k} \cdot \mathbf{a}_1$, was applied to the duplicate dipole. Three electric dipole sources were placed in the supercell in this manner to excite the Bloch modes, with a total number of 6 dipoles after duplication and phase correction. The orientation and phase of the original dipoles was random, except all were oriented perpendicular to the z -direction so that the dipoles oscillate in the plane of the PhC and excite TE modes only. Placement of the dipoles was such that both the original and duplicate were at least 20% of the simulation span away from the Bloch boundaries, to prevent problems with field injection.

The 2D TE band structure was simulated by running a simulation sweep over the desired in-plane wave vectors, which we label \mathbf{k}_{\parallel} , of the Bloch modes. Each simulation had a duration of $t_{\text{sim}} = 1000 \text{ fs}$ and mesh resolution parameters of $\rho_x = \rho_y = 30$, as defined in section 2.2.4. The resolution parameters were chosen based on convergence testing of cavities in hexagonal PhC slabs covered in sections 2.4–2.6. Broadband sources were used to excite the modes, covering a frequency range from 1 THz to 500 THz. 20 \mathbf{k}_{\parallel} points, evenly spaced along each of the high symmetry directions, Γ -M, M-K and K- Γ , were simulated. The bands at each \mathbf{k}_{\parallel} vector were obtained by measuring the electric field in the time domain at 10 random locations in the simulation region. Gaussian apodization was performed on each field-time signal using a Gaussian window centred at $0.5 t_{\text{sim}}$, with a FWHM of $0.25 t_{\text{sim}}$, in order to remove edge effects from the sources at the start of the simulation and also from cutting off the Bloch modes at the end of the simulation. Each apodized signal was Fourier transformed to obtain a frequency-domain spectrum and the contributions from each of the 10 locations were summed. Peaks in this combined spectrum were then identified for each of the \mathbf{k}_{\parallel} vectors to provide a calculation of the band structure, the results

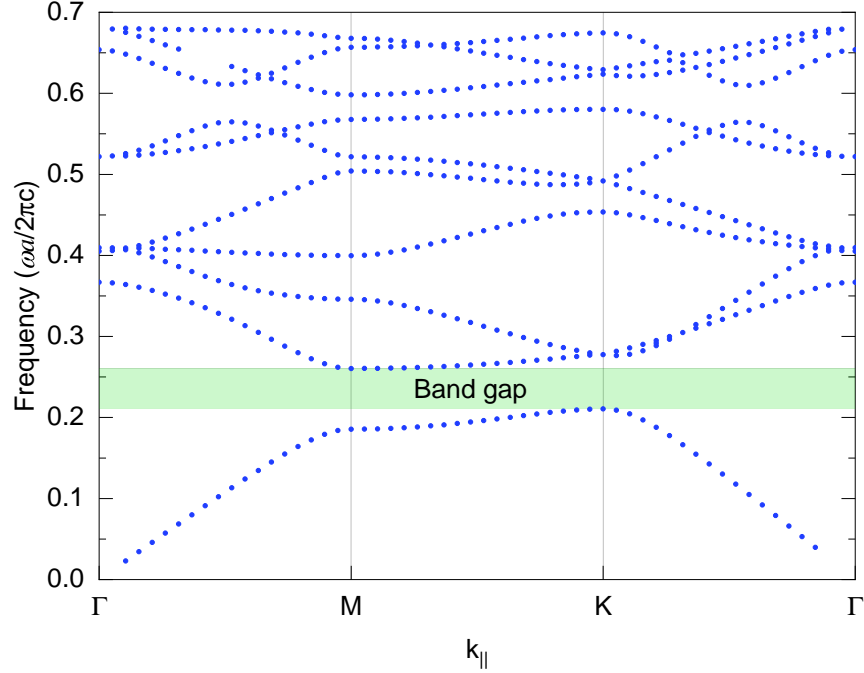


Figure 2.6: TE band structure obtained from 2D FDTD simulations of the hexagonal hole-in-slab PhC. Bands (blue points) are identified from FDTD simulations for multiple in-plane Bloch wave vectors, $\mathbf{k}_{||}$, in the first Brillouin zone. A TE band gap is exhibited.

of which are presented in Fig. 2.6.

From the simulation results in Fig. 2.6, clear bands of the TE Bloch modes can be seen, which exhibit a band gap between $\omega = 0.210a/2\pi c$ and $\omega = 0.260a/2\pi c$. Between these frequencies, light is forbidden from propagating through the PhC due to destructive interference of the Bragg reflections at the refractive index boundaries. Therefore, the structure can be used to confine TE modes at these frequencies, for example to create optical cavities. We will see in section 2.3.4 that, combined with index-guiding in the z -direction, this allows TE-like modes to be confined in the plane of a PhC slab with a finite (but thin) z -extent.

As each of the data points in the band structure in Fig. 2.6 is obtained from peak fitting of the frequency response, they cannot definitively be attributed to a particular band. The bands are therefore not connected. An evident limitation of the technique is that some bands have missing data points, due to peaks not being correctly identified. This is often the case when multiple bands are close together in frequency-space or if artefacts from the Fourier transform (due to incomplete decay of the modes) contribute too much background noise to allow easy identification of the less intense peaks. However, this is often not an issue for the bands of highest interest, near the band gap.

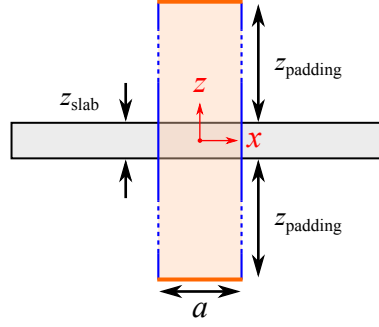


Figure 2.7: Side profile of the PhC slab (not to scale). Bloch boundary conditions are drawn in blue and PML boundary conditions are drawn in orange.

2.3.4 Band structure of a hexagonal photonic crystal slab

We now calculate the band structure of a hexagonal PhC structure with a finite z -extent: a 3D slab with a 2D hexagonal lattice of air holes etched into it. It will be shown that this structure can also exhibit an in-plane band gap, which is facilitated by the vertical confinement provided by index guiding (total internal reflection), due to the refractive index contrast at the top and bottom of the slab.

We consider a 200 nm-thick slab ($z_{\text{slab}} = 200$ nm) surrounded by air. The side-profile of the slab is shown in Fig. 2.7 and the top-down view is the same as in Fig. 2.5(a). The choice of slab thickness is a balance between being thin enough to guide the fundamental mode (with a single node in the z -direction), while still being thick enough to guide the modes effectively (see Ch. 8 in Joannopoulos *et al.* [39] for more details). A slab thickness of ~ 200 nm is typical for air-membrane PhC structures [19, 32, 33, 57, 58, 59] and is the target thickness for experimental devices in this work.

The finite z -extent of the PhC slab means that it possesses z -reflection symmetry only through the plane $z = 0$. A consequence of this is that the Bloch modes cannot be purely TE or TM polarised, as was discussed in section 2.2.2. However, as long as the slab is z -symmetric and thin, it still supports TE-like and TM-like modes, with predominantly their respective components. At the centre of the slab ($z = 0$), these modes are purely TE or TM polarised, but can have any field components away from $z = 0$, due to the effects of confinement from the slab. Despite this, as a result of field continuity, the modes largely maintain their TE-like or TM-like character when confined to a narrow slab. This means that the TE-like and TM-like modes are mostly orthogonally

polarised to each other and interact little, making it possible for the TE-like band gap expected from a hole-in-slab type PhC to still provide in-plane confinement.

The x - y dimensions of the supercell used for the FDTD simulation were the same as those used for the 2D simulation [Fig. 2.5(a)]. The z -extent of the cell is illustrated in Fig. 2.7. PML boundary conditions were placed a distance $z_{\text{padding}} = 1.5\mu\text{m}$ away from the PhC slab, to absorb fields propagating away from it. As explained in section 2.2.3, padding distances should be set to at least half of the longest wavelength in the simulation. The z extent of the supercell would be unfeasibly large if it was matched to the source limit of 1 THz (a wavelength of $\sim 300\mu\text{m}$), so instead the value of $1.5\mu\text{m}$ was chosen as a compromise. This meant that wavelengths up to $3\mu\text{m}$ could be simulated reliably, which is well below the band gap.

Band structure simulations were performed for the same in-plane wave vectors in the first Brillouin zone, \mathbf{k}_{\parallel} , as those for the 2D simulation in section 2.3.3. Unless stated otherwise, simulation parameters were the same as for the 2D simulation. The same rules were used for placement of the dipole sources for exciting TE-like modes (oscillating in the x - y plane); to excite TM-like modes, the dipoles were set perpendicular to the x - y plane instead. S or AS symmetry conditions were set at the $z = 0$ plane to select for TE-like or TM-like modes, respectively. The z positions of the 10 dipoles were set randomly between the middle ($z = 0$) and top ($z = z_{\text{slab}}/2$) of the slab and were appropriately duplicated to the bottom half of the slab according to the applied symmetry boundary conditions (this is handled automatically by the software). The frequency response was measured by the same method as for the 2D simulation, except the field was measured at 20 points, with z -positions randomly selected between $z = 0$ and $z = z_{\text{slab}}$. This range included a region above the slab, to ensure that modes which leak out of the slab (or have a high field concentration just above the slab) would be recorded. Resolution parameters of $\rho_x = \rho_y = \rho_z = 30$ were used.

The results of the photonic band structure calculation for the PhC slab are shown in Fig. 2.8, which shows the TE-like and TM-like Bloch modes. Compared to the band structure of the 2D structure in Fig. 2.6, the bands are generally shifted up in energy and the band gap now occurs for TE-like modes between $\omega = 0.260a/2\pi c$ and $\omega = 0.319a/2\pi c$, corresponding to wavelengths of approximately $1.31\mu\text{m}$ and $1.07\mu\text{m}$. This covers the $\sim 1.3\mu\text{m}$ target wavelength, at which we wish to create optical devices, and we will see that the combination of the band gap and index guiding can be used to confine light at this wavelength. As for the 2D simulation, it is evident that some data points from the bands are missing, but again this is not the case for the most important

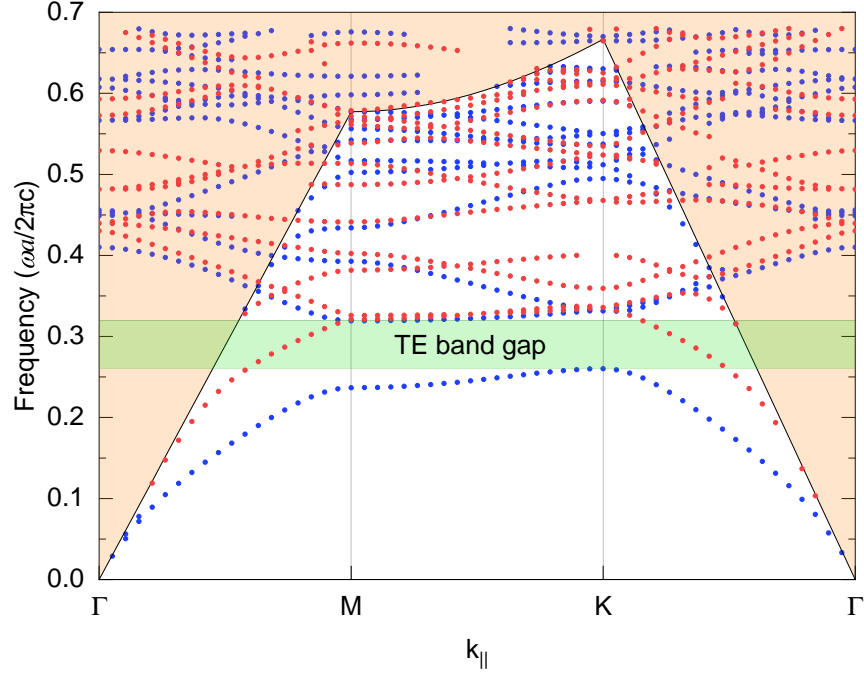


Figure 2.8: Photonic band structure of a hexagonal PhC slab, calculated from 3D FDTD simulations. The TE-like modes are shown by blue points; TM-like modes are shown by red points. The structure exhibits a band gap for TE-like modes. The light cone is shown, with leaky modes in the orange region above it.

bands, close to the band gap.

For a finite slab, the light cone, which is plotted in Fig. 2.8, is an important concept. It represents the boundary between modes which are either guided by the slab or leak into the surrounding air. Only \mathbf{k}_{\parallel} , the in-plane component of the wave vector, is plotted in the band structure, but the k_z component of the wave vector must also be considered. Recalling from Eq. 2.11 that Bloch modes have an $e^{i\mathbf{k}\cdot\mathbf{r}}$ dependence, it is clear that a mode with a real k_z component would propagate away from the slab, which we refer to as a leaky mode. On the other hand, a mode with a purely imaginary k_z is confined to the slab by index guiding and has an evanescent, exponentially-decaying field in the z -direction. These modes are referred to as guided modes. The light cone is defined by

$$\omega_{LC}(\mathbf{k}_{\parallel}) = \frac{c|\mathbf{k}_{\parallel}|}{n_{\text{cladding}}}, \quad (2.20)$$

where n_{cladding} is the refractive index of the surrounding medium and $\omega_{LC}(\mathbf{k}_{\parallel})$ is the frequency of the light cone. In our case, $n_{\text{cladding}} = 1$, since the slab is suspended in air or vacuum. If we consider light outside the slab with $\omega(\mathbf{k}) > \omega_{LC}(\mathbf{k}_{\parallel})$, it follows that $c|\mathbf{k}| > c|\mathbf{k}_{\parallel}|$, which implies k_z is real. Therefore, modes with frequencies above the light cone are leaky. Conversely, modes

with $\omega(\mathbf{k}) < \omega_{LC}(\mathbf{k}_{\parallel})$ have an imaginary k_z and are guided by the slab. We will see in section 2.4.4 that mode leakage to the air is often a limiting factor in PhC cavities, and the device design is frequently optimised to minimise these losses.

The photonic band structure calculated for the hexagonal PhC slab is generally in good agreement with similar structures presented in other work. Examples from the literature [60, 61] and in Ch. 8 of the textbook by Joannopoulos *et al.* [39] for hexagonal PhC slabs with different hole radii and slab thicknesses to those presented here still exhibit similarly shaped bands, especially near the band gap. Good agreement is found with the TE-like band structure in the work by Vučković *et al.* [46], which uses similar parameters to this work. The calculations are also in excellent agreement with results presented by collaborator L. Nuttall in his thesis [1], which were calculated for the same structure using the open source FDTD software, MEEP [62]. The agreement of the presented results with other works provides strong evidence of their accuracy and validity.

2.4 FDTD simulation of a photonic crystal cavity

In this section we will introduce how optical cavities can be created by modifying a 2D PhC slab, like the PhC examined in section 2.3. It will be shown that it is possible to confine light to extremely low-loss cavity modes on a similar scale to its wavelength. As explained in Ch. 3, this is a highly sought-after property, which makes PhC cavities attractive for achieving enhanced light-matter interactions with an embedded emitter.

It was shown in section 2.3.3 that a 2D PhC (with infinite z -extent) can exhibit a complete photonic band gap between certain frequencies, inside which the optical density of states is zero and the propagation of light is forbidden. Cavity modes can be generated in a PhC by perturbing the lattice, so that a region is created which supports a single localized mode, or a set of modes, with frequencies inside the band gap. The simplest perturbation to create a cavity in a PhC slab is to introduce a point defect by altering one of the holes. Alteration of the refractive index [46], hole radius [45], or even complete removal of the hole [63], are all effective methods of generating cavity modes, although the latter two are more easily achieved in a real hole-in-slab type PhC. The modes are confined by the surrounding PhC lattice, inside which the fields must be evanescent (and exponentially decay) because they are at frequencies in the band gap: the PhC acts as a mirror for these frequencies.

In a real PhC slab, with a finite z -span, confinement of light to a cavity mode is still possible

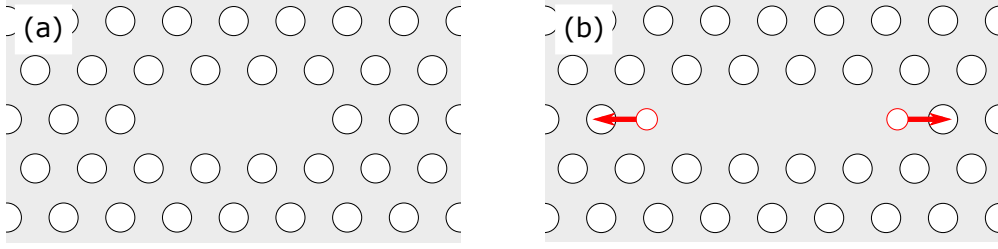


Figure 2.9: L3 cavity formed by removing 3 holes from a hexagonal PhC. (a) Basic L3 cavity, with no alteration of the surrounding holes. (b) An optimised L3 cavity pattern, with the two holes highlighted in red shrunk to a radius of $0.2a$ and shifted by $0.2a$ in the directions indicated by the arrows.

through the combination of index guiding in the z -direction and the in-plane photonic band gap exhibited by the PhC. In section 2.3.4 we demonstrated that a thin slab PhC with a hexagonal lattice of air holes can exhibit an in-plane photonic band gap for TE-like modes, so by introducing a perturbation we expect to be able to confine TE-like cavity modes to the slab. We focus on the L3-type cavity as a simple and highly effective example, which is formed by removing 3 holes in a row from the PhC, as shown in Fig. 2.9(a). The L3 cavity design, which can be optimised by shifting the radii and positions of neighbouring holes [32, 59, 64, 65], is extremely popular in light-matter coupling experiments and has been featured in many high impact publications [19, 20, 66, 67, 68, 69, 70, 71, 72].

The L3 cavity will be used as an example to demonstrate the general methodology applied to perform FDTD simulations of PhC cavities in this work. First, the basic L3 cavity design in Fig. 2.9(a) is simulated, which we will show supports a relatively high quality factor, small mode volume, TE-like cavity mode. This will be compared to an optimised L3 geometry [Fig. 2.9(b)], which introduces an alteration to the position and radius of the neighbouring holes outlined in red. In this example, the highlighted holes are shifted by $0.2a$ in the directions indicated by the arrows and reduced to a radius of $0.2a$. The same design is used in the experimental devices studied in this work, which was chosen based on optimisation work by collaborator F. Brossard. It will be shown that this fine-tuning of the geometry dramatically increases the quality factor of the cavity mode, with minimal effect on the field distribution and the mode volume, as is expected from the literature [32].

2.4.1 Cavity simulation methodology

The general methodology for performing FDTD simulations of cavities in PhC slabs is detailed in this section, using the L3 PhC cavity as an example. The recipe described here is applicable to all other simulations of PhC cavities performed in this work. The PhC structure and simulation region are illustrated schematically in Fig. 2.10: the top-down view of the x - y plane of the PhC is shown in Fig. 2.10(a) and the side profile is shown in Fig. 2.10(b). The FDTD simulation region, which contains the simulation mesh, is shaded orange. The mesh is always defined so that it has the same periodicity as the lattice and for this example resolution parameters (defined in section 2.2.4) of $\rho_x = \rho_y = \rho_z = 30$ are used. Padding regions are inserted between the edges of the PhC structure and the simulation edges, which are terminated by PML boundaries to absorb the radiation propagating away from the structure, as discussed in section 2.2.3. The padding distances are set to $x_{\text{padding}} = y_{\text{padding}} = z_{\text{padding}} = \lambda_0/2$, where λ_0 is the centre wavelength of the source in air (which is set to match the cavity mode). PhC parameters of $a = 340$ nm, $r = 0.27a$ and a slab thickness of $z_{\text{slab}} = 200$ nm are used for simulations, unless stated otherwise.

Symmetry boundary conditions are set to reduce the computation time and also to select for modes with certain symmetries. TE-like or TM-like modes are selected by applying an S or AS symmetry condition at $z = 0$, respectively. The symmetry conditions applied at $x = 0$ and $y = 0$ depend on the geometry of the PhC and the mode of interest: for the fundamental TE-like PhC cavity modes studied in this work (including the L3 cavity), the typical symmetry conditions applied are S at $x = 0$, AS at $y = 0$ and S at $z = 0$. The appropriate $x = 0$ and $y = 0$ symmetries are obtained by examining the field profiles of the modes from shorter initial simulations without the symmetry conditions applied. For the full simulations, as many of these symmetry conditions as possible are applied, except in cases when the structure does not possess the symmetry, or if the mode of interest possesses different symmetry. Electric or magnetic dipole sources are placed in the structure to excite the mode, which are oriented appropriately according to the symmetry conditions (and automatically duplicated by the software to obey the symmetry). At least one of the sources is placed near or at a local antinode of the mode to inject the fields efficiently. As seen in Fig. 2.11, the local antinodes are typically spaced at integer multiples of a or $a/2$ in the x direction, so a strategy frequently applied in this work is to use two dipoles, positioned at $(a/2, 0, 0)$ and $(a, 0, 0)$, to ensure that at least one of them is positioned at an antinode.

To simulate a cavity mode, two FDTD simulations are performed. A shorter, initial simulation is

run, with $t_{\text{sim}} = 1000$ fs and broadband sources to check that a TE-like cavity mode is supported and to record its wavelength via the Fourier transform of the fields (with apodization applied). A second simulation is then performed with a much longer simulation time of $t_{\text{sim}} = 20\,000$ fs and the centre wavelength of the sources set to the value obtained from the first simulation. The longer simulation allows more time for the typically very high Q PhC modes to decay, which enables accurate extraction of parameters from the simulation. It also allows for the sources to be temporally much broader and consequently, much narrower spectrally. Typically the source pulse length is set to ~ 1000 fs FWHM, resulting in a spectral width of ~ 2.5 nm FWHM. The

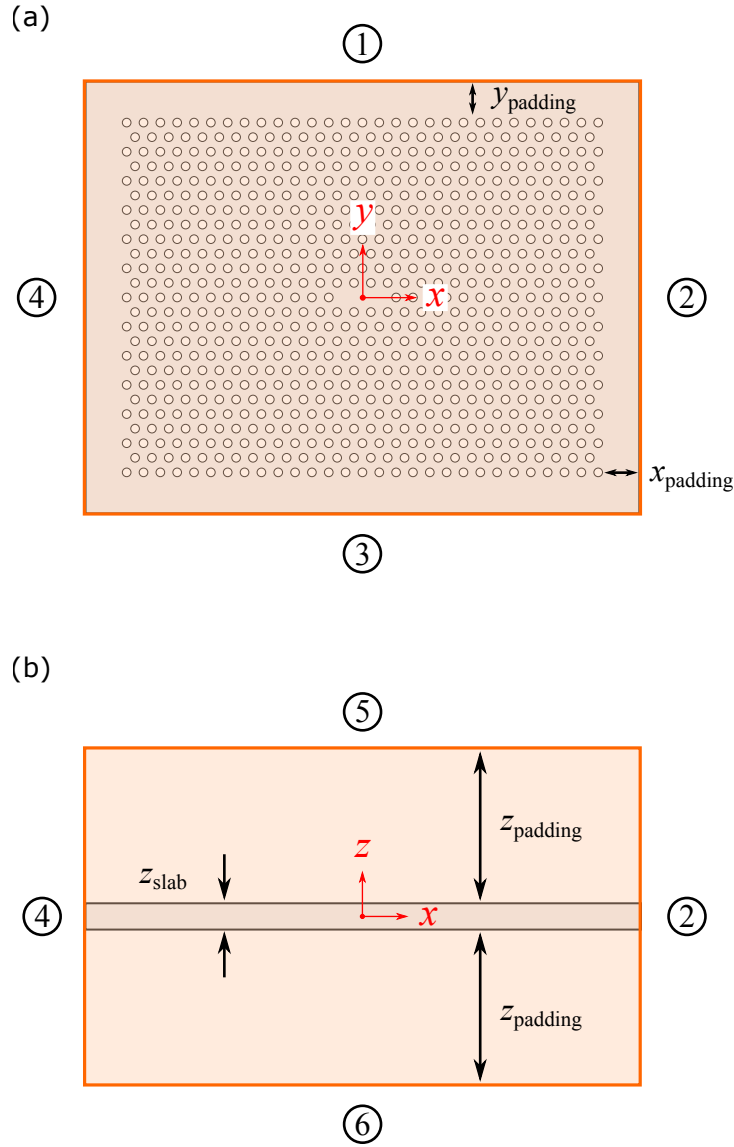


Figure 2.10: Schematic diagram of the simulation region of a PhC cavity, using the L3 cavity as an example. The top-down view (a) and side profile (b) are shown. The FDTD simulation region is shaded in orange, with PML boundaries (labelled 1-6) shown by darker orange planes. Padding distances in each dimension are labelled on the diagrams.

use of narrow sources, combined with selective symmetry conditions, is crucial to ensure that only the mode of interest is excited in the cavity, otherwise extracted parameters (such as the quality factor) will not be valid.

2.4.2 Cavity mode field profiles

It is often useful to visualize the field profile of a simulated cavity mode, in order to understand its field components and distribution. Lumerical FDTD Solutions software uses frequency-domain techniques to extract the profile: the fields are recorded in the time domain and Gaussian apodization is applied to filter out the steady-state oscillations of the cavity (the apodization window is centred at $0.6 t_{\text{sim}}$ with a FWHM of $0.2 t_{\text{sim}}$). A Fourier transform is then performed on the apodized signal, yielding a complex-valued field, $\tilde{\mathbf{E}}(\mathbf{r}, \omega)$ (we focus on the electric field, although similar applies to the magnetic field), which fully encapsulates the magnitude and phase of the field. The field profile of the cavity mode can then be extracted from $\tilde{\mathbf{E}}(\mathbf{r}, \omega)$ at the resonant frequency of the mode, $\omega = \omega_{\text{res}}$. Note that ω_{res} is extracted from Lorentzian peak-fitting of the spectrum.

To obtain a snapshot of the physical field component E_i (where i is x , y , or z), we take $\text{Re} \left[\tilde{E}_i(\mathbf{r}, \omega_{\text{res}}) \right]$. As an example, snapshots of E_x and E_y through the $z = 0$ plane of the L3 cavity (with no hole shift) extracted via this method are presented in Figs. 2.11(a) and 2.11(b). Each has a normalised magnitude between -1 and $+1$, represented by blue and red, respectively. The PhC air-slab boundaries are plotted as the contour $n = (n_{\text{cladding}} + n_{\text{slab}})/2$, extracted directly from the simulation region. It is necessary to take an average index as the contour because the software performs refractive index averaging over boundaries (such as the PhC holes) that do not exactly align with the rectangular simulation cells. Unless stated otherwise, the profiles of individual field components presented in this thesis were acquired and plotted using the method described here.

The field profiles presented in Figs. 2.11(a) and 2.11(b) match those expected for the fundamental mode of the L3 cavity [32, 73, 74], possessing local nodes and antinodes with spacing similar to the lattice. The simulation results also confirmed that the E_z component of the field is always zero at the centre of the slab ($z = 0$), as is expected from a TE-like cavity mode. It is clear that the light is well-confined in-plane by the surrounding PhC, on a scale similar to its wavelength. Additionally, the snapshot of the E_y profile through a cross-section of the slab [the $(x, 0, z)$ plane] in Fig. 2.11(d) demonstrates that the light is relatively well-localized to the slab by index guiding.

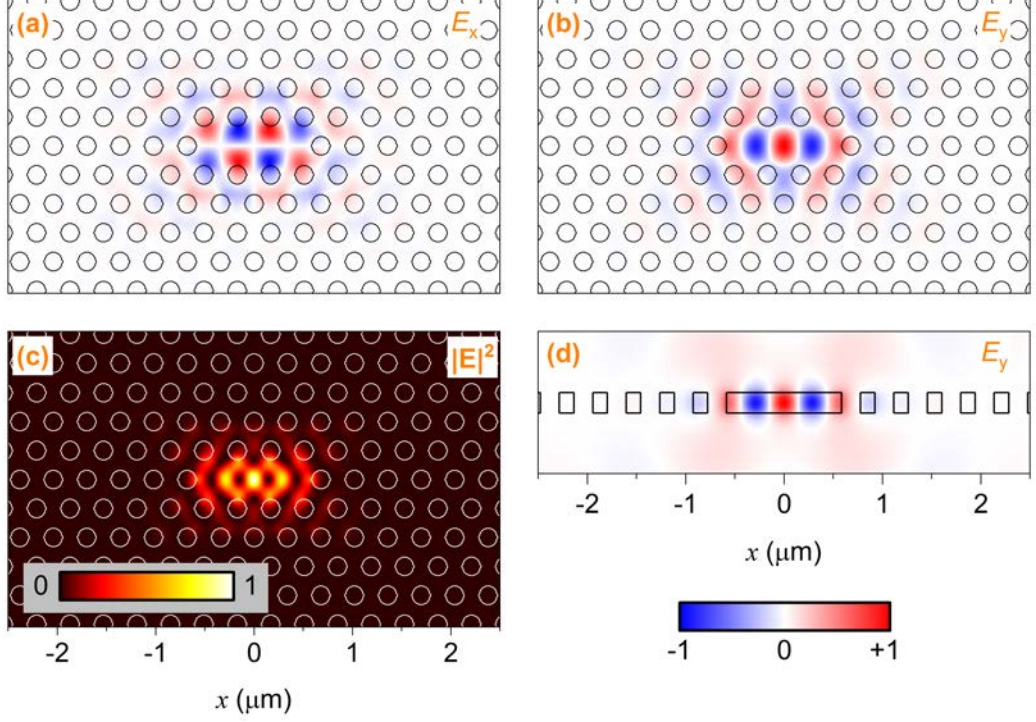


Figure 2.11: Simulated field profile for an L3 cavity with no hole shifts applied. (a) and (b) show snapshots of the E_x and E_y field components through $(x, y, 0)$. (c) $|E|^2$ field envelope of the cavity mode through the same plane. (d) Snapshot of the E_y field component through $(x, 0, z)$. All field magnitudes are normalised; the E_x and E_y components are normalised between -1 (blue) and $+1$ (red) as shown in (d).

We choose to show E_y through this plane because it is the only non-zero electric field component. Some leakage of the mode to the air is evident from the notable fields outside the slab region. It will be shown in section 2.4.4 that this is due to leaky components of the cavity mode with \mathbf{k} vectors outside the light cone.

Another useful visualization of the field profile is to take $|\tilde{\mathbf{E}}(\mathbf{r}, \omega_{\text{res}})|$, which removes the phase dependence and provides the envelope of the field profile. This is useful because it provides information about where the electric field is localized over a full oscillation period of the cavity mode. It is common to plot $|\tilde{\mathbf{E}}(\mathbf{r}, \omega_{\text{res}})|^2$, since the energy contained in the electric field is proportional to E^2 ; this is shown for the L3 cavity in Fig. 2.11(c) (with normalisation applied). The field envelope obtained from $|\tilde{\mathbf{E}}(\mathbf{r}, \omega_{\text{res}})|^2$, which will be referred to as the $|E|^2$ profile in the remainder of this work for brevity, allows the antinodes at which the field energy is concentrated to be identified. We will see in Ch. 3 that this is a crucial consideration, as an emitter must be placed at one of these antinodes to achieve strong light-matter interactions.

2.4.3 Mode parameter calculations

In order to characterise and compare PhC cavity modes – in addition to determining their suitability for experimental implementation – numerical parameters are required to describe their attributes. In this section, we detail the methods used in this work to calculate two of the most important parameters for light-matter coupling applications: the quality factor and mode volume of the cavity mode.

2.4.3.1 Q factor primary calculation

The quality factor is a measure of how well energy is confined to a cavity mode. The primary method applied to calculate the quality factor in this work uses the definition detailed by Englund *et al.* [61]. The total quality factor of the cavity mode, Q_{total} , is defined as:

$$Q_{\text{total}} = \omega_{\text{res}} \frac{\langle U \rangle}{\langle P \rangle}, \quad (2.21)$$

where $\langle U \rangle$ and $\langle P \rangle$ are the time-averaged mode energy and power radiated by the cavity, respectively. The total mode energy can be found by integrating the electromagnetic energy density over the whole simulation region:

$$U = \iiint_{V_{\text{sim}}} \frac{1}{2} \left[\epsilon(\mathbf{r}) |\mathbf{E}(\mathbf{r})|^2 + \mu(\mathbf{r}) |\mathbf{H}(\mathbf{r})|^2 \right] d^3\mathbf{r}, \quad (2.22)$$

where V_{sim} is the simulation volume. The total power loss from the mode, P , is calculated by summing the power transmitted through all 6 planes at the edges of the simulation region, labelled 1-6 in Fig. 2.10. This is obtained from the surface integral of the Poynting vector, $\mathbf{S} = \mathbf{E} \times \mathbf{H}$ over each plane, which is performed by built-in functions in the software. It is often useful to decompose the quality factor into in-plane and out-of-plane components, Q_{in} and Q_{out} , which represent how well the cavity confines light in and out of the plane of the PhC. these are defined by:

$$Q_{\text{in}} = \omega_{\text{res}} \frac{\langle U \rangle}{\langle P_1 \rangle + \langle P_2 \rangle + \langle P_3 \rangle + \langle P_4 \rangle}, \quad (2.23)$$

$$Q_{\text{out}} = \omega_{\text{res}} \frac{\langle U \rangle}{\langle P_5 \rangle + \langle P_6 \rangle}, \quad (2.24)$$

where P_i denotes the power loss through the i th plane marked on Fig. 2.10. The components of the Q factor are related to Q_{total} by:

$$\frac{1}{Q_{\text{total}}} = \frac{1}{Q_{\text{in}}} + \frac{1}{Q_{\text{out}}}. \quad (2.25)$$

To perform the Q factor calculation, similar frequency domain techniques to those discussed in section 2.4.2 are applied. The time-domain fields are recorded in the simulation region with the same apodization settings as mentioned previously and a Fourier transform is then applied to obtain the complex fields $\tilde{\mathbf{E}}(\mathbf{r}, \omega_{\text{res}})$ and $\tilde{\mathbf{H}}(\mathbf{r}, \omega_{\text{res}})$. From these complex-valued fields, $\langle U \rangle$ and $\langle P \rangle$ are calculated, allowing the Q factor and its components to be calculated at the desired resonant frequency of the mode.

2.4.3.2 Q factor secondary calculation

The calculation of Q_{total} is cross-checked using a secondary calculation method (provided by the software), which derives Q_{total} from the envelope of the decaying cavity mode fields in the time domain. Consider that an ideal single cavity mode has an electric field of the form $E(t) = Ae^{(i\omega t - \gamma t)}$, where A is its initial amplitude and γ is a decay constant. This oscillator has a Lorentzian line-shape, with a FWHM of $\Delta\omega_{\text{res}} = 2\gamma$. We can therefore relate Q_{total} to γ by

$$Q_{\text{total}} = \frac{\omega_{\text{res}}}{\Delta\omega_{\text{res}}} = \frac{\omega_{\text{res}}}{2\gamma}. \quad (2.26)$$

Note that Q_{total} generally cannot be obtained from $\omega_{\text{res}}/\Delta\omega_{\text{res}}$ in high Q factor PhC cavity simulations because the fields do not fully decay in the simulation time. Consequently, $\Delta\omega_{\text{res}}$ cannot be accurately determined from their Fourier transform. The method used to obtain Q_{total} instead uses the decay envelope of the real field $|E(t)|$, to find γ . Taking \log_{10} of this envelope yields a straight line of the form $mt + c$, where m is the gradient and c is the value at $t = 0$. It can be shown that

$$\log_{10}(|E(t)|) = -\frac{\omega_{\text{res}}t}{2Q_{\text{total}}} \log_{10}(e) + \log_{10}(|A|) = mt + c, \quad (2.27)$$

and therefore Q_{total} can be obtained by:

$$Q_{\text{total}} = \frac{-\omega_{\text{res}} \log_{10}(e)}{2m}. \quad (2.28)$$

This calculation is performed in practice by recording the time domain field between $0.6t_{\text{sim}}$ and $0.8t_{\text{sim}}$ (note that Gaussian apodization is not used). To ensure the Q factor is calculated for the mode of interest only, the field data is Fourier transformed and a Gaussian spectral filter is applied to the relevant peak. In most cases, the narrow source width and selective symmetry conditions prevent more than one mode from being excited, so this filtering step was not crucial in this work. The process is performed for multiple points in space - usually 6 points spaced by $a/2$ in the region where the cavity mode is concentrated - and the absolute values of the Fourier transform at each point are summed. The real E field is then reconstructed in the time domain from the inverse FT and the gradient $m = \log_{10}(|E(t)|)$ is calculated. The value of Q_{total} is then calculated from Eq. 2.28. For every simulation performed in this work, the value of Q_{total} obtained from the primary and secondary calculation methods were checked for good agreement.

2.4.3.3 Mode volume

An equally important parameter to the quality factor of the cavity is its mode volume, V_0 , which parameterizes the spatial concentration of the electric field energy. The definition of the mode volume used is [60]:

$$V_0 = \frac{\iiint \epsilon(\mathbf{r}) |\mathbf{E}(\mathbf{r})|^2 d^3\mathbf{r}}{\max \left[\epsilon(\mathbf{r}) |\mathbf{E}(\mathbf{r})|^2 \right]}, \quad (2.29)$$

where $\max[f(\mathbf{r})]$ indicates the maximum value of the function f over the entire simulation region. The smaller the mode volume, the more concentrated and localized the electric fields are. A low loss, highly localized cavity mode is characterised by a high Q_{total}/V_0 ratio, which is favourable for light-matter interactions. This is explained in more detail in Ch. 3.

Calculation of the mode volume is performed by analysis scripts provided with the Lumerical software. The same complex field, $\tilde{\mathbf{E}}(\mathbf{r}, \omega_{\text{res}})$ obtained for the primary Q factor calculation is used and the mode volume is calculated using Eq. 2.29.

2.4.3.4 L3 cavity results

Quality factor and mode volume data were extracted from FDTD simulations of the two L3 cavity designs in Fig. 2.9. The results are presented in table 2.1: Δx and Δr represent the translational shift and radius change, respectively, of the two neighbouring holes [highlighted in

| Δx (a) | Δr (a) | λ_0 (nm) | $Q_{\text{total}}(1)$ | $Q_{\text{total}}(2)$ | Q_{in} | Q_{out} | $V_0 [(\lambda_0/n)^3]$ |
|----------------|----------------|------------------|-----------------------|-----------------------|--------------------|--------------------|-------------------------|
| 0 | 0 | 1252.5 | 5010 | 5030 | 8.21×10^4 | 5330 | 0.60 |
| 0.2 | -0.07 | 1266.2 | 1.21×10^5 | 1.22×10^5 | 2.11×10^6 | 1.28×10^5 | 0.81 |

Table 2.1: Parameters of the fundamental L3 cavity mode extracted from FDTD simulations of two different L3 cavity designs: with and without alteration of the two neighbouring holes.

red in Fig. 2.9(b)]. The calculated values of Q_{total} , Q_{in} and Q_{out} are shown, in addition to V_0 and the wavelength of the cavity mode in air, λ_0 . The mode wavelengths are confirmed to be inside the band gap of the PhC (between $1.31 \mu\text{m}$ and $1.07 \mu\text{m}$). The value of $Q_{\text{total}}(1)$ was calculated using the primary method detailed in section 2.4.3.1; also shown is $Q_{\text{total}}(2)$, which was calculated from the secondary method in section 2.4.3.2. Good agreement was found between the two values for both simulations. For the simulations in the rest of this work, we present $Q_{\text{total}} = Q_{\text{total}}(1)$.

We first examine the L3 cavity with no alterations to the neighbouring holes ($\Delta x = 0$, $\Delta r = 0$). Even for this unoptimised design, the cavity mode has a high Q_{total} and small V_0 , as is favourable for light-matter coupling experiments. The calculated value of Q_{total} is in good agreement with theoretical results from the literature [59, 64, 75], which typically lie in the range 5000-6000. The value of $Q_{\text{in}} = 8.21 \times 10^4$ is very high, as should be expected from the strong confinement of the PhC band gap. However, the low $Q_{\text{out}} = 5330$ indicates that Q_{total} is limited by losses to the air above and below the slab.

Considering now the optimised L3 cavity design with $\Delta x = 0.2a$ and $\Delta r = -0.07a$, the $Q_{\text{total}} (= 1.21 \times 10^5)$ is much higher. The optimised design results in reduced leakage above and below the PhC plane, reflected by a much higher $Q_{\text{out}} = 1.28 \times 10^5$. The reason for the large difference in Q_{out} between the two cavity designs is that the neighbouring hole alteration reduces the coupling of the cavity mode to leaky modes in the light cone, which is explained in section 2.4.4. The magnitude of Q_{total} obtained for the optimised design is consistent with similar devices presented in the literature [64, 65, 73].

Note that the simulation results presented here have not been rigorously tested for convergence. However, the results are expected to be accurate: firstly because they match expectations from the literature and secondly because the mesh cell size (largest dimension $\sim 11 \text{ nm}$) is smaller than the hole shifts and radii alterations, which are the finest details of the structure.

2.4.4 Leaky mode components

In most hole-in-slab PhC cavities, the Q factor of the cavity modes is limited by losses to the air or cladding surrounding the slab, resulting in a low Q_{out} . This is evident for the L3 cavity results presented in table 2.1, particularly for the basic L3 design without any alterations to the neighbouring holes. When a cavity mode is created by perturbing the PhC lattice, the translational symmetry of the PhC is broken and the Bloch wave vector is no longer conserved. Consequently, the defect mode can freely couple to leaky modes outside of the light cone, resulting in radiative losses. This is possible because the photonic band gap of the 3D structure is incomplete, having leaky regions which exist at frequencies inside the band gap (see Fig. 2.8). Fortunately, it is possible to suppress these radiative losses without the need for a complete photonic band gap. As shown by Akahane *et al.* [32], coupling to the leaky modes can be inhibited by reducing the (spatial) Fourier components of the field which lie outside the light cone. Consider the 2D spatial Fourier transform of the complex field component, $\tilde{E}_y(x, y, \omega_{\text{res}})$, in the $(x, y, 0)$ plane with area A_{sim} , given by:

$$\tilde{E}_y(\mathbf{k}_{\parallel}, \omega_{\text{res}}) = \iint_{A_{\text{sim}}} \tilde{E}_y(x, y, \omega_{\text{res}}) e^{-i(k_x x + k_y y)} dk_x dk_y. \quad (2.30)$$

The absolute value of the spatial Fourier transform, $|\tilde{E}_y(\mathbf{k}_{\parallel}, \omega_{\text{res}})|$, which will be referred to as $|\text{FT}(E_y)|$ for brevity, provides all necessary information about the in-plane Fourier components of the cavity mode's E_y field. Note that the E_y component is chosen because it is the dominant component of the L3 cavity mode. We compare $|\text{FT}(E_y)|$ for the basic L3 cavity design ($\Delta x = 0$, $\Delta r = 0$) and the optimised cavity design ($\Delta x = 0.2a$, $\Delta r = -0.07a$), for which a snapshot of the real-space E_y profile is shown in Figs. 2.12(a) and 2.12(b), respectively. It is evident that the spatial profiles of the cavity modes are only subtly different, yet their Q_{out} differs by two orders of magnitude (see table 2.1). The reason for this can be determined from their Fourier components, plotted in Figs. 2.12(c) and 2.12(d), which show normalised plots of $|\text{FT}(E_y)|$. Marked on these plots is the light cone contour (red circle), $\mathbf{k}_{\parallel} = n_{\text{cladding}}\omega_{\text{res}}/c$, which encircles the leaky region for the frequency of the cavity mode. Components of the field inside this circle are able to couple to leaky modes outside the light cone. Enlarged versions of the $|\text{FT}(E_y)|$ plots are shown in Figs. 2.12(e) and 2.12(f) for the simple and optimised L3 cavity designs, respectively. These feature a saturated colour scale to more clearly show the differences between the Fourier components,

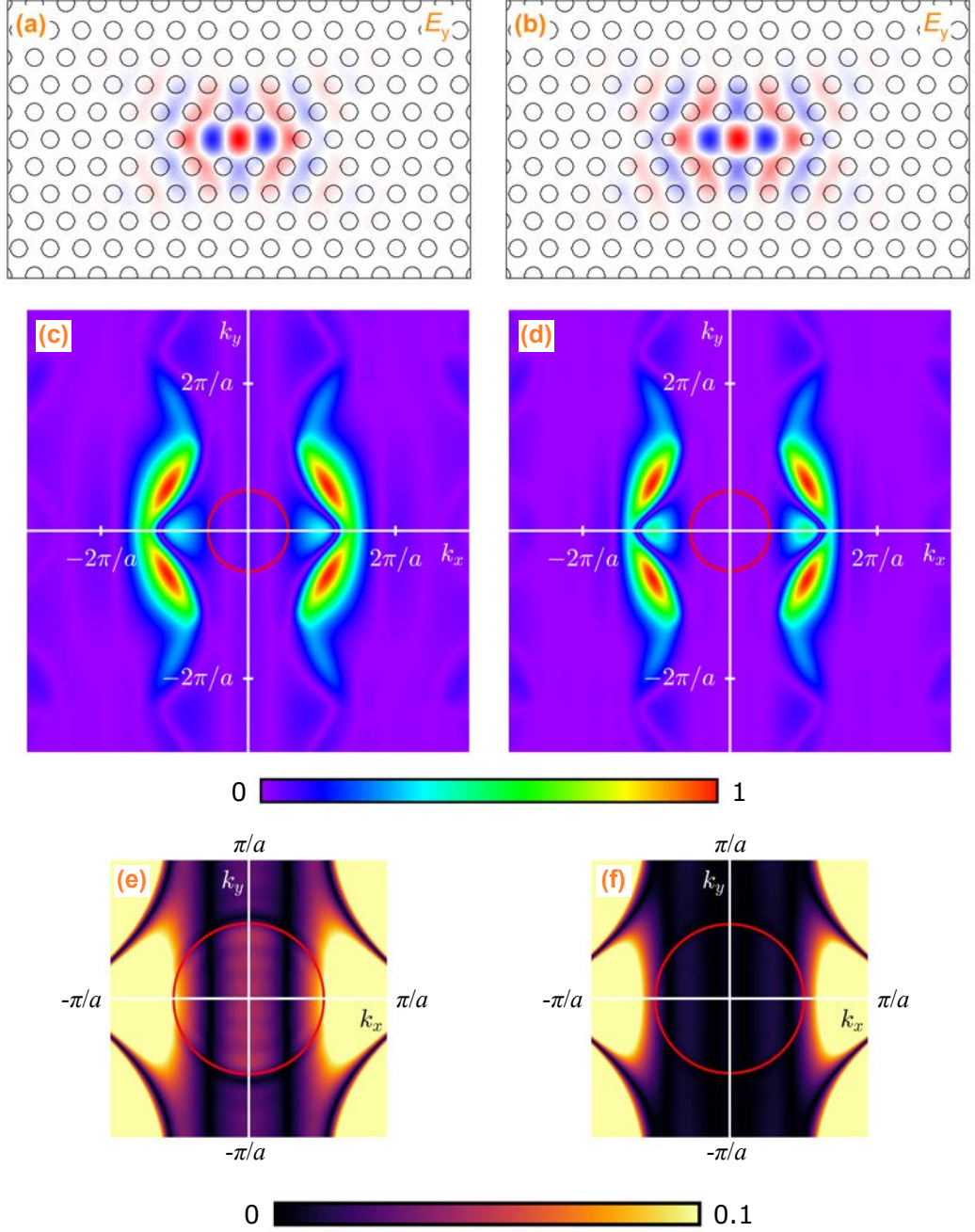


Figure 2.12: Comparison of the E_y field component and its in-plane spatial Fourier transform for simple L3 ($\Delta x = 0$, $\Delta r = 0$) and optimised L3 ($\Delta x = 0.2a$, $\Delta r = -0.07a$) cavity designs, in the $z = 0$ plane. (a) and (b): snapshots of the spatial profile of the E_y component for simple L3 and optimised L3 cavity designs, respectively. Red and blue represent opposite polarities of the field. (c) and (d): magnitude of the spatial Fourier transform of the E_y field, $|\text{FT}(E_y)|$, for the simple L3 and optimised L3 cavity designs, respectively. The red circle indicates the light cone contour - components inside this leaky region are outside the light cone. The graphs are plotted using a normalised scale. (e) and (f) show $|\text{FT}(E_y)|$ for the simple L3 and optimised L3 cavity designs, respectively, enlarged and with a saturated colour scale. The colour scale reaches a maximum at 10% of the maximum $|\text{FT}(E_y)|$ magnitude.

especially within the leaky region.

It is clear from Fig. 2.12(e) that, for the simple L3 design, there are significant Fourier components of E_y inside the leaky region. These are responsible for the high out-of-plane losses, which result in a low Q_{out} and limit Q_{total} . For the optimised cavity design, shown in Fig. 2.12(f), the components inside the leaky region are significantly reduced, resulting in a much higher Q_{out} and allowing a high Q_{total} . Despite using different cavity optimisation parameters to Akahane *et al.* (who only apply a hole shift of $\Delta x = 0.15a$ and do not modify the hole radius), the Fourier transform results presented are consistent with those observed in their work [32]. The effect is explained by Akahane *et al.* in terms of “gentle” confinement of the light: alterations of the neighbouring holes reduce the strength of the Bragg reflections from the surrounding PhC, causing the mode to be more delocalized and extend further into the PhC as an evanescent field. This increased spatial delocalization of the cavity mode causes the spatial Fourier transform to be more localized in \mathbf{k} -space, hence reducing the components inside the leaky region. This can also be understood in real space by considering that the increased delocalization causes the cavity mode to be closer in character to the extended modes of the PhC, which are more effectively guided by the PhC [39].

As explained in the textbook by Joannopoulos *et al.* [39] (Ch. 7, pp. 149-151), the ability to trade-off decreased localization of the cavity mode for decreased losses is an important principle in PhC design. For the L3 designs investigated here, the mode volume only increased slightly from $0.60(\lambda_0/n)^3$ in the simple design to $0.81(\lambda_0/n)^3$ in the optimised structure, enabling a huge increase in Q_{total}/V_0 from $8.4 \times 10^3(n/\lambda_0)^3$ to $1.5 \times 10^5(n/\lambda_0)^3$. This is common for microcavities - often the change in V_0 from increasing the delocalization of the mode is insignificant compared to the increase in Q gained. Arguably more significant than the change in mode volume is the potential for a wider confinement volume to support additional higher order modes, which may be undesirable. The trade-off between cavity mode localization and losses will be important for optimising PhC cavity designs in the chapters to come.

2.5 Photonic crystal waveguides and mode gap cavities

2.5.1 Introduction to photonic crystal waveguides

We saw in section 2.4 that by removing a row of 3 holes from a hexagonal hole-in-slab PhC (known as an L3 defect), a perturbation is introduced to the lattice which allows light to be confined to a

cavity. Light is confined in the plane of the PhC by the photonic band gap and in the z -direction by index guiding. In a similar manner, it is also possible to create a waveguide in the PhC by introducing a linear defect. A common method of achieving this in a hole-in-slab PhC is to remove a row of holes [76], as shown in Fig. 2.13. The created linear defect can then support waveguide modes propagating along the x -direction – confined to the slab by index guiding and directed in-plane by the photonic band gap.

Waveguides formed from linear defects in PhC slabs are frequently used for on-chip control of light. Most applications involve either guiding the light between components, or delaying the light by trapping it or slowing its group velocity [37, 77] - crucial operations for the realisation of on-chip all-optical circuits. PhC waveguides can be optically coupled to defect cavity modes in the same PhC [45, 78], allowing light to be coupled in or out of the cavity mode via the waveguide – one potential use of this is for trapping and delaying of photons for optical processing operations. It is possible to fabricate PhC waveguides with very low propagation losses: for example, losses as low as $\sim 2 \text{ dBcm}^{-1}$ have been achieved in Si-based slabs [79]. Therefore, the waveguides can be used to efficiently couple light into or out of PhC cavities (or components of interest) from a considerable distance, either through the use of grating couplers placed at the end of the waveguide [68, 80, 81] (which are illuminated with a laser spot or collected from using a microscope objective above the sample) or via coupling the end of the waveguide to an optical fibre [37, 45, 82]. A waveguide can even be used to strongly couple two optical cavities over a distance as large as $\sim 80 \mu\text{m}$ [83]. CQED experiments with coupled QD-PhC cavity systems also often implement PhC waveguides to allow the CQED system to be excited and/or collected from remotely [80] and probed by its influence on the transmission properties of the waveguide [68, 81].

Another important aspect of PhC waveguides is their ability to support modes of light with a significantly reduced group velocity, which is referred to as slow light [36]. This phenomenon holds promise for all-optical storage and switching applications in optical circuits [84]. A number of interesting demonstrations of slow light have been shown experimentally, including fast modification (on a $\sim 100 \text{ ns}$ time scale) of the group velocity of light in a PhC waveguide through the use of localized heating [58]. Coupling of a single QD to a slow light mode in a PhC waveguide [82, 85] is also of interest for application as a single photon transistor. We will see in section 2.5.2 that slow light modes in PhC waveguides arise as a consequence of the dispersion relation.

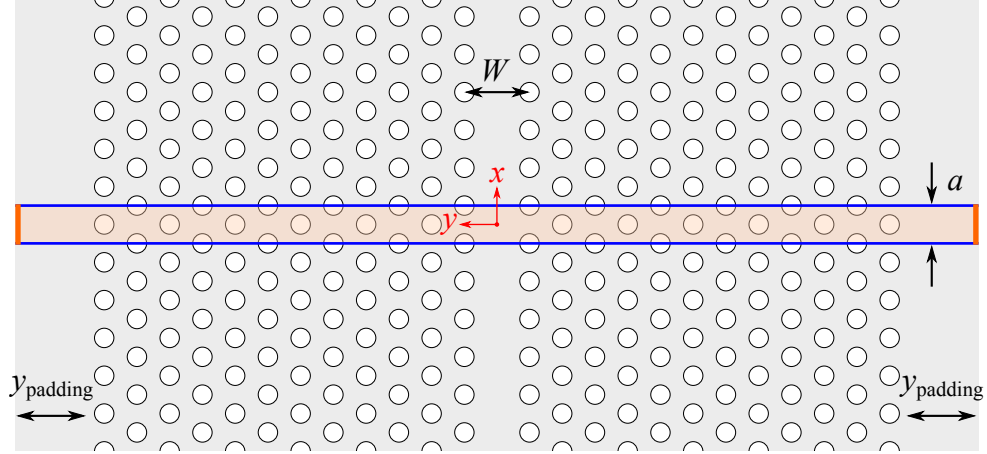


Figure 2.13: Top-down view of the PhC waveguide structure used in the photonic band structure calculation. The FDTD simulation region is shaded orange, bounded by Bloch boundary conditions (blue) at $x = \pm a/2$ and PML boundary conditions (orange) at all other simulation edges. W denotes the width of the waveguide, defined as the distance between the centres of the two adjacent rows of holes. Note that x has been oriented in the vertical direction for ease of visualizing the structure.

2.5.2 FDTD simulation of a photonic crystal waveguide

To characterise a PhC waveguide, photonic band structure calculations were performed using the FDTD simulation techniques detailed in section 2.3. 3D FDTD simulations were performed of the structure shown in Fig. 2.13, which is a hexagonal PhC slab with a linear defect along x of width W , with 12 rows of holes either side. The geometrical parameters of the slab and PhC are the same as in section 2.3.4; the side-profile of the slab and the simulation region match the side profile shown in Fig. 2.7. The width of the waveguide was set to $W = 0.98\sqrt{3}a$, based on the width typically used for mode gap cavities created along a waveguide (which are discussed further in section 2.5.3) [34, 86, 87]. This value of W also matches the measured devices in this work. In this section, we will show that the PhC waveguide structure supports guided modes inside the photonic band gap, which propagate along the x -direction.

The linear defect that forms the PhC waveguide breaks the translational symmetry of the PhC slab in the y -direction, which means that translational symmetry in only the x -direction needs to be considered. The unit cell of the structure, shown by the simulation region highlighted in Fig. 2.13, is now cuboidal and is therefore compatible with the geometry of the FDTD simulation mesh. This simplifies the band structure calculation compared to the slab in section 2.3.4, since we do not need to consider a supercell. Bloch boundary conditions were applied at $x = \pm a/2$ and all other simulation edges were given PML boundary conditions. Padding distances of $y_{\text{padding}} = z_{\text{padding}} = 0.65 \mu\text{m}$ were used, corresponding approximately to half of the wavelength of light from

the lower edge of the band gap. Resolution parameters of $\rho_x = \rho_y = \rho_z = 30$ were applied to the slab region and an S symmetry condition was applied at $z = 0$ to select for TE-like modes.

The method of performing the band structure simulation was very similar to the method described in section 2.3.4 to calculate the TE-like bands of the 3D PhC slab – the parameters and method used were the same, unless stated otherwise. The 3 dipole sources were oriented in the x - y plane (to excite TE-like modes) with otherwise random phase, angle and position. The time-domain field was monitored at 10 random positions (which we refer to as monitor positions) and used to calculate the band structure as described previously. Both the dipole and monitor positions were restricted to focus on the waveguide. The y position was limited to $|y| < W$. The z position of the sources was restricted to $0 < z < z_{\text{slab}}/2$ (and sources were automatically duplicated below the slab, according to symmetry) to inject into the slab and the monitors were set between $0 < z < z_{\text{slab}}$. The frequency range (FWHM) of the sources was set between 220 THz ($\sim 0.25 c/a$) and 290 THz ($\sim 0.33 c/a$) to focus on waveguide modes inside the photonic band gap.

A simulation sweep was performed for 40 values of k_x from 0 to π/a . The latter of these corresponds to the edge of the first Brillouin zone for the PhC waveguide, which has translational symmetry in the x dimension only and a reciprocal lattice primitive vector $(2\pi/a, 0, 0)$. The TE-like photonic band structure was calculated from peak-fitting of the simulation results and is shown in Fig. 2.14. The TE-like bands extracted from the simulation results are mostly shown by the blue, unconnected points – these correspond to bands outside the photonic band gap, which form part of the extended modes of the PhC. As was the case for the band structure simulations in section 2.3, not all bands are identified due to limitations of the method, and the points are not usually connected as we cannot determine which band they belong to with certainty. The expected regions of the extended modes (including the band gap edges) are bounded by dark blue lines and shaded light blue. These were extracted from a second band structure simulation of the PhC slab for which the linear defect was not present: 23 uninterrupted rows of holes were instead simulated. This allows us to compare the TE-like bands with and without the waveguide present. We see that outside the photonic band gap, the TE-like bands of the PhC waveguide slab lie mostly in the expected region, showing that the upper and lower bands of the photonic band gap do not shift significantly when the waveguide is introduced. However, it is clear that two bands are introduced inside the band gap, which are labelled WM1 and WM2.

The bands WM1 and WM2 enable the linear defect to support waveguide modes: for a range of

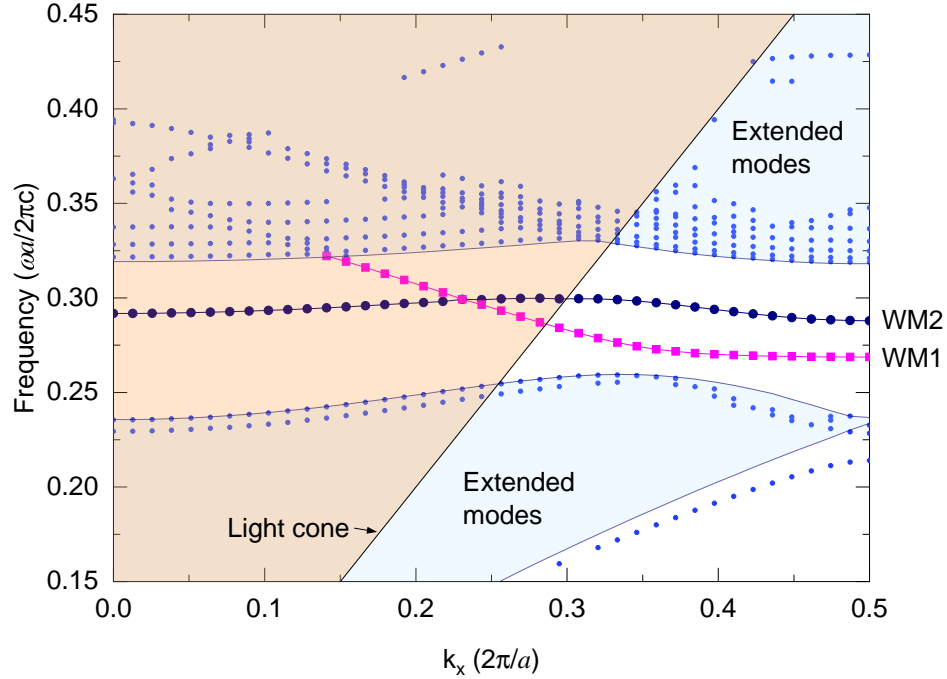


Figure 2.14: Simulated TE-like photonic band structure of a PhC waveguide slab. Two waveguide bands, WM1 (connected magenta squares) and WM2 (connected navy circles), are identified, which exist inside the photonic band gap of the unperturbed PhC slab. The region encompassing the extended modes of the unperturbed slab are shaded in light blue and bounded by darker blue lines. TE-like modes of the PhC waveguide that could not be definitively attributed to WM1 or WM2 are marked by blue points. The light cone is shown by the black line; the leaky region is shaded orange.

frequencies and k_x , the bands are inside the photonic band gap and inside the light cone, meaning that the PhC waveguide can support modes which are successfully guided by the band gap in the plane and confined to the slab by index guiding. These modes have a non-zero k_x and therefore propagate along the direction of the waveguide. The presence and dispersion characteristics of the waveguide modes matches expectations from similar PhC waveguides reported in the literature [33, 76, 87, 88, 89, 90] and textbooks [39](Ch.8, p. 142-147), in addition to work presented by collaborator L. Nutall in his thesis [1]. The origin of slow light in a PhC waveguide also becomes apparent from this dispersion relation: recalling that the group velocity is defined by $v_g = d\omega/dk$, it is intuitive that, near the Brillouin zone edge, the group velocity of light propagating in the waveguide modes is significantly reduced. Indeed, the group velocity of light in a PhC waveguide has been experimentally shown to be reduced by a factor of ~ 100 or more [36, 58]. Note that in the photonic band structure we also see bands at a frequency below the lower extended modes, which we anticipate is due to purely index-guided slab modes, as reported in several sources [36, 39].

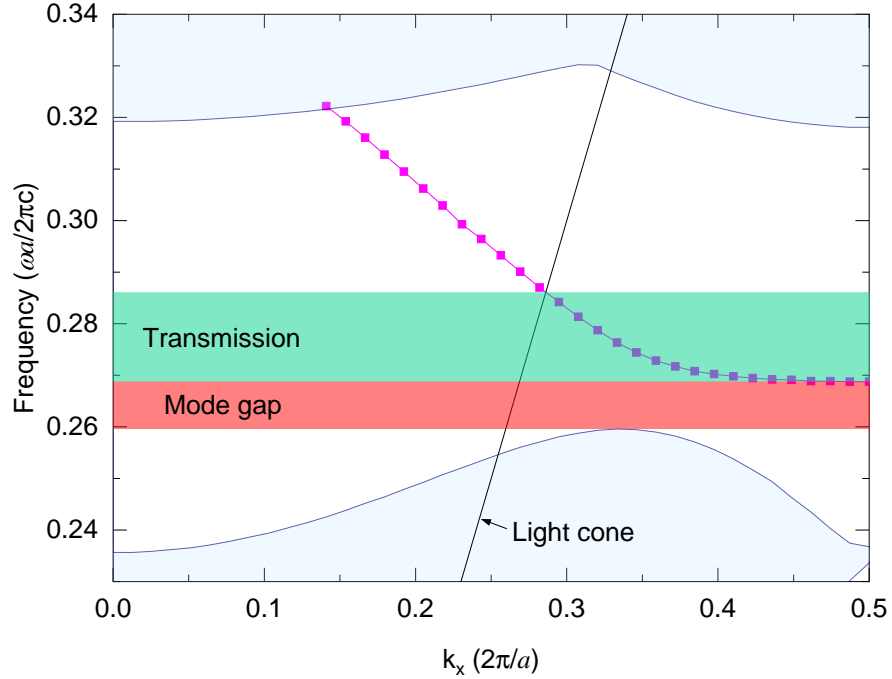


Figure 2.15: Transmission band (green) and mode gap (red) associated with the WM1 fundamental waveguide mode (connected magenta squares) of the PhC waveguide. The WM2 mode has been omitted for simplicity. The approximate regions of the extended modes of the PhC are shaded light blue and bound with a darker blue; the extended mode regions are extracted from simulations without the waveguide. The light cone is shown by the indicated black line.

2.5.3 Mode gap cavities

The main source of interest in PhC waveguides in this work is the ability to form cavity modes along a defined section of the waveguide by creating what is referred to as a mode gap cavity. The concept of the PhC mode gap cavity was first introduced and experimentally demonstrated by Song *et al.* in a double-heterostructure PhC [33], and involves altering a section of the waveguide to change the allowed frequencies of the supported waveguide modes. To illustrate the concept, we focus on the lowest energy, fundamental waveguide mode, WM1, which is shown in Fig. 2.15. The WM2 mode is ignored for simplicity and, in practice, is sufficiently energetically separated from WM1 that it generally does not need to be considered. Light is transmitted (without leakage to the air) by the waveguide mode WM1 in the range of frequencies indicated by the green transmission band in Fig. 2.15. However, at a range of frequencies between the lower band edge of the photonic band gap and the lowest energy point of the WM1 band at the Brillouin zone edge, propagation of light is forbidden by a mode gap. By modifying a section of the waveguide in a way that pulls the WM1 band down in energy, the top frequency of the mode gap is lowered relative to the rest of the waveguide, and a confinement potential is produced.

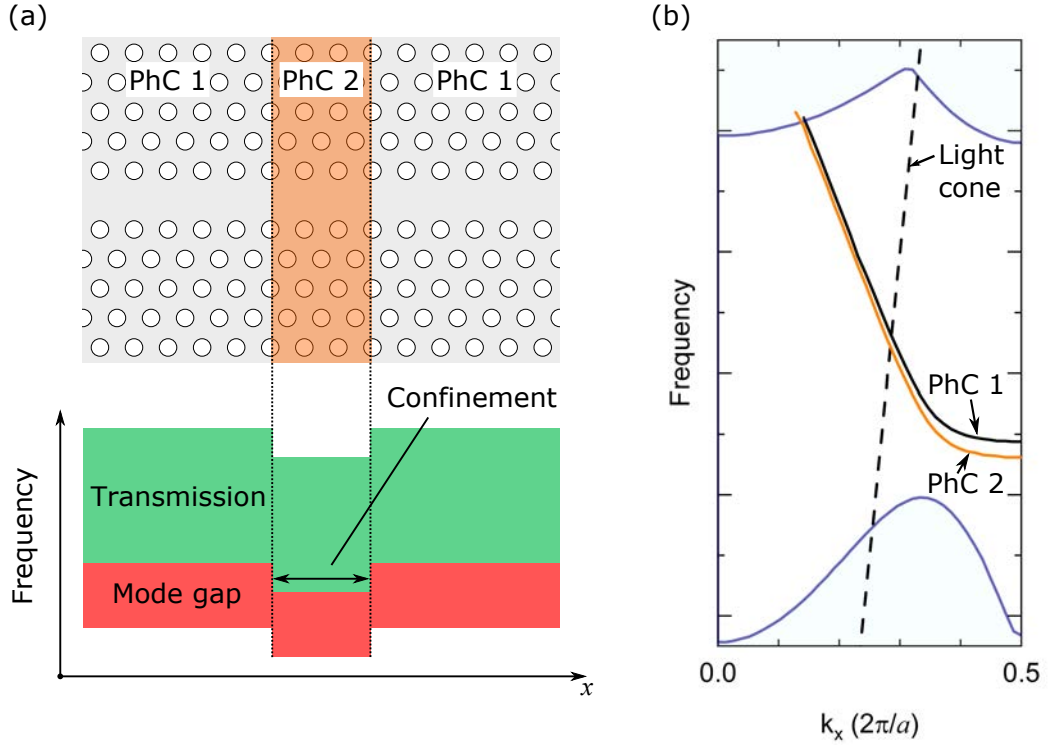


Figure 2.16: Schematic diagrams showing the principle of a mode gap cavity. (a) A PhC waveguide slab consisting of two regions of the same parameters, PhC 1, is bisected by a region with different lattice parameters, PhC 2 (highlighted in orange), with a lower frequency mode gap. Light is confined to the PhC 2 region by mode gap confinement. (b) Possible dispersion relation of the two PhC regions that would result in a mode gap cavity. The fundamental WM1 waveguide band is shown for PhC 1 (black) and PhC 2 (orange), in addition to the light cone and approximate position of the extended modes (light blue region) and photonic band gap edges (dark blue lines).

The concept of mode gap confinement is illustrated in Fig. 2.16, which shows the general mechanism responsible for creating a mode gap cavity. We consider the PhC waveguide slab shown in Fig. 2.16(a), which consists of two regions with the same PhC lattice and waveguide parameters, labelled PhC 1, bisected by a region of the PhC waveguide with different parameters, PhC 2 (highlighted orange). Note that the width of the PhC 2 region shown here is arbitrary. If the region PhC 2 is modified in such a way that the top of the mode gap of the waveguide is shifted down in frequency (such as by altering the lattice geometry or refractive indices of the slab and/or holes), then optical confinement can be generated in this region of the PhC waveguide and a mode gap cavity is formed. The principle is also illustrated in Fig. 2.16(b): a schematic showing two possible WM1 bands associated with PhC 1 and PhC 2. If the lowest frequency of the waveguide band associated with PhC 2 is below that of the PhC 1 band (at the Brillouin zone edge), then mode gap confinement is possible.

The simplest method of generating a mode gap cavity is by alteration of the PhC holes around the waveguide. The double-heterostructure example by Song *et al.* [33] defines a mode gap cavity

by modifying the lattice of the PhC 2 region: the lattice spacing is increased in the x -direction, changing the lattice from hexagonal to face-centred-rectangular. This cavity design yielded a record-high Q factor of $\sim 6 \times 10^5$ reported from experimental measurements of Si slabs (at the time of publication), and proposed a “multistep” double-heterostructure design (with several regions of different lattice constant), with a theoretical $Q_{\text{total}} \sim 2 \times 10^7$. The very high Q factors are attributed to a more Gaussian-like field envelope of the profile, resulting from “gentler” confinement than other designs, such as the L3 cavity. Mode gap cavities of similar design have continued to produce the highest Q factors in PhC cavities, with experimentally-obtained Q factors of order 10^7 reported in Si-based PhCs [48, 91].

2.5.4 The width-modulated line defect cavity

As an example of a well-established and popular mode gap cavity, we focus on the width-modulated line defect (WMLD) cavity presented by Kuramochi *et al.* [34]: a simple design that relies only on shifting the position of some PhC holes in the proximity of the waveguide. By shifting holes in the y -direction, as shown in Fig. 2.17(a), a section of the line defect can be made wider, which lowers the top frequency of the mode gap associated with that section. A mode gap cavity is then formed due to the adjacent, unaltered section of the waveguide, for which the mode gap extends to a higher frequency. Kuramochi *et al.* show that it is possible to create a cavity in this manner by moving as few as two holes, but here we focus on the design in Fig. 2.17(a), which features tapered hole shifts for an optimal Q factor. The holes are shifted in the directions indicated by the arrows by a distance of 12 nm (red), 8 nm (yellow) or 4 nm (green) to define the WMLD mode gap cavity.

FDTD simulations were performed of the WMLD cavity design using the general methodology detailed in section 2.4. The simulated PhC structure had 12 rows of holes either side of the waveguide and 51 holes along x . S, AS and S symmetry conditions were applied at $x = 0$, $y = 0$ and $z = 0$, respectively. A high Q , small V_0 fundamental cavity mode confined by the WMLD cavity was identified, the $|\mathbf{E}|^2$ profile of which is shown in Fig. 2.17(b). As for the L3 cavity, the field pattern has local antinodes at which an emitter would need to be placed to observe CQED effects [20, 86]. The field of the WMLD cavity mode is evidently more delocalized than that of the L3 cavity, which enables a higher Q factor to be achieved. The results presented in table 2.2 show $Q_{\text{total}} \sim 2 \times 10^7$, 2 orders of magnitude higher than even the optimised L3 cavity design

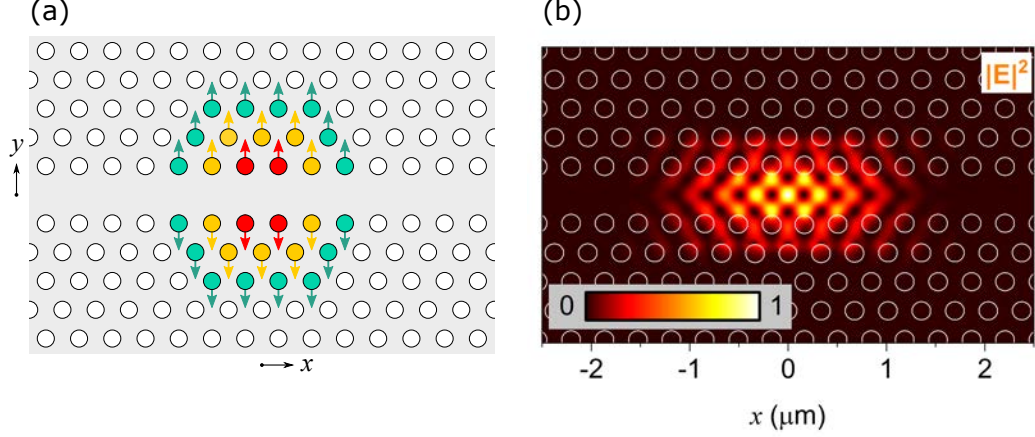


Figure 2.17: WMLD mode gap cavity formed by shifting holes away from the waveguide. (a) Schematic of the hole shifts applied to create the WMLD cavity: holes are shifted in the directions indicated by the arrows by a distance of 12 nm (red), 8 nm (yellow) or 4 nm (green). The hole shifts are too small to be resolved by eye. (b) $|E|^2$ profile of the fundamental mode of the corresponding WMLD cavity from FDTD simulations.

| λ_0 (nm) | Q_{total} | Q_{in} | Q_{out} | $V_0 [(\lambda_0/n)^3]$ |
|------------------|--------------------|-------------------|-------------------|-------------------------|
| 1275.4 | 2.4×10^7 | 1.7×10^8 | 2.7×10^7 | 1.29 |

Table 2.2: Parameters of the fundamental WMLD cavity mode extracted from FDTD simulations. Note that full convergence of these results has not been confirmed.

in section 2.4. The increased delocalization is reflected by a larger mode volume of $1.29(\lambda_0/n)^3$ [versus $0.81(\lambda_0/n)^3$ for the optimised L3], but clearly the increase in Q factor granted outweighs the change in mode volume when considering the Q_{total}/V_0 ratio. It is no surprise, then, that the WMLD cavity (and mode gap cavities in general) are of interest in light-matter coupling experiments [78, 86, 92].

Convergence testing was performed by running multiple simulations at different resolution parameter values, which we label ρ_{xyz} , since $\rho_x = \rho_y = \rho_z$ in this instance. Results of the convergence test, in which Q_{total} and V_0 were monitored for resolution parameters up to $\rho_{xyz} = 40$, are shown in Fig. 2.18. We also define a convergence parameter, C , which is derived from the three-point moving average. If p is the index of the data point along the horizontal axis, then the three data points used for calculating $C(Q_p)$, the convergence parameter of quantity Q (such as the Q factor) at point p , are Q_{p-1} , Q_p and Q_{p+1} . $C(Q_p)$ is defined as the standard deviation of these three values divided by their mean; a small value of $C(Q_p)$ indicates convergence of the parameter Q . At $\rho_{xyz} = 35$, we find $C(V_0) < 1\%$ and $C(Q_{\text{total}}) \sim 30\%$. This indicates excellent convergence of V_0 , although Q_{total} does not converge as strongly as we might like. The Q factor of the WMLD

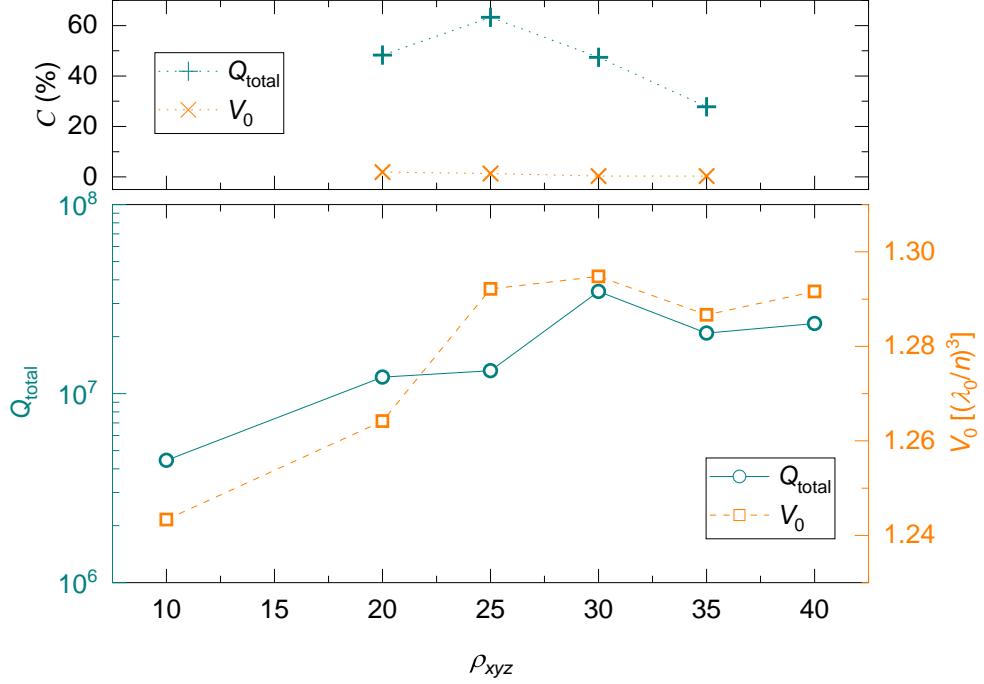


Figure 2.18: Convergence testing results for the WMLD cavity. The values of Q_{total} and V_0 are tracked as the resolution parameter, ρ_{xyz} , is varied. The convergence parameter, C , is also shown for each quantity.

cavity mode is particularly sensitive to the mesh resolution, because the hole shifts are extremely small. At $\rho_{xyz} = 40$, the y -dimension of the cells in the mesh override region is ~ 7 nm, which is a very high resolution, but is still larger than the finest hole shift of 4 nm. Therefore, the Q factors presented in table 2.2, which are for $\rho_{xyz} = 40$, may not have fully converged and are anticipated to be within only $\sim 30\%$ accuracy. Nevertheless, the results are consistent with theoretical results from the literature [34, 86] and are expected to be of more than sufficient accuracy for an order of magnitude comparison with the L3 design. Simulations were not performed at a higher resolution due to increasingly large and unfeasible memory requirements as the mesh resolution is increased further.

The origin of the high Q factor of the WMLD cavity can be better understood by considering the spatial Fourier transform of the fields, as was the case for the L3 cavity design in section 2.4.4. We consider the E_y component of the field for ease of comparison with the L3 cavity profile and Fourier transform (which can be found in Fig. 2.12). Snapshots of the E_y field of the WMLD cavity mode through $z = 0$ and $y = 0$ are presented in Figs. 2.19(a) and 2.19(b), respectively. These demonstrate a more spatially delocalized mode in the plane of the PhC for the WMLD cavity, but which is also well-confined to the slab in the z -direction. The spatial Fourier transform,

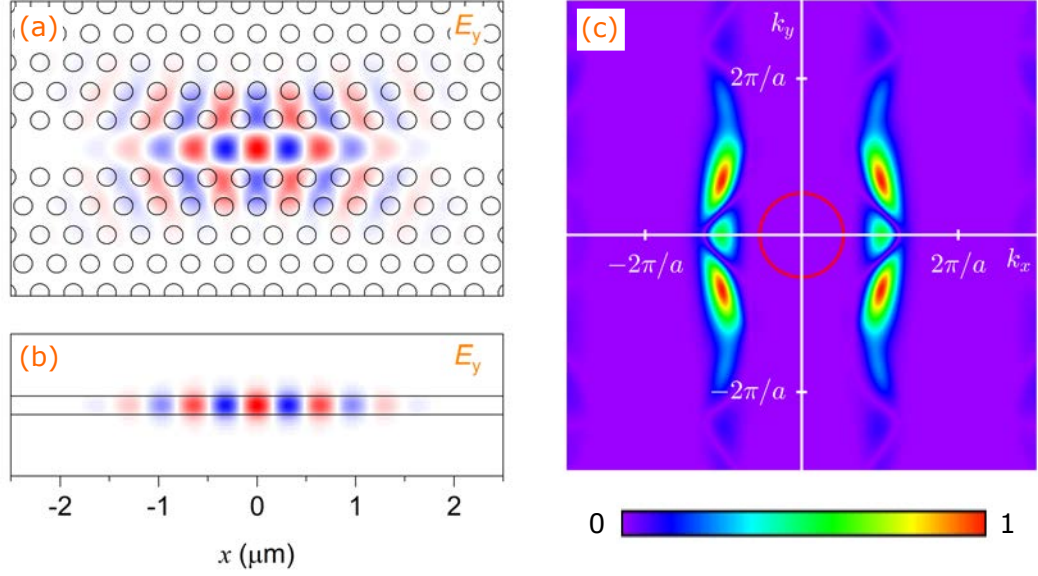


Figure 2.19: E_y field profile of the WMLD cavity mode and its spatial Fourier transform. (a) and (b): snapshots of the E_y field at $z = 0$ and $y = 0$, respectively. Red and blue represent opposite polarities of the field. (c) Spatial Fourier transform, $|FT(E_y)|$, in the $z = 0$ plane. The leaky region is marked by the red circle. The normalised colour scale is shown below.

$|FT(E_y)|$ (defined in section 2.4.4), in the $z = 0$ plane is presented in Fig. 2.19(c). We observe that the Fourier transform is highly localized in k_x , as a result of the spatial delocalization of the mode along the waveguide. Consequently, the Fourier components inside the leaky region are even smaller than for the optimised L3 design [see Fig. 2.12(d)], and an even higher Q factor is achievable from further inhibition of radiative losses to the surrounding medium.

2.5.5 Alternative mode gap cavity designs

The conventional method of creating a mode gap cavity by altering the hole geometry and positioning along a section of the PhC waveguide has yielded a number of successful cavity designs. These include alteration of the lattice shape and dimensions [33, 48, 91, 93], shifting of holes away from the waveguide [34, 78] (as for the WMLD cavity) and even alteration of only the radii of the air holes near the waveguide [94]. However, there have also been a number of proposed and experimentally verified methods of generating a mode gap cavity using less conventional means, which typically involve depositing material on the already-existing PhC waveguide or altering its refractive index. These are of particular interest for the goal of this project – to develop and apply a cavity that can be positioned to overlap and couple to a QD – because the majority of these methods are applied after the e-beam lithography steps used to fabricate the PhC membranes. The advantage of this is the potential to locate a QD embedded in the PhC waveguide (for example,

using optical measurements) and then define the cavity to overlap with it. This is discussed in more detail in section 3.5.

The general approach to creating a mode gap cavity in an existing PhC waveguide is to increase the average refractive index of a section of the waveguide, at which the cavity is desired. Referring back to the mode gap cavity schematic in Fig. 2.16, this means that we wish to increase the average refractive index of the PhC 2 region. The increase in refractive index typically lowers the frequency of the photonic bands associated with that section of the PhC, most notably the WM1 band, which causes the mode gap cavity to be formed [95, 96]. Two intuitive options are to either increase n_{slab} or to fill in the holes of the PhC with a higher index material than the surrounding medium. Generation of a mode gap cavity by infiltration of the holes of the PhC 2 region with fluid was proposed by Tomljenovic-Hanic *et al.* [95] and shown theoretically to be capable of achieving Q factors up to $\sim 10^6$. The same group also proposed creating mode gap cavities in PhC waveguide slabs made of photosensitive materials [96], such as chalcogenide glass, which exhibit a permanent change in refractive index when exposed to light of specific wavelengths. By increasing n_{slab} in the PhC 2 region, cavity modes with Q factors up to $\sim 10^6$ were also predicted from this method. Both of these cavity types have since been demonstrated experimentally: fluid-infiltrated cavities were achieved by drawing immersion oil across a Si PhC waveguide slab using a glass microtip, achieving Q factors up to $\sim 5.7 \times 10^4$ [97]. Even higher Q factors, up to 1.25×10^5 , were demonstrated in a mode gap cavity defined in a chalcogenide glass PhC waveguide [98], which was created by negative exposure – n_{slab} was reduced in the PhC 1 regions by exposure.

Unfortunately, the successful fluid infiltration and photosensitive mode gap PhC techniques are not applicable to the desired application of cavity-QD coupling for this project. As explained in Ch. 3, the experiments take place under vacuum at a temperature of $\sim 8\text{ K}$ and require the PhC waveguide slab to have QDs embedded at the centre. Under these conditions, application of fluid to the surface of the sample is not likely to be possible, and fabrication of the PhC membrane from chalcogenide glass is not compatible with the fabrication of the telecoms-wavelength self-assembled InGaAs QDs required. Other methods of mode gap cavity formation from refractive index modulation have also been proposed, such as creating an increase in n_{slab} in the proximity of the waveguide due to non-linear optical effects induced by a laser spot [87]. However, the strong pump power required is likely to saturate the QDs in the sample with carriers – making single QD measurements extremely difficult – thus, the technique is likely not suitable.

A more promising technology for the goal of deterministic QD-cavity coupling is to create mode gap cavities by depositing material on top of the existing PhC waveguide – another concept proposed by Tomljenovic-Hanic *et al.* [90]. The authors showed that by placing a dielectric strip (such as a polymer) on top of the PhC waveguide slab to define the PhC 2 region, a mode gap cavity can be formed. The altered refractive index contrast between the PhC slab and the surrounding medium (due to the presence of the polymer strip) results in the waveguide bands being shifted to a lower frequency, thus allowing mode gap confinement. This has been realised experimentally by Gardin *et al.* [89], who created a mode gap cavity by patterning a ~ 100 nm-thick PMMA [poly(methyl methacrylate)] strip on top of a PhC waveguide slab. Another interesting demonstration by Seo *et al.* [88] defines a mode gap cavity by deposition of a carbonaceous nano-block at the centre of the waveguide. While effective, both of these methods require additional fabrication steps which would make positioning the cavity mode to overlap with an embedded emitter difficult: the PMMA strip requires processing via e-beam lithography and the carbonaceous nano-block is deposited in an SEM chamber. Another notable method demonstrated by Brossard *et al.* [99] is to define the mode gap cavity by an inkjet-printed strip on top of the PhC waveguide. However, this is incompatible with the low temperature optical methods we wish to use to search for individual QDs to couple the cavity mode to.

For this project, we propose a novel concept for defining a mode gap cavity in a PhC waveguide by deposition, selective exposure and development of a negative photoresist on top of the device. FDTD simulations of this cavity design are presented in section 2.6.

2.6 The SU-8 strip cavity

In this work we study a cavity design devised to exploit the high Q/V_0 ratio possible in mode gap cavities defined on a PhC waveguide, while also having the benefit of deterministic positioning of the cavity using optical techniques. We use a design that employs SU-8, a commercially available epoxy-based negative photoresist, on top of a PhC waveguide to define the cavity. The proposed cavity fabrication procedure is to spin-coat a thin layer of photoresist onto the top surface of the PhC membrane and choose the cavity position by selectively exposing the sample to UV light at the desired location on the PhC waveguide. The sample can then be processed to remove the unexposed SU-8, leaving a cross-linked SU-8 structure such as a disk or strip on top of the PhC waveguide, which defines a mode gap cavity by its alteration of the refractive-index contrast. As

explained in Ch. 3, the potential advantage of this technique is to use all-optical methods to locate a single QD in the PhC waveguide and fabricate a cavity at its position, to achieve coupling. In this section we focus on FDTD simulations of a mode gap cavity defined by an SU-8 strip on top of the PhC waveguide; cavities defined by an SU-8 disk are explored in Ch. 4. Further details of the fabrication techniques are given in Ch. 3.

2.6.1 Band structure of an SU-8-coated photonic crystal waveguide

As was shown in section 2.5, the creation of a mode gap cavity typically relies on altering a section of the PhC waveguide so that the WM1 waveguide band is shifted down in frequency relative to the neighbouring sections. We therefore begin by simulating the band structure of a PhC waveguide with a layer of cross-linked (exposed and developed) SU-8 on top and comparing this to the band structure of the blank PhC waveguide.

Band structure simulations were performed that were identical to those for the PhC waveguide in section 2.5.2, except for the addition of a 0.1 μm -thick layer of dielectric material placed on top of the PhC, to represent a layer of cross-linked SU-8. Side profiles of the PhC slab with and without the SU-8 film applied are shown in Figs. 2.20(a) and 2.20(b), respectively. In the simulations, the layer of SU-8 is a uniform cuboid which does not infiltrate the PhC holes. The refractive index of the film is set to 1.57, which corresponds to the refractive index of cross-linked SU-8 at the telecoms wavelengths of interest in this project [100]. The presence of the film breaks the z -symmetry of the structure, so it was necessary to remove the symmetry condition at $z = 0$ in the band structure calculation. Note that the simulation mesh override region, defined in section 2.2.4, was extended in the z -direction to fully cover the SU-8 film.

The WM1 band was extracted from the FDTD simulation results and is plotted in Fig. 2.20(c), along with the WM1 band for the blank PhC waveguide (and the approximate regions of the extended modes and band edges). We see that the presence of the film causes the WM1 band to shift to a lower frequency: the waveguide topped with SU-8 is able to support modes at a lower frequency than the blank PhC waveguide, near the edge of the first Brillouin zone. The WM1 band of the blank PhC waveguide intercepts the edge of the first Brillouin zone at $0.269c/a$, whereas the SU-8-topped PhC waveguide supports a lower frequency mode at $0.266c/a$. These correspond to wavelengths of 1.265 μm and 1.277 μm , respectively. Thus, the simulated WM1 bands demonstrate that the condition required for mode gap confinement is satisfied, implying that a mode gap cavity

can be created by placing a layer of SU-8 on top of a particular region of the PhC waveguide. Specifically, we replace the PhC 2 region in Fig. 2.16 with a PhC waveguide topped with SU-8, to create an SU-8 strip-defined mode gap cavity.

2.6.2 FDTD simulations of the SU-8 strip cavity

FDTD simulations were performed of the SU-8 strip mode gap cavity, represented schematically in Fig. 2.21. A strip of dielectric material (shown in blue) with refractive index $n_{\text{strip}} = 1.57$ is positioned on top of the PhC waveguide to represent a strip of cross-linked SU-8. The strip has a width $w_{\text{strip}} = 1 \mu\text{m}$, which corresponds approximately to the diffraction-limited spot size of

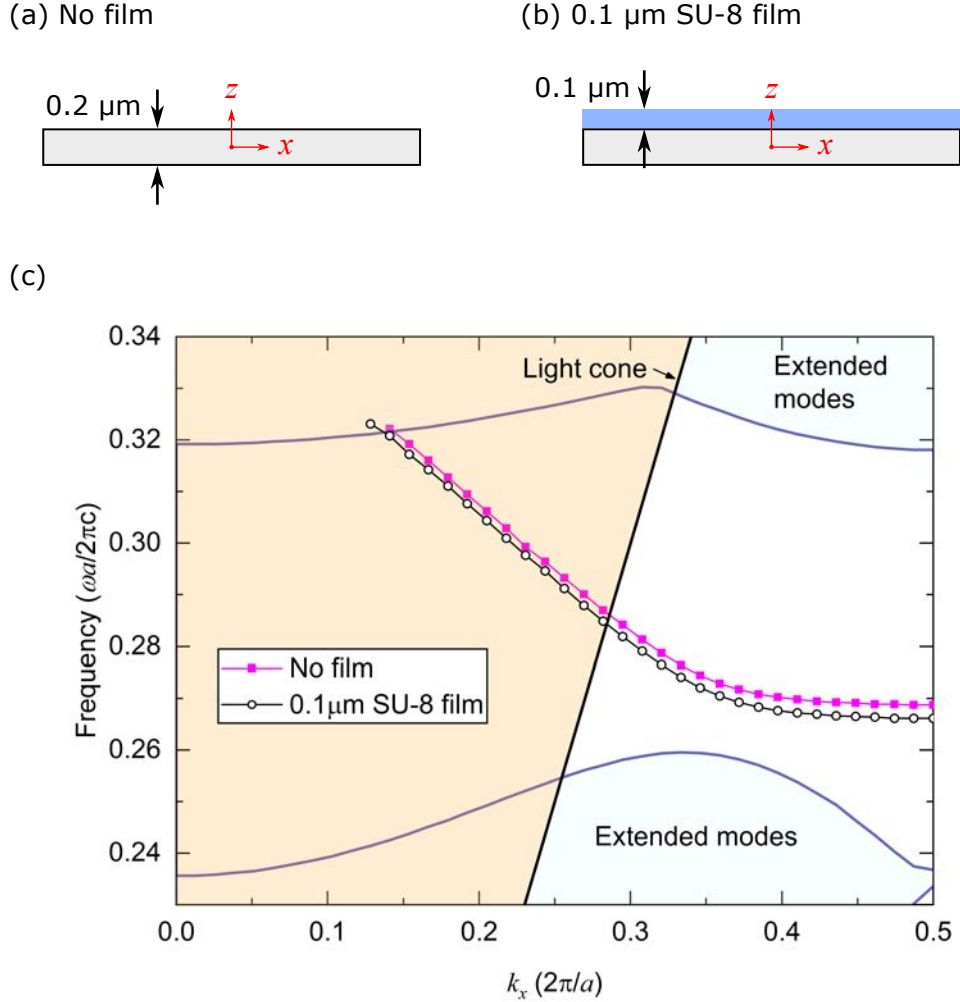


Figure 2.20: Comparison of the WM1 band of a PhC waveguide with and without a layer of $0.1 \mu\text{m}$ -thick cross-linked SU-8 on the top surface. (a) and (b): schematics of the side-profile of the simulated structures, without and with the film, respectively. (c) WM1 band extracted from the band structure simulations of the blank waveguide and with the SU-8 film. The band is shifted down in frequency by the film. Approximate locations of extended modes and band gap edges are shown, extracted from simulations of a blank PhC with no waveguide.

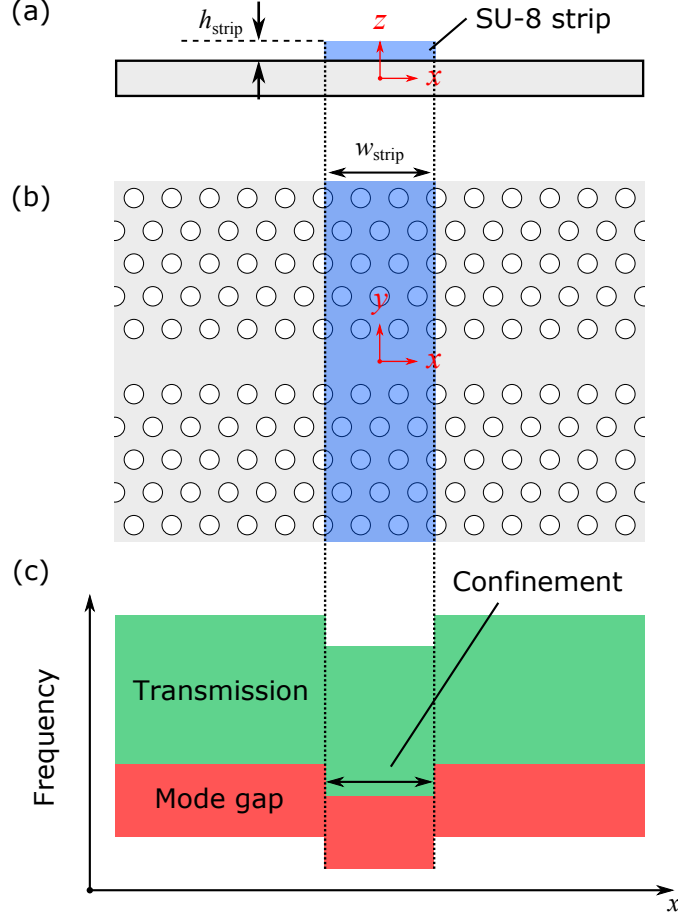


Figure 2.21: Schematics of the SU-8 strip-defined mode gap cavity that FDTD simulations were performed of. (a) and (b): side profile and top-down view of the device, which consists of a PhC waveguide with a strip of SU-8 placed on top. The strip is a cuboid with a width w_{strip} and height h_{strip} , which extends across the y -extent of the PhC and does not infiltrate the holes of the PhC. Note that the z -dimension in (a) is enlarged. (c) Simple representation of the mode gap confinement resulting from the SU-8 strip.

the laser that will be used to write the strip in practice (see Ch. 3). The height, or thickness, of the strip is $h_{\text{strip}} = 0.1 \mu\text{m}$, also corresponding to an experimentally achievable value. The strip extends across the entire y -extent of the FDTD simulation region and is a uniform cuboid; the SU-8 does not infiltrate the holes of the PhC in the simulation. We know from the band structure simulations in section 2.6.1 that the WM1 band associated with the SU-8-topped section of the waveguide is at a lower frequency, due to the altered refractive index contrast at the top of the slab. Therefore, we anticipate the structure to exhibit mode gap confinement at the position of the strip, as illustrated schematically in the mode gap diagram in Fig. 2.21(c).

The structure simulated had 12 rows of holes either side of the waveguide and 51 holes along x . S and AS symmetry conditions were applied at $x = 0$ and $y = 0$ respectively, but symmetry conditions could not be applied at $z = 0$, due to the broken z -symmetry. The field profiles of the

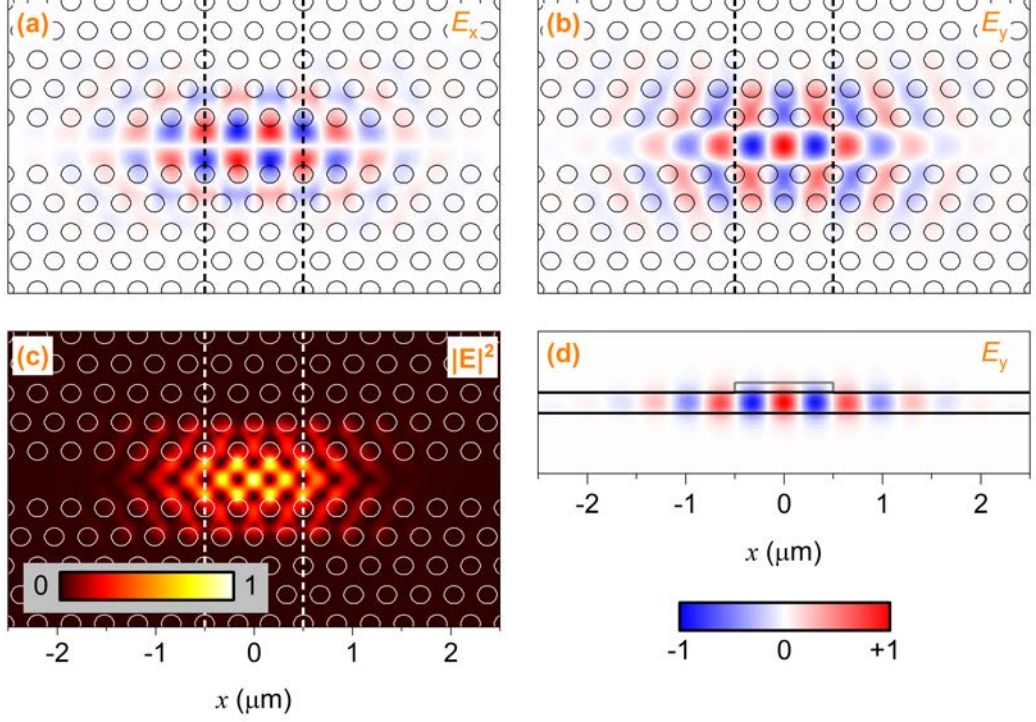


Figure 2.22: Field profiles of the fundamental mode of the SU-8 strip cavity. (a) and (b): snapshots of the E_x and E_y field components through $z = 0$. (c) $|\mathbf{E}|^2$ field envelope of the cavity mode in the same plane. (d) Snapshot of the E_y field component at $y = 0$. All field magnitudes are normalised; the E_x and E_y components are normalised between -1 (blue) and $+1$ (red) as shown in (d). Results presented are from simulations performed with a resolution of $\rho_{xy} = 20$ and $\rho_z = 30$

fundamental cavity mode generated by the presence of the SU-8 strip are shown in Fig. 2.22. The E_x , E_y and $|\mathbf{E}|^2$ profiles through the centre of the slab, $z = 0$, are shown in Figs. 2.22(a), 2.22(b) and 2.22(c), with the position of the SU-8 strip indicated by the dashed lines. Fig. 2.22(d) shows the E_y profile at a cross section through $y = 0$ (the only non-zero field component). Evidently, a cavity mode is created which is well-localized to the PhC slab and corresponds strongly to the position of the SU-8 strip along the waveguide. The structure of the mode is very similar to that of the WMLD cavity presented in section 2.5.4, which is promising, given the success of the WMLD cavity design.

Convergence testing was performed to identify resolution parameters with a good balance between accuracy and computational speed that could be applied for the remainder of the simulations presented in this thesis. Tests were first performed for ρ_{xyz} up to 30 – good convergence was found for $\rho_{xyz} \gtrsim 25$. Note that the simulation mesh override region, defined in section 2.2.4, is extended in the z -direction to fully cover the SU-8 strip in all SU-8 strip cavity simulations. A less uniform mesh was then tested, with $\rho_{xy} = \rho_x = \rho_y$ different to ρ_z , to improve the simulation speed. This mesh was to have high resolution in z , to be able to resolve small details in the SU-8 geometry,

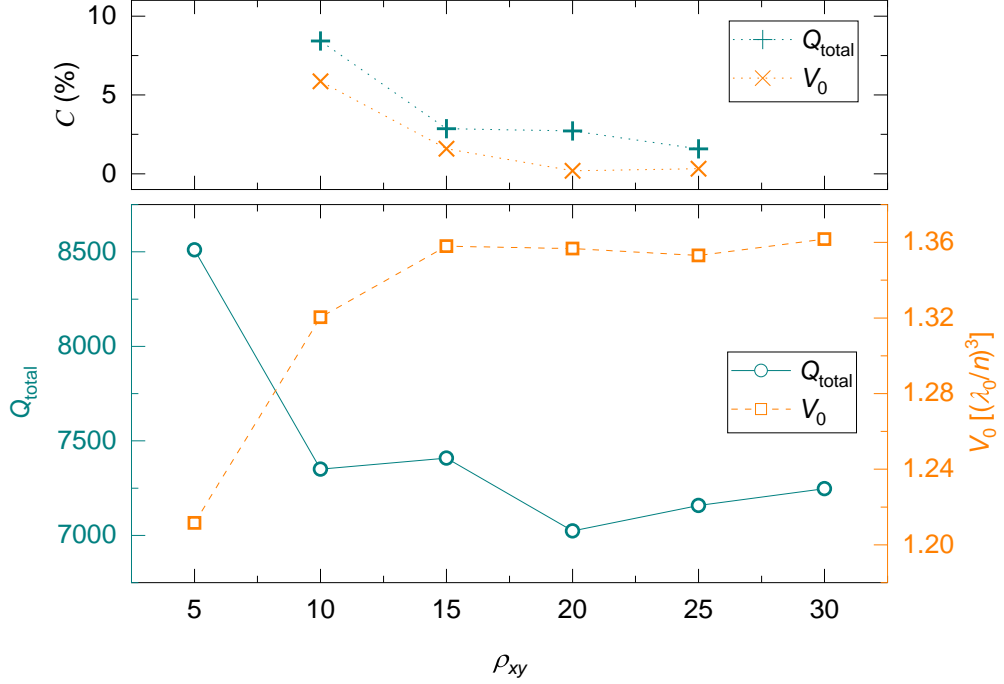


Figure 2.23: Convergence testing results for the SU-8 strip cavity. Extracted results for Q_{total} and V_0 for different values of ρ_{xy} are shown in the lower graph. The upper graph shows the value of the convergence parameter, C , for these two quantities. $\rho_z = 30$ was used for all simulations.

while having a lower resolution in x and y , since positional and geometrical shifts of the PhC holes (which demand higher lateral mesh resolution) are not applied in this structure. The value $\rho_z = 30$ was kept fixed and ρ_{xy} was varied; convergence of Q_{total} and V_0 was measured, the results of which are shown in Fig. 2.23. Also plotted is the convergence parameter, C , defined in section 2.5.4, which we wish to minimise for each quantity. Good convergence of Q_{total} and V_0 is observed as ρ_{xy} is increased beyond 15, which we confirm from the low value of C for both parameters. We note that convergence of Q_{total} is obtained at a much lower mesh resolution than for the higher Q WMLD cavity tested in section 2.5.4. Resolution parameters $\rho_{xy} = 20$ and $\rho_z = 30$ were chosen to present the results for this simulation and to use for the rest of the FDTD simulations in this project (unless stated otherwise). These correspond to mesh cell dimensions of $\sim 17 \times 15 \times 10\text{nm}$ in the slab and SU-8 region. The values of parameters, such as the Q factor, extracted from simulation results are expected to be accurate to within $\sim 5\%$, as suggested by $C < 5\%$ obtained for both Q_{total} and V_0 at the resolution parameters chosen.

Parameters of the SU-8 strip fundamental cavity mode, extracted from the FDTD simulation, are presented in table 2.3. As expected, the wavelength of the cavity mode, $\lambda_0 = 1270.8\text{nm}$, lies in the mode gap confinement region calculated from simulations of the WM1 bands in section 2.6.1:

| λ_0 (nm) | Q_{total} | Q_{in} | Q_{out} | $V_0 [(\lambda_0/n)^3]$ |
|------------------|--------------------|-----------------|-------------------|-------------------------|
| 1270.8 | 7000 | 8200 | 4.8×10^4 | 1.36 |

Table 2.3: Parameters of the fundamental SU-8 strip cavity mode extracted from the FDTD simulation of a strip with $w_{\text{strip}} = 1 \mu\text{m}$ and $h_{\text{strip}} = 0.1 \mu\text{m}$.

between 1265 nm and 1277 nm. The mode volume, $V_0 = 1.36(\lambda_0/n)^3$, is small and very similar to the mode volume of the WMLD cavity $[1.29(\lambda_0/n)^3]$, as one might expect from the similarity of their field profiles. The SU-8 strip cavity has a moderate $Q_{\text{total}} = 7000$, which is higher than the simple unoptimised L3 cavity (5010), but much lower than the optimised L3 (1.21×10^5) and WMLD cavity mode (2.4×10^7). The Q factor is clearly limited by $Q_{\text{in}} = 8200$, which is an order of magnitude smaller than Q_{out} . This suggests that the Q factor is not limited by leaky mode components outside the light cone, as with the L3 cavity (see section 2.4.4), but rather another mechanism which causes losses in the PhC plane. The mechanism responsible for these losses is discussed in section 2.6.3. Despite this limiting factor, the Q_{total} and Q_{total}/V_0 ratio of the SU-8 strip cavity mode are still moderately high and expected to be suitable for CQED applications, as explained in section 3.6.

There are relatively few examples of theoretical results for similar cavity designs to the SU-8 strip cavity available in the literature for comparison, but perhaps the closest are those presented by Gardin *et al.* [89] and Tomljenovic-Hanic *et al.* [90]. Gardin *et al.* present results from a 110 nm-thick PMMA strip (refractive index ~ 1.5) of width $6a$ on an InP membrane, which yielded a cavity mode with $Q_{\text{total}} \approx 4300$ and a mode volume of $V_0 = 1.31(\lambda_0/n)^3$. This is comparable in magnitude to the values obtained for the SU-8 strip cavity. The lower Q reported for the PMMA strip cavity can be attributed to the presence of silica cladding below the PhC membrane, which is expected to reduce the Q factor [75].

The results presented by Tomljenovic-Hanic *et al.* [90] are less comparable to those obtained for the SU-8 strip cavity: Q factors of order 10^5 or higher and mode volumes in the range $1.8 - 2.3(\lambda_0/n)^3$ are reported for a polymer strip, with refractive index 1.45, on top of a PhC membrane. Part of the reason for the difference in the magnitude of the Q factor is due to differences in the strip geometry. We will see in Ch. 5 that an optimised SU-8 strip cavity design (defined by a wider strip) can reach similar theoretical values.

2.6.3 TE-TM mode coupling

As noted in section 2.6.2, the Q_{total} of the SU-8 strip cavity mode is limited by in-plane losses. The mechanism responsible for these losses is referred to as TE-TM mode coupling: a process which is usually inhibited by the orthogonality of the TE-like and TM-like modes in a PhC slab cavity which is symmetric about $z = 0$ (see section 2.3.4). If the z -symmetry is broken (as is the case for a PhC waveguide with a layer of SU-8 on the top surface), the TE-like and TM-like modes are no longer constrained to be solely TE or TM polarised at $z = 0$, and the orthogonality between them is lost. The breaking of the z -symmetry therefore facilitates coupling of TE-like and TM-like modes with the same \mathbf{k}_{\parallel} to one another. Such TE-TM mode coupling can result in energy being transferred from an otherwise well-confined TE-like cavity mode to a TM-like mode which is not confined by the photonic band gap, and is free to propagate away from the cavity, along the slab. Clear evidence of losses due to TE-TM coupling in the SU-8 strip cavity system is observed from a snapshot of the E_z field in the $z = 0$ plane, shown in Fig. 2.24. In a PhC cavity with preserved z -symmetry, the cavity mode is completely TE-polarised in this plane and the E_z component is zero. However, for the SU-8 strip cavity with broken z -symmetry, a significant E_z component is clearly observed, which propagates away from the cavity along the PhC slab. We attribute this to a TM-like mode: energy is transferred from the TE-like cavity mode to the TM-like slab mode via TE-TM coupling. The resulting losses in the plane of the PhC slab limit the Q factor.

2.6.4 Fourier analysis of TE-TM coupling

The TE-TM coupling in the SU-8 strip cavity is further understood by investigating the spatial Fourier components of the fields. We first reproduce results from Tanaka *et al.* [75] to prove the validity of the method, before applying it to the SU-8 strip cavity.

2.6.4.1 Example: L3 cavity on cladding

In their publication, Tanaka *et al.* [75] investigate losses of a simple L3 cavity (with no hole shifts or radius alteration) in a Si slab, placed on top of an SiO₂ cladding layer. The PhC has a lattice constant $a = 420$ nm, hole radius $r = 0.29a$ and a slab thickness $z_{\text{slab}} = 0.6a$; the cladding layer is assumed to extend infinitely below the PhC slab. We performed FDTD simulations of this structure to check for consistency with the FDTD results published by Tanaka *et al.* A resolution

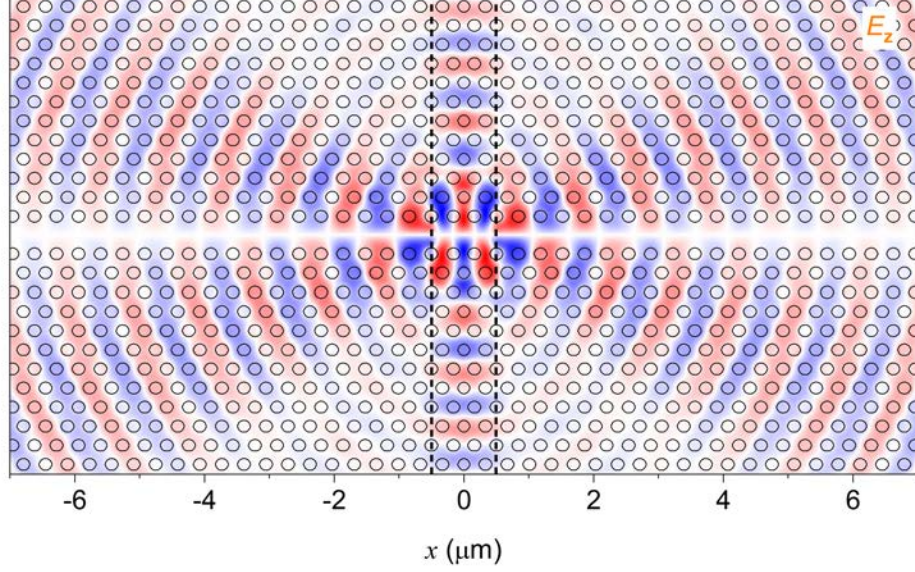


Figure 2.24: Snapshot of the E_z field through the plane $z = 0$ obtained from exciting the fundamental cavity mode of an SU-8 strip mode gap cavity. The dimensions of the SU-8 strip are $h_{\text{strip}} = 0.1 \mu\text{m}$ and $w_{\text{strip}} = 1 \mu\text{m}$. The strip position is indicated by the dashed lines; red and blue indicate opposite field polarities.

of $\rho_{xyz} = 20$ was used, with S and AS symmetry conditions applied at $x = 0$ and $y = 0$, respectively. The cavity was at the centre of a 22×21 hole PhC. Refractive indices used for the materials are not specified in the publication; we used material databases included with the Lumerical software, which give $n_{\text{slab}} = 3.47$ for Si and $n_{\text{cladding}} = 1.44$ for the SiO_2 cladding at the cavity mode wavelength, $\lambda_0 = 1.603 \mu\text{m}$ (frequency $0.262c/a$). The wavelength obtained by Tanaka *et al.* was $1.59 \mu\text{m}$, which is in reasonable agreement. The thickness of the SiO_2 cladding layer was set to $\lambda_0/2$ in our FDTD simulation – the same as the padding distances.

In table 2.4 we compare values of the Q factor and its components obtained from the FDTD simulation to those reported by Tanaka *et al.* Q_{upper} and Q_{lower} are Q components associated with planes above and below the slab, respectively (planes 5 and 6 in Fig. 2.10), and are related to Q_{out} by:

$$\frac{1}{Q_{\text{out}}} = \frac{1}{Q_{\text{upper}}} + \frac{1}{Q_{\text{lower}}}. \quad (2.31)$$

Good consistency is found between the results, which suggests sufficient convergence of the FDTD simulation results for the purposes of this demonstration.

To analyse the sources of loss, the spatial Fourier transform of the E_y field component, $|\text{FT}(E_y)|$ is computed in the planes $z = z_{\text{slab}}/2$ and $z = -z_{\text{slab}}/2$: the top and bottom of the PhC slab,

| Result | Q_{total} | Q_{in} | Q_{upper} | Q_{lower} | Q_{out} |
|----------------------|--------------------|-----------------|--------------------|--------------------|------------------|
| FDTD | 950 | 2700 | 8440 | 1780 | 1500 |
| Tanaka <i>et al.</i> | 750 | 1960 | 8170 | 1380 | 1180 |

Table 2.4: Comparison of FDTD results for the Q factor and its components with the results presented by Tanaka *et al.* [75].

at the air-slab and SiO₂-slab boundaries, respectively. The results obtained by Tanaka *et al.* are shown in Figs. 2.25(a) and 2.25(b), while the FDTD results we obtained are shown in Figs. 2.25(c) and 2.25(d). In general, good agreement is found between our results and those published, with some minor discrepancies likely arising from slightly different simulation parameters (such as the mesh resolution or refractive indices of the materials). The light cone is shown by the solid red circle, which encircles the leaky region for out-of-plane losses. Note that the leaky region is larger in diameter at the bottom of the slab, due to the reduced refractive index contrast at the SiO₂-slab side, relative to the air-slab side. This results in larger losses out of this side of the slab, hence Q_{lower} is significantly lower than Q_{upper} .

In addition to losses to the air and SiO₂ cladding, losses due to TE-TM mode coupling are evident from the low Q_{in} , which can be identified in the Fourier transform. Fourier components of the TE-like cavity mode with a \mathbf{k}_{\parallel} vector matching that of the TM-like mode at the cavity mode frequency are able to couple to the TM-like mode. Therefore, in the first Brillouin zone, a contour of a given k_{\parallel} exists at which the TE-TM mode coupling can occur. This contour was extracted from band structure simulations, which found that the TM-like mode crosses the cavity mode frequency, $0.262c/a$, at $k_{\parallel} = 0.434(2\pi/a)$. The method for extracting this value is demonstrated in section 2.6.4.2 for the SU-8 strip cavity, rather than for this example. The contour is shown on the plots of $|\text{FT}(E_y)|$ by the dashed red lines. Strong indications of TE-TM mode coupling are clearly visible, especially at the air-slab boundary [Figs. 2.25(a) and 2.25(c)], for which a significant component of the field adheres to the TM contour. Also shown are copies of the TM contour displaced by reciprocal lattice vector, \mathbf{G} , giving \mathbf{k}_{\parallel} vectors at which the TM mode also crosses the cavity mode, due to the periodicity of the PhC. Some evidence of TE-TM coupling is also seen around these contours.

From the comparison to the work by Tanaka *et al.* performed here, we find an effective tool for analysing TE-TM mode coupling via Fourier transformation techniques and demonstrate that our own FDTD simulations yield valid results, by their close agreement. This analysis is therefore

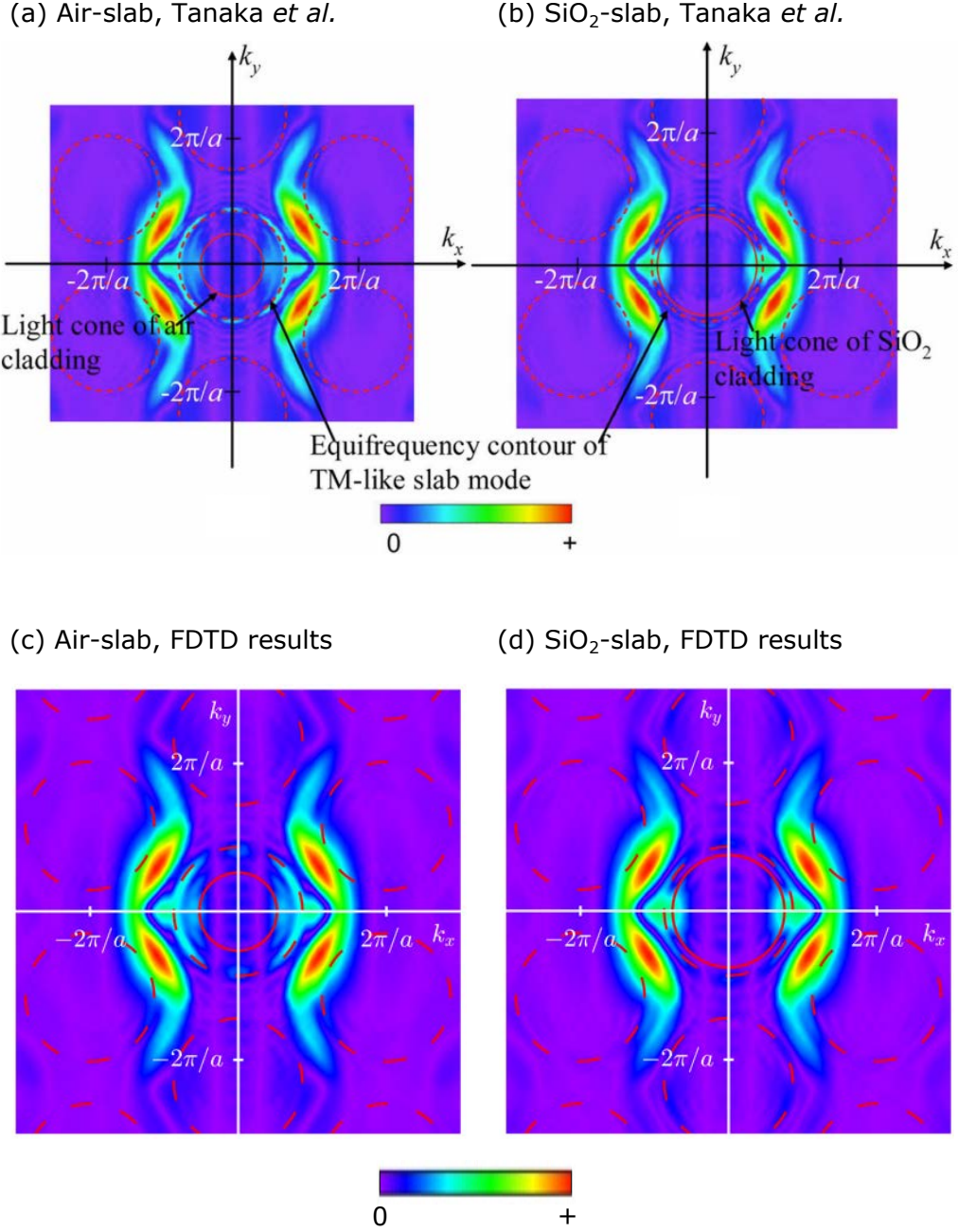


Figure 2.25: Comparison of calculated $|FT(E_y)|$ at the air-slab ($z = z_{\text{slab}}/2$) and SiO₂-slab ($z = -z_{\text{slab}}/2$) boundaries of the L3-on-cladding structure, with comparison to published results. (a) and (b): results extracted directly from the publication by Tanaka *et al.* [75]. (c) and (d): results obtained by our FDTD simulations. The light cone is marked on as a solid red circle; contours of the TM-like slab mode, at which TE-TM coupling can occur, are marked by dashed red lines.

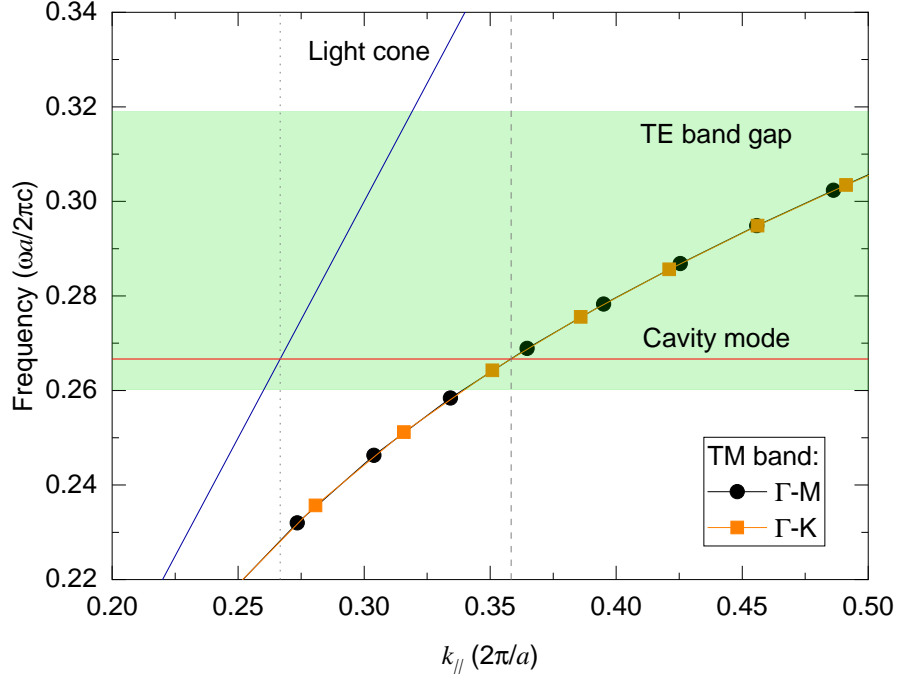


Figure 2.26: Identifying the $k_{||}$ crossing point of the TM-like band and the TE-like cavity mode. The TM-like band is plotted for the Γ -M and Γ -K symmetry directions and the typical cavity mode frequency is marked on by the red line. The TE-like band gap is shaded green and the light cone is indicated by the blue line.

suitable to apply to the SU-8 strip cavity, which is carried out in section 2.6.4.2.

2.6.4.2 SU-8 strip cavity

Fourier analysis of the TE-TM mode coupling was applied to FDTD simulations of the SU-8 strip cavity with $w_{\text{strip}} = 1 \mu\text{m}$ and $h_{\text{strip}} = 0.1 \mu\text{m}$. Firstly, the $k_{||}$ contour at which the TM-like mode is expected to couple to the TE-like cavity mode was estimated from band structure simulation results. We use the calculated band structure for the PhC slab presented in Fig. 2.8 of section 2.3.4, in which a TM-like band clearly crosses into the TE-like band gap. To find the value of $k_{||}$ at which the TM-like mode crosses the SU-8 strip cavity mode (at a frequency of $0.267c/a$ for this example), the frequency of the TM-like band along the Γ -M and Γ -K symmetry directions extracted from Fig. 2.8 is plotted against $k_{||}$ in Fig. 2.26. The cavity mode and TM-like band cross at $k_{||} = 0.358(2\pi/a)$, so we expect field components along this contour due to TE-TM coupling. The cavity mode intercepts the light cone at $k_{||} = 0.267(2\pi/a)$, which defines the leaky region for out-of-plane losses.

The spatial Fourier transform of the electric field components was obtained for the plane $z =$

$z_{\text{slab}}/2$, the top surface of the PhC slab; the results are presented in Fig. 2.27. On each diagram, the light cone contour at $k_{\parallel} = 0.267(2\pi/a)$ is shown by the solid red circle, which encloses the leaky region. The TM mode contour at which TE-TM coupling is expected, $k_{\parallel} = 0.358(2\pi/a)$, is indicated by the dashed red line (along with repeated contours separated by reciprocal lattice vector, \mathbf{G}). In Figs. 2.27(a) and 2.27(b), $|\text{FT}(E_x)|$ and $|\text{FT}(E_y)|$ are shown – the two main electric field components of the TE-like cavity mode. The distribution of $|\text{FT}(E_y)|$ is similar to that of the WMLD cavity, shown in Fig. 2.19 of section 2.5.4, as one would expect from the similar spatial profile of the cavity mode. However, for the SU-8 strip cavity, additional components are observed around the TM contours, which are indicative of TE-TM coupling facilitated by the broken z -symmetry.

The TE-TM coupling is perhaps most apparent in $|\text{FT}(E_x)|$ [Fig. 2.27(a)], which has intense field components at the TM contour of the first Brillouin zone. In the example by Tanaka *et al.* [75] for an L3 cavity on SiO_2 cladding, only $|\text{FT}(E_y)|$ is considered because E_y is the dominant field component of the L3 cavity mode [32]. However, the E_x and E_y field components are of comparable magnitude for the SU-8 strip cavity mode, so both need to be considered. For this reason, it is helpful to visualize $|\text{FT}(E_x)| + |\text{FT}(E_y)|$, shown in Fig. 2.27(c), as an overview of the \mathbf{k}_{\parallel} -space distribution of the TE electric field components, which provides an indication of the extent of the TE-TM mode coupling in a single diagram. Therefore, we choose to present $|\text{FT}(E_x)| + |\text{FT}(E_y)|$ in cases where the TE-TM coupling analysis is performed elsewhere in this thesis, rather than plotting the components individually.

The observations of TE-TM coupling from the TE field components are also consistent with the behaviour of $|\text{FT}(E_z)|$, shown in Fig. 2.27(d), which is expected to be the main electric field component of the TM-like mode. In particular, four intense lobes are seen along the TM contour of the first Brillouin zone, which match those observed for the TE components. \mathbf{k}_{\parallel} components are also seen away from the TM contours, which are likely E_z components of the TE-like cavity mode.

The Fourier transform analysis presented here has allowed us to visualize and confirm the presence of TE-TM coupling, which limits the Q factor of the SU-8 strip cavity due to the resulting in-plane losses. Note that the analysis was also applied to a plane at $z = -z_{\text{slab}}/2$ (the bottom of the slab), but no significant difference in the spatial Fourier components of the fields was found. In Ch. 5, the utility of the technique is exercised, as it is applied to help optimise the SU-8 strip cavity

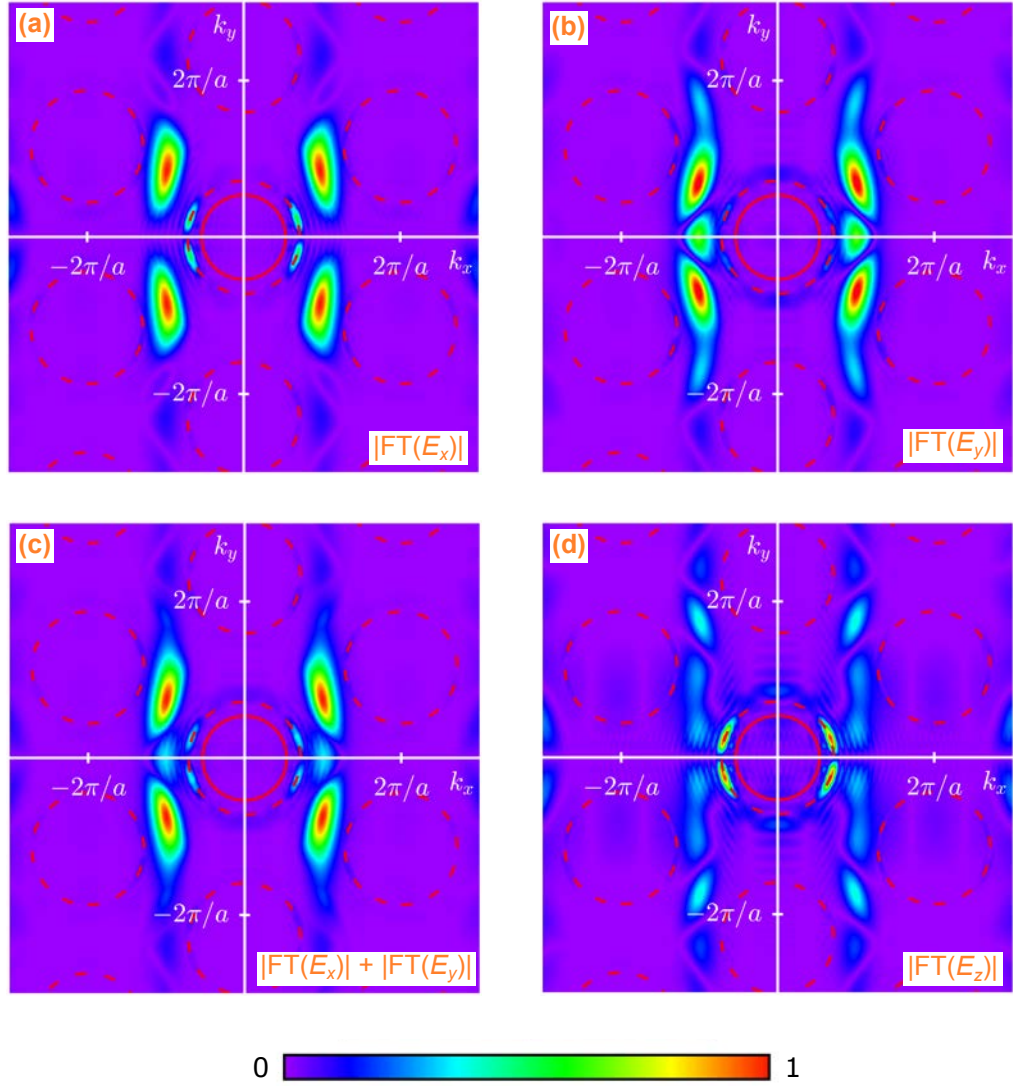


Figure 2.27: Spatial Fourier transform of different electric field components extracted from FDTD simulations at $z = z_{\text{slab}}/2$ for an SU-8 strip cavity with $w_{\text{strip}} = 1\mu\text{m}$ and $h_{\text{strip}} = 0.1\mu\text{m}$. The component is marked at the corner of each sub-figure (a)–(d). The light cone is marked on as a solid red circle; contours of the TM-like slab mode, at which TE-TM coupling can occur, are marked by dashed red lines. Each result is normalised.

design and theoretically achieve much higher Q factors through reduction of the TE-TM coupling.

2.7 Summary

This chapter has laid the groundwork required to understand the physics of PhC slabs, cavities and waveguides, in addition to the application of FDTD methods to simulate the structures. Band structure calculations were performed to demonstrate that the hexagonal hole-in-slab PhC, which forms the basis of the PhC devices investigated in this work, exhibits a photonic band gap for

TE-like modes. This intuitively led to the concept of the L3 defect cavity [32], which confines a TE-like cavity mode to the slab. Such L3 cavities were commonly used in QD samples as alignment and calibration markers for optical measurements in this project. The L3 cavity was used as an example to demonstrate the FDTD simulation methodology that was applied to all PhC cavity simulations performed for this work, including Q and V_0 calculations and analysis of the spatial Fourier transform.

The concept of the mode gap cavity [33] was introduced and examples of devices and applications from the literature were reviewed. The WMLD mode gap cavity [34] was simulated as an example, to show that high Q cavities can be formed by locally altering the mode gap of a PhC waveguide to generate a confinement potential. This paved the way to the concept of a mode gap cavity defined by SU-8 photoresist on top of a PhC waveguide, which is the focus of this project. Simulations were performed of an SU-8 strip cavity to prove its effectiveness, with some limitations due to TE-TM mode coupling identified, which will need to be considered going forward.

The rest of this thesis concerns the successful experimental realisation and optimisation of SU-8-defined mode gap cavities, towards the goal of achieving CQED applications. In Ch. 3, the SU-8 cavity technology is put into context within the field of CQED and the experimental method for implementing the technique is detailed. This is followed by results chapters which report successful fabrication of mode gap cavities defined by SU-8 disks (Ch. 4) and SU-8 strips (chapters 5 and 6).

3

Overview of cavity quantum electrodynamics and experimental techniques

3.1 Single photon sources

Single photon sources (SPSs) are highly sought after for applications in the fields of quantum information processing and quantum communication, in which the polarization state of a single photon is commonly used as a qubit. Single photons offer the benefit that they are robust to decoherence relative to other media [5] and single qubit operations are easily performed using waveplates to rotate the polarization. However, a downside to this choice of qubit is that it can be a significant challenge to achieve strong enough interactions between the photons to perform operations involving multiple qubits. Initially, it was believed that such interactions would need to be facilitated by strong optical non-linearities unattainable in conventional media [7], but in 2001 Knill *et al.* [101] devised a linear optical quantum computing regime which enables scalable quantum computing using only SPSs, single photon detectors and linear optical circuits. Experimental implementations of this technique have seen success, including the demonstration of quantum logic gates [6, 8] and the operation of simple quantum algorithms using on-chip silica waveguide photonic circuits [9]. Parallel to the development of these photonic circuits, work is ongoing to develop SPSs with improved performance for these applications [102].

SPSs are also in demand for quantum communication applications, such as the well-known BB84

quantum key distribution protocol [3]. By encoding information in the polarization states of a stream of single photons, this protocol allows for the guaranteed security of cryptographic key sharing, due to the inability of an eavesdropper to completely replicate the quantum state of an intercepted photon [4]. For this application, it is important to have access to an efficient SPS, which is preferably effective over long distances for real-life implementations. This drives the need to develop SPSs operating at the wavelengths used for optical telecommunications: 1.3 μm or 1.55 μm , which correspond to the zero dispersion wavelength and absorption minimum, respectively, of commercially available silica fibres.

In general, a useful SPS must satisfy three criteria. Firstly, and most importantly, the SPS should generate exactly one single photon on demand in response to an external trigger, such as a laser pulse or an electrical pulse. High single photon purity is crucial for applications such as quantum key distribution, which are otherwise potentially vulnerable to eavesdropping if multiple photons are triggered from the source [11, 103]. The test for single photon purity is to perform a Hanbury Brown and Twiss (HBT) experiment [104], in which the stream of photons is divided by a 50:50 beamsplitter and recorded by a single photon detector in each of the divided paths. The second order correlation function, $g^{(2)}(\tau)$ is measured, given by

$$g^{(2)}(\tau) = \frac{\langle n_1(t)n_2(t+\tau) \rangle}{\langle n_1(t) \rangle \langle n_2(t+\tau) \rangle}, \quad (3.1)$$

where $n_i(t)$ is the number of photon counts registered at detector i at time t . τ is the time delay between a photon measured at detector 1 at time t and a photon measured at detector 2 at time $t + \tau$; the angular brackets indicate a time average. For coherent light with Poissonian photon statistics, $g^{(2)}(0) = 1$, since the timing between the photons is uncorrelated. On the other hand, a stream of triggered single photons exhibits antibunched photon statistics, for which the timing between the photons is ideally constant and $g^{(2)}(0) < 1$. Indeed, a perfect SPS would have $g^{(2)}(0) = 0$, since a single photon can trigger only one of the detectors. It can be shown that for photon number states, $g^{(2)}(0) = 1 - 1/n$, where n is the number of photons (see Ch. 8, pp. 160-163 of Ref. [105]). It is therefore important to be able to demonstrate $g^{(2)}(0) < 0.5$ from an SPS, implying that on average less than 2 photons are contained in a pulse, although generally a $g^{(2)}(0)$ much closer to zero is sought after. Measurement of $g^{(2)}(\tau)$ via the HBT experiment was employed in early demonstrations of SPSs [15, 106, 107, 108] and is now a standard procedure for reporting single photon operation [14, 102].

The second requirement for a SPS is that for each trigger, there should be a high probability of extracting a single photon from the device, which is generally referred to as the SPS having a high efficiency or a high brightness. The brightness of a SPS generally determines the speed of quantum information and communication protocols. A commonly used figure of merit to quantify the SPS brightness is the brightness at the first lens, B_{lens} , which describes the probability of a single photon being output from the device per trigger pulse.

Finally, for applications which involve interactions between multiple photons (such as linear optical quantum computing [101]), it is often a requirement that the photons must be indistinguishable: each photon must be described by the same pure quantum state, which cannot be distinguished by any measurement. The indistinguishability of the photons can be tested by performing a Hong-Ou-Mandel (HOM) two photon interference measurement [109], in which two photons are fed simultaneously into the same input of a 50:50 beam splitter. If the photons are indistinguishable, a destructive quantum interference effect causes both photons to exit the beam splitter via the same path.

A SPS that satisfies the three desired criteria can be achieved by utilising non-linear optical effects with attenuated laser pulses. The most widely-used and historically best-performing SPSs are based on spontaneous parametric down-conversion (SPDC) to generate pairs of photons from higher energy photons in trains of laser pulses [6, 8, 9, 110]. The two photons in each generated pair are then separated: one photon of the pair forms the output of the SPS and the other “heralds” its presence when it arrives at a single photon detector. An inherent disadvantage of generating single photons via this method is that SPDC is a non-deterministic process, which always has a finite probability of generating more than one photon pair [14]. This limits the brightness of the SPS, since increasing the pump power in an attempt to increase the rate of heralded single photon production also greatly increases the probability of generating more than one photon pair per pulse. There is therefore an inherent trade-off between brightness and single photon purity [111], which ultimately limits the performance and scalability of the source.

An alternative approach to making a SPS is to use triggered spontaneous emission from a quantum two-level system, which is attractive because in an ideal system, exactly one photon is emitted upon radiative decay and no more photons can be emitted until the system is excited again. Such a system therefore holds the potential for a more deterministic SPS, able to achieve high brightness (with an operation rate only limited by the radiative lifetime of the transition) without

sacrificing single photon purity. The first SPS of this kind was demonstrated using resonance fluorescence from a low density vapour of sodium atoms [106]. Since this experiment, SPSs have been demonstrated using a wide variety of quantum systems, including trapped ions [107], single molecules [108, 112] and nitrogen vacancy centres in diamond [113, 114].

Semiconductor QDs are attractive candidates for SPSs because they exhibit quantum confinement of charge carriers (electrons and holes) in all three spatial dimensions, and so exhibit quantised energy levels. This thesis focuses on self-assembled semiconductor QDs – specifically those based on the III-V semiconductors InAs and GaAs – which are grown in a solid state medium. As will be covered in section 3.2.2, this type of QD has excellent optical properties and can be conveniently incorporated into on-chip optical devices, such as optical microcavities, to achieve high single photon extraction efficiencies. Over the past few decades, significant work has gone into developing SPSs based on self-assembled In(Ga)As/GaAs QDs, which are now able to compete with those based on SPDC [14].

This chapter introduces self-assembled QDs, beginning with an overview of their optical properties and growth methods. This is followed by a review of SPSs based on self-assembled In(Ga)As/GaAs QDs, with a focus on incorporation of the QDs into microcavity devices to exploit the effects of cavity quantum electrodynamics (CQED). The fundamental theory of CQED is covered and methods of deterministically achieving coupling between a QD and cavity, which is a significant technical challenge, are reviewed. Finally, we detail the experimental techniques used in this project, towards the goal of achieving deterministic QD-cavity coupling for application as a telecommunications wavelength, on-demand SPSs.

3.2 Self-assembled In(Ga)As/GaAs quantum dots

3.2.1 Growth

Self-assembled QDs are typically formed via epitaxial growth of lattice mismatched semiconductors, in which layers of material are deposited on a substrate with sub-monolayer precision using a technique such as molecular beam epitaxy (MBE) [115] or metal-organic chemical vapour deposition [116]. For the case of InAs QDs grown on a GaAs substrate, the lattice mismatch is approximately 7%, which enables formation of self-assembled QDs through the Stranski-Krastanov (SK) growth mode [117]. Initially, deposition of InAs on the substrate creates a planar layer, known

as the wetting layer (WL), but due to the larger lattice constant of InAs, this layer is biaxially compressed to the GaAs lattice. As the thickness of the WL is increased by further deposition of material, the strain energy between the layers increases. At a critical thickness it becomes energetically favourable for the strain to be relieved by the formation of 3D islands. These islands form the self-assembled QDs.

The properties of self-assembled QDs strongly depend on the materials used and the growth conditions, such as the substrate temperature [118] and material deposition rate [29] during growth. For conventional InAs/GaAs QDs, the QDs form at a critical thickness of approximately 1.7 monolayers (ML) [119], although the precise thickness depends on the growth conditions. The islands formed typically have a height between 3 – 10 nm and a diameter of a few tens of nm [31]: sufficiently small to exhibit quantum confinement effects on charge carriers. Due to the nature of the self-assembled growth mechanism, the QDs are formed at random positions with a distribution of sizes, as seen from the example in Fig. 3.1(a), which shows an atomic force microscope (AFM) image of a sample with a high density of InAs/GaAs QDs ($\sim 120/\mu\text{m}^2$), taken from Ref. [31]. The QD density can be altered by careful control of the InAs growth rate, with densities between 1 – $1000/\mu\text{m}^2$ typically achievable using MBE growth [29]. High density QD samples are optically bright and are therefore useful as a light source for characterising microcavity structures [56], as is performed in this thesis. Low density samples, on the other hand, are ideal for single QD spectroscopy [22, 120] and are essential for SPSs. The QD layer is often buried by overgrowth of GaAs – a process known as capping – which enables the QDs to be embedded in microcavity devices and improves their optical properties by preventing non-radiative recombination of charge carriers at surface states [121]. An example of a capped QD, imaged by a scanning tunnelling microscope, is shown in Fig. 3.1(b) (taken from Ref. [102]). The capping process can have a significant impact on the structural properties of the QDs, such as a reduction of their height and intermixing between the In and Ga of the surrounding capping layer [122].

The more conventional GaAs-capped InAs/GaAs QDs are usually optically active in the 900 – 1000 nm wavelength range [15, 22, 123], but a number of growth recipes can be used to extend their emission to telecommunications wavelengths. These methods mostly involve the formation of InGaAs/GaAs QDs with reduced strain and a larger lateral size compared to InAs/GaAs QDs. The techniques include using one of, or a combination of, low growth rates [124], interrupted sub-monolayer deposition [125] and/or capping the QDs with a strain-reducing InGaAs capping layer [126]. A typical approach is to grow InAs QDs at a low growth rate and apply a thin (a few

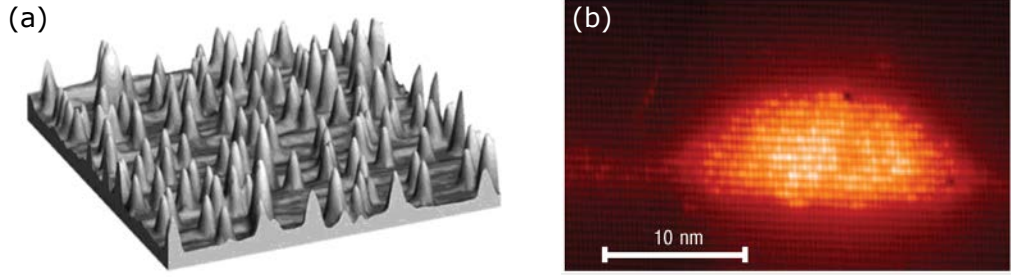


Figure 3.1: Images of InAs/GaAs self-assembled QDs. (a) AFM image of a $1\ \mu\text{m} \times 1\ \mu\text{m}$ area of uncapped QDs with a density of $\sim 120/\mu\text{m}^2$, taken from Ref. [31]. (b) Cross-sectional scanning tunnelling microscope image of a capped QD embedded in a device, taken from Ref. [102].

nm) InGaAs capping layer before the conventional capping with GaAs, which can produce QDs which emit at $1.3\ \mu\text{m}$ [29] at the cryogenic temperatures necessary for single QD spectroscopy. The redshift of the emission wavelength is attributed to a reduction of the compressive strain in the growth direction [116], which can be controlled by altering the In content of the InGaAs capping layer [127]. The QD emission wavelength can be further increased by incorporating QD bilayers into the sample: growing a “seed” layer of QDs followed by a second layer enables the strain interactions between the two layers to be exploited to achieve optical activity beyond $1.3\ \mu\text{m}$ [30, 128].

3.2.2 Optical properties

The optical activity of self-assembled QDs stems from the radiative recombination of confined electrons and holes, which occupy discrete energy levels inside the QD. The quantised carrier energy levels are a result of quantum confinement in all three spatial dimensions, imposed by the nanometre-scale confinement potential of the QD. This results in efficient radiative recombination due to the delta function-like density of states [31] and strong overlap of the confined electron and hole wavefunctions [129, 130]. Single QDs are therefore promising for integration into triggered SPSs, with favourable optical properties that can be tailored by the choice of material and growth methods. For example, while the $900 - 1300\ \text{nm}$ (and longer) range can be covered by In(Ga)As/GaAs QDs, single photons can be extracted from QDs operating at blue and UV wavelengths based on GaN [131, 132], green and red wavelengths based on CdSe and InP [133], and the telecommunications wavelength of $1.55\ \mu\text{m}$ based on InAs/InP [134].

A simplified representation of the carrier injection, capture and recombination processes in a self-assembled InGaAs/GaAs QD is illustrated in Fig. 3.2(a) which follows the explanation in Ref. [31]. The gross electronic structure of the QD is represented, with discrete electron (hole) energy levels

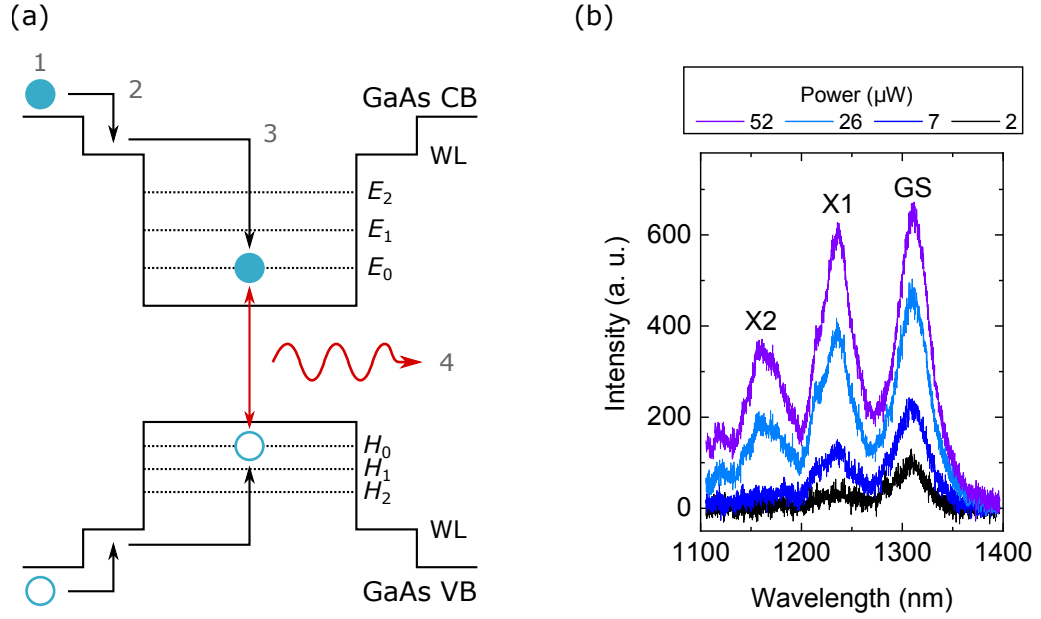


Figure 3.2: Photoluminescence from self-assembled QDs. (a) Schematic diagram demonstrating the processes of carrier excitation, capture, relaxation and radiative recombination which lead to emission of photons by a QD. (b) μ PL spectrum collected from an ensemble of InGaAs/GaAs QDs, demonstrating inhomogeneously broadened peaks which correspond to recombination from the GS, X1 and X2 states. Measurements were taken at a temperature of ~ 4.2 K; the excitation power shown was measured after the objective lens. The expected QD density is $\sim 20/\mu\text{m}^2$.

represented by E_0 (H_0), E_1 (H_1) and so on. We consider the case of above band-gap excitation via a laser, which is applicable to the μ PL measurements performed for this thesis. Electron-hole pairs are injected into the conduction band (CB) and valence band (VB) of the bulk GaAs, respectively (1), by the laser. These carriers are then captured into the WL (2), due to its narrower band gap. The carriers are then captured into the QDs and rapidly relax to the ground state (3) on a ps timescale [135]. Once the carriers reach the ground state, radiative recombination can take place (4), emitting a single photon per pair of electrons and holes (which form an exciton inside the QD) that recombine. Radiative lifetimes for the ground state transition in In(Ga)As/GaAs QDs are typically ~ 1 ns [136, 137, 138].

If the rate of carrier excitation is sufficient for multiple carriers to be captured into a QD on a timescale shorter than the radiative lifetime, then state-filling can occur due to the Pauli exclusion principle and carriers occupying higher energy levels can recombine. This results in emission from excited states of the QD, as seen in the μ PL spectrum, obtained from a QD ensemble excited above band-gap with a HeNe laser, displayed in Fig. 3.2(b). The three peaks in the intensity correspond to emission from the ground state (GS), first (X1) and second (X2) excited states of QDs in the ensemble. Recombination takes place between electron and hole energy levels with the

same quantum number ($E_0 - H_0$, $E_1 - H_1$, etc.) to give these transitions [139]. Evidently, as the excitation power is increased, the emission from the excited states increases, which is due to an increased rate of carrier excitation and therefore a higher degree of state filling in the QDs. Each of the peaks is inhomogeneously broadened due to the distribution of sizes of the many QDs excited by the $\sim 1\ \mu\text{m}$ laser spot; the different QD sizes result in variation of the confinement potential, which in turn leads to differences in the energy levels and therefore the transition energies. The inhomogeneous broadening of the QD ensemble is typically $\sim 30\ \text{nm}$ (FWHM) for the samples studied in this work. In comparison, the single exciton linewidth of a QD is often narrower than the resolution of the spectrometer used (see section 3.8.2) and is usually reported to be around $0.06\text{--}0.08\ \text{nm}$ [86, 137, 140].

Emission lines from single excitonic transitions in QDs can be observed via μPL measurements of QD ensembles with a sufficiently low areal density by using a regime of weak excitation power, so that carriers are captured by fewer QDs. This is shown by the example spectrum in Fig. 3.3, which was obtained from a sample containing a low density ($20\text{--}30\ /\mu\text{m}^2$) of InGaAs-capped InAs QDs using a low excitation power of $\sim 140\ \text{nW}$ (measured after the objective). A “forest” of narrow emission lines is seen, corresponding to individual excitonic transitions in the QDs. Note that μPL measurements of InGaAs/GaAs QDs, especially for single QD spectroscopy, typically have to be performed at cryogenic temperatures less than $\sim 50\ \text{K}$, due to the detrimental effects of non-radiative processes at higher temperatures. Thermal carrier escape [141] and non-radiative recombination [142] reduce the emission intensity from the QDs as the temperature is increased, while the linewidth of individual QD transitions is significantly broadened by acoustic phonon interactions [143]. Additionally, the QD emission redshifts with temperature: the ensemble emission is typically $\sim 100\ \text{nm}$ longer in wavelength at room temperature, compared to $4.2\ \text{K}$ [30]. In section 3.8.4 we will see that small increases in temperature (staying below $50\ \text{K}$) can be beneficial to tune the wavelength of an exciton line via the induced redshift.

3.2.3 Excitons and biexcitons in quantum dots

In order to understand how a single QD can be implemented into a SPS, some understanding of the excitonic states and transitions in a QD is required. A brief overview of some of the lowest energy transitions is provided here; a more detailed discussion can be found in Refs. [144, 145]. InAs and GaAs have a zinc-blende crystal structure, which supports degenerate heavy hole and

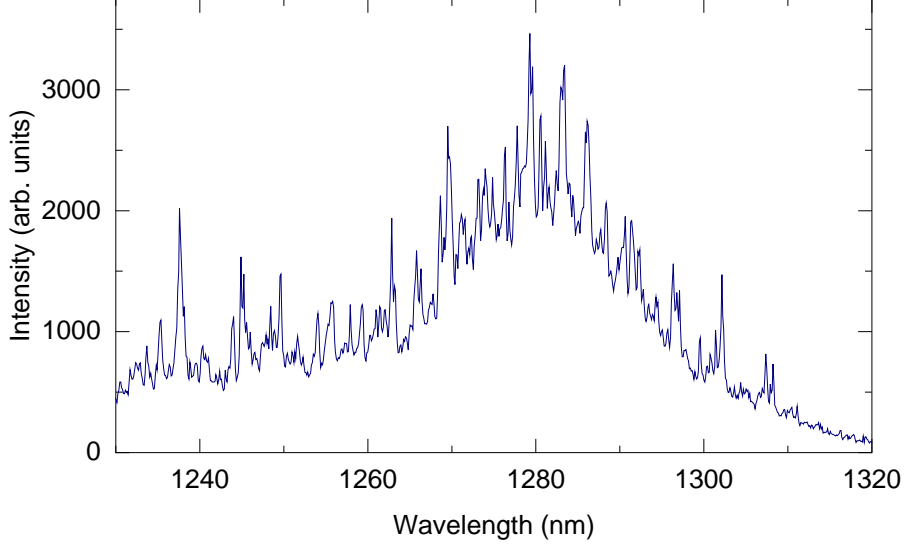


Figure 3.3: μ PL spectrum collected from an ensemble of InGaAs/GaAs QDs using a low excitation power (with a 532 nm CW laser diode) and 10 s acquisition time, showing a forest of single QD emission lines. Measurements were taken at a temperature of ~ 8 K.

light hole valence bands at $k = 0$. Quantum confinement in a QD lifts this degeneracy, so that the lowest energy transition is between the heavy hole valence band and the conduction band. The lowest energy exciton transition in an InGaAs/GaAs QD is therefore between an electron in the conduction band with spin $S_e = 1/2$ and a heavy hole in the valence band with spin $J_h = 3/2$. Four possible exciton states are formed, which are characterised by their angular momentum projection, $M = S_z + J_z$, along the growth direction (z). The two exciton states with $M = \pm 1$ are bright exciton states, which are able to couple to a photon, whereas the two states with $M = \pm 2$ are dark exciton states. These dark exciton states are mixed by the exchange interaction and are energetically separate from the bright exciton states, which are degenerate in a spherically symmetric QD.

In actual self-assembled InGaAs/GaAs QDs, there is usually a structural asymmetry: QDs grown on (001) substrates are generally elongated along the $(1\bar{1}0)$ plane [146]. In an asymmetric QD, the anisotropic exchange interaction results in a mixing of the bright exciton states into symmetric and anti-symmetric combinations: $|X\rangle = \frac{1}{\sqrt{2}}(|+1\rangle \pm |-1\rangle)$. The two bright exciton states exhibit a small fine structure splitting, s , and couple to photons with orthogonal linear polarisations to decay to the ground state, $|0\rangle$. One of the bright exciton states couples to horizontally-polarised (H) photons, linearly polarised in the (110) plane, whereas the other state couples to vertically-polarised (V) photons, which are polarised in the $(1\bar{1}0)$ plane [147]. The fine structure splitting in InGaAs/GaAs QDs is typically on the order of 10–100 μ eV (less than ~ 0.1 nm) [148].

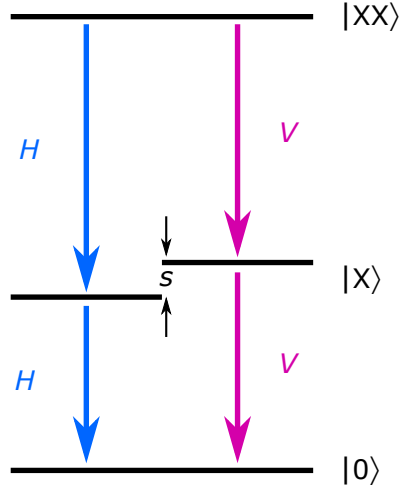


Figure 3.4: Schematic diagram of the biexciton cascade decay in a single QD.

If two electron-hole pairs are captured into the QD, a single bright biexciton state, $|XX\rangle$ is formed, which can decay to one of the $|X\rangle$ states by radiative recombination of an electron-hole pair. This can then decay to $|0\rangle$ by further radiative combination, in what is known as the biexciton cascade decay, which is illustrated schematically in Fig. 3.4. The two photons emitted in this cascade have the same polarisation: either two H or two V polarised photons. Due to the Coulomb interaction between the carriers, the energy of the $|XX\rangle \rightarrow |X\rangle$ transition is different to the energy of the $|X\rangle \rightarrow |0\rangle$ transition (even for the case $s = 0$). This means that the biexciton and exciton emission lines from a single QD are spectrally separated, typically by a few meV (a few nm) [120, 137, 147, 149], hence they can be spectrally filtered. This is important from the perspective of creating SPSs, as it enables single photons to be collected from a QD, even when using non-resonant excitation [15, 150]. By applying spectral filtering to select photons emitted either by the $|XX\rangle \rightarrow |X\rangle$ or $|X\rangle \rightarrow |0\rangle$ transition, a triggered SPS can be achieved [120], since in theory only one photon can be collected per biexciton cascade (and therefore per trigger pulse, for example a laser pulse).

The biexciton cascade decay can also be exploited to create a triggered source of entangled photon pairs [151]. This is achieved by tuning s to zero (or to a magnitude much smaller than the exciton linewidth), for example by applying electric fields [147], magnetic fields [151], controlled strain [152] or using specific growth methods [153, 154]. The pair of emitted photons is then polarisation entangled.

3.3 CQED with quantum dot-microcavity systems

A common approach to creating a SPS based on an individual QD is to embed it into a microcavity structure. By achieving spectral resonance between a QD emission line and a cavity mode, a coupling can be achieved in which photons are emitted into the cavity mode. This can benefit a SPS in a number of ways. Firstly, coupling the emitted photons into a cavity mode offers the potential to more effectively direct them into the collection optics, for example by designing the microcavity to have highly directional free-space emission [65, 155] or to couple into optical fibres [156] or waveguides [157]. The cavity mode also modifies the optical density of states experienced by the emitter, which enables modification of the spontaneous emission dynamics. For the purposes of an SPS, the increased optical density of states at the cavity mode resonance is used to enhance the rate of spontaneous emission from the QD. This benefits both the brightness of the SPS [155], due to the increased proportion of photons emitted into the cavity mode, as well as the indistinguishability of the photons, due to a reduced dephasing of the QD exciton state [158]. The alteration of the spontaneous emission rate is known as the Purcell effect [18], which is a consequence of the weak coupling regime of CQED: the interaction between a coupled cavity-emitter system. In this section, the theory of CQED and its application to QD-based SPSs is covered, including both the weak coupling regime and the strong coupling regime, in which photons are reversibly exchanged between the emitter and cavity, inducing inherently quantum phenomena.

The treatment of CQED presented here follows the methodology laid out by J. Vučković in Ref. [60]. We give the key results and steps in the derivations, but a more detailed discussion can be found in the reference. We consider a two level emitter with ground state $|g\rangle$ and excited state $|ex\rangle$, separated by an energy $E = \hbar\nu$, where ν is the angular frequency of the transition. This could approximate a single quantum emitter such as an atom, or, in our case, an exciton transition of a single QD. We consider the situation in which the emitter is close to resonance with a fundamental cavity mode of angular frequency ω , which is spectrally isolated from any other modes supported by the cavity. We first consider a lossless system, in which the two-level emitter is coupled to the single cavity mode without losses to the surrounding environment. The coupled system is described by the Jaynes-Cummings Hamiltonian, given by:

$$H = H_E + H_F + H_{\text{int}}, \quad (3.2)$$

$$H_E = \frac{\hbar\nu}{2} \sigma_z, \quad (3.3)$$

$$H_F = \hbar\omega \left(a^\dagger a + \frac{1}{2} \right), \quad (3.4)$$

$$H_{\text{int}} = i\hbar \left[g^*(\mathbf{r}_E) a^\dagger \sigma_- - g(\mathbf{r}_E) \sigma_+ a \right], \quad (3.5)$$

where H_E is the emitter Hamiltonian, H_F is the field Hamiltonian and H_{int} is the Hamiltonian encapsulating the interaction between the emitter and field. σ_z is the population operator for the two level system: $\sigma_z = |\text{ex}\rangle\langle\text{ex}| - |\text{g}\rangle\langle\text{g}|$, where the isolated emitter has energy eigenvalues $\hbar\nu/2$ and $-\hbar\nu/2$, corresponding to eigenstates $|\text{ex}\rangle$ and $|\text{g}\rangle$, respectively. The field operators a and a^\dagger are the photon annihilation and creation operators, respectively ($a^\dagger a$ is the photon number operator), and the eigenstates of the field are described by photon number states $|n\rangle$, with energy eigenvalues $\hbar\omega (n + 1/2)$. The eigenstates of the uncoupled system ($H_{\text{int}} = 0$) are denoted $|\text{ex}, n\rangle$ and $|\text{g}, n + 1\rangle$; the corresponding energy eigenvalues are simply the sum of the emitter and field energies.

The expression for H_{int} (Eq. 3.5) is derived by considering the quantum mechanical representation of the cavity-emitter interaction under the dipole approximation: $-\mathbf{d} \cdot \mathbf{E}$, where \mathbf{d} is the dipole moment of the emitter. The approximation $\mathbf{d} = e\mathbf{r}$ is made for a single electron atom, where e is the charge of the electron and \mathbf{r} is its position relative to the nucleus. For an exciton in a QD, \mathbf{r} can be approximated as the distance between the electron and hole. By applying a quantum mechanical treatment, the expression for H_{int} in Eq. 3.5 is obtained (please see Ref. [60]). The operators σ_+ and σ_- are raising and lowering operators of the emitter, respectively. The term $g(\mathbf{r}_E)$ is a coupling parameter between the emitter and cavity field, which is evaluated at \mathbf{r}_E , the position of the emitter. The coupling parameter can be expressed as a product of three terms, which encapsulate different dependencies of the system, as follows:

$$g(\mathbf{r}_E) = g_0 \Psi(\mathbf{r}_E) \cos(\xi), \quad (3.6)$$

where:

$$g_0 = \sqrt{\frac{\mu_{eg}^2 \omega}{2\epsilon(\mathbf{r}_M) \hbar V_0}}, \quad (3.7)$$

$$\Psi(\mathbf{r}_E) = \frac{E(\mathbf{r}_E)}{|E(\mathbf{r}_M)|}, \quad (3.8)$$

$$\cos(\xi) = \frac{\boldsymbol{\mu}_{eg} \cdot \hat{\mathbf{e}}}{\mu_{eg}}. \quad (3.9)$$

The term $\Psi(\mathbf{r}_E)$ summarises the dependence of $g(\mathbf{r}_E)$ on the emitter position. It depends on the ratio of the electric field of the cavity mode at \mathbf{r}_E relative to \mathbf{r}_M : the position at which the energy density of the electric field is at a maximum (i.e. $\epsilon(\mathbf{r}) |E(\mathbf{r})|^2$ is maximised). $\Psi(\mathbf{r}_E)$ reaches a maximum value of 1 when the emitter is positioned at the energy density maximum, $\mathbf{r}_E = \mathbf{r}_M$. The $\cos(\xi)$ term encapsulates the polarization dependence of the coupling parameter: it is dependent on the alignment between the electric field orientation, $\hat{\mathbf{e}}$, at the emitter position and the transition dipole moment matrix element $\boldsymbol{\mu}_{eg} = \langle \text{ex} | e\mathbf{r} | g \rangle$. A maximum value of 1 is achieved when the dipole moment and electric field are aligned.

The g_0 term (Eq. 3.7) of the coupling parameter is the maximum coupling strength for a given system, attained when the dipole moment of the emitter is perfectly aligned with the electric field of the cavity mode ($\cos(\xi) = 1$) and the emitter is positioned at \mathbf{r}_M ($\Psi(\mathbf{r}_E) = 1$). It depends on the properties of both the emitter (μ_{eg}) and cavity mode – the latter introduces a $1/\sqrt{V_0}$ dependence, where V_0 is the cavity mode volume, as defined in Eq. 2.29. It is therefore preferable to achieve a small V_0 in order to maximise g_0 , which is an advantage of using microcavities such as PhC cavities.

The coupling induced by a non-zero H_{int} results in new eigenstates of the emitter-cavity system. It can be shown that the coupled system supports an anharmonic ladder of eigenstates, with energy eigenvalues given by

$$E_{\pm} = \hbar\omega(n+1) \pm \sqrt{\left(\frac{\hbar\delta}{2}\right)^2 + \hbar^2 g^2(n+1)}, \quad (3.10)$$

where $\delta = \nu - \omega$ is the spectral detuning between the cavity mode and emitter and $g = |g(\mathbf{r}_E)|$. For zero detuning, $\delta = 0$, this reduces to

$$E_{\pm} = \hbar\omega(n+1) \pm \hbar g \sqrt{n+1}. \quad (3.11)$$

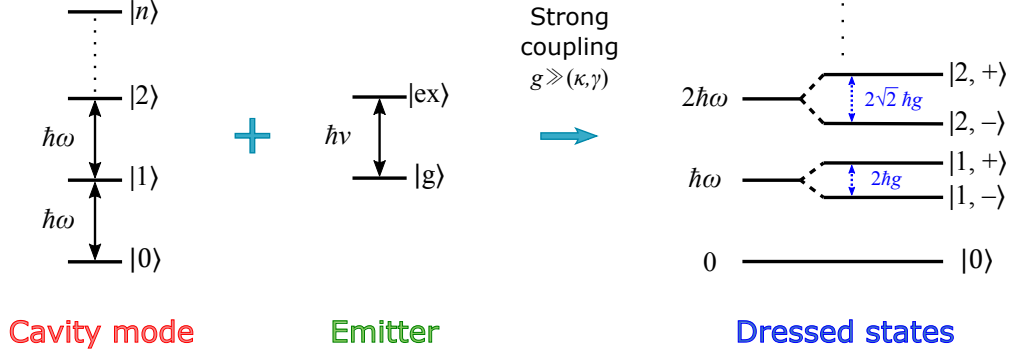


Figure 3.5: Schematic diagram of the Jaynes-Cummings model. The bare states of the uncoupled emitter and cavity are shown (left) which, when strongly coupled, form an anharmonic ladder of dressed states (right).

The corresponding eigenstates, termed dressed states, are denoted $|n + 1, +\rangle$ and $|n + 1, -\rangle$, which are superpositions of the bare (uncoupled) states. The first and second dressed states of the ladder are shown in Fig. 3.5: the $n = 0$ states, $|1, \pm\rangle$ have an energy splitting of $2\hbar g$ and the $n = 1$ states, $|2, \pm\rangle$, have an energy splitting of $2\sqrt{2}\hbar g$. Such splitting of the bare states is a signature of what is referred to as the strong coupling regime between the emitter and cavity.

3.3.1 CQED with losses

We now examine the conditions required to achieve the phenomena predicted by the strong coupling regime of the Jaynes-Cummings Hamiltonian, by considering the effects of losses to the environment. This again follows the methodology laid out by J. Vučković in Ref. [60]. A simple semi-classical approach is applied, in which the effects of losses are accounted for by introducing imaginary components to the cavity and emitter frequencies. We consider the first dressed state ($n = 0$) and redefine the ground state energy as zero for both the field and emitter. Eq. 3.10 can then be redefined to give the eigenfrequencies of the dressed states:

$$\omega_{\pm} = \frac{\omega + \nu}{2} \pm \sqrt{\left(\frac{\delta}{2}\right)^2 + g^2}. \quad (3.12)$$

We consider the cavity mode to have a field decay rate, κ to the surroundings. Similarly, the emitter has a non-resonant decay rate γ due to spontaneous emission losses into other optical modes and non-radiative losses. The linewidths of the cavity mode and emitter are then given by 2κ and 2γ , respectively. The frequencies ω and ν are replaced by the corresponding complex

frequencies, $\omega - i\kappa$ and $\nu - i\gamma$, to represent the cavity and emitter with losses. Substituting these values into Eq. 3.12 gives complex eigenfrequencies of the dressed states

$$\omega_{\pm} = \frac{\omega + \nu}{2} - i\frac{\kappa + \gamma}{2} \pm \sqrt{\left(\frac{\delta - i(\kappa - \gamma)}{2}\right)^2 + g^2}, \quad (3.13)$$

where the real part gives the frequency and the imaginary part describes the damping. For $\delta = 0$, the energy splitting between the states is therefore given by

$$\Delta E = 2\hbar\sqrt{g^2 - \left(\frac{\kappa - \gamma}{2}\right)^2}. \quad (3.14)$$

Evidently, for the strong coupling regime (in which the splitting of the dressed states is non-zero) to be reached, the term inside the square root must be positive. The requirement for strong coupling is therefore $g \gg (\gamma, \kappa)$, where the notation (γ, κ) indicates the largest of the two values. This represents a regime in which photons can be reversibly exchanged between the cavity mode and emitter before escaping to the surroundings. Typically, the linewidth of an atom or QD is significantly narrower than the linewidth of the cavity mode that it is coupled to, so losses from the cavity mode are usually dominant ($\kappa \gg \gamma$). The target for strong coupling under these circumstances is then $g \gg \kappa$. Assuming that the emitter is positioned at \mathbf{r}_M , with its dipole moment aligned with the field, g takes its maximum value of g_0 (see Eq. 3.6). It is therefore desirable to maximise the ratio g_0/κ to achieve the strong coupling regime. By combining Eq. 3.7 with the relation $2\kappa = \omega/Q$, this ratio can be expressed in terms of the properties of the cavity and emitter:

$$\frac{g_0}{\kappa} = \frac{2g_0Q}{\omega} = \eta \left(\frac{\mu_{eg}^2}{\pi\epsilon_0\hbar c} \right)^{1/2}, \quad (3.15)$$

$$\eta = \frac{Q}{n} \left(\frac{\lambda_0}{V_0} \right)^{1/2}, \quad (3.16)$$

where η has been defined as a figure of merit for the cavity parameters. Note that we have assumed a dielectric medium, with $\mu_r = 1$ and $\epsilon = \epsilon_0\epsilon_r = \epsilon_0n^2$. The ratio g_0/κ has a $Q/\sqrt{V_0}$ dependence, which is an important figure of merit for the strong coupling regime [19, 159]. We also see that $g_0/\kappa \propto \eta\mu_{eg}$, where η encapsulates the parameters determined by the cavity design and μ_{eg} is an

inherent property of the emitter. Therefore, from the perspective of cavity design, η should be maximised in order to increase the likelihood of achieving strong coupling.

It is also possible to derive the theoretical minimum cavity parameters required to reach the strong coupling regime. For $\kappa \gg \gamma$ and assuming ideal cavity-emitter alignment ($g = g_0$), the onset of strong coupling occurs for $g_0 \gtrsim \kappa/2$, as the square root in Eq. 3.14 is positive. Using Eq. 3.15, we find that the minimum η required for strong coupling is given by

$$\eta \gtrsim \left(\frac{\pi \epsilon_0 \hbar c}{4 \mu_{\text{eg}}^2} \right)^{1/2}. \quad (3.17)$$

Similarly, the minimum Q factor of the cavity mode, Q_{SC} , required for the onset of strong coupling is obtained from $g_0 \approx \kappa/2$ using the relation $2\kappa = \omega/Q$. This yields

$$Q_{\text{SC}} \approx \frac{\omega}{4g_0}. \quad (3.18)$$

The quantities Q_{SC} and η are useful figures of merit for the design of cavities capable of reaching the strong coupling regime. They are further considered in section 3.6 for the case of PhC cavity design, including application to the SU-8 strip cavity that is the focus of this work.

3.3.2 The weak coupling regime

For the case $g < |\kappa - \gamma|/2$, the square root in Eq. 3.14 is negative and there is no energy splitting between the dressed eigenstates. The strong coupling regime is lost and the system approaches what is referred to as the weak coupling regime, in which the losses dominate over the coupling strength. We consider a system in the weak coupling regime with $\kappa \gg g \gg \gamma$ and $\delta = 0$, for which it can be shown that the imaginary parts of ω_{\pm} (Eq. 3.13) are given by

$$\text{Im}(\omega_{\pm}) = \frac{\kappa}{2} \mp \sqrt{\frac{\kappa^2}{4} - g^2} = \frac{\kappa}{2} \left(1 \mp \sqrt{1 - \frac{4g^2}{\kappa^2}} \right) \approx \frac{\kappa}{2} \left[1 \mp \left(1 - \frac{2g^2}{\kappa^2} \right) \right], \quad (3.19)$$

which yields values of g^2/κ and κ . As a result, in the weak coupling regime, no splitting is observed but the decay rate is modified: the two eigenstates have energy decay rates 2κ and $2g^2/\kappa$, which are exhibited by the cavity mode and emitter, respectively. The spontaneous emission rate of the emitter weakly coupled to the cavity is therefore altered, which is referred to as the Purcell effect. For the purposes of SPSs, the QD is usually coupled to the cavity mode in order to enhance the

rate of spontaneous emission relative to emitting into the bulk material. The ratio between the two spontaneous emission rates is referred to as the Purcell factor, defined as $F_P = W_{\text{cav}}/W_{\text{bulk}}$, where W_{cav} and W_{bulk} are the spontaneous emission rates in the cavity and in bulk material of refractive index n , respectively. The emission rate in the bulk material is given by $W_{\text{bulk}} = nW_{\text{FS}}$, where

$$W_{\text{FS}} = \frac{\mu_{\text{eg}}^2 \nu^3}{3\pi\epsilon_0 \hbar c^3} \quad (3.20)$$

is the spontaneous emission rate in free space. The Purcell factor for an emitter in a cavity is therefore given by

$$F_P = \frac{W_{\text{cav}}}{W_{\text{bulk}}} = \frac{2g^2}{nW_{\text{FS}}\kappa}. \quad (3.21)$$

The maximum value of F_P is achieved when the coupling strength $g = |g(\mathbf{r}_E)|$ takes its maximum value, g_0 . In this scenario, the Purcell factor is given by

$$F_P = \frac{3}{4\pi^2} \frac{Q}{V_0} \left(\frac{\lambda_0}{n} \right)^3. \quad (3.22)$$

This expression can alternatively be derived by considering the modification to the optical density of states experienced by the emitter due to the cavity mode, such as in Ch. 10 of Ref. [105]. Clearly, in order to achieve a high F_P , we wish to couple a QD to a cavity mode with a high Q/V_0 ratio, which is an important figure of merit for cavity design. Typically, optical microcavities such as micropillar and photonic crystal cavities support modes with a Q factor of at least several 10^3 and a mode volume of order $(\lambda_0/n)^3$, making them a popular choice to enhance the emission rate from QDs.

3.4 Literature review

SPSs which rely on a single In(Ga)As QD typically depend on coupling the emission from the QD to the cavity mode of an optical microcavity, due to the benefits discussed in section 3.3. Here, we present an overview of the research conducted in the field of QD-cavity coupling using In(Ga)As QDs and its application to produce efficient SPSs. More extensive reviews of the field can be found in Refs. [14, 102, 144]. The literature review concludes with an examination of

existing deterministic cavity-QD coupling techniques, which are compared to the SU-8 cavity writing technique proposed in this work.

Early work on QD-cavity coupling demonstrated the Purcell enhancement of emission from many QDs weakly coupled to the same cavity mode, via radiative lifetime measurements of high density QD samples [136]. Progress in growth techniques now allows reliable fabrication of low density QD samples [29], which are suitable for coupling a single QD to a cavity mode to achieve a Purcell-enhanced SPS. The first example of triggered single photon emission from a QD was by Michler *et al.* [15], by optically pumping a QD weakly coupled to a whispering gallery mode of a microdisk cavity [Fig. 3.6(a)]. As is now standard procedure for demonstrating a SPS, an HBT experiment (see section 3.1) was performed to confirm antibunching of the emitted photons [Fig. 3.6(b)].

Following the seminal work by Michler *et al.* [15], many In(Ga)As QD-based SPSs have been reported. A popular choice is to embed the QD in a micropillar cavity, like the one shown in Fig. 3.6(c) (from Ref. [159]). Micropillar cavities are formed by placing distributed Bragg reflector mirrors on either side of the QD layer and etching the structure to form a cylindrical pillar. Cavity modes supported by micropillar cavities have highly directive emission, allowing for high photon extraction efficiencies via collection with a microscope objective. Mode volumes are small, typically of order a few $(\lambda_0/n)^3$ and Q factors usually range from 10^3 up to several 10^4 , although Q factors as high as a few 10^5 have been reported from some designs [160, 161]. The high Q/V_0 ratio of micropillar cavities is favourable for Purcell enhancement of a single QD in the weakly coupled regime [162], which has been used to achieve enhanced, optically-pumped SPSs [155, 163, 164, 165]. SPSs can also be achieved using electrical injection by incorporating the QDs in a p-i-n diode and applying a train of voltage pulses via contacts. This was first shown by Yuan *et al.* [166] for a QD isolated using a μm -sized aperture. The design has since been improved upon by incorporating the QD in a planar microcavity structure to significantly enhance the SPS efficiency [167].

PhC cavities offer smaller mode volumes than micropillar cavities, with V_0 usually of order $(\lambda_0/n)^3$. Q factors range from $\sim 10^3$ to several 10^4 for In(Ga)As/GaAs QD samples, and can reach as high as 10^7 for PhCs in Si wafers, which are less fabrication-limited [91]. In addition to their high Q/V_0 ratio, PhC cavities can be integrated into on-chip optical circuits, offering the potential for integrated SPSs by outcoupling the photons into PhC waveguides [157]. Alternatively, PhC cavities can be designed for efficient free space emission [65]. Early examples of on-demand SPSs based on a QD weakly coupled to a PhC cavity tend to use the H1 cavity design [23, 168, 169],

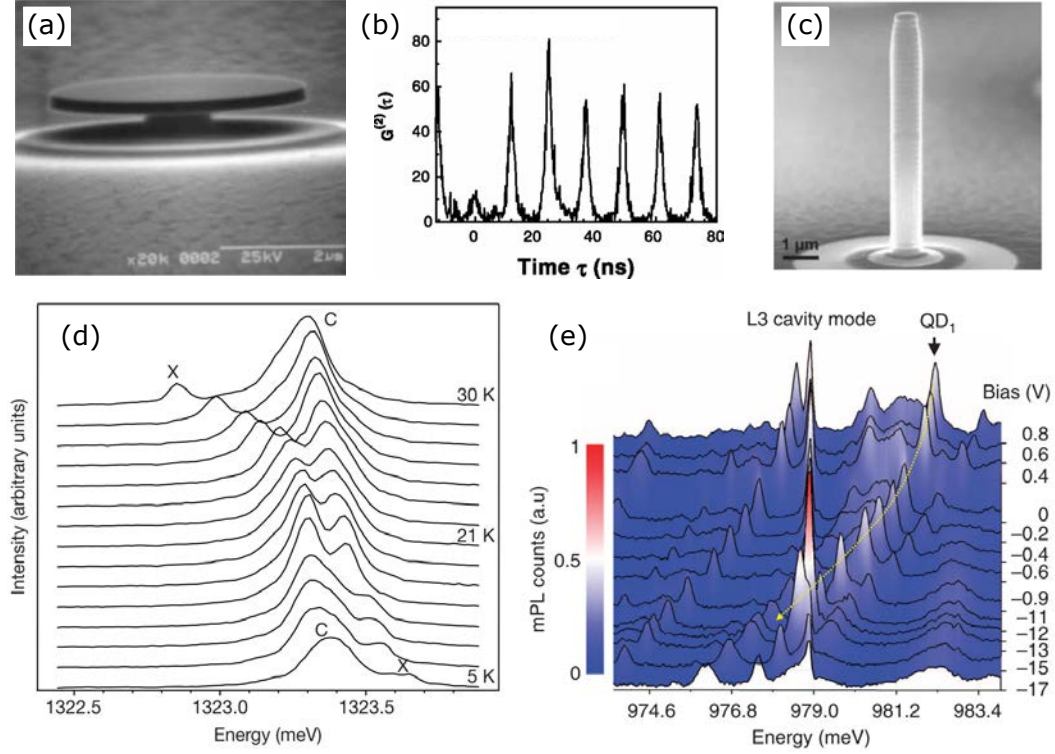


Figure 3.6: Examples of work from the literature. (a) SEM image of a microdisk cavity and (b) measured unnormalised $g^{(2)}(\tau)$ function from a QD coupled to the cavity mode, from Ref. [15]. (c) SEM image of a micropillar cavity and (d) anticrossing of an exciton line (X) and the cavity mode (C) in the strong coupling regime, from Ref. [159]. The anticrossing is performed using temperature tuning. (e) Tuning of a QD into resonance with an L3 PhC cavity mode (in the weak coupling regime) by application of an electric field, from Ref. [71].

in which one hole is removed from the PhC. More recent examples generally employ higher Q/V_0 designs such as the L3 [32] and mode gap [33] cavities, which were covered in Ch. 2.

The strong coupling regime, $g \gg (\gamma, \kappa)$, has also been demonstrated between single QDs and microcavity modes in micropillar, PhC and other cavity types. This is more technically challenging to achieve due to the requirement of a high $Q/\sqrt{V_0}$ ratio of the cavity mode and generally more stringent alignment requirements between the QD position and cavity mode, in order to maximise $g(\mathbf{r}_E)$ (see Eq. 3.6 in section 3.3). This is especially the case for PhC cavities, due to the non-trivial field profile distribution of the mode, which has local nodes and antinodes spaced by $\sim a$, the PhC lattice constant (see Fig. 3.7(b), for example). Strongly coupled InAs QD-cavity systems were first reported for a QD coupled to a micropillar cavity [159] and a QD coupled to an L3 PhC cavity [19] by temperature tuning the QD into resonance with the cavity mode - a method which is now commonly used in strong coupling demonstrations. The signature of the strong coupling regime is an anti-crossing between the cavity mode and exciton line as they cross, due to the energy splitting of the dressed states in a strongly coupled system (see section 3.3). An example of this is shown

in Fig. 3.6(d), from Ref. [159]. Similar characteristic anticrossing has been observed from single QDs strongly coupled to other microcavity designs [72, 81, 86, 170, 171].

Single photon emission has been demonstrated from QD-cavity systems in the strong coupling regime [20, 25, 172], which, similar to the weak coupling regime, greatly enhances the efficiency of the SPS. However, a unique benefit of the strong coupling regime is that single photons can be generated by the photon blockade effect [173] when the system is pumped resonantly to one of the first dressed states. Due to the anharmonic nature of the dressed state ladder, the probability of absorbing a second photon is suppressed and antibunching is observed from the system. SPSs operating via the photon blockade have been demonstrated in both atom-cavity [174] and QD-cavity [67] strongly coupled systems.

As discussed in section 3.1, a SPS preferably has a high brightness and high single photon indistinguishability, both of which are improved by coupling the emission of a QD into a cavity mode. Further optimisation of QD-based SPSs to obtain a higher B_{lens} and photon indistinguishability is an area of active research. A B_{lens} as high as $\sim 80\%$ has been demonstrated from a QD deterministically coupled to an optimal micropillar cavity design [16]; a high B_{lens} in excess of 40% has been reported from free-space emission of a QD coupled to an L3 PhC cavity [17]. Indistinguishable single photon emission from In(Ga)As QDs was first demonstrated via the HOM two-photon interference measurement from a QD coupled to a micropillar cavity [123]. It has since been demonstrated from QDs coupled to other planar [175] and micropillar cavity devices [176, 177], in addition to QD-PhC coupled cavity systems [169]. Indistinguishable photons have even been demonstrated from two remote InGaAs QD SPSs [178]. While QD-based SPSs can be pumped above band gap, resonant excitation is preferable to achieve high single photon indistinguishability, because it reduces the temporal uncertainty in the radiative decay which is otherwise present from the carrier dynamics [175]. Other dephasing effects are also reduced by the increased spontaneous emission rate from coupling the QD to a cavity mode [158]. Using resonant pumping, very high indistinguishabilities have been successfully achieved from In(Ga)As QD-based SPSs, with photon wavepacket overlaps greater than 95% reported [175, 177].

For quantum communication over long distances, SPSs at the telecommunications wavelengths of $1.3\mu\text{m}$ or $1.55\mu\text{m}$ are preferable, both of which have been demonstrated from self-assembled QD-based SPSs. As discussed in section 3.2, conventionally grown InAs QDs typically emit in the 900-1000 nm, but through specialised growth methods, InGaAs QDs can emit at $1.3\mu\text{m}$. Single

photon emission in the telecommunications O-band (1260-1360 nm) has been demonstrated from single InGaAs/GaAs QDs (with a strain-reducing InGaAs capping layer) embedded in micropillar cavities [138, 179] and planar microcavities [137], including an electrically-driven SPS [180]. Kim *et al.* [140] have demonstrated a bright ($B_{\text{lens}} \sim 36\%$) SPS which emits at $1.3\,\mu\text{m}$ from an InAs/InP QD coupled to an L3 PhC cavity mode. InAs/InP self-assembled QDs have also been used to create longer wavelength SPSs emitting at $1.55\,\mu\text{m}$ [134], which have been used to demonstrate quantum key distribution [13]. Biruwosuto *et al.* [181] have reported a $1.55\,\mu\text{m}$ SPS from a QD coupled to the mode of a WMLD PhC cavity [34], which operates on a similar mode-gap confinement principle to the cavities studied in this work.

3.4.1 Deterministic quantum dot-cavity coupling techniques

To date, many examples of efficient SPSs based on single self-assembled In(Ga)As QDs coupled to microcavities have been demonstrated, with a high brightness and single photon indistinguishability shown to be possible. Going forward, a challenge to be addressed is the ability to reliably produce such devices on a larger scale, for real-world applications. This is made difficult by the requirement for precise spectral and spatial overlap between the QD and cavity mode to create a coupled system.

The yield of successfully coupled self-assembled QD-microcavity devices is limited by the random nature of the self-assembled SK growth process. The QDs are randomly positioned and generally covered with a capping layer, so are difficult to locate. Furthermore, the size and composition variation between the QDs results in different emission wavelengths between QDs, with a typical inhomogeneous broadening of $\sim 30\,\text{nm}$ across the ensemble. These factors make achieving the precise spectral and spatial overlap between the QD and cavity mode a significant challenge, since the QD properties cannot be predetermined. Conventional techniques aim to achieve coupling by a brute force method, in which large arrays of cavities are fabricated on a low density QD sample [19, 86, 159]. Often hundreds of cavities are measured until a suitable device is found, for which a QD is close to the cavity resonance and is positioned at or sufficiently near the E field maximum of the mode. This method of finding coupling by chance to fabricate SPSs is typically reported to have a yield of less than 1% [14]. While this is sufficient for demonstrating single examples of SPSs, a more deterministic method of achieving coupling with a higher yield is sought after to fabricate cavity-coupled QD SPSs on a larger scale.

A variety of methods exist which address the requirement of spectral overlap between the QD and cavity mode, most of which allow the QD to be tuned into resonance with a spectrally proximate cavity mode. The simplest method of tuning the QD emission wavelength is by controlling the temperature, since an increase in temperature causes the emission to redshift. This allows an exciton line to typically be redshifted by up to ~ 1 nm from 4 K to ~ 30 -40 K (see section 3.8.4). As the temperature is increased higher than this, the line is significantly broadened and increasingly less bright. Within the temperature range, the cavity mode shift is usually much smaller, as the refractive index of the material has a different temperature dependency. Therefore, temperature tuning can be used to tune a QD into resonance with a cavity mode [19, 67, 86, 159, 171], but only over a small ~ 1 nm range. An example of temperature tuning can be found in Fig. 3.6(d), in which it is used to demonstrate anticrossing in a strongly coupled system [159].

The QD emission wavelength can be tuned over a larger wavelength range by applying electric fields [71, 147, 182, 183], although these methods require that the cavity-QD system is integrated into specialised structures, typically with the QDs embedded in a p-i-n diode with applied electrical contacts. An example showing a single QD tuned into resonance with an L3 PhC cavity mode using an applied electric field [71] is shown in Fig. 3.6(e). QDs have also been tuned into resonance with a cavity mode by sophisticated optical techniques, in which an auxiliary cavity evanescently coupled to the first cavity is used to apply a Stark shift to the QD [72, 184]. In another method, tuning of the QD emission wavelength has been demonstrated by applying strain to the QDs [185, 186]. Alternative methods allow tuning of the wavelength of the PhC cavity mode rather than the QD emission; these include deposition of nitrogen on the PhC to redshift the mode [171, 187] and application of a photochromic film on top of the PhC cavity [188].

Achieving deterministic spatial overlap between a QD and cavity mode requires precisely controlled placement of the cavity and/or the QD. Control of the QD position can be achieved by using site-controlled growth, in which nano-scale depressions etched into the surface of the sample act as nucleation sites for QDs [189]. Subsequent epitaxial growth results in QDs at these well-defined locations, around which microcavity structures can be fabricated. The location of a site-controlled QD embedded in a microcavity structure has been controlled to a precision of ~ 50 nm in a PhC cavity and ~ 200 nm in a micropillar cavity [190]. A Purcell-enhanced SPS has been achieved using this deterministic fabrication method [191], demonstrating the successes of the technique. However, a significant disadvantage of site-controlled QDs is that their optical quality is worse than SK self-assembled QDs due to their proximity to processed surfaces. This results in reduced

quantum efficiencies and stronger dephasing effects, which negatively impact SPS brightness and indistinguishability. For this reason, most deterministic SPS techniques focus on SK self-assembled QDs and aim to position the cavity mode over a randomly located QD.

A wide range of creative techniques have been developed to position a cavity around a QD, usually to an accuracy of order a few 10s of nm for a PhC cavity. A. Imamoglu's group pioneered a technique to deterministically fabricate a PhC so that an embedded single QD is located at the electric field maximum of the cavity mode, to an accuracy of ~ 30 nm. The technique was first demonstrated [23] with a sample containing a very low density of QD stacks (much less than $1/\mu\text{m}^2$), which could be detected via SEM images of the surface (note that this is not usually the case for more conventional capped single layer samples). The position of the QD stacks were mapped relative to metallic markers on the sample surface, which were used as reference markers to pattern PhC cavities around each QD. The weak coupling regime was verified. The technique was developed further to achieve the strong coupling regime from an L3 cavity coupled to a single QD, located via AFM measurements [20]. Figs. 3.7(a) and 3.7(b) show key elements of the technique from Ref. [20]: Fig. 3.7(a) shows an AFM image of the L3 cavity, which has a small mound detectable at the QD location. Fig. 3.7(b) shows the $|\mathbf{E}|^2$ profile of the cavity mode and the location of the QD. Evidently, accurate positioning of the QD relative to the field profile is crucial to achieve a high $g(\mathbf{r}_E)$ with a PhC cavity, as the central antinode (where the field maximum is located) is $\lesssim a/2$ across. Using a similar technique [25], the strong coupling regime has also been reached via deterministic coupling of an L3 cavity to a QD located via μPL mapping measurements. QD registration for the purpose of deterministic coupling has also been demonstrated using *in situ* cryogenic laser photolithography with SU-8 photoresist [192], where the QD position is recorded by exposing markers in the SU-8 and transferring the pattern to create metallic registration marks.

A deterministic fabrication technique for creating coupled QD-micropillar cavity devices, which has seen significant success, was introduced by P. Senellart's group [24]. The technique relies on *in situ* cryogenic laser photolithography, as follows. A sample containing low density QDs between DBR mirrors is spin-coated with photoresist and a 750 nm excitation laser (which does not expose the photoresist) is used to locate a single QD via μPL mapping techniques, as shown in Fig. 3.7(c). The photoresist is exposed using a 532 nm laser at the QD location and through a series of developing and etching processes, a micropillar cavity is created with the single QD embedded. The technique has been applied to reach the strong coupling regime [193], create electrically-tunable SPSs [26] and even a Purcell-enhanced source of entangled photons by coupling the exciton and biexciton

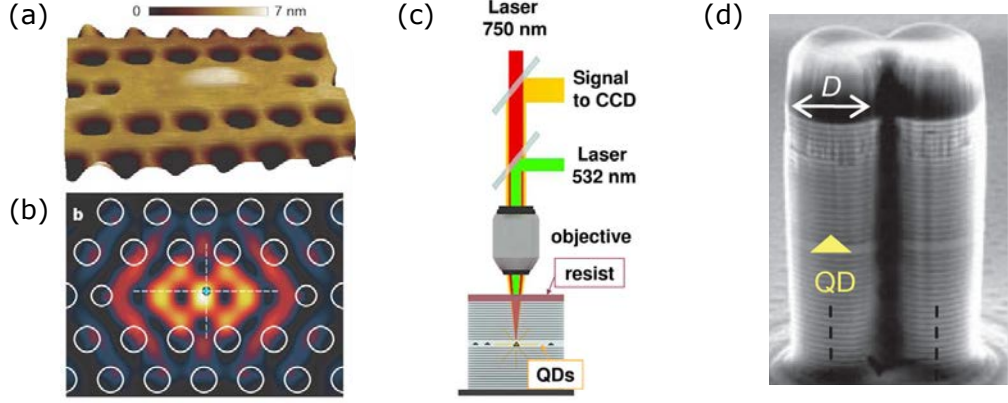


Figure 3.7: Examples of deterministic QD-cavity coupling techniques from the literature. (a) and (b): Deterministic coupling to an L3 PhC cavity from Ref. [20]. (a) shows an AFM image of the device, with $a = 240$ nm, (b) shows the $|E|^2$ field profile and the location of the QD. (c) Schematic of *in situ* cryogenic laser photolithography method for deterministic QD-micropillar coupling, from Ref. [193]. (d) Micropillar photonic molecule fabricated using the technique shown in (c), from Ref. [154]. The pillar diameter, $D \sim 3 \mu\text{m}$.

lines of a QD to two modes of a micropillar photonic molecule [154]. A photonic molecule refers to a system of two optically coupled cavities [38], which is explored in more detail in Ch. 6. The photonic molecule design from Ref. [154], which was deterministically coupled to the two exciton lines using this technique, is shown in Fig. 3.7(d).

The novel SU-8 cavity fabrication technique presented in this thesis is inspired by the deterministic coupling methods that make use of *in situ* cryogenic laser photolithography. The SU-8 cavity writing technique presented in section 3.5 is intended as a means to obtain deterministic coupling between a QD and PhC cavity mode using *in situ* cryogenic μPL techniques. It is unique in that, to the best of our knowledge, it is the only reported PhC cavity generated by photoresist deposited on top of a PhC waveguide to define the cavity mode. While other positionable mode gap cavity designs have been achieved by depositing material on a PhC waveguide [88, 89, 90, 99], altering the refractive index of a section of the waveguide [96, 98], or filling holes of the PhC [95, 97], the SU-8 cavity possesses the novelty that it can be applied to a PhC waveguide with embedded InGaAs QDs to potentially achieve deterministic coupling via *in situ* cryogenic all-optical methods. The full details of the proposed procedure are outlined in section 3.5.

3.5 The SU-8 cavity-writing technique

In this section, an overview of the SU-8 cavity writing technique is provided, including its intended use for deterministic QD-cavity coupling.

3.5.1 SU-8 photoresist

SU-8 is an epoxy-based negative photoresist [35] which is commercially-available and commonly used to make a wide variety of laser-patterned structures [194]. A few notable examples include SU-8 waveguides written on a substrate [195, 196] and laser patterning of 3D PhCs [197]. The photoresist is generally applied to samples via a spin-coating procedure, followed by a soft bake (which removes excess solvent) to obtain a uniform film. The SU-8 can be exposed by UV light, typically in the 350-400 nm range, which initiates cross-linking of the exposed region by a two-step process. Firstly, the exposure generates an acid, which is referred to as a photoacid catalyst. This is because in the second step the acid catalyses cross-linking of the epoxy in the SU-8, which is thermally driven by a post-exposure bake process. After the cross-linked SU-8 is formed, the sample can be developed to remove SU-8 that is not cross-linked, leaving cross-linked SU-8 at the exposed locations.

In this project we use MicroChem’s SU-8 2007 diluted in cyclopentanone solvent to obtain thin (sub-1 μm) SU-8 films. Optimisation work on parameters including the photoresist concentration, spin coating parameters and exposure doses has been performed by L. Nuttall in his thesis [1], which we use as a starting point and build on. Exposures are performed with a 405 nm continuous wave (CW) laser diode and propylene glycol monomethyl ether acetate (PGMEA) is used as a developer. Details of the parameters used for each SU-8 spin-coating, exposure and development process are provided as relevant in each chapter of experimental work.

3.5.2 Proposed technique

The proposed technique for writing an SU-8 mode gap cavity to overlap with a single QD (and potentially couple) is illustrated schematically in Fig. 3.8. A sample is used which contains suspended PhC waveguide membranes with an underlying air gap, which are fabricated using conventional e-beam lithography techniques. Full sample details are provided in section 3.7. The PhCs contain a layer of self-assembled InGaAs QDs at the centre of the membrane. In Fig. 3.8, an ideal scenario is considered in which a single InGaAs QD is located at the centre of the PhC waveguide.

In the first step of the process, a spin coating procedure is applied to achieve a thin SU-8 film on the surface of the sample, as shown in Fig. 3.8(a). Next, cryogenic μPL mapping techniques are used to locate a suitable single QD [Fig. 3.8(b)], with the desired position and emission wavelength to couple to the cavity mode that will be created. Above band-gap excitation is used for the μPL

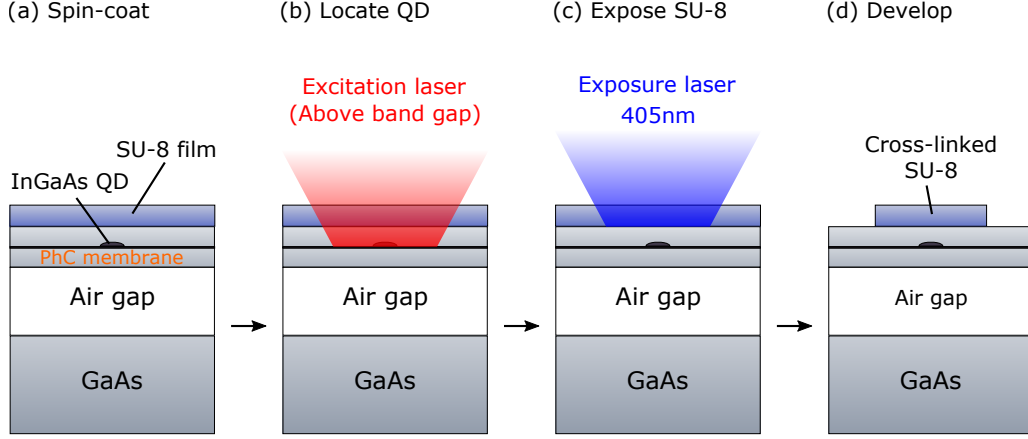


Figure 3.8: Schematic representation of the proposed SU-8 cavity writing technique. Not to scale.

measurements, with a laser wavelength that is too long to expose the SU-8. The μ PL system, which is fully described in section 3.8.2, focuses the excitation laser to a spot size of $\sim 1 \mu\text{m}$ and is capable of determining a QD position to an accuracy of $\sim 50 \text{ nm}$ [192].

Once a suitable target QD (positioned at the centre of the PhC waveguide) has been found, a second laser (wavelength 405 nm) is directed onto the sample, which exposes the SU-8 at the location of the QD [Fig. 3.8(c)]. This step is also performed at cryogenic temperatures: successful exposure of SU-8 under these temperature conditions has been demonstrated previously [192]. The exposure laser is used to write the pattern required to form an SU-8 mode gap cavity in the PhC waveguide, such as the SU-8 strip cavity covered in section 2.6, centred on the QD location. In this project, a single cavity is formed either by writing a disk of SU-8 on the waveguide, as in Ch. 4, or a strip running perpendicular to the waveguide, as in Ch. 5.

After development of the sample, a cross-linked SU-8 structure is left on top of the PhC waveguide [Fig. 3.8(d)], which defines a fundamental cavity mode within the waveguide at the location of the target QD. It is hoped that through this process, successful coupling can be achieved between the target QD and the fundamental mode of the written SU-8 cavity. A height of $\lesssim 100 \text{ nm}$ is targeted for the cross-linked SU-8 for an optimal Q mode (see chapters 4 and 5), which is atypically thin for SU-8 structures. However, a few groups have reported successfully written structures of similar thickness [198, 199], so this target seems achievable.

It should be noted that the proposed technique outlined here corresponds to the ultimate goal of the SU-8 cavity writing technique, which requires samples with a sufficiently low QD density. For the work of this thesis, high density QD samples were used, which provide a bright light source to characterise the cavity modes, but are not suitable for coupling experiments. The work performed

for this project instead mostly concerns the verification of successful SU-8 cavity creation, in addition to characterisation and optimisation of the cavity modes, with the aim to develop the technique to a point at which it is ready for the proposed QD-cavity coupling experiments. The procedure used for writing the SU-8 cavities therefore did not require step (b): instead, the laser spot was aligned with the waveguide. Additionally, exposures were performed at room temperature for convenience, but are also expected to work at cryogenic temperatures, based on previous studies [1, 192].

3.6 Requirements for strong coupling

The typical SU-8 strip cavity design simulated in section 2.6 (with strip height $h_{\text{strip}} = 100$ nm and width $w_{\text{strip}} = 1$ μm) was shown to support a fundamental mode with a high Q_{total}/V_0 ratio. If the SU-8 writing technique detailed in section 3.5 could be used to successfully couple the cavity mode to a QD, the spontaneous emission rate of the QD would be enhanced by a factor up to the theoretical maximum $F_P = 390$ (see Eq. 3.22) in the weak coupling regime. In this section, we address the question of whether the strong coupling regime can theoretically be reached with this cavity design, and the factors influencing this.

We first consider the case in which a QD is located at the E field energy density maximum of the cavity mode and its dipole moment aligned with the field, so that the coupling strength takes its maximum value g_0 (see section 3.3). We assume a transition dipole moment $\mu_{\text{eg}} \approx 9.76 \times 10^{-29}$ C m for the QD [200] and SU-8 strip cavity parameters extracted from FDTD simulations: $n = 3.33$, $\lambda_0 = 1270.8$ nm and $V_0 = 1.36(\lambda_0/n)^3 = 0.0754$ μm^3 . It is also assumed that the exciton linewidth is significantly narrower than the cavity linewidth, $\kappa \gg \gamma$, which is usually the case for self-assembled In(Ga)As QDs embedded in microcavities [20, 67, 201]. In this case, the predicted coupling strength of the system (using Eq. 3.7) is $g_0/2\pi \approx 15.1$ GHz. For this value of g_0 , the minimum Q factor of the cavity mode (Q_{SC}) theoretically required to reach the strong coupling regime can be obtained from Eq. 3.18, which yields $Q_{\text{SC}} \approx 3900$. This estimate of Q_{SC} is well below the theoretical $Q_{\text{total}} = 7000$ of the SU-8 strip cavity mode, which suggests that the SU-8 strip cavity is a suitable cavity design for achieving the strong coupling regime. This calculation has also been performed by Brossard *et al.* [86] to predict $Q_{\text{SC}} \sim 3000$ for a WMLD cavity, with estimated parameters $\lambda_0 = 974.6$ nm, $n = 3.46$, and $V_0 = 1.3(\lambda_0/n)^3$. We verified that we could reproduce this value: using Eq. 3.7 we obtain $g_0/2\pi \approx 26.8$ GHz and an estimate of $Q_{\text{SC}} \approx 2900$ is

given by Eq. 3.18.

In practice, an important factor to consider is the effect of imperfect alignment between the QD and cavity mode, which manifests as a reduction in the coupling strength from its maximum value g_0 , in accordance with Eq. 3.6. Even with the potential for improved QD-cavity mode overlap using the SU-8 strip writing technique, exact alignment of the QD with a local maximum of the cavity field is not expected (the μ PL system does not possess sufficiently high spatial resolution), so we would not expect to achieve the theoretical maximum coupling strength. Here we will consider the effects of spatial misalignment between the QD and cavity mode, which alters the coupling strength by a factor $\Psi(\mathbf{r}_E)$ defined in Eq. 3.8. It will be assumed that the QD dipole is well aligned with the cavity mode so that $\cos(\xi)$ (defined in Eq. 3.9) takes a maximum value of 1 and therefore $g(\mathbf{r}_E) = g_0\Psi(\mathbf{r}_E)$.

The coupling parameter $g(\mathbf{r}_E)$ was calculated as a function of emitter position in the $z = 0$ plane of the PhC, using the $|\mathbf{E}|$ field profile of the SU-8 strip cavity mode to calculate $\Psi(\mathbf{r}_E)$ and the previously obtained value of $g_0/2\pi = 15.1$ GHz. This was then used to find $\Delta\lambda(\mathbf{r}_E)$, the theoretical wavelength splitting between the first dressed states, as a function of the QD position. The value of $\Delta\lambda(\mathbf{r}_E)$ was calculated by first applying Eq. 3.14 to find $\Delta E(\mathbf{r}_E)$ (with $\gamma = 0$) and using the relation $|\Delta\lambda| = (hc/E^2)|\Delta E|$. The result, plotted in Fig. 3.9(a), shows the predicted spatial region in which the QD must be located for the coupling strength to be sufficient to reach the strong coupling regime, with a non-zero splitting between the dressed states. A QD positioned in the unshaded area cannot strongly couple to the cavity mode and areas which coincide with an air hole should be ignored, as the QD cannot be located here. Intuitively, the locations at which the mode splitting is largest correspond to the local antinodes of the $|\mathbf{E}|^2$ field pattern of the mode (see Fig. 2.22). The result indicates the high sensitivity of the coupling strength to the positioning of the QD, which makes reaching the strong coupling regime difficult in practice.

An additional consideration for observing the strong coupling regime is that $\Delta\lambda$ must be large enough for the two dressed state peaks to be resolved by the spectrometer. As detailed in section 3.8.2, the spectrometer used in this work has a maximum resolution of 0.03 nm per pixel width at 1.3 μ m. Therefore, to fully resolve the splitting, we require $\Delta\lambda > 0.09$ nm (3 pixel widths). The areas in which this is the case are encircled by the blue contours in Fig. 3.9(a). Evidently, the area is significantly reduced compared to the $\Delta\lambda > 0$ case, suggesting that even with deterministic positioning of the cavity mode, the strong coupling regime will be experimentally challenging to

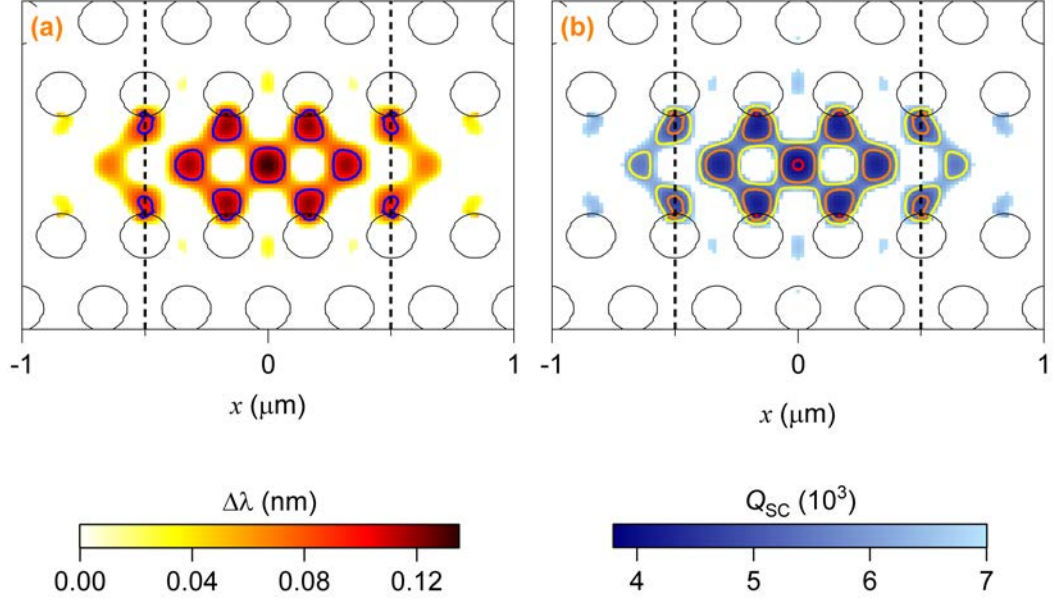


Figure 3.9: Calculated values of (a) $\Delta\lambda$ and (b) Q_{SC} as a function of QD position for the SU-8 strip cavity ($h_{\text{strip}} = 100$ nm and width $w_{\text{strip}} = 1$ μm).

observe. However, even if the splitting cannot be resolved for a QD located within the shaded area ($\Delta\lambda > 0$) but outside the blue contours ($\Delta\lambda < 0.09$ nm), the spontaneous emission rate from the QD should still be greatly enhanced, which is beneficial for the purposes of creating an efficient SPS. Note that the region in which strong coupling can be resolved would be reduced for $\cos(\xi) < 1$, so the effects of misalignment between the transition dipole moment and field make strong coupling even more challenging to achieve.

We also computed the value of $Q_{SC}(\mathbf{r}_E)$, obtained from Eq. 3.18 but with g_0 replaced with $g(\mathbf{r}_E)$ to account for the effects of spatial misalignment. The result is plotted in Fig. 3.9(b). $Q_{SC}(\mathbf{r}_E)$ may be interpreted as the magnitude of Q required for strong coupling to be achieved, depending on the position of the QD. Contours are shown at Q_{SC} values of 4000, 5000 and 6000 by red, orange and yellow lines, respectively. The unshaded area represents $Q_{SC} > 7000$, in which the strong coupling regime is not possible because Q_{SC} exceeds the $Q_{\text{total}} = 7000$ of the cavity mode. Evidently, the previously calculated value of $Q_{SC} \approx 3900$ for $g = g_0$ only applies if the QD is positioned within a very small area of the cavity mode, at the middle of the central antinode. Assuming that $Q = 7000$ can be achieved, the area in which a QD can be positioned in the SU-8 strip cavity is significantly larger than this, coinciding with most of the antinodes of the field pattern. However, the results suggest that if the Q of the cavity mode is lower than this, for example due to fabrication imperfections, then the area in which the QD can achieve the strong

coupling regime is reduced (note that interpreting the results in this way assumes the other cavity mode parameters are unchanged). This highlights why a high Q factor cavity mode is essential to improve the chances of strong coupling.

A more general assessment of a cavity design's suitability for strong coupling is provided by comparing the cavity design figure of merit, η , defined in Eq. 3.16, which depends only on the cavity properties. This quantity is particularly useful to compare cavities with different V_0 , λ_0 and/or n , which would result in a different minimum Q_{SC} . Assuming $\mu_{\text{eg}} \approx 9.6 \times 10^{-29} \text{ C m}$, the strong coupling regime is predicted (using Eq. 3.17) for $\eta \gtrsim 5 \times 10^9 \text{ m}^{-1}$, which provides us with an order of magnitude estimate to surpass in our devices. Of course, this is the minimum possible value, requiring perfect alignment of the QD and cavity that may not be realistically achievable. In practice it is perhaps more useful to evaluate η for PhC devices which have been experimentally verified to achieve the strong coupling regime. We estimated the value of η for 11 reported strongly coupled QD-PhC cavity systems which use self-assembled In(Ga)As/GaAs QDs [19, 20, 66, 69, 70, 72, 81, 86, 171, 184, 201] and found that η is typically in the range $1 \times 10^{10} \text{ m}^{-1}$ to $3 \times 10^{10} \text{ m}^{-1}$, with a mean of $\sim 2 \times 10^{10} \text{ m}^{-1}$. These values were calculated using the experimentally measured Q of the cavity mode and the best estimate available of n and V_0 ; the simulated value of V_0 from the article was used if provided, otherwise it was estimated using known mode volumes for the typical cavity designs (L3, WMLD etc.). Unless provided in the article, $n = 3.4$ was used as an approximation. Clearly, the examples from the literature indicate that if we wish to target a strongly coupled system, we should aim for $\eta \sim 10^{10} \text{ m}^{-1}$, which we will use as a figure of merit when optimising the cavity design in later sections. The simulated SU-8 strip cavity (with $h_{\text{strip}} = 100 \text{ nm}$ and $w_{\text{strip}} = 1 \mu\text{m}$) possesses a theoretical $\eta = 8.6 \times 10^9 \text{ m}^{-1}$, which exceeds the predicted theoretical minimum for strong coupling and approaches the desired order of magnitude, but would ideally be higher to match devices in the literature. As an example, the WMLD cavity presented by Brossard *et al.* [86] (which is strongly coupled to a QD) exhibits $\eta \sim 1.3 \times 10^{10} \text{ m}^{-1}$, so some optimisation of the SU-8 strip cavity design would be recommended for strong coupling applications. Optimisation of the cavity design is explored in Ch. 5.

It should be noted that the value of μ_{eg} is likely to vary depending on growth properties of the QDs and is expected to contribute the largest source of uncertainty to the calculations performed here. The value used was obtained from Ref. [200], which reports an oscillator strength $f = 2m_e\nu\mu_{\text{eg}}^2/e^2\hbar$ (where m_e is the electron rest mass and ν is the angular frequency of the oscillator transition), of 10.7. This value of f is used by Brossard *et al.* [86] in their prediction of Q_{SC} . The

quoted value of f is extracted from measurements of QDs which emit at ~ 1.1 eV (~ 1128 nm) at 4.2 K, from which we estimate $\nu \approx 1.67 \times 10^{15} \text{ rad s}^{-1}$ and therefore $\mu_{\text{eg}} \approx 9.76 \times 10^{-29} \text{ C m}$. The obtained value of μ_{eg} is in good agreement with an estimate of $\mu_{\text{eg}} \approx 9.6 \times 10^{-29} \text{ C m}$ found for QDs emitting at $\sim 1.24 \mu\text{m}$ at room temperature [202]. However, μ_{eg} may differ for InGaAs QDs emitting at $\sim 1.3 \mu\text{m}$ at ~ 4 K, which the devices in this work are intended for coupling to. A benefit of using the parameter η as a figure of merit for strong coupling is that it does not depend directly on μ_{eg} .

3.7 Sample details

The experimental work covered in the following chapters of this thesis was performed on samples containing a high density layer of self-assembled InGaAs QDs embedded in PhC waveguide suspended membrane devices. All samples were derived from the same MBE-grown wafer made by collaborator J. Wu at University College London, the structure of which is illustrated schematically in Fig. 3.10(a). On top of a GaAs substrate, the samples contain a $1 \mu\text{m}$ -thick sacrificial $\text{Al}_{0.7}\text{Ga}_{0.3}\text{As}$ layer, which is required to create suspended PhC membranes. A further 100 nm of GaAs was deposited onto the $\text{Al}_{0.7}\text{Ga}_{0.3}\text{As}$ layer, which makes up half the thickness of the PhC membrane. A layer of self-assembled InGaAs QDs was grown by the SK growth mode (see section 3.2.1) and capped with GaAs, giving a 200 nm -thick GaAs layer with InGaAs QDs (and an InAs WL) embedded at the centre. The processing of this layer allows the formation of PhCs. The expected density of the QDs is $\sim 100 / \mu\text{m}^2$ and the ensemble emission is centred at a wavelength of $\sim 1220 \text{ nm}$ at $\sim 8 \text{ K}$, as shown in Fig. 3.10(b).

PhC devices were fabricated on the samples using conventional e-beam lithography methods by collaborators F. Brossard at Hitachi Cambridge Laboratory and J. Griffiths at the University of Cambridge. A 100 kV VB6 Leica e-beam machine was used to pattern the PhCs into a layer of positive e-beam resist, poly(methyl methacrylate) (PMMA), coating the sample surface. The PhC pattern was transferred to the substrate by reactive ion etching, after which the PMMA was removed. In order to create suspended PhC membranes, treatment with HF or HCl acid was used to remove the sacrificial $\text{Al}_{0.7}\text{Ga}_{0.3}\text{As}$ layer beneath the devices. This is possible because the acid etches the $\text{Al}_{0.7}\text{Ga}_{0.3}\text{As}$ at a much faster rate than the GaAs.

On a given sample, a few hundred PhC devices were typically fabricated. For the purposes of creating and characterising SU-8 cavities, sets of PhC devices like the example shown in Fig. 3.11(a)

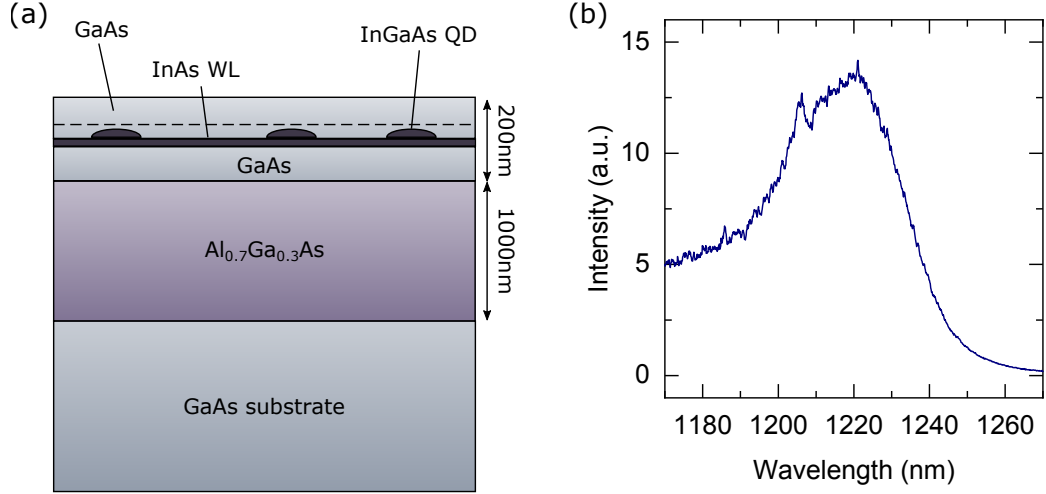


Figure 3.10: (a) Schematic diagram showing the layers of material in the MBE-grown wafer used for the samples. (b) μ PL spectrum of the InGaAs QD ensemble, taken at 8 K using HeNe laser excitation with a power of 9 μ W after the objective.

were used. This consists of a PhC waveguide at the centre, which is used to make the SU-8 defined cavity, with two L3 cavities either side. Higher magnification SEM images of the PhC waveguide and an L3 cavity are shown in Figs. 3.11(b) and 3.11(c). The L3 cavities were included as reference cavities for alignment and calibration purposes. Throughout this work their fundamental cavity modes were used as alignment markers for the μ PL mapping procedures, especially those performed along the PhC waveguide. Additionally, cavity mode parameters such as Q and λ_0 could be compared to the created SU-8 cavities. An optimised L3 cavity design was used, as detailed in section 2.4.1.

3.8 Experimental apparatus

The optical measurements in this project were performed using a μ PL system with high resolution mapping capabilities. The experimental apparatus used is shown schematically in Fig. 3.12, which is described in detail here. A photograph of the apparatus is also shown in Fig. 3.13.

3.8.1 Laser sources

Photoluminescence measurements were performed by illuminating samples with above band-gap (~ 816 nm, or 1.52 eV, for GaAs at 4 K [14]) laser excitation, focused through a microscope objective to a ~ 1 μ m spot size at the sample surface. A choice of three different lasers were used for μ PL measurements, which are shown in the top half of Fig. 3.12. A 632.8 nm CW HeNe gas laser

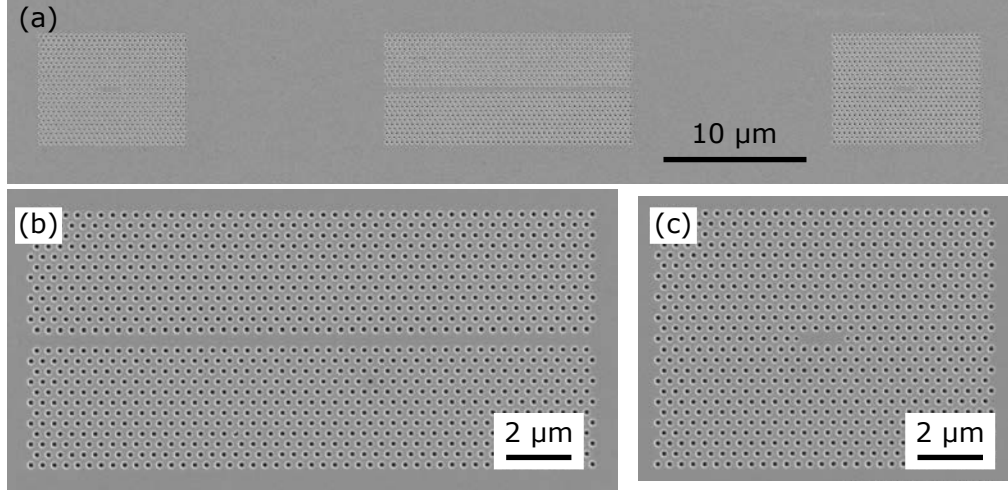


Figure 3.11: SEM images of the PhC devices used in this work. (a) A PhC waveguide with an L3 cavity on either side. (b) A PhC waveguide. (c) An L3 cavity.

was primarily used for PhC mode characterisation, which has a power output of ~ 1.7 mW. For measurements, a power of order a few to a few tens of μ W at the sample surface was typically required.

A second option for CW excitation was a diode-pumped 532 nm frequency-doubled Nd:YAG laser with a power output of ~ 60 mW. The advantage of this laser is that its wavelength is short enough to allow it to be coupled into a single mode combiner fibre with the 405 nm laser used for exposing SU-8, so that the two beams are co-axial. Both the 632.8 nm and 532 nm lasers are sufficiently long wavelength to not expose SU-8 photoresist on the samples.

Pulsed excitation for time-resolved photoluminescence (TRPL) measurements was provided by a Spectra Physics Mai Tai mode-locked Ti:Sapphire (Ti:S) laser, which operates at a wavelength of 800 nm with a power output of ~ 0.75 W, a pulse repetition rate of 80 MHz and a pulse duration of 100 fs. The Ti^{3+} -doped Al_2O_3 crystal is pumped by a (diode-pumped) 532 nm frequency-doubled Nd:YVO₄ laser; mode locking is achieved via the non-linear optical Kerr effect. The Ti:S and HeNe beams were overlapped by directing them through a polarising beam splitter (PBS). Half waveplates were used in each of the two beam paths to rotate the polarisation of the lasers in order to maximise the transmitted or reflected (as appropriate) power. Theoretically, this is when the beams are orthogonally polarised.

Exposure of SU-8 on the samples was performed using a Thorlabs CPS405 405 nm CW laser diode with an output power of ~ 4 mW. This was always coupled into a single mode fibre and out-coupled to free space to improve the beam profile, which was otherwise elliptical. In the ideal

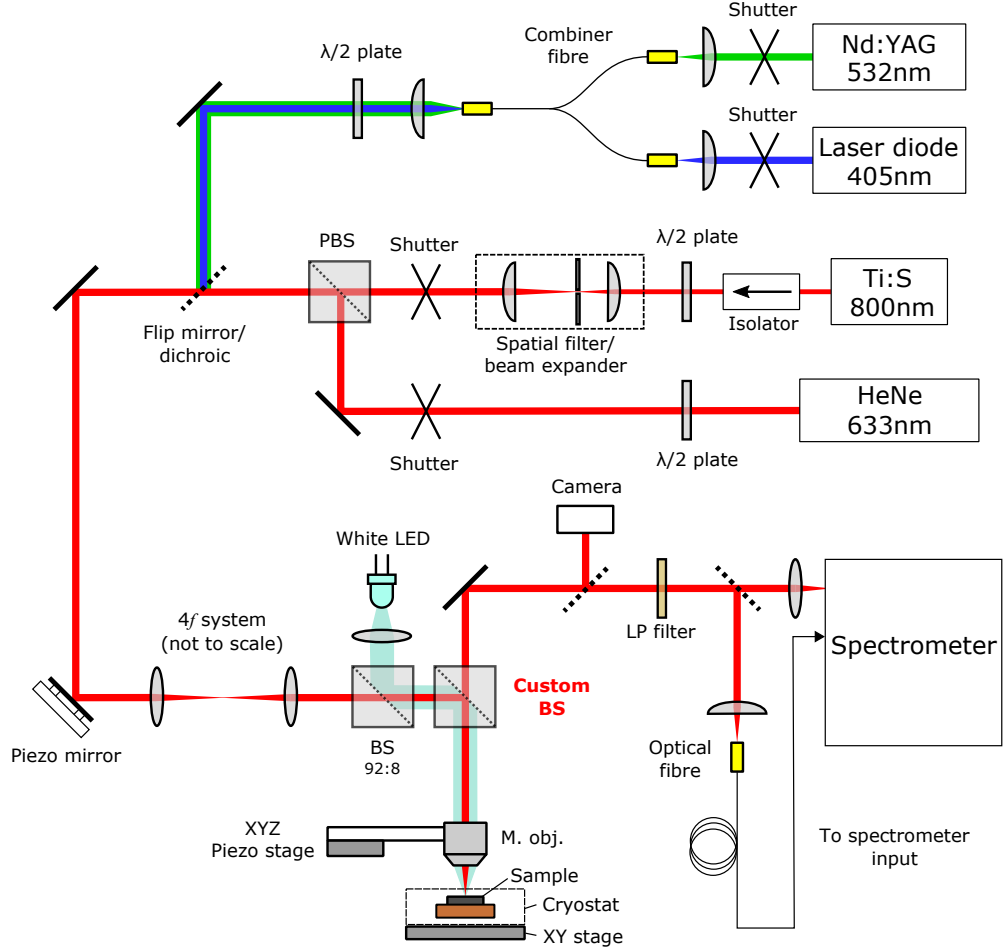


Figure 3.12: Schematic diagram of the μ PL system used for optical measurements in this project. Dashed lines represent removable mirrors or changeable paths.

set-up, the laser was coupled into a single mode combiner fibre with the 532 nm laser as shown in Fig. 3.12, so that the SU-8 exposure laser and μ PL excitation laser were co-axial, which is an advantage for the proposed QD-cavity coupling technique (see section 3.5). However, this system was installed in the latter stages of the project. In prior measurements, the HeNe laser was used for μ PL excitation and was overlapped with the 405 nm beam in free space using a dichroic mirror which transmits the HeNe but reflects the 405 nm laser. The lasers used in each experiment are detailed in the following work chapters.

Illumination of the sample was controlled using two electronically-controlled Uniblitz shutters, which were positioned according to the lasers being used. The shutters were particularly important to control the timing of SU-8 exposures and also useful to block the excitation when taking spectra for background subtraction. All spectra presented in this thesis are background corrected.

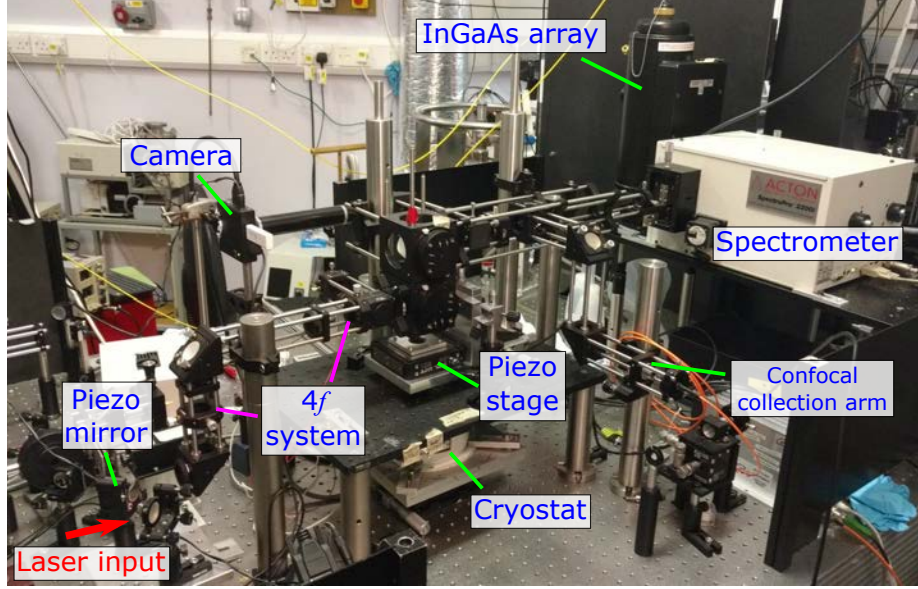


Figure 3.13: Photograph of the experimental apparatus used, with key components labelled.

3.8.2 Micro-photoluminescence apparatus

The excitation and exposure lasers are guided in free space to the μ PL system shown in the bottom half of Fig. 3.12. The chosen laser is focused onto the sample through a $100\times$, 0.5 NA Mitutoyo infrared long working distance microscope objective. Emission from the sample is collected by the same objective and directed into a spectrometer, with an 850 nm long-pass (filter) placed in the optical path to filter out the laser. The surface of the sample can be imaged using illumination from a white LED, which is also directed through the microscope objective using a beam splitter (BS). The reflected light is collected and directed into a camera to form an image.

The BS before the objective, which was custom made by the University of Oxford's Thin Film Facility, was designed to act as an approximately 50:50 BS for wavelengths shorter than $\sim 1\ \mu\text{m}$ and to fully transmit light at longer wavelengths. This is so that the BS reflects a significant proportion of the laser excitation into the objective, but transmits as much of the collected emission (at $\sim 1.3\ \mu\text{m}$) from the sample as possible. The transmission of the custom-made BS, as measured with unpolarised light at a 45° angle of incidence by a PerkinElmer Lambda1050 spectrophotometer, is shown in Fig. 3.14.

During experiments, each sample was mounted on a cold finger inside a Janis ST-500 continuous flow liquid helium cryostat. For cold measurements, with the sample kept under vacuum, the system is capable of reaching temperatures as low as 4.2 K. Higher temperatures are possible by controlling a heating element inside the cryostat. Most measurements were performed at a

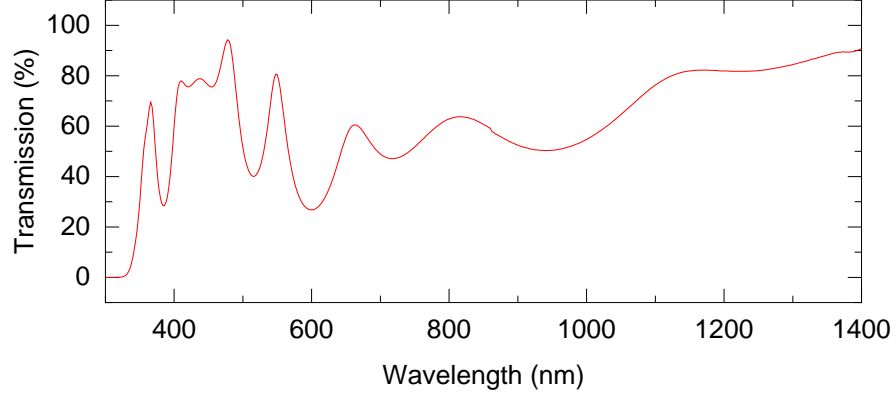


Figure 3.14: Transmission of the custom-made BS as a function of wavelength, for unpolarised light incident at 45° .

temperature of ~ 8 K, which was found to be more stable than 4.2 K. For room temperature experiments, the sample was usually not kept under vacuum. The cryostat was mounted on a micrometer-controlled XY translation stage for coarse positioning. Samples were attached to the cold finger either using Apiezon vacuum grease or Copydex glue (a latex-based rubber cement) as an adhesive.

The spectrometer used was an Acton SpectraPro 2300i 0.3 m triple grating spectrograph with a liquid nitrogen-cooled (-100°C) 1024 pixel InGaAs array. A lower resolution 600 lines/mm grating (blazed at $1\ \mu\text{m}$) was generally used for μPL mapping and characterisation measurements, with a maximum effective resolution of $0.1\ \text{nm}$ at $\sim 1.3\ \mu\text{m}$. A higher resolution 1200 lines/mm grating (blazed at $750\ \text{nm}$) was used for Q factor measurements, which demand a higher resolution to determine the cavity linewidth. The 1200 lines/mm grating has a maximum effective resolution of $0.03\ \text{nm}$ at $\sim 1.3\ \mu\text{m}$, defined from one pixel width. To resolve the FWHM of a peak, it must be 3 pixel widths across, so the narrowest linewidth that can be resolved is $0.09\ \text{nm}$. Therefore, the highest Q factor that can be resolved by the system is approximately 14,000. This resolution can be expected as long as the entrance slit width is less than or equal to $25\ \mu\text{m}$, the pixel width. A slit width of $20\ \mu\text{m}$ was typically used for Q factor measurements.

3.8.3 Mapping capabilities

The μPL system used supports extensive mapping capabilities, all controlled via labVIEW software. The microscope objective was mounted on a Physik Instrumente P-733.3CD piezo-actuated XYZ translation stage, to allow fine positioning of the objective and therefore the position of the laser spot on the surface of the sample. The stage enables a travel range of $100\ \mu\text{m}$ in the X and

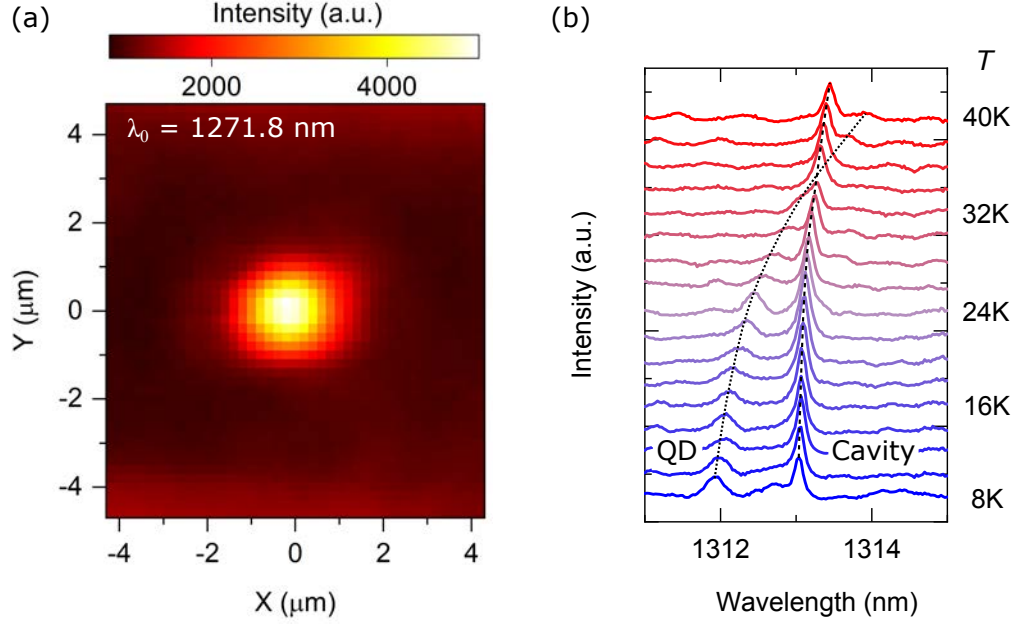


Figure 3.15: (a) 2D μ PL objective map of the fundamental cavity mode of an L3 cavity. (b) μ PL spectra showing temperature tuning of a single QD, in close proximity to a WMLD cavity mode. The temperature, T , is shown to the right, the dashed lines are to guide the eye.

Y directions with 0.3 nm resolution and a travel range of 10 μm in the Z direction with 0.2 nm resolution. Moving the objective in the X - Y plane moves both the laser spot and the light collection area simultaneously across the sample surface. This is particularly useful for characterising the profile of cavity modes, by taking an objective map in which the objective position is scanned in small steps over an area and spectra are acquired at each position. An example demonstrating the capabilities of objective mapping is presented in Fig. 3.15(a), which shows a 2D objective map of a fundamental L3 cavity mode in one of the high density QD samples. The map was performed using a step size of 0.2 μm , with HeNe excitation ($\sim 36 \mu\text{W}$ after the objective) and the sample at 8 K. A clear intensity peak is seen at the cavity mode location. Finer details of the field profile are not observed because the mapping resolution is limited by the $\sim 1 \mu\text{m}$ laser spot size.

The μ PL system also possesses the capability to move the laser spot independently of the light collection area by using a piezo-controlled scanning mirror to change the angle at which the laser enters the objective. To do this, a mirror is mounted in a Newport CONEX-AG-M100D piezo motor driven mirror mount, which is positioned at one end of a telecentric $4f$ lens system, shown in Fig. 3.16. The $4f$ system consists of a pair of lenses with the same focal length f , separated by a distance $2f$. The first lens is a distance f from the piezo-controlled mirror and the microscope objective is placed a distance f from the second lens. Collimated light incident on the first lens at an angle θ is focused to a point in the focal plane, which is collected and re-collimated by the

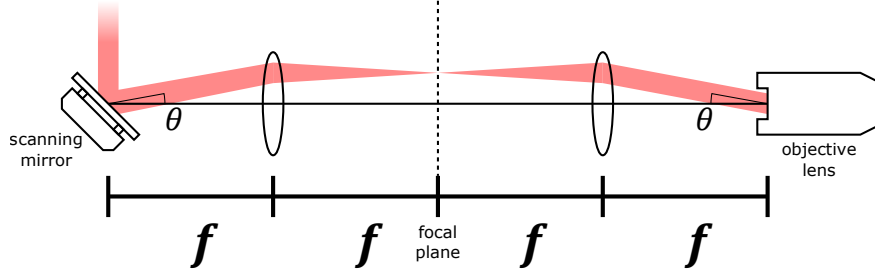


Figure 3.16: Schematic diagram of a $4f$ telecentric lens system, from Ref. [1].

second lens. The collimated light is then incident on the objective at the same angle θ . Therefore, the $4f$ lens system allows the angle of incidence of the laser into the objective to be controlled by the mirror, while always entering the objective at the same position.

Mapping measurements can be performed by moving the laser spot using the scanning mirror and acquiring spectra at each position. In performing these mirror maps, the scanning mirror is moved by less than a degree, so the paraxial approximation is assumed to hold. A linear relation is therefore expected between the change in mirror angle and the change in the laser spot's position on the surface. The system was calibrated for mapping using known dimensions of PhC devices on a sample surface. Further details of scanning mirror techniques can be found in L. Nuttall's thesis, which uses them extensively [1].

Most of the mapping performed in this project was by moving the objective. Maps utilising the scanning mirror are presented in Ch. 6 to investigate photonic molecules. Confocal collection techniques were used for this mirror mapping to reduce the collection area, which was achieved by focusing the collected PL through a multi-mode fibre. The other end of the fibre was then coupled into the spectrometer, as shown in Fig. 3.12.

3.8.4 Temperature tuning

The proposed application of the SU-8 cavity writing technique to QD-cavity coupling depends on the ability to spectrally tune the QD into resonance with the cavity mode. This could potentially be achieved using the current μ PL system via temperature tuning. The temperature tuning capability of the system is demonstrated in Fig. 3.15(b), which shows μ PL spectra obtained at different temperatures from a sample with low density ($20\text{--}30/\mu\text{m}^2$) InGaAs/GaAs QDs embedded in a WMLD PhC cavity [34]. The spectra were acquired using low power HeNe excitation ($\sim 0.5\text{ }\mu\text{W}$ after the objective) with 60 s acquisition times. As the temperature is increased from 8 K in steps of

2 K, the QD emission line redshifts at a faster rate than the WMLD cavity mode, allowing spectral overlap to be achieved. In this instance, however, no evidence of coupling is seen, likely due to insufficient spatial overlap between the QD and cavity mode. Evidently, a tuning range of order ~ 1 nm is possible via increasing the temperature up to ~ 30 K. As the temperature is increased beyond this, the QD emission is significantly broadened and difficult to detect. Precise control of the SU-8 cavity mode wavelength is therefore desirable in order to maximise the probability of achieving spectral overlap.

3.8.5 Time-resolved photoluminescence

TRPL measurements in this project were used to measure the radiative lifetime of cavity modes and QD ensembles. An IDQ id220-FR-SMF infrared single photon counter (SPC) was used, which operates using a cooled InGaAs/InP avalanche photodiode. The highest available detection efficiency of 20% and a 5 μ s detector dead time (to prevent after-pulsing) were used, with the detector in free-running mode. Data were recorded using a Picoquant TimeHarp 260 PICO time correlated single photon counting (TCSPC) card, with a 25 ps bin width. This was synchronised with the Ti:S laser pulses by partially reflecting a weak signal from the laser onto a Becker and Hickl PHD-400-N fast photodiode trigger module, which delivered electrical pulses to the TCSPC card.

The instrument response function (IRF) of the detector is shown in Fig. 3.17, which was measured using heavily attenuated 180 fs laser pulses, with the help of I. Walmsley's group at Oxford. The pulses were generated by a Chameleon compact optical parametric oscillator, which generated 1550 nm pulses at a repetition rate of 80 MHz. This was pumped by a Coherent Chameleon tunable Ti:S with an 80 MHz pulse repetition rate, generating 160 fs pulses at 830 nm. Measurement of the IRF was necessary in order to fit radiative lifetimes to acquired data, by fitting data with the relevant decay curve convolved with the IRF.

To acquire TRPL measurements, the spectrometer was used as a tunable spectral filter. Rather than being directed onto the InGaAs array, the PL was directed through an exit slit in the spectrometer and focused into a 50 μ m core diameter multimode fibre. This was coupled directly into the SPC. Using a second spectrometer (an Andor Shamrock 0.3 m spectrometer with an Andor iDus InGaAs array), the effective spectral filter window of the primary Acton spectrometer was found to have a FWHM of ~ 0.7 nm.

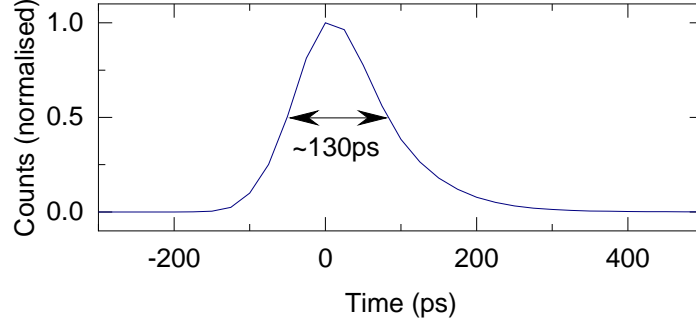


Figure 3.17: Measured IRF of the SPC detector used for TRPL measurements. The IRF has a FWHM of ~ 130 ps.

3.9 Summary

In this chapter, an overview of SPSs and CQED with a focus on self-assembled InGaAs/GaAs QDs coupled to PhC cavities has been given, providing the context for the experimental work in the following chapters. The novel SU-8 cavity writing technique has been introduced, including its proposed end goal of achieving coupling between a cavity and QD. The theoretical feasibility of the design for the strong coupling regime has been demonstrated and the effect of spatial misalignment considered. Through the examination of strongly coupled devices reported in the literature, a figure of merit, $\eta \sim 1 \times 10^{10} \text{ m}^{-1}$, has been deduced as a target parameter to aim for in actual SU-8 cavity devices. Finally, details have been provided of the samples studied and the capabilities of the μ PPL system used have been laid out.

4

SU-8 disk cavities

The initial concept for creating a deterministically-positioned cavity defined by SU-8 photoresist was to expose a single disk of SU-8 on top of a PhC waveguide, as shown by the schematic diagram in Fig. 4.1. For cavity-QD coupling applications, the approach outlined in section 3.5 would be applied, using μ PL mapping techniques to locate a single QD and write a disk of SU-8 over the PhC waveguide at its position. In this chapter, we present results from simulated and experimentally realised SU-8 disk-defined cavities on PhC waveguides, which formed the precursor to the work performed on the SU-8 strip cavity design in the rest of this thesis. Key parts of the presented work on SU-8 disk cavities have been published in Ref. [203]. Additionally, much of the groundwork by collaborator L. Nuttall leading up to and including the successful fabrication of SU-8 disk-defined cavities is detailed in his thesis [1]. This work is extended upon in the latter part of this chapter, in which the prospect of improving the Q/V_0 of the cavity mode by writing larger SU-8 disks is investigated.

4.1 FDTD simulations of SU-8 disk cavities

The SU-8 disk cavity is believed to operate via the same principle of mode gap confinement as the SU-8 strip cavity, which was simulated in section 2.6. For the disk cavity, the mode gap confinement occurs in the region of the waveguide covered by the disk. FDTD simulations were performed using the methods outlined in Ch. 2 for an SU-8 disk with diameter $d_{\text{disk}} = 1 \mu\text{m}$ and height $h_{\text{disk}} = 100 \text{ nm}$ (with refractive index $n_{\text{disk}} = 1.57$) on a PhC waveguide with the same parameters as for the SU-8 strip cavity in section 2.6 ($a = 340 \text{ nm}$, $r/a = 0.27$, $n = 3.33$). The properties of the fundamental cavity mode from the simulation are shown in table 4.1. Convergence

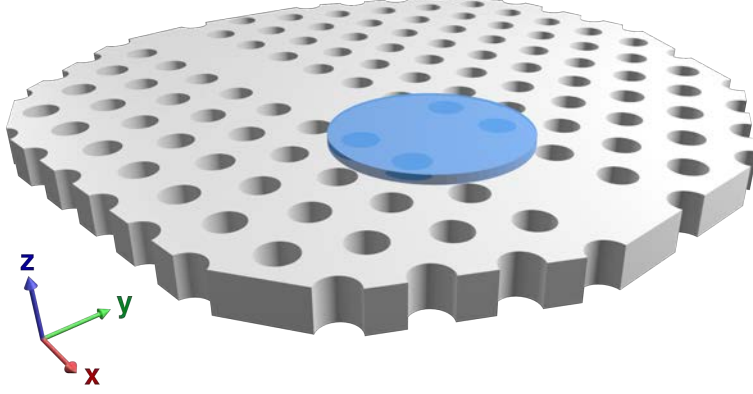


Figure 4.1: Schematic 3D render of an SU-8 disk cavity, formed by depositing a disk of SU-8 photoresist on top of a PhC waveguide. Figure provided by collaborator L. Nuttall [1].

| λ_0 (nm) | Q_{total} | Q_{in} | Q_{out} | $V_0 [(\lambda_0/n)^3]$ |
|------------------|--------------------|-----------------|-------------------|-------------------------|
| 1269.3 | 7100 | 7700 | 9.1×10^4 | 1.44 |

Table 4.1: Parameters of the fundamental cavity mode, extracted from FDTD simulations (using Lumerical FDTD Solutions [49]) of an SU-8 disk-defined cavity with $h_{\text{disk}} = 100$ nm and $d_{\text{disk}} = 1$ μm .

testing suggests that these parameters are accurate to within 5%. Electric field profiles of the mode are also shown in Fig. 4.2. Evidently, the mode generated by the disk has a high Q_{total}/V_0 for coupling applications and is similar in character to the SU-8 strip cavity mode. The order of magnitude difference between the Q_{in} and Q_{out} of the mode suggests that Q_{total} is limited by the in-plane losses, which we attribute to TE-TM coupling due to the broken z -symmetry of the structure. The concept of TE-TM coupling losses, which is also the dominant loss mechanism for the SU-8 strip cavity, is explained in more detail in section 2.6.

The FDTD results presented in Fig. 4.2 and table 4.1, which were obtained using Lumerical FDTD Solutions software [49], complement those performed by collaborator F. Brossard using the freely-available, open-source FDTD software, MEEP [62]. These simulations were run for an SU-8 disk with $d_{\text{disk}} = 1$ μm and variable h_{disk} on a PhC waveguide. The refractive indices of the materials and the PhC lattice parameters were the same as for the simulations performed using Lumerical FDTD solutions; there were minor differences in the size of the PhC and the slab thickness which are not expected to significantly affect the results. For $h_{\text{disk}} = 100$ nm, good consistency was found between the results obtained from MEEP and from Lumerical FDTD solutions: the Q factors agree within $\sim 12\%$ and V_0 is consistent within $\sim 5\%$. The obtained values of the Q components and V_0 from the MEEP simulations are presented in Fig. 4.3 as a function of h_{disk} . The significant increase in Q_{total} as h_{disk} is reduced below 100 nm is attributed to a reduction of the in-plane TE-

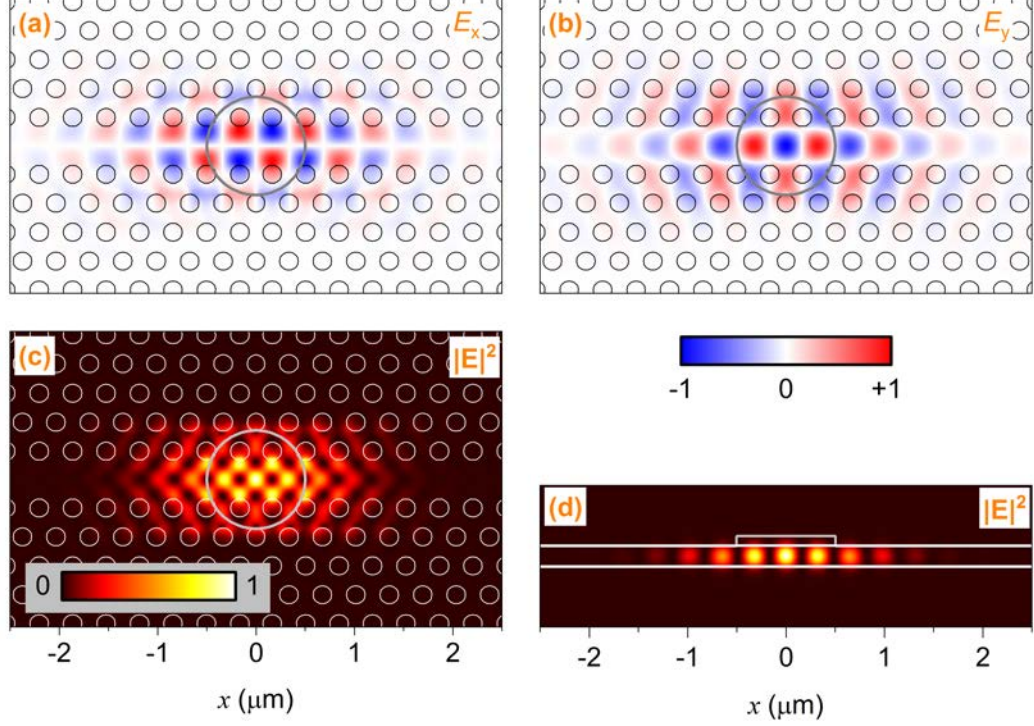


Figure 4.2: Field profiles of the fundamental mode of the simulated SU-8 disk cavity with $h_{\text{disk}} = 100 \text{ nm}$ and $d_{\text{disk}} = 1 \mu\text{m}$. (a) and (b): snapshots of the E_x and E_y field components through $z = 0$. (c) and (d): $|\mathbf{E}|^2$ field envelope of the cavity mode through $z = 0$ and $y = 0$, respectively. All field magnitudes are normalised. The position of the SU-8 disk is marked by a grey circle.

TM coupling losses, which is suggested by the increase of the limiting Q_{in} component. Possible explanations for this are explored in section 5.2 for SU-8 strip cavities, which exhibit similar behaviour. The mode volume also increases as the height of the disk is reduced, but the order of magnitude increase in Q_{total} more than compensates to yield a high Q_{total}/V_0 ratio, so a thin sub-100 nm SU-8 disk cavity is preferable in theory for QD-cavity coupling.

4.2 Fabrication and characterisation of SU-8 disk cavities

Fabrication of a batch of SU-8 disk cavities was attempted in order to test the feasibility of the cavity design and characterise the generated cavity modes. Experiments were performed on a sample with a high density of InGaAs QDs embedded in suspended PhC devices, as described in section 3.7. Over 200 of the PhC devices pictured in Fig. 3.11(a) were patterned onto the surface of a $\sim 5 \times 5 \text{ mm}$ chip. For this sample, HF treatment was used to remove the sacrificial AlGaAs layer in order to create suspended PhC membranes.

A spin-coating process was used to apply a thin film of SU-8 photoresist to the surface of the

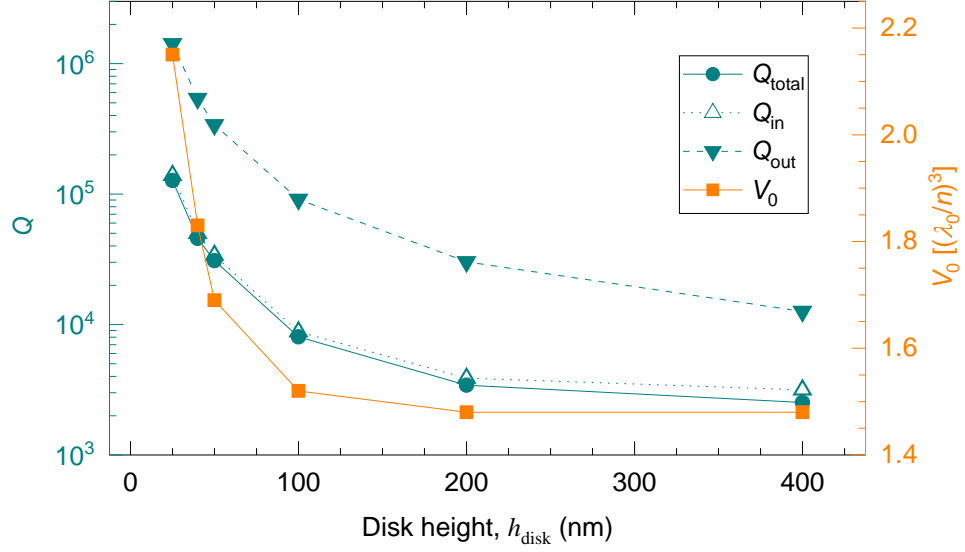


Figure 4.3: Parameters of the fundamental mode of an SU-8 disk cavity with $d_{\text{disk}} = 1 \mu\text{m}$ and variable h_{disk} , extracted from FDTD simulations performed by collaborator F. Brossard using MEEP software.

sample. The recipe used was devised following optimisation work by collaborator L. Nuttall, which is reported in his thesis [1]. The general recipe is as follows. SU-8 2007 is diluted using cyclopentanone as a solvent with an 8:1 ratio of cyclopentanone to SU-8 2007; the dilution is performed using a 20 μL micropipette. A 20 μL drop of the photoresist solution is placed onto the sample surface, which is spun at 2800-3000 rpm for 90 s, with an angular acceleration of 1000 rpm/s. A pre-exposure bake is then performed for 5 minutes at a temperature of 95 $^{\circ}\text{C}$ on a hotplate. Exposures of SU-8 disks on the PhC waveguides are performed using a 405 nm CW laser diode, focused to a $\sim 1 \mu\text{m}$ spot size. These exposures are performed at room temperature, but successful exposure of SU-8 has also been demonstrated at cryogenic temperatures [1, 192, 203]. After performing the exposures, the sample undergoes a post-exposure bake for 5 minutes on a 95 $^{\circ}\text{C}$ hotplate. This causes cross-linking of the polymer strands of the photoresist in the regions which have been exposed, where the cross-linking is catalysed by photo-acid catalyst generated during the exposure. The rest of the non-cross-linked SU-8 is removed by immersing the sample in propylene glycol monomethyl ether acetate (PGMEA) for 5 minutes, followed by a rinse with isopropyl alcohol (IPA).

The results presented in this section are from SU-8 disk cavities which were fabricated from two runs of SU-8 spin-coating, exposure and development on the same sample. A total of 40 blank PhC devices were investigated. The first fabrication run was using a spin speed of 3000 rpm: exposure of SU-8 disks was attempted on 20 of the blank devices, of which only 6 had a successfully written

SU-8 disk after development. These successful disks were exposed using a 5 s exposure time at a power of $\sim 9.4 \mu\text{W}$, measured after the objective. A second SU-8 fabrication run was then attempted on the sample, with a reduced spin speed of 2800 rpm (to provide more reliable SU-8 coverage). Exposures were performed on the 14 devices on which exposures failed in the first run, in addition to 20 other devices. 24 of the devices were exposed using a power of $\sim 9.4 \mu\text{W}$ after the objective; the other 10 were exposed with a power of $\sim 4.7 \mu\text{W}$. The exposure time was 5 s in all cases. 33 of these 34 devices had an SU-8 spot after developing the sample, demonstrating that a high yield of SU-8 disks on PhC waveguides is possible using optimal fabrication parameters. In total, 39 of the 40 devices showed evidence of an SU-8 spot on the waveguide via optical microscope images. An example of a successful SU-8 disk cavity is presented in Fig. 4.4(a): an SEM image which clearly shows a spot of SU-8 located on a PhC waveguide.

The SU-8 disk cavities were characterised by μPL measurements using the experimental apparatus detailed in section 3.8. The sample was cooled in the cryostat and a HeNe laser was used for excitation, with a power of $\sim 10 \mu\text{W}$ (measured after the objective). μPL objective mapping measurements were performed on the sample (see section 3.8.3), which move the excitation spot and collection area simultaneously. An example of such a map is shown in Fig. 4.4(b), which is a 2D map of the SU-8 disk cavity in Fig. 4.4(a). The map was obtained by raster scanning the objective in steps of $0.5 \mu\text{m}$ and acquiring for 0.5 s at each position. The 600 lines/mm spectrometer grating (see section 3.8.2) was used with a slit width of $50 \mu\text{m}$. The intensity collected at the wavelength of the SU-8 disk cavity mode, $\lambda_0 = 1253.7 \text{ nm}$, at each spatial position, is plotted in Fig. 4.4(b), to provide a 2D visualization of the cavity mode. Evidently, a highly localized cavity mode is present at the position of the SU-8 disk.

To verify the creation of SU-8 disk cavity modes, 1D μPL objective mapping measurements were performed along the waveguide of each device. The L3 cavities either side of each PhC waveguide (see section 3.7) were used as alignment markers in order to ensure that the scanning direction was parallel to the waveguide. The objective was scanned in steps of $0.2 \mu\text{m}$ and the same acquisition settings as outlined previously were used. For the rest of the measurements presented in this chapter, the sample was kept at a temperature of $\sim 8 \text{ K}$. For each device, 1D μPL maps were performed along the waveguide both before and after writing the SU-8 disks, in order to test whether new cavity modes were created by the presence of the disk on the waveguide. Examples from three selected devices are presented in Fig. 4.5: maps taken before writing the SU-8 disk [Figs. 4.5(a), 4.5(c) and 4.5(e)] and maps taken after writing the disk [Figs. 4.5(b), 4.5(d) and

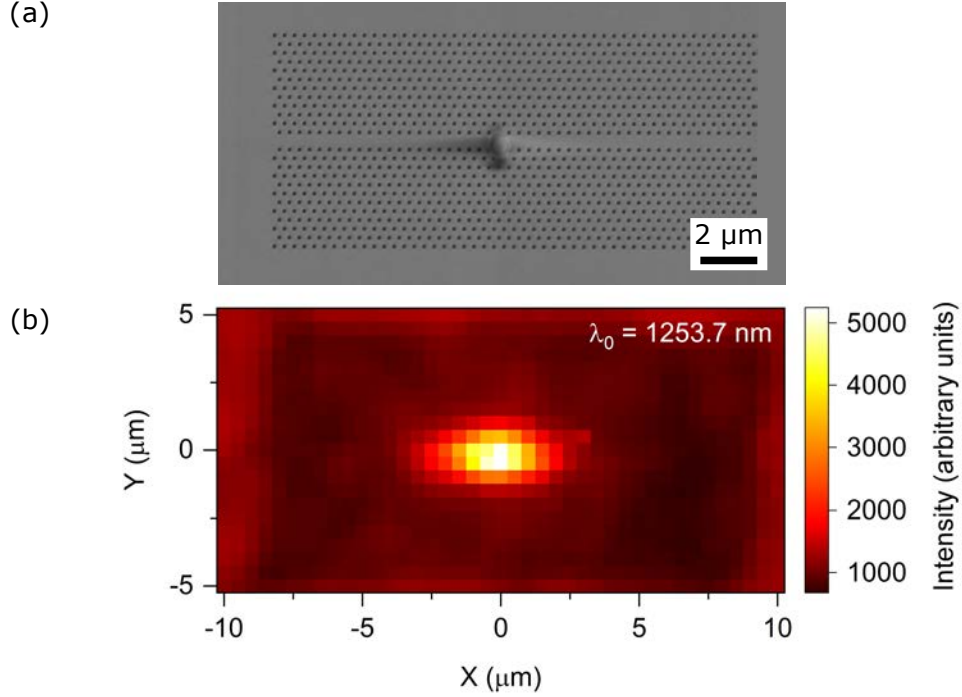


Figure 4.4: A successfully created SU-8 disk cavity. (a) SEM image, clearly showing an SU-8 spot on a PhC waveguide. (b) 2D μ PL map of the cavity mode created by the SU-8 disk, with the sample cooled to 4.2 K. The Q factor of the mode was 5600; the height of the SU-8 disk was (230 ± 30) nm.

4.5(f)] are shown for devices A, B and C. In all cases, clear evidence of new, highly localized cavity modes is found after writing an SU-8 disk on the waveguide. The fundamental mode created, which we label M1, is located at the position of the SU-8 disk. The (generally lower intensity) modes present in the blank PhC waveguides before deposition of SU-8 are thought to be Fabry-Perot-like modes supported by the waveguide [204]. 36 of the devices were confirmed to have cavity modes created by writing the SU-8 disk – a promisingly high yield of 90%.

Measurements of the Q factor of the fundamental (M1) cavity mode were carried out on the successful SU-8 disk cavities. Point spectra were taken using the 1200 lines/mm grating with an acquisition time of 0.5-1 s, after maximising the collected signal from the cavity mode (by moving the objective using the piezo-controlled stage). Examples of spectra taken from devices A, B and C are presented in Fig. 4.6. The Q factor of each mode (shown in the corresponding sub-figure) was estimated by fitting the spectrum with a Lorentzian peak fit plus a straight line (to approximate the ensemble background). The Q factor is then given by $Q = \lambda_0/\Delta\lambda$, where $\Delta\lambda$ is the FWHM of the Lorentzian peak. The variation of the Q factor between the 3 devices is attributed predominantly to differences in the SU-8 disk shape and size. Differences in the geometry of the SU-8 disk are evident from the SEM images of devices A and C presented in Figs. 4.7(a) and 4.7(b); an SEM

and AFM image of device B can be found in Figs. 5.1(a) and 5.1(b).

The geometry of the SU-8 disks was measured using AFM imaging and 3D profile-fitting techniques. Most of the AFM measurements and techniques detailed in this section were performed by collaborator L. Nuttall. 34 of the 36 successful SU-8 disk cavities were characterised via AFM measurements: 2 devices were excluded due to damage to the sample that occurred after the μ PL measurements.

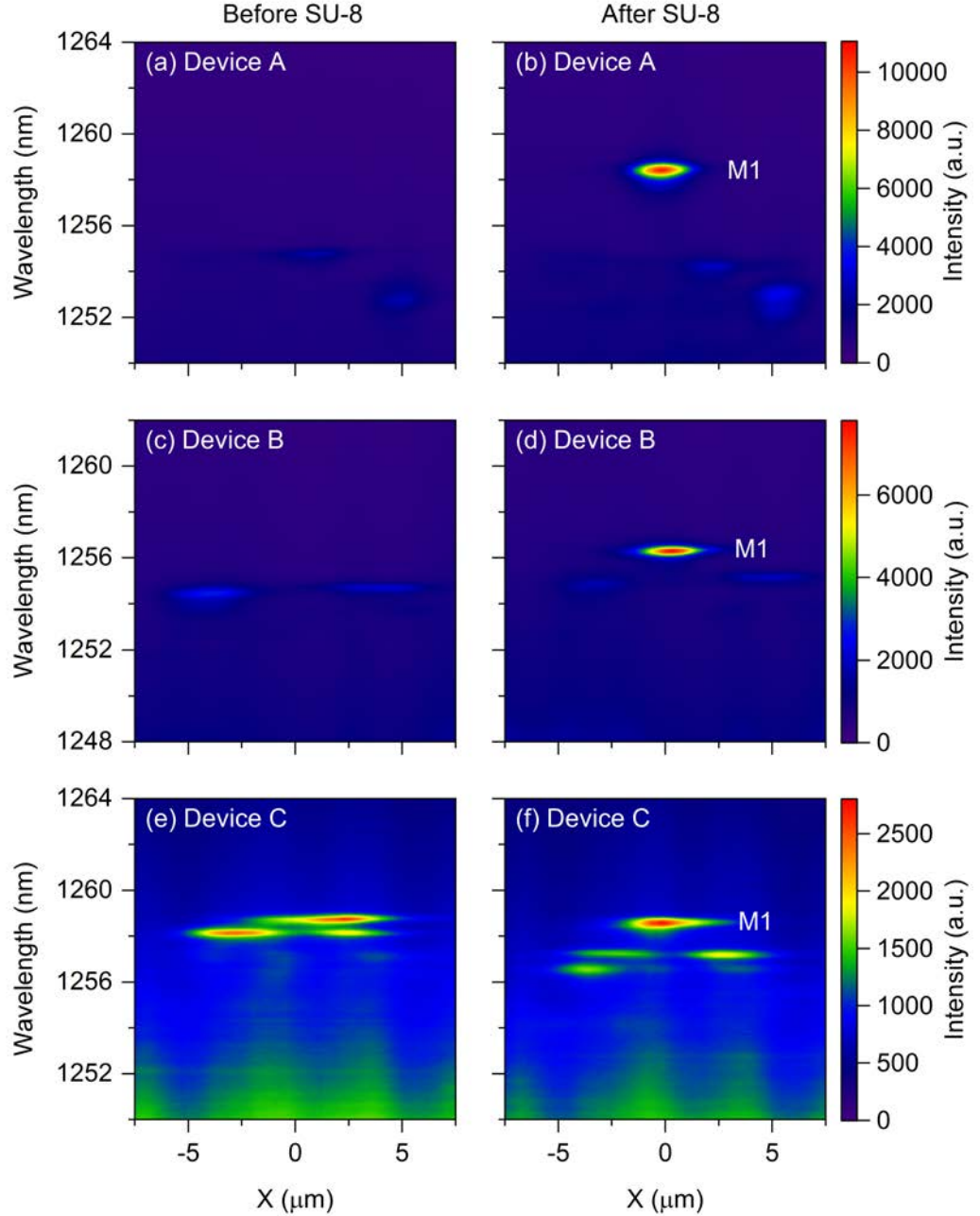


Figure 4.5: 1D μ PL maps (along the waveguide) of three selected devices taken before and after writing an SU-8 disk on the PhC waveguide. (a), (c) and (e): maps of devices A, B, and C before applying SU-8. (b), (d) and (f): maps of devices A, B, and C after writing SU-8 disks. All maps use the same position (X) scale.

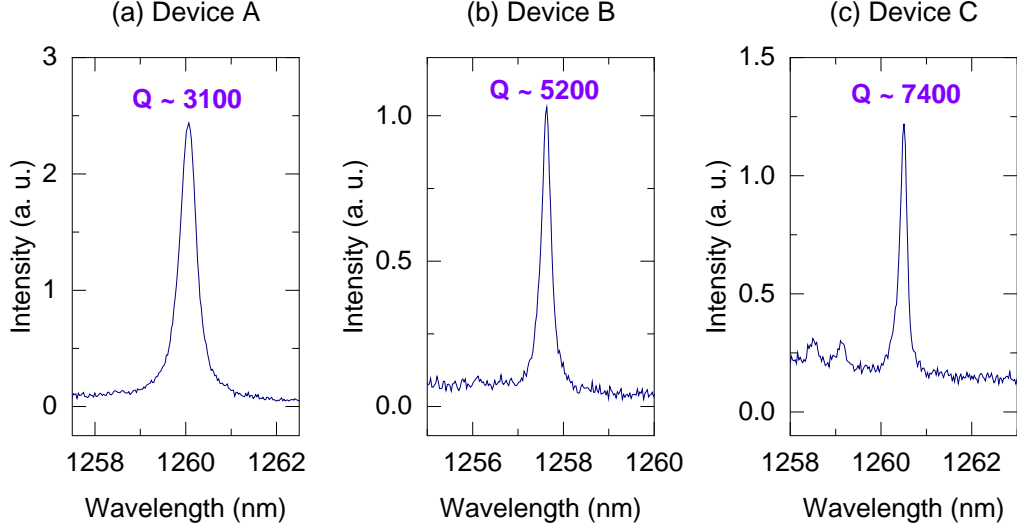


Figure 4.6: High resolution spectra of the fundamental cavity mode, M1, taken from the 3 selected devices A (a), B (b) and C (c). The estimated Q factor of the mode is labelled on each sub-figure.

| Device | H (nm) | R (nm) | Q |
|--------|--------------|---------------|------|
| A | 307 ± 49 | 1.2 ± 0.3 | 3100 |
| B | 147 ± 18 | 0.9 ± 0.2 | 5200 |
| C | 60 ± 6 | 0.5 ± 0.1 | 7400 |

Table 4.2: Parameters of the three selected devices, A, B and C. Estimated values of the disk radius, R and height, H , extracted from AFM measurements are shown.

measurements. An example of an AFM image is presented in Fig. 4.7(c), which shows the SU-8 disk of device C. To approximate the shape, a conical frustum was fitted to each SU-8 disk, from which an average radius, R , and height, H , were extracted. The SU-8 disks were generally found to be slightly elliptical (possibly due to astigmatism of the writing laser spot), so the radius was approximated as that of a circle with the same area as the ellipse. The fitting of the conical frustum was performed using the Levenberg-Marquardt algorithm [205]. The dimensions of the SU-8 disks on the three selected devices are displayed in table 4.2 – clearly device C, which supports the highest Q cavity mode, has the thinnest disk, as we might expect from the simulation results in section 4.1. The converse is true for device A, which has the lowest Q and the thickest disk.

Data from all 34 SU-8 disk cavities characterised via AFM measurements are plotted in Fig. 4.8, which shows the Q factor and disk radius R as a function of the estimated height of the disk, H . Evidently, disks with a wide range of H were fabricated, which we attribute to variation of the SU-8 film thickness between PhC devices, in addition to the variation of the exposure dose.

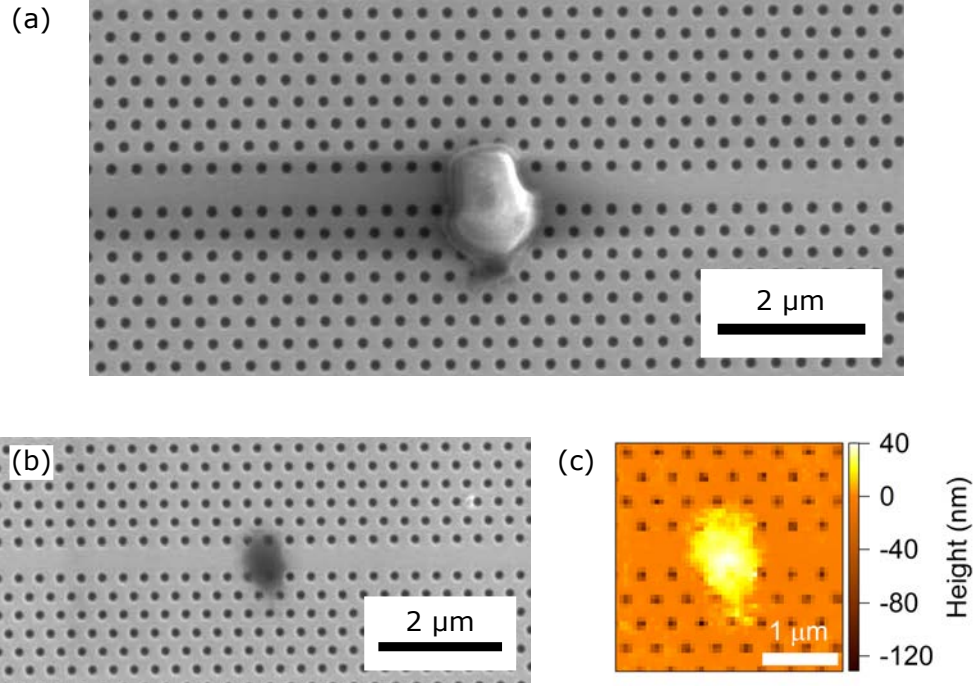


Figure 4.7: SEM and AFM images of selected SU-8 disk cavity devices. (a) SEM image of device A. (b) SEM image of device C. (c) AFM image of the SU-8 disk on device C.

Indeed, SU-8 disks written using a power of $\sim 4.7 \mu\text{W}$ had a mean height, $\bar{H} = (172 \pm 28) \text{ nm}$ (and mean radius $\bar{R} = (0.58 \pm 0.05) \mu\text{m}$), whereas those written with a higher power of $\sim 9.4 \mu\text{W}$ had $\bar{H} = (257 \pm 15) \text{ nm}$ (and $\bar{R} = (0.93 \pm 0.04) \mu\text{m}$). The uncertainties presented for \bar{H} and \bar{R} are the estimated standard error of the mean. A positive correlation was found between R and H (as seen from Fig. 4.8), which demonstrates that a thicker SU-8 disk is generally expected to have a larger radius. We suggest that this is due to a larger quantity of photoacid catalyst generated when writing thicker disks (due to a thicker SU-8 film and/or a higher exposure dose). The effects of altering the SU-8 disk radius are explored further in section 4.3.

The SU-8 disk cavities exhibit a general trend of higher Q for thinner disks (see Fig. 4.8), which is in agreement with expectations from the FDTD simulation results presented in Fig. 4.3. This confirms that targeting thin SU-8 on the PhC waveguide is necessary to maximise the Q factor of the created cavity mode. Q factors in the range 2300 to 7400 were observed, with some significant random variation apparent for a given disk thickness. This variation is attributed to differences in the SU-8 disk shape (and radius) between devices, in addition to random misalignment between the SU-8 disk and the PhC waveguide. Misalignment of the SU-8 disk with the waveguide (in the y -direction) is expected to be detrimental to the Q factor of the cavity mode, as shown in

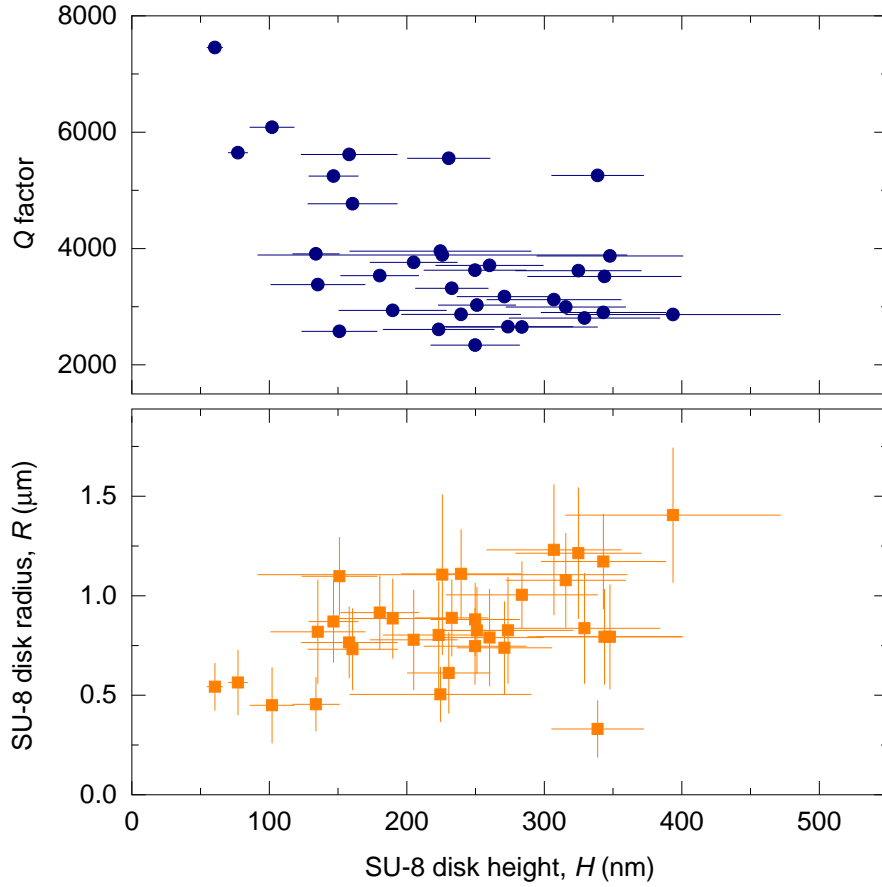


Figure 4.8: Fundamental cavity mode Q factor and SU-8 disk radius, R , compared to SU-8 disk height, H , for the batch of 34 SU-8 disk cavities.

section 5.1. This was an issue because the SU-8 disks were written by manually aligning the exposure laser spot with the PhC waveguide (while the laser was heavily attenuated, to prevent unwanted exposure of the SU-8) using the visualization system of the μPL setup. We anticipate that this would be less of an issue if a single QD could be used as a target to write the SU-8 disk. Alternatively, the SU-8 strip cavity design, which is explored in Ch. 5, may be preferable due to its less stringent alignment requirements.

We now consider the suitability of the SU-8 disk cavity modes for single QD-cavity coupling experiments, for which a high Q/V_0 ratio (or $Q/\sqrt{V_0}$ for strong coupling) and consistent λ_0 between devices (to achieve spectral overlap with a target QD) are important. For strong coupling, we focus on the figure of merit, η (defined in Eq. 3.16), which was estimated for each of the SU-8 disk cavities. The obtained values of η , which are presented in Fig. 4.9(a), were estimated using the experimentally observed Q and λ_0 for each cavity mode, in addition to an approximation of V_0

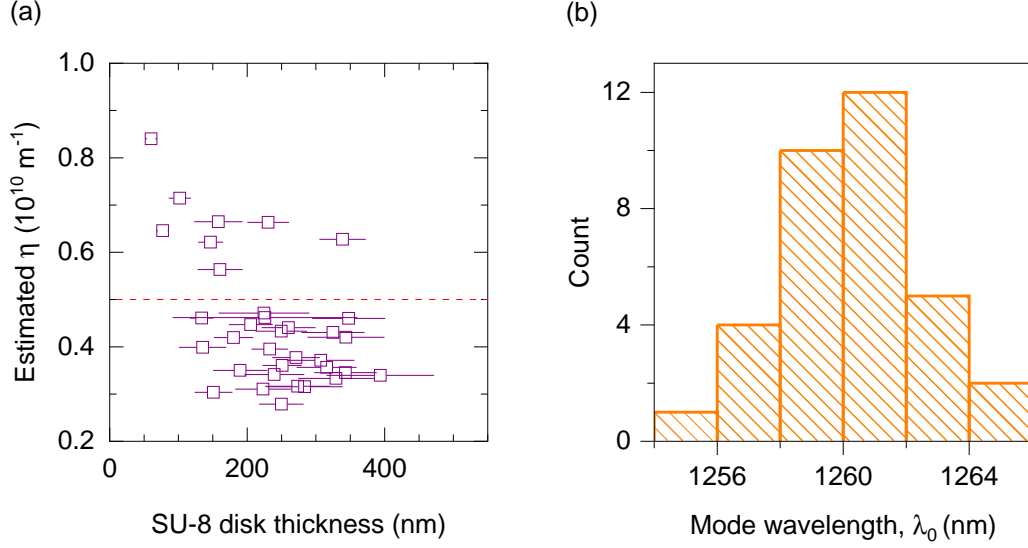


Figure 4.9: Parameters extracted from the fundamental cavity modes of the 34 SU-8 disk cavities. (a) Estimated value of η , the strong coupling figure of merit. The red dashed line indicates the predicted minimum value of η required for the onset of strong coupling. (b) Distribution of the cavity mode wavelength, λ_0 , for the devices.

obtained from FDTD simulation results. The value of V_0 used to calculate η was extracted from the FDTD results presented in Fig. 4.3 by interpolating the data to the relevant disk height. A refractive index of $n = 3.33$ was used for the calculations. As discussed in section 3.6, the theoretical onset of strong coupling is expected for $\eta \gtrsim 5 \times 10^9 \text{ m}^{-1}$, but a target value of $\eta \sim 10^{10} \text{ m}^{-1}$ is recommended, based on reported cases of strongly coupled QD-PhC cavities in the literature. The results in Fig. 4.9(a) therefore show that strong coupling may be possible using this cavity design: the highest η device (device C) even approaches the $\eta \sim 10^{10} \text{ m}^{-1}$ target for strong coupling. However, the majority of the fabricated devices lie below the $\eta \sim 5 \times 10^9 \text{ m}^{-1}$ estimated for the onset of strong coupling. Hence, for strong coupling applications, improvements to the cavity design would be recommended. Despite this, the cavities still possess a high Q/V_0 ratio, so are well suited to weak coupling: in the worst-case scenario, $Q \approx 2300$ and $V_0 \approx 1.48$ can be expected, giving a maximum theoretical Purcell factor of 120.

The distribution of fundamental cavity mode wavelengths, λ_0 , measured from the 34 SU-8 disk cavities is shown in Fig. 4.9(b). The wavelengths are distributed about a mean of $(1260.2 \pm 0.4) \text{ nm}$, with a standard deviation of 2.2 nm and a range of 9.6 nm. We attribute the variation of λ_0 between devices to differences in the SU-8 disk shape, size and alignment with the PhC waveguide, in addition to random fabrication imperfections between PhC waveguides. Given the $\sim 1 \text{ nm}$ temperature-tuning range of a single QD (see section 3.8.4), the distribution of λ_0 is wider than

desirable for coupling applications. We anticipate that the spread of λ_0 is not so unacceptably large that spectral overlap could not be achieved between a QD and cavity mode, but improvements to the cavity design and/or fabrication technique would be recommended to achieve a more consistent, more narrowly distributed λ_0 . FDTD simulation results suggest that for a disk with $d_{\text{disk}} = 1\ \mu\text{m}$, λ_0 should vary by only $\sim 2\ \text{nm}$ as h_{disk} is increased from 50 nm to 200 nm; therefore, if the SU-8 disks can be patterned with a consistent radius and good alignment with the waveguide, a narrow range of λ_0 should be possible.

4.3 Varying the disk diameter

Following the successful demonstration of the SU-8 disk cavity, investigations were conducted into the optimisation of the cavity design. Specifically, we sought a design with an improved strong coupling figure of merit, η , which would be feasible without the need for a sub-100 nm-thick SU-8 disk (which is experimentally challenging to fabricate). In section 2.4, it was shown using the L3 cavity as an example [32] that a PhC cavity can generally be optimised to achieve a higher Q , while V_0 remains of a similar size. Therefore, in order to find a more optimal cavity design with a higher η (which is proportional to $Q/\sqrt{V_0}$), we sought to increase the Q of the SU-8 disk cavity mode.

The effect of altering the SU-8 disk diameter, d_{disk} , was investigated, which can be easily controlled in practice by either changing the size of the writing laser spot or by writing a circular pattern with the $\sim 1\ \mu\text{m}$ diameter spot. FDTD simulations were performed to calculate the Q factor (and its components) and V_0 of the fundamental cavity mode supported by placing an SU-8 disk with height $h_{\text{disk}} = 100\ \text{nm}$ and variable diameter on a PhC waveguide. The results, presented in Fig. 4.10, show that the Q_{total} of the cavity mode is theoretically expected to increase by an order of magnitude as d_{disk} is increased from $1\ \mu\text{m}$ to $4\ \mu\text{m}$, while V_0 changes by less than a factor of 2. Increasing the SU-8 disk diameter therefore presents a potential convenient method of improving the cavity's figures of merit for coupling: the theoretical η increases from $8.6 \times 10^9\ \text{m}^{-1}$ to $8.2 \times 10^{10}\ \text{m}^{-1}$ and the Q_{total}/V_0 from $5000\ (n/\lambda_0)^3$ (maximum theoretical $F_P = 380$) to $4.0 \times 10^4\ (n/\lambda_0)^3$ (maximum theoretical $F_P = 3000$) by increasing d_{disk} from $1\ \mu\text{m}$ to $4\ \mu\text{m}$. The proposed mechanisms responsible for the dramatic increase in the Q factor are explored in detail in section 5.4 for the SU-8 strip cavity, for which a similar phenomenon occurs.

An example of a real SU-8 disk cavity with a large diameter is presented in Fig. 4.11. This was

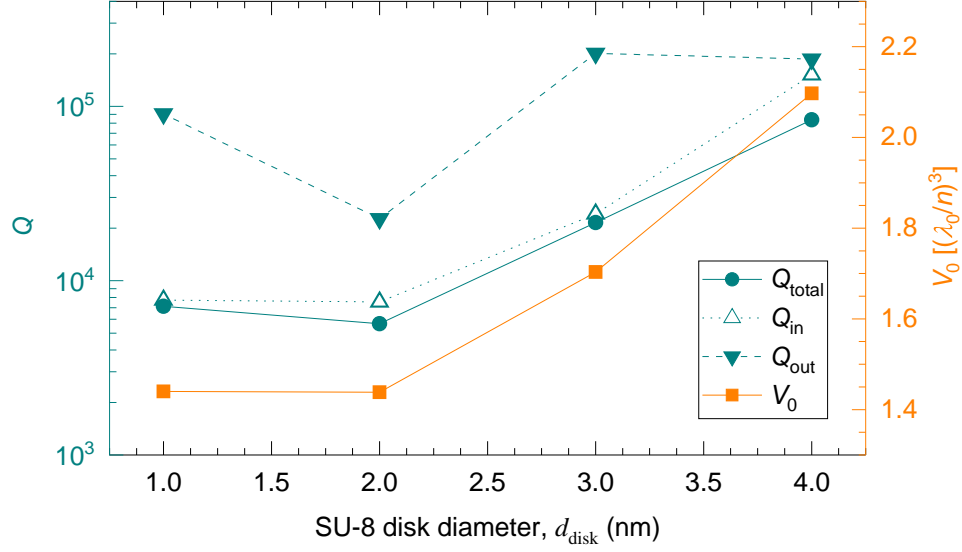


Figure 4.10: Parameters of the fundamental mode of an SU-8 disk cavity with $h_{\text{disk}} = 100$ nm and variable d_{disk} , extracted from FDTD simulations performed using Lumerical FDTD Solutions software.

fabricated on the same sample as used for the SU-8 disk cavities detailed in section 4.2, using the same SU-8 spin-coating procedure (with spin speed 2800 rpm). The SU-8 disk was written by controlling the $\sim 1 \mu\text{m}$ writing laser spot using the piezo-actuated translation stage-mounted objective to trace out a spiral pattern in the SU-8 film. The laser spot was initially positioned over the centre of the PhC waveguide, and moved in a spiral pattern according to the polar co-ordinate equation $r = s\theta/2\pi$, where s corresponds to the spacing between consecutive arcs of the spiral. This pattern was traced at a writing speed $v_w = 1 \mu\text{m s}^{-1}$ with $s = 0.5 \mu\text{m}$ (the approximate spot radius) and a laser power of $\sim 17.5 \mu\text{W}$, measured after the objective. The spiral pattern was traced by incrementing θ until $r = R_{\text{target}}$, where $R_{\text{target}} = 2.5 \mu\text{m}$ was the target radius of the SU-8 disk. Once this radius was reached, a circle of radius R_{target} was traced by the writing spot to complete the exposure. Note that we chose to write the SU-8 disk via this method rather than by using a stationary exposure with a larger spot size, in order to maintain a small focused spot size for high-resolution μPL mapping. The SU-8 development process was the same as described previously in section 4.2.

The AFM image in Fig. 4.11(a) shows that a large SU-8 disk with good height uniformity and alignment with the waveguide was successfully fabricated using the described method. The diameter of the disk is estimated to be $\sim 5 \mu\text{m}$, with a typical height of ~ 20 nm. As for the SU-8 disk devices discussed in section 4.1, 1D μPL mapping measurements were performed along the waveguide of the PhC both before and after writing the disk. These measurements confirmed that

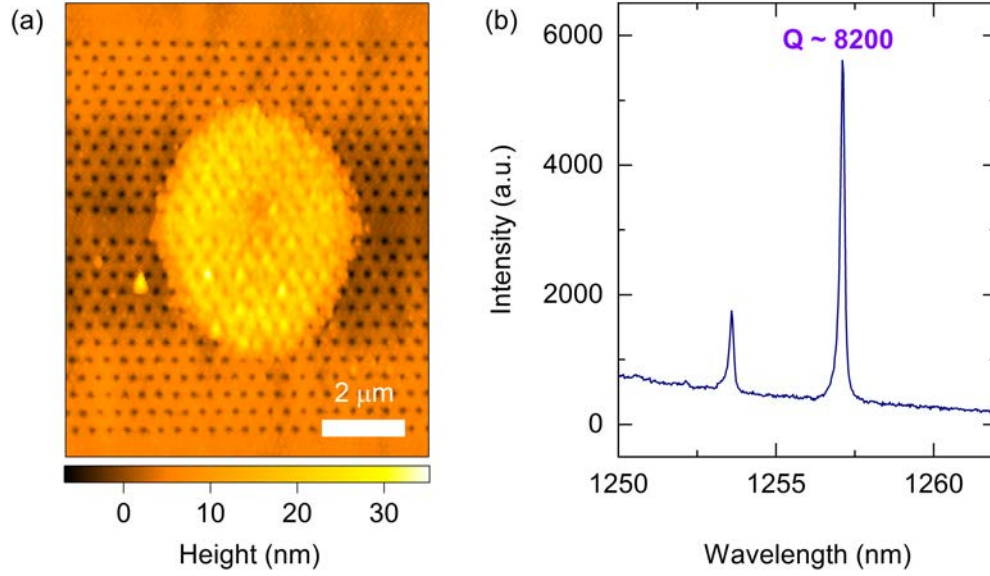


Figure 4.11: An SU-8 disk cavity defined by writing a large disk with a target diameter of 5 μm . (a) AFM image of the device. (b) Spectrum of the cavity modes generated by the disk, taken by optimising on the lower energy, fundamental cavity mode. A Q of 8200 was measured from this mode.

new cavity modes were generated by the presence of the disk on the waveguide; the spectrum in Fig. 4.11(b) shows the first and second order modes supported by the cavity. The spectrum was acquired using the 1200 lines/mm grating with a slit width of 20 μm , 5 s acquisition time and an excitation power of $\sim 5.5 \mu\text{W}$ after the objective.

The SU-8 disk cavity was found to support a high $Q = 8200$ cavity mode, which exceeds those measured from the batch of cavities reported in section 4.2 and is the highest Q factor SU-8 disk cavity mode that was measured in this work. The improved Q of the mode is attributed to the increased disk diameter in addition to the narrow height of the disk, which was possible due to better dose optimisation during the exposure procedure. The Q factor does not reach the orders of magnitude expected from FDTD simulation results, which we attribute to limitations of the sample wafer. This is discussed in more detail in Ch. 5. Other SU-8 disk cavities with large diameters were successfully fabricated, but alignment of the disk with the waveguide proved to be an issue, which we show in section 5.1 can limit the Q factor. This was one of the key reasons why the SU-8 strip cavity design was preferred for the rest of the work in this thesis.

4.4 Summary

The SU-8 disk cavity has been introduced as the original concept for creating a deterministically-positioned cavity in a PhC waveguide by exposing photoresist deposited on its top surface [203]. The cavity design has been shown via FDTD simulations and practical application to successfully generate a high Q/V_0 , localized cavity mode. SU-8 disk cavities fabricated by exposing the photoresist at a single position on the PhC waveguide exhibited Q factors in the range 2300 to 7400 and an estimated η (strong coupling figure of merit) of up to $\sim 8.4 \times 10^9 \text{ m}^{-1}$, suggesting that strong coupling may be possible between an SU-8 disk cavity mode and a single QD using this technique (if good spectral and spatial overlap can be achieved). However, limitations of the cavity design and fabrication technique present some issues that would likely decrease the yield of coupling for these applications. Significant variation of the ground mode wavelength, λ_0 , is likely to reduce the success rate of achieving spectral overlap between the mode and a target single QD and the wide variation of the Q factor is expected to prevent most of the (lower Q) created cavity modes from being eligible for strong coupling. The variation of Q and λ_0 is attributed principally to variation of the SU-8 disk shape, size and alignment with the PhC waveguide between devices. We anticipate that achieving better consistency between fabricated devices would result in cavity modes with a higher average Q and narrower distribution of λ_0 , which would be preferable for coupling applications.

Increasing the SU-8 disk diameter has been shown theoretically as a potential convenient method to significantly increase the Q/V_0 ratio (and η) of the cavity mode and larger SU-8 disks have been successfully fabricated in experiments. For both the small and large SU-8 disk cavities, misalignment between the SU-8 disk and waveguide was found to be an issue in practice. In Ch. 5, it is shown that this misalignment has the potential to be detrimental to the Q factor of the cavity modes, which leads to the development of the SU-8 strip cavity as an alternative design which does not require precise alignment with the waveguide.

5

SU-8 strip cavities

The focus of this chapter is on the SU-8 strip-defined mode gap cavity: a cavity created by writing a strip of SU-8 on a section of a PhC waveguide, which was introduced in Ch. 2. The FDTD simulation work performed previously is extended upon, beginning with a comparison of the SU-8 strip-defined cavity to the SU-8 disk-defined cavity that was the subject matter of Ch. 4. We show that the SU-8 strip cavity design is generally favourable due to inherently less strict alignment requirements. Additional FDTD simulations of the SU-8 strip cavity are performed to further characterise the cavity mode properties, including their dependence on the strip height. Following this, a batch of fabricated SU-8 strip cavities is characterised using similar μ PL mapping and AFM techniques to those introduced in Ch. 4. Key results from these FDTD simulations and characterisation measurements are published in Ref. [206]. The work of this chapter also goes beyond this published work, presenting time-resolved μ PL measurements and an investigation into the effects of altering the SU-8 strip width.

5.1 Limitations of the SU-8 disk cavity design

In Ch. 4, we demonstrated the successful implementation of the SU-8 disk mode gap cavity, formed by exposing a disk of SU-8 on top of a PhC waveguide. Devices were fabricated with a moderate to high Q in the range 2300 to 7400. During this fabrication process, an inherent limitation of the SU-8 disk cavity design became apparent, which is the potential for misalignment of the disk perpendicular to the waveguide (in the y -direction). In a number of cases, the centre of the developed SU-8 disk did not coincide with the centre of the PhC waveguide ($y = 0$) to the desired accuracy. Some examples of this issue are presented in Fig. 5.1, which shows AFM and

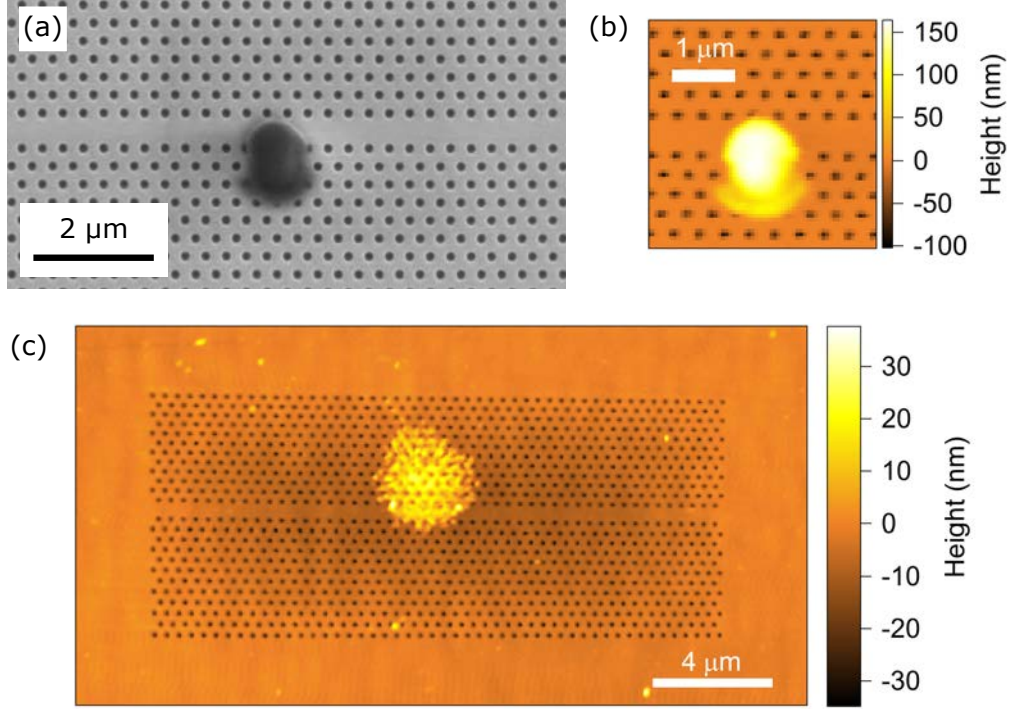


Figure 5.1: Example devices for which the SU-8 disk is misaligned with the waveguide. (a) SEM image and (b) AFM image of a device with an SU-8 spot misaligned by $\sim 0.3 \mu\text{m}$. (c) AFM image of a device with a larger SU-8 spot, misaligned by $\sim 1 \mu\text{m}$.

SEM images of otherwise successful devices. In Fig. 5.1(a) a device with an SU-8 disk of $\sim 1 \mu\text{m}$ diameter is shown, which is evidently not centred on the waveguide – we estimate that the exposure was misaligned by $\sim 0.3 \mu\text{m}$ in the y -direction. An AFM image of the same SU-8 disk is shown in Fig. 5.1(b). In Fig. 5.1(c), we show a more extreme example of misalignment between the SU-8 disk and waveguide. In this case a disk of $\sim 4 \mu\text{m}$ diameter is significantly misaligned with the centre of the waveguide by $\sim 1 \mu\text{m}$. We attribute the misalignment of the SU-8 disk in both cases to misalignment between the exposure laser spot and waveguide, which were aligned by eye using the visualisation system of the μPL apparatus (see section 3.8).

FDTD simulations were performed to investigate the effects of misalignment between the SU-8 disk and PhC waveguide for a disk with height $h_{\text{disk}} = 100 \text{ nm}$ and diameter $d_{\text{disk}} = 4 \mu\text{m}$. An offset Δy was applied to the y -position of the disk, as indicated by the schematic diagram in Fig. 5.1(a) (for an SU-8 disk of arbitrary diameter); the symmetry boundary condition at $y = 0$ was removed as necessary. The results of the simulations for various offsets up to $1.5 \mu\text{m}$ are summarised in Fig. 5.3. As the offset is altered from $\Delta y = 0$ (perfect alignment) to $\Delta y = 1.5 \mu\text{m}$, the value of Q_{total} , which is limited by Q_{in} , falls by almost an order of magnitude. This result highlights just how detrimental misalignment of the SU-8 disk with the waveguide has the potential to be. We

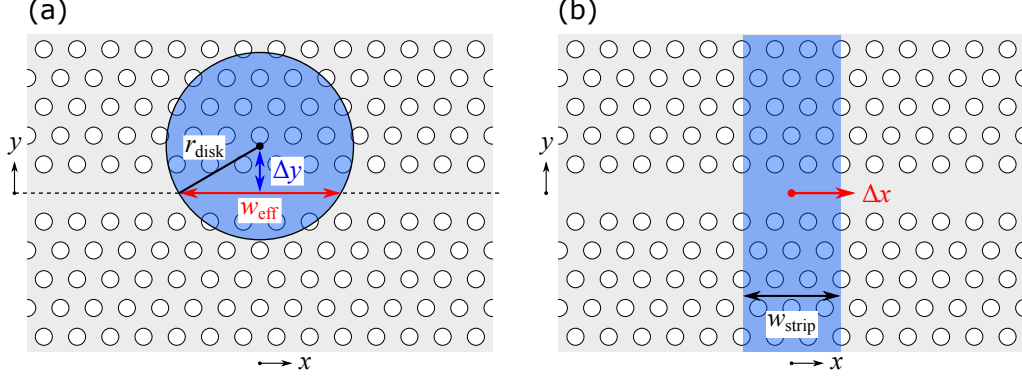


Figure 5.2: Schematic diagrams of SU-8 disk and strip cavity designs, with shifted positions. (a) SU-8 disk shifted in the y -direction by Δy , with approximate effective width of the cavity marked by w_{eff} . (b) SU-8 strip cavity, shifted in the x -direction by Δx . A y -offset is not applicable. The sizes of the disk and strip are arbitrary.

also see that the mode blueshifts by over 2 nm, suggesting that variation in the SU-8 disk alignment with the waveguide will add unwanted variation to the mode wavelength (which we wish to keep as controlled as possible for coupling applications). We note that the field profile of the mode remains localized to the waveguide for the range of Δy examined, as expected for a mode-gap cavity.

The reduction in Q factor as Δy is increased is attributed to a reduction of the effective width of the mode gap confinement potential (see section 2.5). As Δy is increased, the cross-section of the SU-8 disk covering the waveguide decreases, which is expected to correspond to the cavity region. The effective width of the cavity is therefore made narrower as Δy is increased, which is consistent with the reduction in V_0 shown in Fig. 5.3. We approximate an effective width of the cavity mode, w_{eff} , as illustrated in Fig. 5.2(a), defined by $w_{\text{eff}} = 2\sqrt{r_{\text{disk}}^2 - (\Delta y)^2}$, where r_{disk} is the radius of the SU-8 disk. The Q_{total} and V_0 of the offset $h_{\text{disk}} = 100$ nm, $d_{\text{disk}} = 4$ μm disk cavity mode are plotted as a function of w_{eff} in Fig. 5.4. Also plotted in this figure for comparison are simulation results for SU-8 disk cavities with $h_{\text{disk}} = 100$ nm and a range of d_{disk} , with no alignment offset ($\Delta y = 0$), for which $w_{\text{eff}} = d_{\text{disk}}$. Evidently, cavities with the same w_{eff} support cavity modes with similar Q_{total} and V_0 , suggesting that offsetting the SU-8 disk from the waveguide is analogous to reducing its diameter. The increased Q_{total} for larger w_{eff} is attributed to a suppression of TE-TM coupling losses, explained in section 5.4.

We predict that as $w_{\text{eff}} \rightarrow 0$, a cavity mode would not be formed in the waveguide. Such a situation was difficult to simulate in practice, because for large Δy (for which $w_{\text{eff}} = 0$) the modes supported by the system became too closely spaced (spectrally) to isolate. These modes appeared to be similar in character to the FP-like modes supported by the blank PhC waveguide (see for

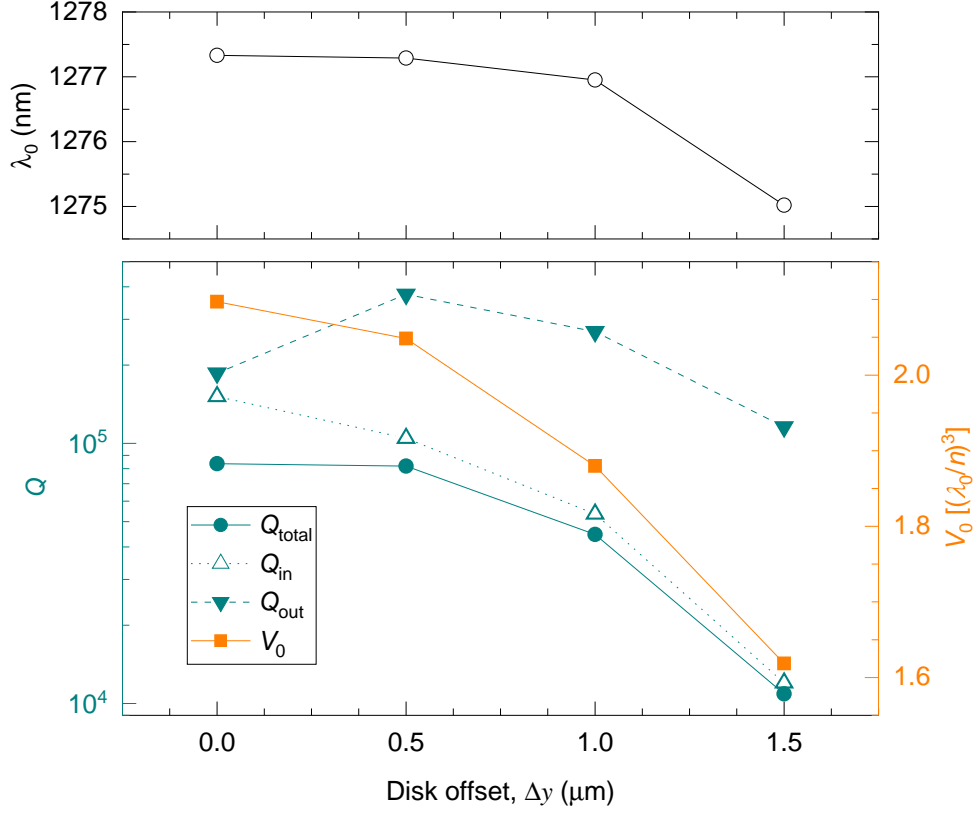


Figure 5.3: FDTD simulation results for an SU-8 disk cavity with $h_{\text{disk}} = 100 \text{ nm}$, $d_{\text{disk}} = 4 \mu\text{m}$ and variable offset Δy from the waveguide.

example Ch. 2 in Ref. [1]); further investigation would be recommended to determine whether the disk generates a useful (and positionable) cavity mode for large offsets such as this.

The FDTD simulation results presented here demonstrate the detrimental effect that SU-8 disk misalignment can have on the cavity mode properties, in particular the Q factor. This issue could potentially be avoided by applying fabrication techniques which allow more consistent disk-waveguide alignment, such as using the combiner fibre discussed in section 3.8 to co-axially align the excitation and exposure lasers. However, a more convenient solution is to use a different cavity design, which does not have such strict alignment requirements. This paved the way to the SU-8 strip writing technique detailed in the rest of this chapter, which offers the significant advantage that it inherently does not require precise alignment with the waveguide [Fig. 5.2(b)].

It should be noted that despite the alignment issues, moderately high Q factors were possible in the fabricated SU-8 disk devices: $Q = 5200$ was measured from the device in Figs. 5.1(a) and 5.1(b), and $Q = 5900$ was measured from the device in 5.1(c). However, it is likely a higher Q could have been reached if the alignment was better and disk misalignment could become a limiting factor on

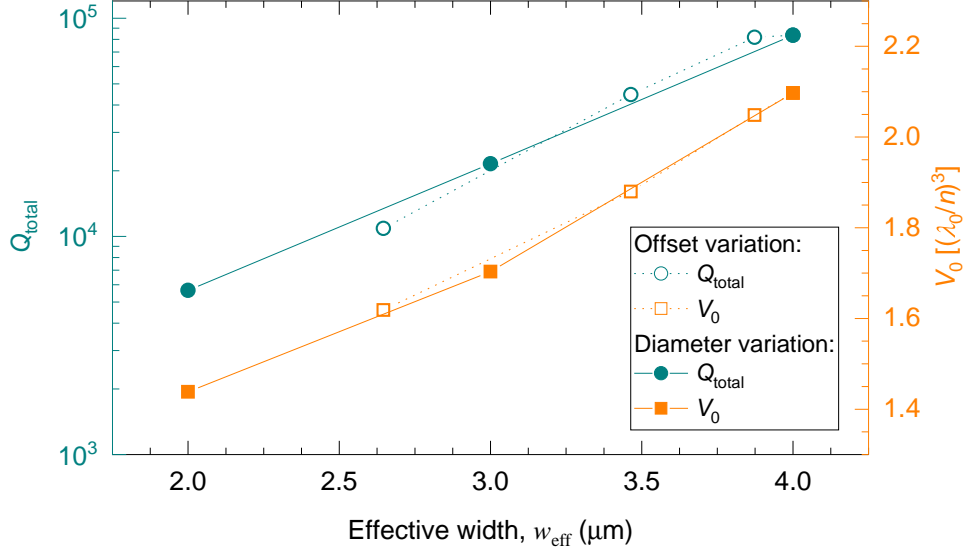


Figure 5.4: FDTD simulation results comparing Q_{total} and V_0 of an SU-8 disk cavity with $h_{\text{disk}} = 100$ nm, $d_{\text{disk}} = 4 \mu\text{m}$ and variable Δy (offset variation) to an SU-8 disk cavity with $h_{\text{disk}} = 100$ nm, $\Delta y = 0$ and variable diameter (diameter variation). Results are plotted as a function of effective width.

the Q going forward.

5.2 Simulating the SU-8 strip cavity performance

FDTD simulations for a basic SU-8 strip cavity with $h_{\text{strip}} = 100$ nm and $w_{\text{strip}} = 1 \mu\text{m}$ (approximately the writing spot size) have already been presented in section 2.6. Here, we extend upon these results, first comparing the performance to an SU-8 disk cavity and then examining the effects of altering the strip geometry on the cavity mode properties. In table 5.1, we present the fundamental cavity mode parameters extracted from FDTD simulations of comparable SU-8 disk and strip cavity devices: an SU-8 strip cavity with $h_{\text{strip}} = 100$ nm and $w_{\text{strip}} = 1 \mu\text{m}$ and an SU-8 disk cavity with $h_{\text{disk}} = 100$ nm and $d_{\text{disk}} = 1 \mu\text{m}$. We find that the performance of the two cavities is similar: although the disk cavity exhibits a Q_{out} almost double that of the strip cavity mode, both are evidently limited by similar in-plane losses (attributed to TE-TM coupling) which result in a comparable Q_{in} and crucially almost the same Q_{total} of around 7000. Given the similarly high Q_{total} and small V_0 of the two cavity designs, they can be expected to offer comparable performance for coupling applications. This, combined with the less stringent alignment requirements, presents a strong case for the SU-8 strip cavity design, which the rest of this work will focus on.

| Design | λ_0 (nm) | Q_{total} | Q_{in} | Q_{out} | $V_0 [(\lambda_0/n)^3]$ |
|--------|------------------|--------------------|-----------------|-------------------|-------------------------|
| Disk | 1269.3 | 7100 | 7700 | 9.1×10^4 | 1.44 |
| Strip | 1270.8 | 7000 | 8200 | 4.8×10^4 | 1.36 |

Table 5.1: Comparison of the simulated parameters of the fundamental cavity mode, extracted from an SU-8 disk-defined cavity with $h_{\text{disk}} = 100 \text{ nm}$ and $d_{\text{disk}} = 1 \mu\text{m}$, and an SU-8 strip-defined cavity with $h_{\text{strip}} = 100 \text{ nm}$ and $w_{\text{strip}} = 1 \mu\text{m}$.

The effect of altering the SU-8 strip height was investigated through FDTD simulations – an important consideration, as we have seen from the work on SU-8 disk cavities in Ch. 4 that the SU-8 thickness is critical to the Q factor of the cavity. The results for a $1 \mu\text{m}$ -wide strip are shown in Fig. 5.5, which displays the Q components, V_0 and λ_0 as a function of h_{strip} . Similar to the behaviour found for SU-8 disk cavities, thin SU-8 with $h_{\text{strip}} \lesssim 100 \text{ nm}$ is required for high $Q_{\text{total}} \gtrsim 10^4$ (which is generally limited by in-plane losses due to TE-TM coupling, as shown by the significantly lower Q_{in} than Q_{out}) so it will be crucial to target this thickness for experimental applications. The results also show that for thicknesses of this order, the mode wavelength is very sensitive to variation in h_{strip} , exhibiting a redshift of $\sim 5 \text{ nm}$ as the thickness is increased from 20 nm to 200 nm . For this reason, achieving a consistent strip height is particularly important for thin strips, in order to achieve cavities with a consistent λ_0 for coupling applications. As the strip height is increased beyond 200 nm , both λ_0 and V_0 are expected to remain fairly constant; however, Q_{total} falls as low as 1500, so a thin strip is certainly preferable for coupling applications. The electric field profiles of cavities with different SU-8 strip heights are examined in Fig. 5.6, which shows the $|\mathbf{E}|^2$ profile of a strip with $h_{\text{strip}} = 400 \text{ nm}$ [Figs. 5.6(a), 5.6(c)] and a strip with $h_{\text{strip}} = 50 \text{ nm}$ [Figs. 5.6(b), 5.6(d)]; both strips have $w_{\text{strip}} = 1 \mu\text{m}$. The field profile of the 400 nm -thick strip cavity is almost identical to that of a 100 nm -thick strip [see Figs. 5.24(a) and 5.24(c)], with the local antinodes well-localized to the centre of the slab ($z = 0$). Clearly, this is important for coupling experiments, as this is where the self-assembled QDs are located. We also confirmed that the field profile of a cavity with $h_{\text{strip}} = 1 \mu\text{m}$, $w_{\text{strip}} = 1 \mu\text{m}$ is almost unchanged, suggesting that for any reasonable SU-8 strip thickness, the cavity mode is well-localized to the slab. Indeed, for the case of $h_{\text{strip}} = 400 \text{ nm}$, $|\mathbf{E}|^2$ decays to $\sim 5\%$ of its maximum value along $x, y = 0$ at a depth of 100 nm into the SU-8 strip, so it is unsurprising that the cavity field and parameters are not particularly sensitive to changes in the strip height when h_{strip} is significantly larger than 100 nm . Turning our attention to the cavity with $h_{\text{strip}} = 50 \text{ nm}$ in Figs. 5.6(b) and 5.6(d), we observe that

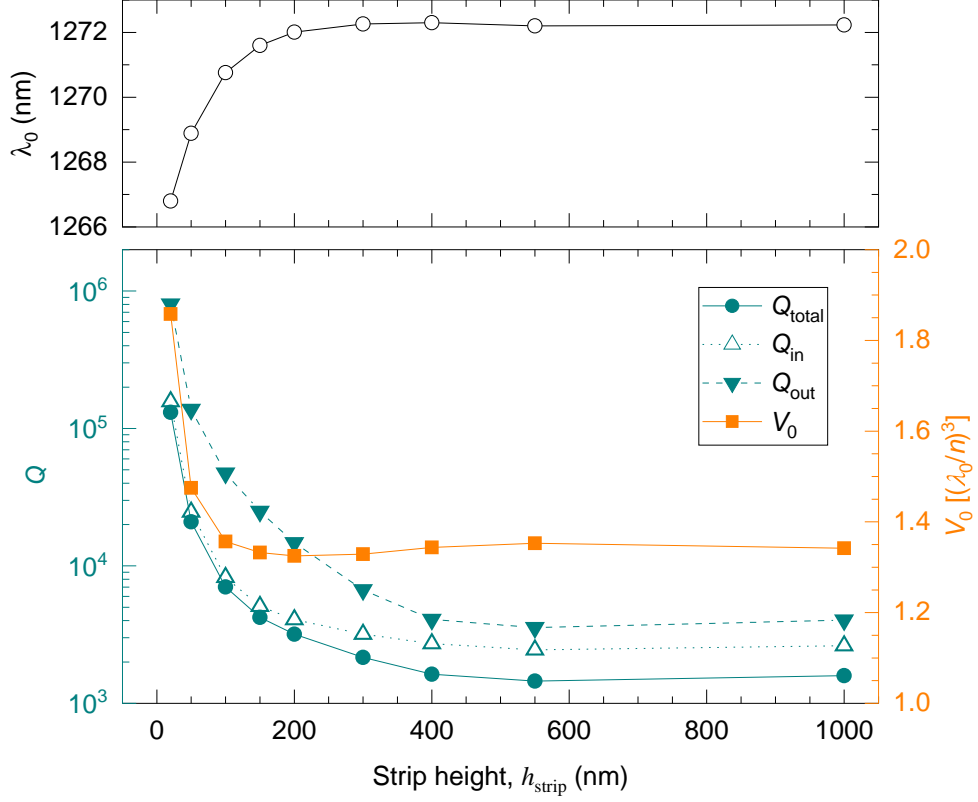


Figure 5.5: FDTD simulation results for an SU-8 strip-defined PhC cavity with $w_{\text{strip}} = 1 \mu\text{m}$ and variable strip height, h_{strip} .

the mode is less localized, extending further into the surrounding PhC and waveguide, as well as further above and below the slab. This is reflected by the increased V_0 shown in Fig. 5.5. The increased delocalization of the mode for thinner SU-8 strips may be partly responsible for their increased Q , as it results in more localized Fourier components in k -space, which may not overlap as significantly with the TM contours, thus inhibiting losses from TE-TM coupling. This concept is explored in more detail in section 5.4, for cavities defined by wider SU-8 strips. Another potential contributing factor to the reduced in-plane losses is that the z -symmetry of the structure is less severely broken by a thinner SU-8 strip: the index profile above $z = 0$ is more similar to the profile below $z = 0$ when the strip is thinner. As broken z -symmetry is the cause of TE-TM coupling losses (see section 2.6.3), the less severe breaking of the symmetry by a thinner strip might reduce these losses.

Simulations of the photonic band structure of the PhC waveguide, with and without SU-8 film covering the top, provide another useful tool to help explain the behaviour of the SU-8 strip cavities. In section 2.6, we showed through band structure calculations that the presence of the

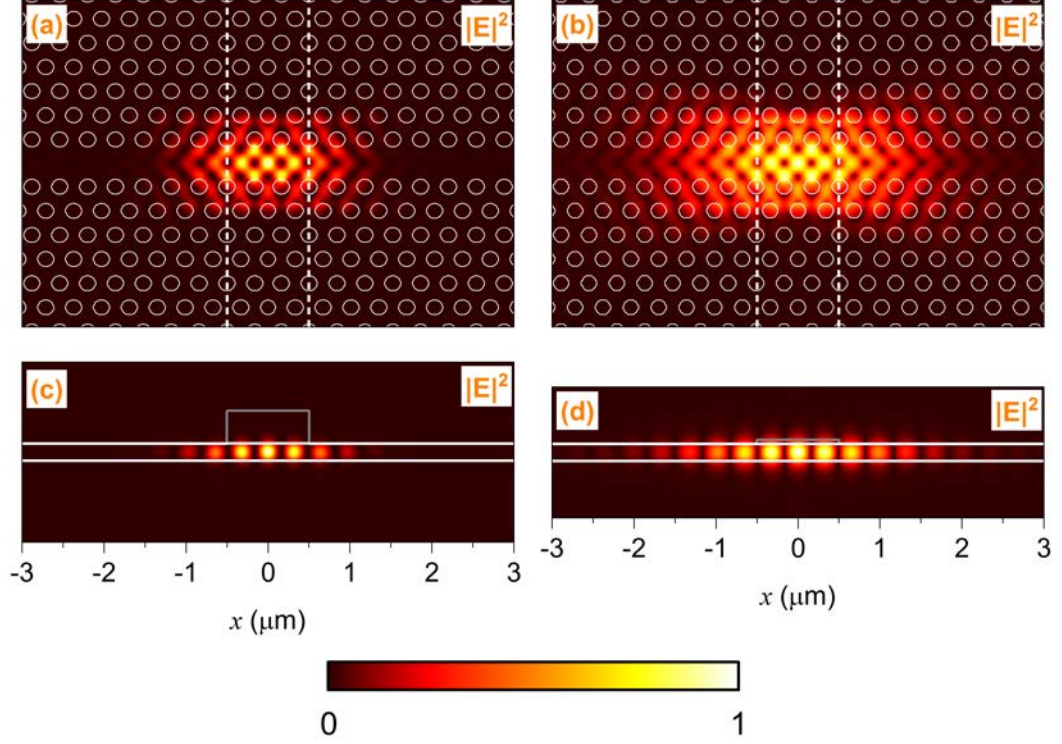


Figure 5.6: $|E|^2$ field profile extracted from FDTD simulations of SU-8 strip-defined PhC cavities with $w_{\text{strip}} = 1 \mu\text{m}$ and different strip height, h_{strip} . (a) and (c): SU-8 strip with $h_{\text{strip}} = 400 \text{ nm}$, shown through the planes $z = 0$ and $y = 0$. (b) and (d): SU-8 strip with $h_{\text{strip}} = 50 \text{ nm}$, shown through the planes $z = 0$ and $y = 0$, respectively. Each profile shows the normalised intensity – the colour scale used is displayed at the bottom of the figure.

SU-8 shifts the WM1 guided mode band down in energy, which we proposed as the origin of the mode gap confinement by the SU-8 strip cavity. Here, we present additional band structure simulation results for a PhC waveguide coated with SU-8 film of different thicknesses; the extracted WM1 bands near the first Brillouin zone edge (where the band energy is at its lowest) are shown in Fig. 5.7(a). Evidently, as the film thickness is increased, the band tends to shift further down in energy, likely due to the increased average refractive index. We plot in Fig. 5.7(b) the wavelength (in air) of the WM1 band at the edge of the first Brillouin zone, $\lambda_{\text{WM1}}(k_x = \pi/a)$ which loosely corresponds to the anticipated λ_0 of an SU-8 strip cavity of that thickness (in fact we would expect it to be between the wavelength shown and that of the Brillouin zone edge for the waveguide with no film, which is at $1.265 \mu\text{m}$). We observe that $\lambda_{\text{WM1}}(k_x = \pi/a)$ exhibits a similar redshift with thickness as the cavity mode does (Fig. 5.5), which levels off for an SU-8 thickness greater than $\sim 200 \text{ nm}$. This suggests that the downward frequency shift of the WM1 band as the SU-8 thickness is increased is responsible for the redshift of the cavity mode. We will see in section 5.4 that as the SU-8 strip is made wider, the wavelength of the cavity mode converges towards $\lambda_{\text{WM1}}(k_x = \pi/a)$

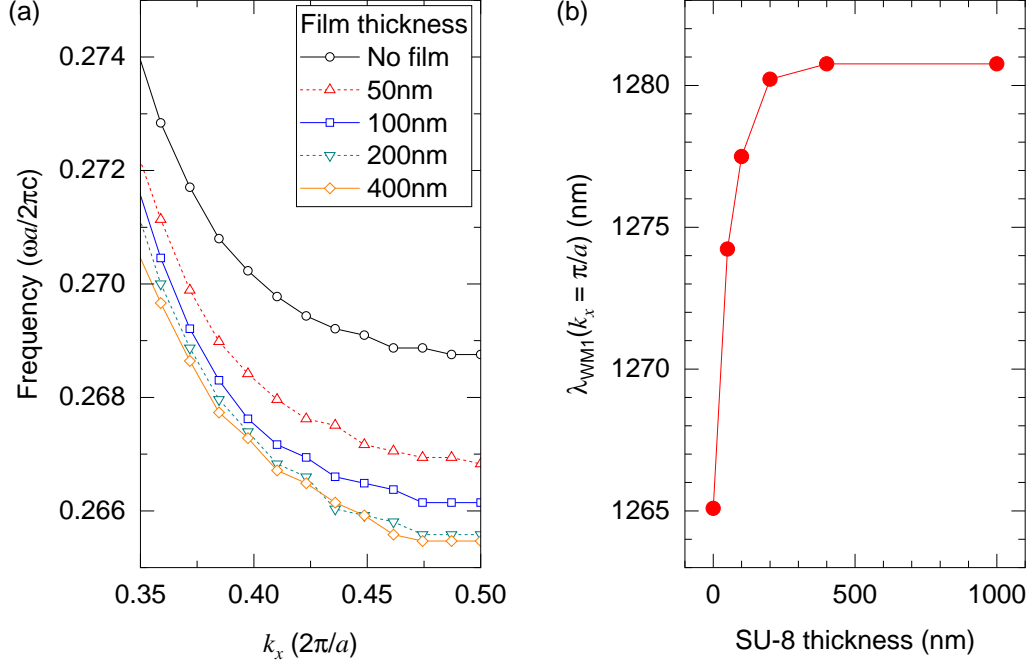


Figure 5.7: WM1 band extracted from photonic band structure simulations of a PhC waveguide with varying SU-8 film thickness on top. (a) Frequency of the WM1 band close to the edge of the first Brillouin zone, for different SU-8 film thicknesses. (b) Wavelength of the WM1 band at the Brillouin zone edge, $\lambda_{WM1}(k_x = \pi/a)$, as a function of SU-8 film thickness. The WM1 band for a PhC waveguide topped with 1 μm -thick SU-8 film, not shown in (a), is similar to the bands displayed for a PhC waveguide with 200 nm and 400 nm-thick film.

for a film thickness equivalent to the strip height.

The WM1 band simulation results also suggest an intuitive interpretation of the increase in Q_{total} and V_0 as the strip thickness is reduced below ~ 200 nm, by making the approximation that the mode gap confinement potential generated by the SU-8 strip cavity corresponds to the difference in energy between the minimum of the WM1 band of the plain waveguide and the waveguide with SU-8 film. As the film thickness is reduced, the difference in energy between these WM1 bands is reduced, which corresponds a shallower confinement potential. Such a potential is likely to lead to a more delocalized mode (higher V_0) which then leads to a higher Q_{total} by suppression of TE-TM mode coupling losses (see section 5.4). This is consistent with what we observe in Fig. 5.5.

5.2.1 Additional geometry considerations

In this section we consider additional factors of the SU-8 strip geometry that may be of concern to the function of the SU-8 strip cavities, namely, the alignment of the strip with the PhC lattice and the possibility of hole-filling with SU-8. We do not expect to have precise control over either

of these two factors using the current SU-8 writing method, so it will be important to account for any random variation that may arise from this lack of control. Exploration of the effects of altering w_{strip} is left to section 5.4.

We first investigated the effect of altering the alignment of the SU-8 strip with the PhC lattice on the Q , V_0 and λ_0 of the generated cavity mode. FDTD simulations were performed with a shift in the x position of the strip, Δx , applied as shown in Fig. 5.2(b). As is necessary, the $x = 0$ symmetry condition was removed. The results, for a device with $h_{\text{strip}} = 100 \text{ nm}$, $w_{\text{strip}} = 1 \mu\text{m}$ and a positional shift up to $\Delta x = a$, are shown in Fig. 5.8. We see that in general the shift has a minimal effect on the cavity parameters – Q_{total} and V_0 are expected to vary by less than 5% – and, as expected from the symmetry of the structure, the values are approximately symmetric about $\Delta x = 0.5a$. Note that fewer values of Δx were simulated between $0.5a$ and a due to high computational demands of the simulation (which possesses only one plane of symmetry). Evidently, Q_{total} is maximised for $\Delta x = 0.5a$, when the edges of the SU-8 strip intersect the high index region between the PhC holes, rather than cutting across the holes (as for $\Delta x = 0$). This is consistent with the findings by Tomljenovic-Hanic *et al.* [90] from simulation results of a polymer strip on a PhC waveguide. The maximum Q_{total} coincides with a maximum V_0 , which actually results in a lower $Q_{\text{total}}/V_0 = 5070 (n/\lambda_0)^3$ compared to $5170 (n/\lambda_0)^3$ for $\Delta x = 0$. In general, however, we can be confident that the alignment of the strip with the PhC lattice will not have a significant effect on Q_{total} and V_0 . It does place a fundamental limitation on the minimum variation of λ_0 between devices of $\sim 0.3 \text{ nm}$, but we expect other factors to limit this in practice, such as random PhC variation and SU-8 thickness variation.

Finally, we consider the effect of PhC hole filling with SU-8, which may be more of a concern for the strip-defined cavity design than for the disk-defined design, since the strip lies over many of the holes. An FDTD simulation of a device with $h_{\text{strip}} = 100 \text{ nm}$ and $w_{\text{strip}} = 1 \mu\text{m}$ (and $\Delta x = 0$) was run as before, except any holes that were completely covered by the strip were filled in with SU-8. Each of these filled holes was edited to contain a cylinder of dielectric material with refractive index 1.57 to represent SU-8 [100]; each cylinder had the same radius as the hole and spanned the depth of the PhC slab, from $z = -z_{\text{slab}}/2$ to $z = z_{\text{slab}}/2$. The parameters of the fundamental cavity mode extracted from the simulation are displayed in table 5.2, from which we see that the simulated cavity with filled holes in fact has a higher Q_{total} and smaller V_0 compared to the case of unfilled holes (also shown in table 5.2). Therefore, filling of the PhC holes beneath the SU-8 strip is unlikely to be detrimental to the Q_{total}/V_0 of the cavity mode and is not expected to be

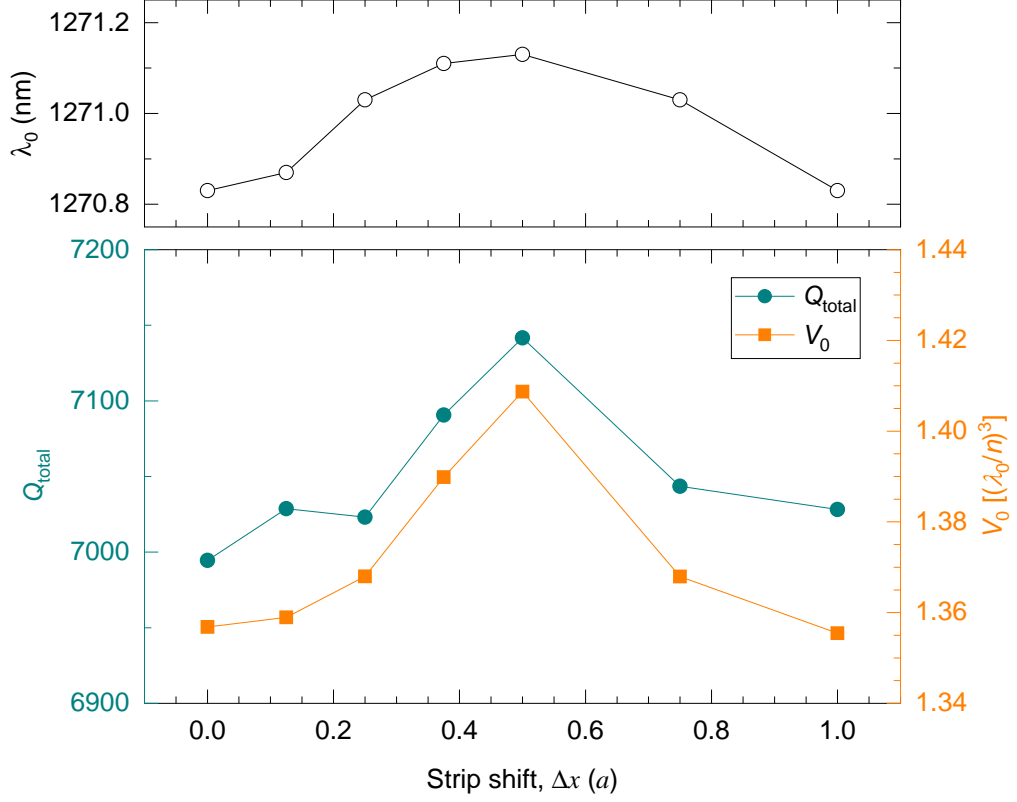


Figure 5.8: Parameters of the fundamental cavity mode extracted from FDTD simulations on an SU-8 strip cavity with $h_{\text{strip}} = 100$ nm, $w_{\text{strip}} = 1$ μm and variable positional shift along the waveguide, Δx .

an issue for coupling experiments in this regard. Indeed, filling of the holes may even improve the Q_{total}/V_0 ratio, although this could depend on the extent of the hole-filling, which may differ from the simple model applied here.

From the simulation results, we observe that λ_0 is significantly redshifted by ~ 10 nm due to filling of the PhC holes under the strip, which suggests that variation in the hole filling might lead to variation of the cavity mode wavelength. As we cannot easily measure whether the cross-linked SU-8 remains in the PhC holes, it is difficult to determine how much of an issue this is. However, we see from the experimental results in section 5.3.2 that variation in the wavelength is typically less than the ~ 10 nm range suggested by these simulation results.

| Holes filled? | λ_0 (nm) | Q_{total} | Q_{in} | Q_{out} | $V_0 [(\lambda_0/n)^3]$ |
|---------------|------------------|--------------------|-------------------|-------------------|-------------------------|
| Yes | 1281.0 | 7900 | 1.0×10^4 | 3.3×10^4 | 1.20 |
| No | 1270.8 | 7000 | 8200 | 4.8×10^4 | 1.36 |

Table 5.2: Simulated parameters of the fundamental cavity mode of an SU-8 strip-defined cavity with and without filled holes under the strip. The cavity parameters are $h_{\text{strip}} = 100$ nm, $w_{\text{strip}} = 1$ μm and for the case of filled holes, only holes which are completely covered by the strip are filled in with SU-8.

5.3 SU-8 strip cavities: experimental results

5.3.1 Fabrication and atomic force microscope characterisation

A batch of SU-8 strip cavities was fabricated in order to test the cavity design's viability and its performance. A high density QD sample with PhC membranes was used, as described in section 3.7. The only notable difference to the sample used for the SU-8 disk cavities in Ch. 4 was that the removal of the sacrificial AlGaAs layer was performed using a 32% treatment with HCl for 5 minutes, instead of HF. A coat of SU-8 film was applied to the surface using a similar spin-coating process, except with an additional spin phase at 500 rpm (with an angular acceleration of 200 rpm/s) for 10 s implemented before the usual spin phase at 2800 rpm (intended to improve adhesion of the film to the surface and PhCs). An initial spin coat with an 8:1 ratio of cyclopentanone to SU-8 2007 was attempted, but was unsuccessful in coating the PhC membranes. This coat was removed with PGMEA (and the sample rinsed with IPA) before applying another coat with a thicker 7:1 ratio of cyclopentanone to SU-8 2007, which successfully coated most of the PhCs.

An optical microscope was used to identify regions of the sample with consistent SU-8 coverage, by examining the thickness-dependent colouration of the SU-8 film. Two categories of coverage could be reliably identified, which are shown by the 500 \times microscope images in Fig. 5.9. In Fig. 5.9(a), 9 devices are shown, which are coated in a thick layer of SU-8 film with green/purple colouration that is not perceptibly altered by the PhC devices. In Fig. 5.9(b) a different set of 9 devices is shown, which is likely covered by a thinner SU-8 film. Evidently, the film exhibits a significant change in colouration from yellow to blue near the PhCs, which, as shown in the thesis by L. Nuttall [1](Ch. 5), is expected to be due to a reduction in the film thickness over the devices. In his thesis, Nuttall presented FDTD simulation results to predict the apparent colour of the SU-8 film coating over a PhC membrane by measuring the reflected spectrum under white LED

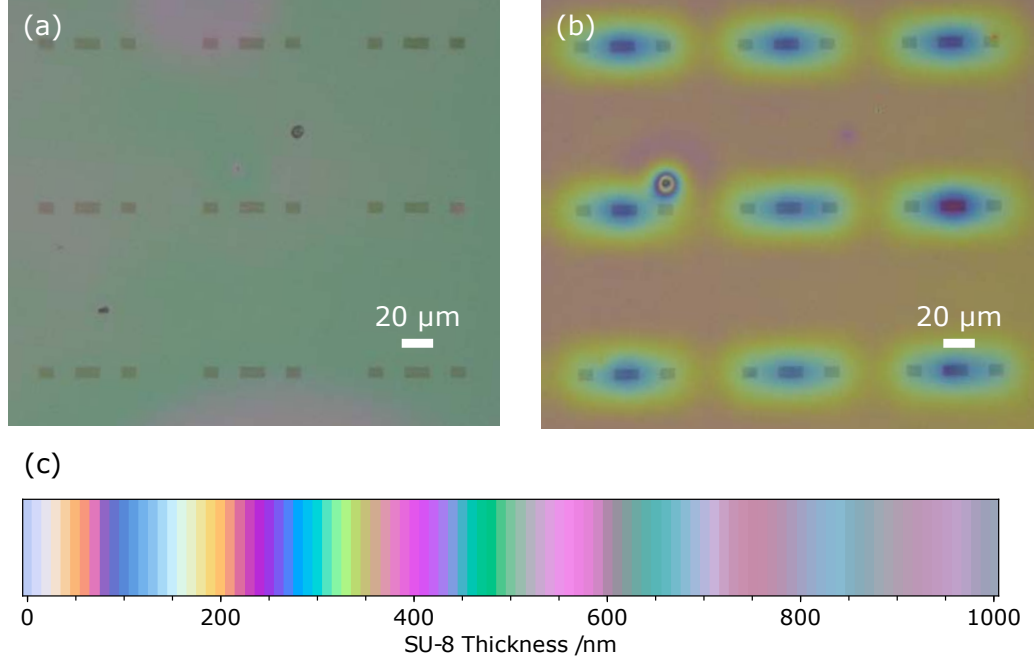


Figure 5.9: 500 \times optical microscope images of PhC devices in different regions of the sample, coated with SU-8 film. (a) 9 devices coated with a thick film of SU-8 (estimated thickness 400–1000 nm). (b) 9 devices coated with a thin film of SU-8 (estimated thickness 100–350 nm). (c) Colour of the SU-8 film predicted as a function of thickness, from simulation results presented by collaborator L. Nuttall [1].

illumination (see Ch. 5 of Ref. [1]). We are now able to use these results, which are presented in Fig. 5.9(c), to estimate the thickness, T_{film} , of the actual SU-8 films. We predict that the thick film in Fig. 5.9(a) is likely to have a T_{film} in the range 400–1000 nm, while the thin film shown in Fig. 5.9(b) is likely to have T_{film} between 100 nm and 350 nm. For brevity, we will refer to these as thick film and thin film, respectively, in the discussion of the results from this fabrication run. Note that T_{film} is particularly difficult to estimate to a high accuracy for the thick film, because films with $T_{\text{film}} > 400$ nm are predicted to have a similar purple/green colouration. The method of SU-8 film thickness estimation applied here can also be used to distinguish more subtle variations of the thickness, as shown in section 5.5.1.

To fabricate SU-8 strips on the PhC waveguides, the 405 nm exposure laser was controlled using the piezo stage-mounted objective (see section 3.8) to write lines in the SU-8 film at room temperature. The L3 cavities either side of the PhC waveguides were used as alignment markers in order to write strips perpendicular to the waveguide. The laser was focused to a $\sim 1 \mu\text{m}$ spot size with a power of $\sim 17.5 \mu\text{W}$ after the objective. For each device, the laser spot was moved perpendicular to the waveguide at a writing speed, v_w , selected between $0.2 \mu\text{m s}^{-1}$ and $5 \mu\text{m s}^{-1}$, to trace a single line of length $20 \mu\text{m}$ in an attempt to write an SU-8 strip on top of the PhC. After this writing process, the sample was developed via the usual procedure, outlined in section 4.2.

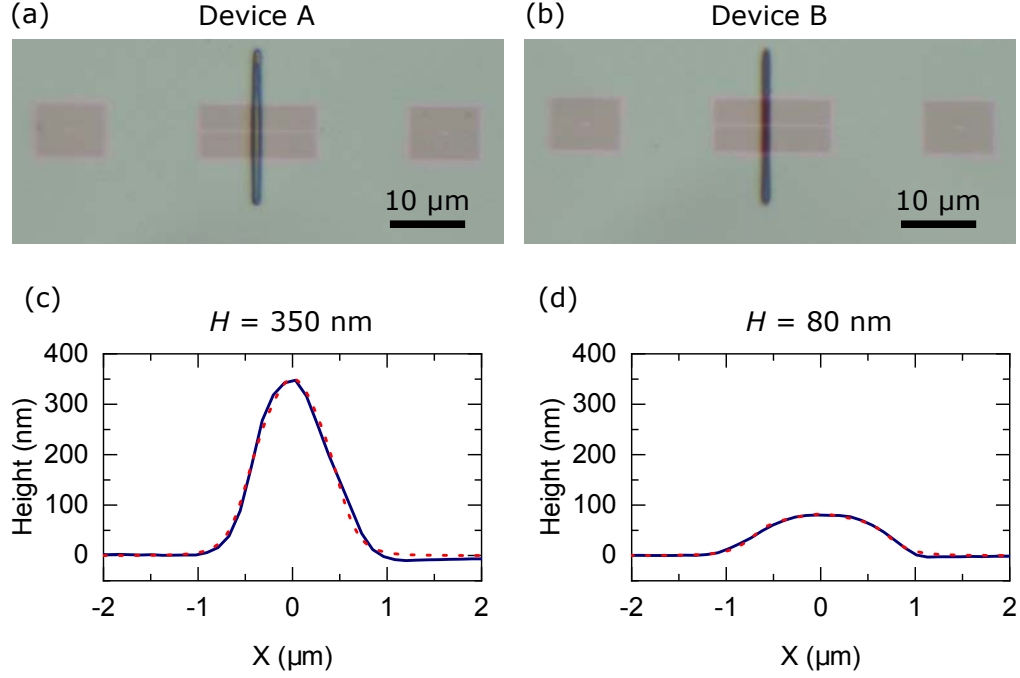


Figure 5.10: Two examples of successfully fabricated SU-8 strip cavities: device A and device B. (a) and (b): 3000 \times optical microscope images of the devices. (c) and (d): height profile of the SU-8 strip from devices A and B, respectively, extracted from AFM measurements and profile averaging techniques. An inverse polynomial fit to each profile is shown (dashed red line).

Two examples of successfully created SU-8 strip cavity devices from this fabrication run are shown in Fig. 5.10, which we refer to as devices A and B. Images of these two devices, obtained using a 3000 \times optical microscope, are shown in Figs. 5.10(a) and 5.10(b): in both cases, a well-defined, uniform SU-8 strip is present on the PhC waveguide. The two SU-8 strips shown were written under significantly different conditions: device A was coated in thick SU-8 film and the strip was written with $v_w = 0.5 \mu\text{m s}^{-1}$ whereas device B was coated in thin SU-8 film and the strip was written with a much slower writing speed of $v_w = 0.125 \mu\text{m s}^{-1}$. Despite the much higher exposure dose applied to device B, we see from the height profiles of the SU-8 strips in Figs. 5.10(c) and 5.10(d) that the strip over device B is much thinner. This confirms that the SU-8 film covering device B was indeed thinner (as predicted) and highlights how significantly the film thickness can affect the strip-writing process.

The height profiles of devices A and B [Figs. 5.10(c) and 5.10(d)], in addition to other selected devices from this fabrication run, were obtained via AFM measurements. For each device, an average height profile of the SU-8 strip was extracted using Gwyddion software's [207] profile extraction tool, which performs averaging over multiple scan lines of the AFM image. Each profile was extracted as a function of X , the distance along the waveguide, by averaging the height at each

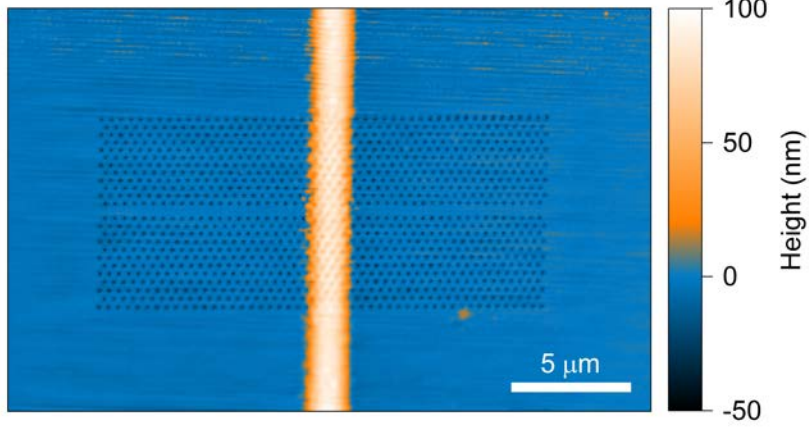


Figure 5.11: AFM image of a successful SU-8 strip cavity with an average strip height $H = 90$ nm and a Q of 7400.

X position over a region extending at least $1\ \mu\text{m}$ either side of the waveguide in the y -direction. In order to obtain an estimate of the average height of an SU-8 strip, we apply an inverse polynomial peak function as an arbitrary fit to the extracted height profile. The function used is given by

$$f(x) = c_0 + \frac{H}{1 + A_1(2\frac{x-x_c}{w})^2 + A_2(2\frac{x-x_c}{w})^3 + A_3(2\frac{x-x_c}{w})^6}, \quad (5.1)$$

where H is the amplitude of the peak, c_0 is the vertical offset, A_1 , A_2 , and A_3 are coefficients of the polynomial and w corresponds to the width of the peak. We see from the two examples in Figs. 5.10(c) and 5.10(d) (devices A and B) that this inverse polynomial peak function provides an excellent fit to the profile of the strip; this was also the case for other strip profiles fitted with this function. We can therefore use H , the amplitude of the peak, as a reliable representation of the approximate average height of the SU-8 strip on each successful device. For device A, we obtain $H = 350$ nm and for device B, we obtain $H = 80$ nm. Values of H are presented to the nearest 5 nm. An example of another successful SU-8 strip cavity device is shown in Fig. 5.11, a full AFM image of the device. This image demonstrates the high uniformity of the SU-8 strip across the y -extent of the PhC waveguide, which was found via profile averaging to have an average height $H = 90$ nm.

In Fig. 5.12 we compare the yields of successfully written SU-8 strips on PhC waveguides coated in (predicted) thick or thin SU-8 film, as defined previously. For the purposes of these yield measurements, a confirmed SU-8 strip is counted as one that extends across the full y -extent of the PhC waveguide with good uniformity [such as the examples in Figs. 5.10(a) and 5.10(b)]; a

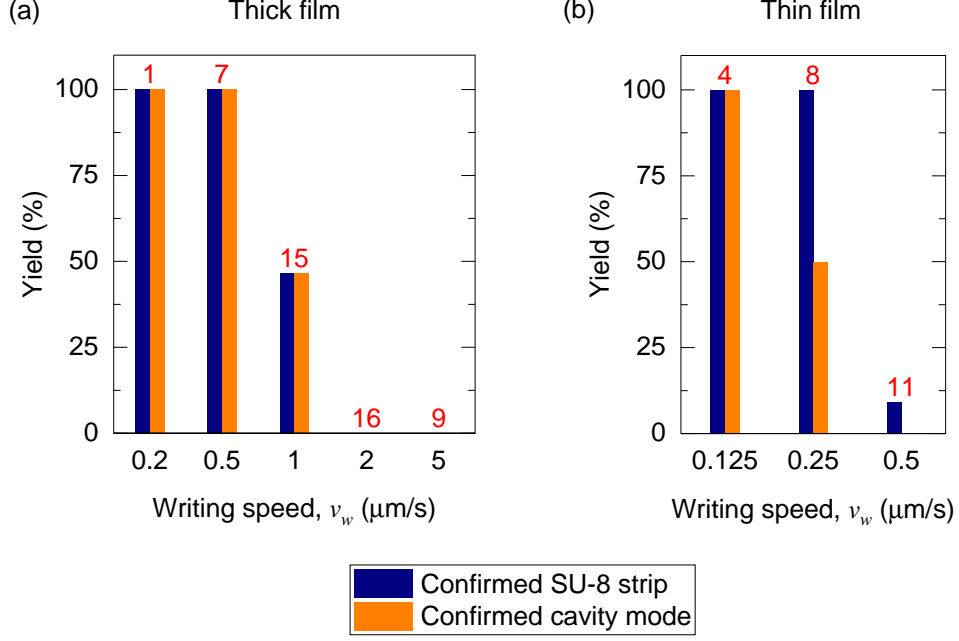


Figure 5.12: Yields of devices with successfully written SU-8 strips (blue) and with confirmed cavity modes after writing the strip (orange), categorised by film thickness and writing speed, v_w . Yields for regions of the sample identified to have thick SU-8 film (a) or thin SU-8 film (b) are shown separately. The red number at the top of each bar shows the number of devices attempted.

confirmed cavity mode is determined by comparing μPL mapping measurements of the waveguide before and after writing the strip, which is expanded on in section 5.3.2. We see that for a given film thickness, the yield tends to increase as v_w is reduced, which is to be expected, since a slower writing speed results in a higher exposure dose. Comparing the yield for thick film in Fig. 5.12(a) to that of the thin film in 5.12(b), it is evident that the thin film requires a slower writing speed of $v_w \lesssim 0.25 \mu\text{m s}^{-1}$ to obtain a reliable (close to 100%) yield of successful SU-8 strips, whereas strips can be reliably written in thick film with speeds up to $\sim 0.5 \mu\text{m s}^{-1}$. Overall, we found that 82% of the devices with a successfully written SU-8 strip supported a new, localized cavity mode at the strip position, which is a reasonably high success rate for the technique.

A consideration of similar importance to the fabrication yield is the effect of film thickness and writing speed on the height of the fabricated SU-8 strips, particularly as a thin strip is expected to be critical to achieving a high Q factor cavity mode. In Fig. 5.13, the mean strip height, \overline{H} , is plotted for selected SU-8 strip devices (see section 5.3.2 for the selection criteria) as a function of v_w and categorised by the predicted film thickness. It should be noted that some data points were obtained from 1 or 2 devices, so conclusions made from this data should be treated with due caution. The number of devices measured is labelled on each data point for transparency. Where possible, error bars are plotted to show the standard error of \overline{H} . Two intuitive observations

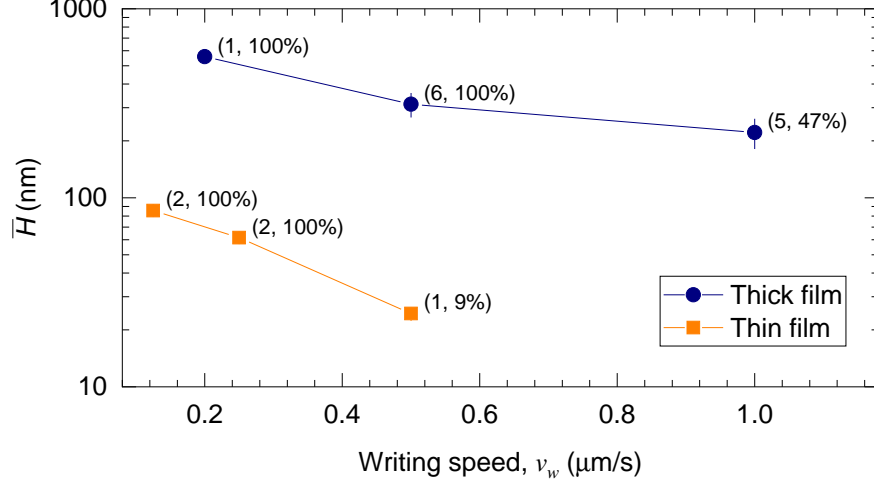


Figure 5.13: Mean strip height, \bar{H} , measured via AFM profiling of selected devices fabricated with different writing speed and film thickness. Each data point is annotated with the number of devices measured and the percentage yield of successfully written strips under the given parameters.

are immediately apparent: firstly, for a given v_w , \bar{H} is much smaller for strips written in thin film than those written in thick film; secondly, \bar{H} decreases as v_w is increased due to a lower exposure dose. We see that sub-100 nm-thick strips were achieved by writing in thin film, and that strips with heights in the range 60–90 nm were reliably fabricated with 100% yields (shown in brackets next to each data point). Thinner strips than this can be produced by increasing v_w , but we see from the results that this comes at the cost of a much lower yield. Strips as thin as ~ 300 nm could be written reliably in thick film without sacrificing the yield, which, while not as thin as the ~ 100 nm target height, is still capable of creating cavity modes with a moderate Q factor, as shown in section 5.3.2. The ability to write cavities with sufficient parameters for coupling in thick film is potentially very useful, as spin-coating a layer of thick SU-8 film over the PhC devices is significantly less challenging than obtaining a thin film.

Overall, the sensitivity of the strip height to v_w and the film thickness apparent from Fig. 5.13 highlights the importance of controlling the exposure dose based on the SU-8 film thickness, in order to achieve both a reliable yield and the desired strip thickness. This is arguably the most significant challenge in the fabrication process of SU-8-defined cavities. An exposure calibration chart to use as a guide for writing SU-8 strips can be found in appendix A, which is intended to help address this challenge.

It should be noted that some regions of the sample did not have consistent coverage by the SU-8 coat that could easily be categorised as either the thick or thin film presented in Fig. 5.9. In some parts of the sample, the SU-8 film varied significantly in thickness over short distances ($\sim 10 \mu\text{m}$)

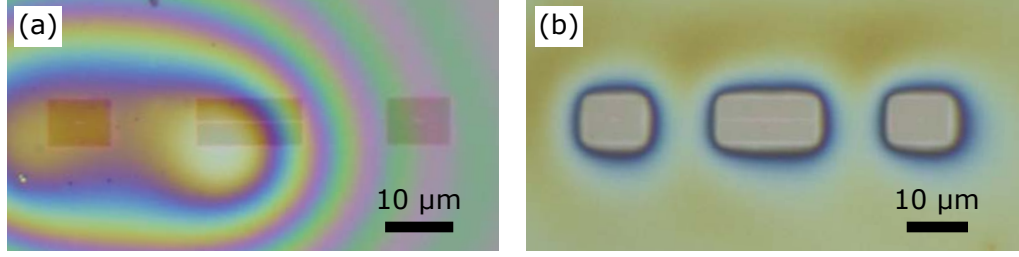


Figure 5.14: Optical microscope images of devices with inconsistent SU-8 film coverage. (a) A device coated with SU-8 film which varies significantly in thickness over its extent. (b) A device for which the film has not wet the PhC membranes, resulting in no SU-8 coverage over the PhC waveguide.

or did not coat the PhC devices at all. Examples of inconsistent SU-8 film coverage are shown by the optical microscope images of devices in Fig. 5.14. In Fig. 5.14(a), the film is predicted to vary drastically in thickness over the device, as indicated by the presence of many different coloured fringes. The image in Fig. 5.14(b) shows an example from the first unsuccessful coat (with an 8:1 ratio of cyclopentanone to SU-8 2007), in which the SU-8 film did not wet the PhC membrane at all. Devices with SU-8 coverage similar to the examples in Fig. 5.14 or which could not clearly be categorised as thick or thin film (as in Fig. 5.9) were excluded from the investigation.

Similar SU-8 film coverage problems to those reported here have been investigated by collaborator L. Nuttall in his thesis [1], but have proven a significant challenge to overcome. Inconsistent SU-8 film coverage over regions of the sample has a detrimental effect on the yield of successful devices, which is potentially problematic for applying the technique to coupling experiments. This issue might be solved by further optimisation of the spin-coating process, such as pre-treatment of the sample to improve SU-8 adhesion. Another solution might be to spin-coat onto larger chips than the $\sim 5 \times 5$ mm samples used in this work, which would likely result in a coat with a more even thickness distribution due to a reduced influence from the edges of the chip. Pre-treatment of the sample surface with an oxygen plasma ash before spin-coating was attempted on other samples, but this did not show any evidence of improving the wetting of the SU-8 to the PhC waveguide devices. Further optimisation work would be recommended to improve the process, but for the purposes of testing SU-8 defined cavities, the current procedure was sufficient.

5.3.2 Micro-photoluminescence mapping and characterisation

The fabricated batch of SU-8 strip cavity devices was characterised using the 1D μ PL mapping technique applied to the SU-8 disk cavities in Ch. 4. Mapping measurements along the PhC

waveguide were carried out both before and after writing the SU-8 strip on each device, using HeNe laser excitation with a power of $\sim 10 \mu\text{W}$ after the objective. A step size of $0.2 \mu\text{m}$ was used for mapping, with an acquisition time of 0.5 s . The sample was maintained at a temperature of $\sim 8 \text{ K}$.

Examples of μPL maps taken before and after writing the strip for three devices are presented in Fig. 5.15. The maps shown in Figs. 5.15(a), 5.15(b), 5.15(c) and 5.15(d) are before and after maps for the same devices A and B previously identified in section 5.3.1 (see Fig. 5.10). For both of these devices we see clear evidence of an isolated, well-localized cavity mode (labelled M1) generated after writing the strip, confirming that a successful SU-8 strip cavity has been fabricated. Additional μPL measurements were taken to measure the Q factor of each cavity mode, using the same method as for the SU-8 disk cavities. These Q factor measurements were performed using the 1200 lines/mm grating (slit width $20 \mu\text{m}$) with an acquisition time of 10 s . For device A (strip height $H = 350 \text{ nm}$), a Q factor of 4200 was measured and for device B, which has a thinner SU-8 strip ($H = 80 \text{ nm}$), a higher Q of 8300 was measured. Some devices were also found to support a second order cavity mode, which for typical mode-gap cavities is double-peaked [86]. This was the case for device C, for which before and after μPL maps are shown in Figs. 5.15(e) and 5.15(f). The ground mode, M1 and a second order mode M2, are generated by the presence of the strip, which had a height $H = 560 \text{ nm}$. The Q factor of the M1 mode was measured to be 3300 for this thick strip. Note that all μPL measurements of the devices were performed before AFM measurements.

The AFM profiling techniques detailed in section 5.3.1 were applied to a selected sample of SU-8 strip cavities with confirmed cavity modes. From a total of 23 devices which were concluded to support cavity modes, 16 were selected for measurement. Of the excluded devices, 3 were omitted due to contamination of, or damage to, the PhCs that occurred after the μPL measurements were performed; the other 4 were omitted because it was not as clear that new cavity modes had been generated as for the other devices. In Fig. 5.16, we plot the measured Q and wavelength, λ_0 , of the M1 cavity mode against H for all the selected devices. A strong negative correlation between Q and H is observed in Fig. 5.16(a), as expected from the simulation results presented in section 5.2. The values of H varied between $60\text{--}560 \text{ nm}$, with the highest and lowest Q of 8700 and 3300 recorded for devices with $H = 110 \text{ nm}$ and $H = 560 \text{ nm}$ (device C), respectively. In general, high Q modes exceeding the maximum $Q \sim 7000$ measured from the SU-8 disk cavities were measured from devices with $H \lesssim 100 \text{ nm}$. The higher Q measured from the SU-8 strip devices is expected to result from the improved cavity design, which has less stringent alignment requirements than the

SU-8 disk defined cavity (as discussed in section 5.1) and thus can be fabricated more consistently. It should be noted, however, that the cavity modes generated by the SU-8 strips were ~ 20 nm longer in wavelength than those generated by the SU-8 disks, which we attribute to differences in the PhC etching between the two samples (the modes of the reference L3 cavities confirmed this). The SU-8 strip cavity modes are therefore spectrally further away from the centre of the

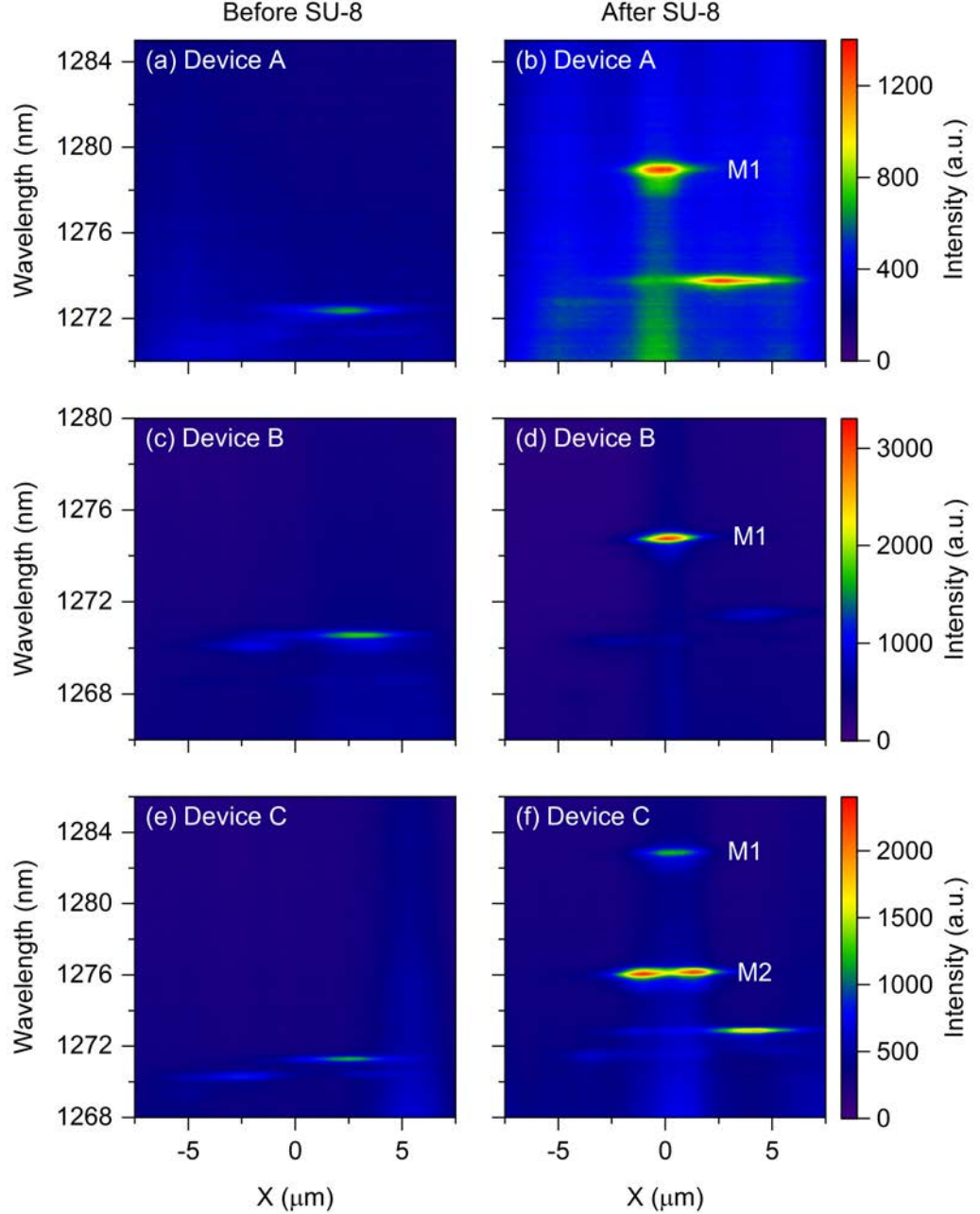


Figure 5.15: 1D μ PL maps of three selected devices (along the waveguide) taken before and after writing an SU-8 strip on the PhC waveguide. (a), (c) and (e): maps of devices A, B, and C before applying SU-8. (b), (d) and (f): maps of devices A, B, and C after writing SU-8 strips. The intensity scale is shown beside the corresponding map (in arbitrary units); all maps use the same position (X) scale.

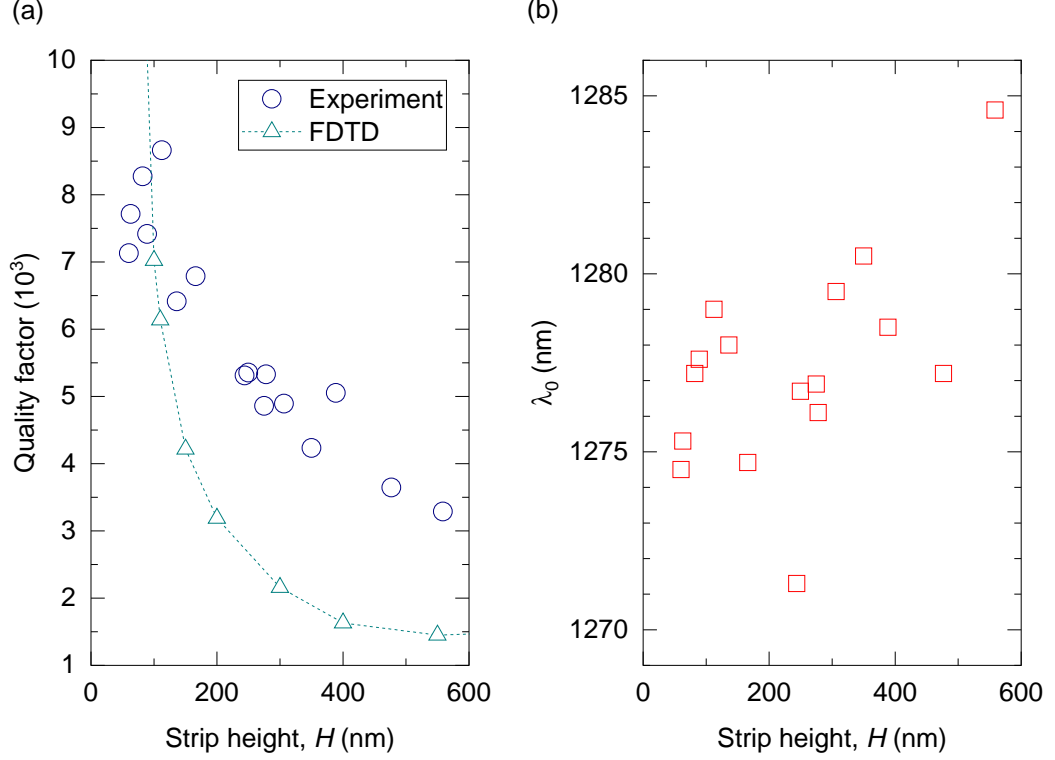


Figure 5.16: Parameters extracted from the selected sample of 16 successful SU-8 strip cavities. (a) Measured Q factor (blue circles) of the M1 mode as a function of H and predicted Q from FDTD simulation results (dark cyan triangles) for an SU-8 strip cavity with $w_{\text{strip}} = 1 \mu\text{m}$ and $h_{\text{strip}} = H$. (b) Measured λ_0 of the M1 cavity mode.

QD ensemble emission, which may increase the observed Q due to reduced reabsorption by the QD ensemble [208]. Further investigation would be required to quantify the contribution of this effect, but it is likely that the performance of the SU-8 strip cavities is at least as favourable as the SU-8 disk cavities.

The Q factors of the fabricated SU-8 strip cavities also compare favourably to other types of mode gap cavities formed from material deposited onto a PhC waveguide. The Q factor of ~ 3000 reported for a carbonaceous nano-block deposited on a PhC waveguide [88] and the $Q \sim 4300$ for a PMMA strip deposited perpendicular to the waveguide [89] are exceeded by the majority of the fabricated SU-8 strip cavity devices. The SU-8 strip cavity Q factors are also comparable to the typical range of 6000–7000 reported by Brossard *et al.* [99] for similar cavity structures formed by inkjet-printing strips of sub-100 nm thickness on a PhC waveguide.

The measured Q factors of the experimentally realised devices exhibit some notable discrepancies from the values expected from FDTD simulations, which are also plotted in Fig. 5.16(a). The simulation results shown are the Q_{total} obtained from a device with $w_{\text{strip}} = 1 \mu\text{m}$ and a height

$h_{\text{strip}} = H$. For moderately thick strips with $H > 200$ nm, the experimentally achieved Q is actually higher than the Q predicted from the FDTD simulation results. This is of course a positive result, as it means that moderately high Q cavities can be created from thick strips, which are less challenging to fabricate. For example, as noted in section 5.3.1, strips with $H \sim 300$ nm were reliably fabricated in thick SU-8 film (400–1000 nm thickness) – these devices were found to have $Q \sim 5000$, which is considerably higher than the $Q \sim 2200$ predicted theoretically. The cause of the discrepancy between the simulated and experimentally obtained Q factors is not certain, but is likely to be due to differences in the geometry of the strip and/or PhC between the simulated device and actual device. In section 5.3.4, a device is simulated with a more realistic SU-8 strip profile to investigate this further.

It is clear that the Q of the SU-8 strip cavities is limited for thin strips, as it does not reach the values exceeding 10^4 predicted for $H < 100$ nm. We attribute this to fabrication limitations of the PhC devices etched into the wafer, for example due to hole roughness or tapering. Most examples of PhC cavities etched into GaAs wafers (with embedded self-assembled QD layers) reported in the literature exhibit typical Q factors in the range $\sim 10,000 - 15,000$ [19, 20, 66, 69, 86] or lower, despite the cavity designs having much higher theoretical Q factors than this. Q factors which are much closer to the ultrahigh theoretical values are possible in PhC cavities etched in Si [33, 48, 91] or GaAs wafers without QD layers [209]. In order to verify that the wafer was the limiting factor, Q measurements were performed on 18 of the reference L3 cavities distributed across the surface of the sample. The results, presented in Fig. 5.17(a), gave a mean Q of 5200 and a maximum of 6600 – significantly lower than the theoretical $Q_{\text{total}} \sim 10^5$ predicted for the cavity design from FDTD simulation results (see section 2.4.3.4).

We now consider the suitability of the fabricated SU-8 strip cavities for coupling applications, which ideally requires a high Q , small V_0 and consistent cavity mode properties between devices. The wavelength of the fundamental cavity mode from each device, λ_0 , is shown in Fig. 5.16(b), as a function of the strip thickness. A weak positive correlation between λ_0 and H is suggested, which is consistent with predictions from FDTD simulations (see section 5.2). Evidently, it will be important to achieve consistent strip thickness for practical applications in order to minimise the variation of λ_0 from one device to another. The results suggest that, for a given H , λ_0 can typically be expected to be within a range of ~ 5 nm. This variation is likely to negatively impact the success rate of coupling an SU-8 strip cavity to a QD, as the range of wavelengths is larger than the ~ 1 nm temperature tuning range of a single QD (see section 3.8.4). However, we believe that

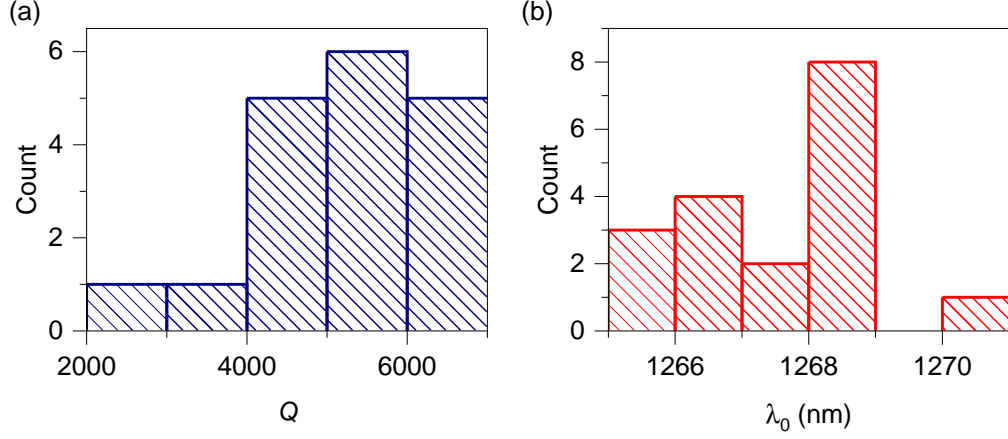


Figure 5.17: Measured Q factors (a) and mode wavelength, λ_0 (b), of 18 reference L3 cavities distributed across the surface of the sample that the SU-8 strip devices were fabricated on.

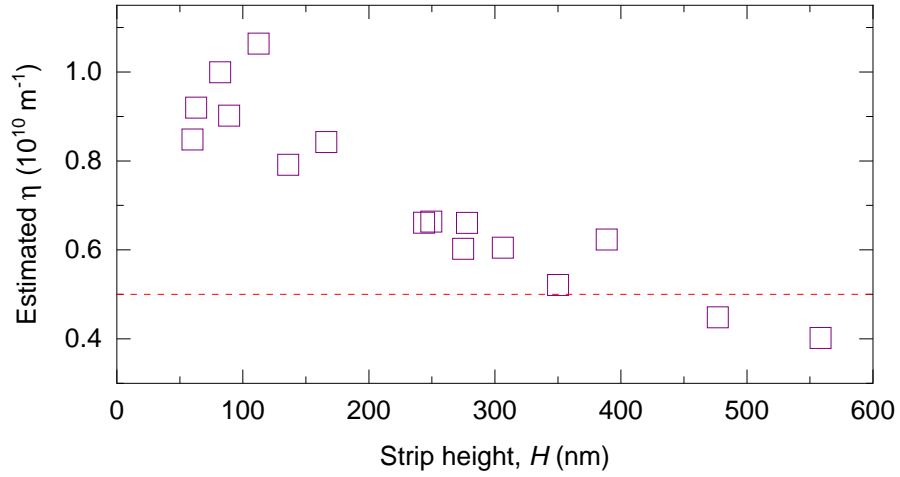


Figure 5.18: Estimated value of η , the strong coupling figure of merit, for the selected SU-8 strip cavity devices, as a function of their strip height, H . The dashed red line indicates the estimated theoretical value of η required for the onset of the strong coupling regime.

the magnitude of the variation is not so unacceptably large as to make the technique unviable. For comparison, we examined the wavelength of the same 18 reference L3 cavity modes that Q factors were recorded from; the results are shown in Fig. 5.17(b). These L3 cavity modes also exhibit a significant variation in wavelength, likely due to fabrication imperfections. The full range of λ_0 for the measured L3 cavities was 5.3 nm and the interquartile range, which likely gives a better representation of the typical spread of λ_0 , was 2.2 nm. It is promising that the range of λ_0 exhibited by the SU-8 strip cavities (provided the strip height is consistent) is not drastically wider than that of the L3 cavities, which are typical candidates for strong coupling experiments [19, 20, 66].

Finally, we consider the suitability of the SU-8 strip cavities for strong coupling experiments, by

estimating the strong coupling figure of merit, η , discussed in section 3.6. In this section it was predicted that, if the cavity mode is well-aligned with a single QD, the onset of strong coupling is expected to occur for $\eta \gtrsim 5 \times 10^9 \text{ m}^{-1}$ and that a value of $\eta \sim 10^{10} \text{ m}^{-1}$ should be targeted to match PhC cavity devices for which strong coupling has been achieved in the literature. For each of the 16 measured devices, we computed an estimate of η (Eq. 3.16). This was calculated using the measured values of Q and λ_0 , together with an estimate of V_0 obtained by extrapolating the simulation results in Fig. 5.5 to the relevant strip height. $n = 3.33$ was used for the refractive index. The calculated values are presented in Fig. 5.18, in which we see that the target $\eta \sim 10^{10} \text{ m}^{-1}$ is achieved for a strip height $H \lesssim 100 \text{ nm}$. Therefore, if we target this strip thickness and successfully achieve good spectral and spatial overlap between the cavity mode and a QD, the strong coupling regime should be possible. Taking the theoretical minimum $\eta \gtrsim 5 \times 10^9 \text{ m}^{-1}$, the results suggest that strong coupling may even be possible for thicker strips up to 300 – 400 nm. Whether this could be observed in practice is questionable, but such thicknesses would certainly be acceptable for achieving Purcell-enhanced emission from a QD: the theoretical maximum Purcell factor for a cavity with $Q = 5000$ and $V = 1.33 (\lambda/n)^3$ (estimated for $H = 300 \text{ nm}$) is ~ 290 .

5.3.3 Focus on a high Q device

We now focus on device B, one of the highest Q (8300) SU-8 strip cavities fabricated. An AFM image of this device is presented in Fig. 5.19, showing the high uniformity of the strip across the PhC, which has a height $H = 80 \text{ nm}$ (the height profile of this strip was presented in Fig. 5.10). In this section we first present time-resolved μPL (TRPL) measurements of the device to show that the spontaneous emission rate of the QD ensemble is altered by the cavity mode. This is compared to an L3 cavity as a reference. Finally, FDTD simulations are performed of an SU-8 strip cavity with a strip profile matching that of device B, to investigate the performance differences between this realistic strip shape and the simplified cuboidal strips used in the other simulations.

5.3.3.1 Time-resolved measurements

TRPL measurements of device B were performed using the experimental apparatus detailed in section 3.8.5 and the Ti:S pulsed laser (section 3.8.1) to provide excitation (with a power of $\sim 8 \mu\text{W}$ after the objective). Measurements were performed with the objective position optimised over the relevant cavity mode. The spectral filtering provided by the spectrometer (FWHM $\sim 0.7 \text{ nm}$)

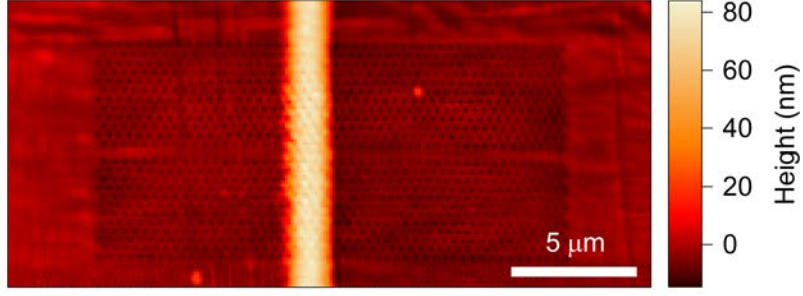


Figure 5.19: AFM image of device B, an SU-8 strip cavity with $H = 80$ nm and $Q = 8300$.

was tuned by moving the grating to position the centre wavelength of the filtering window, λ_c , either at λ_0 , the wavelength of the SU-8 strip cavity mode, or ± 2 nm either side of λ_0 . The results, presented in Fig. 5.20, clearly show a slower radiative decay rate for QDs which are off-resonance compared to those which are resonant with the cavity mode, which verifies that the SU-8 strip cavity is able to alter the spontaneous emission rate of the QDs. Each of the TRPL traces is fitted with a mono-exponential decay, convolved with the IRF of the detector, in order to estimate the radiative lifetime. Relatively good consistency is found between the two off-resonant measurements, which exhibit radiative lifetimes of $\tau_R(\lambda_0 - 2 \text{ nm}) = (364 \pm 9) \text{ ps}$ and $\tau_R(\lambda_0 + 2 \text{ nm}) = (307 \pm 8) \text{ ps}$. In comparison, the lifetime measured from QDs resonant with the cavity mode was $\tau_R(\lambda_0) = (162 \pm 2) \text{ ps}$.

In order to find an estimate of the Purcell factor (defined in section 3.3.2), the radiative lifetime of the on-resonant QDs needs to be compared to QDs which can be approximated as emitting into free-space. We therefore need measure the lifetime of QDs in the wafer which are not embedded in a PhC, since the modification to the optical density of states by the PhC typically inhibits the spontaneous emission rate of (off-resonant) QDs, resulting in longer radiative lifetimes [210, 211]. Using a similar TRPL measurement technique, but instead exciting the QD ensemble in an off-cavity location with no etched PhCs, the radiative lifetime of the QD ensemble at $\lambda_c = \lambda_0$ was found to be $\tau_{oc} \sim 260 \text{ ps}$. This gives an estimated Purcell factor of $F_P = \tau_{oc}/\tau_R \sim 1.6$.

For comparison to the SU-8 strip cavity device, TRPL measurements were also performed on one of the reference L3 cavities forming part of device B. The fundamental L3 cavity mode investigated had $Q = 5900$ and $\lambda_0 = 1273.7 \text{ nm}$. As for the SU-8 strip cavity, measurements were obtained by optimising over the L3 cavity mode and moving the spectral filter position to either the cavity mode resonance or 2 nm either side of it. The resulting traces, along with the appropriate mono-

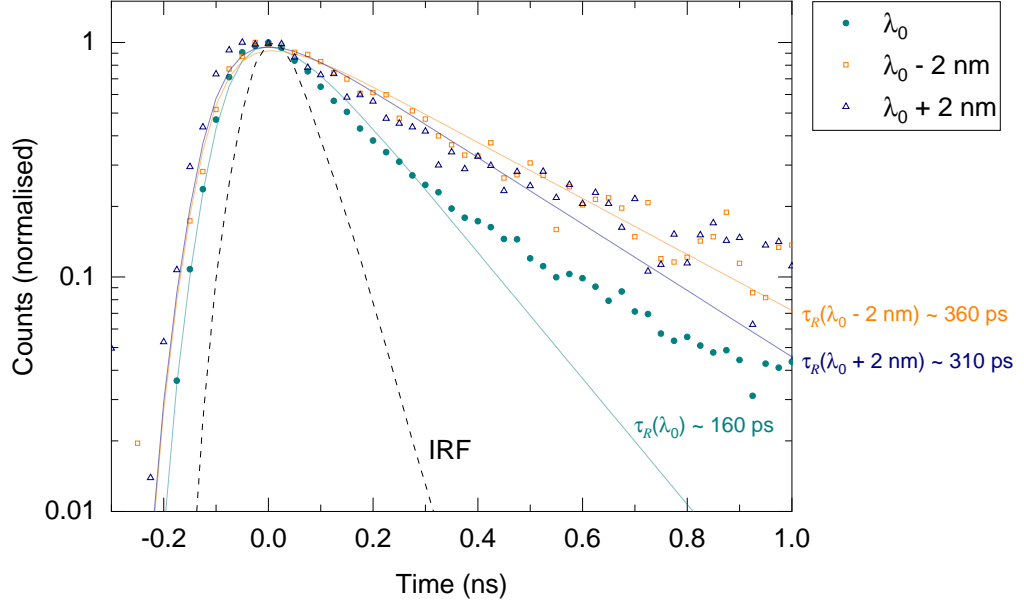


Figure 5.20: TRPL results from device B, showing TRPL traces and mono-exponential fits (convolved with the detector IRF) for collection on and off resonance with the cavity mode, λ_0 . The TRPL trace is shown by unconnected symbols, according to the legend; the fits are shown by the corresponding coloured lines, with radiative lifetimes marked by text of the same colour. The legend denotes the value of λ_c , the wavelength that the centre of the spectral filter was set to. The IRF of the detector is shown by the dashed black line.

exponential fit (convolved with the IRF), for collection filtered at $\lambda_c = \lambda_0$ and $\lambda_c = \lambda_0 + 2 \text{ nm}$ are shown in Fig. 5.21. For $\lambda_c = \lambda_0$, we find a radiative lifetime $\tau_R(\lambda_0) = (188 \pm 2) \text{ ps}$ and for $\lambda_c = \lambda_0 + 2 \text{ nm}$ we find a radiative lifetime $\tau_R(\lambda_0 + 2 \text{ nm}) = (347 \pm 5) \text{ ps}$. Note that for $\lambda_c = \lambda_0 - 2 \text{ nm}$ (not shown) a radiative lifetime of $(353 \pm 4) \text{ ps}$ was found, consistent with $\tau_R(\lambda_0 + 2 \text{ nm})$. Also shown in Fig. 5.21 is the TRPL trace and fit obtained from the QD ensemble, at an off-cavity (and off-PhC) position near device B with the filter set to $\lambda_c = \lambda_0$, which gave a radiative lifetime $\tau_{oc} = (309 \pm 5) \text{ ps}$. We therefore derive a Purcell factor of $F_P \sim 1.6$ for the L3 cavity mode, demonstrating that the SU-8 strip cavity offers similar performance to the well-established L3 cavity design in this regard.

For both the L3 and SU-8 strip cavities, Purcell enhancement of the QD ensemble has been demonstrated at the cavity mode resonance, likely resulting from many QDs weakly coupled to the cavity mode. The relatively low magnitude of the estimated Purcell factor (~ 1.6) is unsurprising given the limitations of the measurement. Most notably, measurement of the Purcell factor from an ensemble of QDs is typically limited by the varying degrees of coupling between the QDs and the cavity mode [212]. Typically, for a high density ensemble of QDs coupled to a cavity

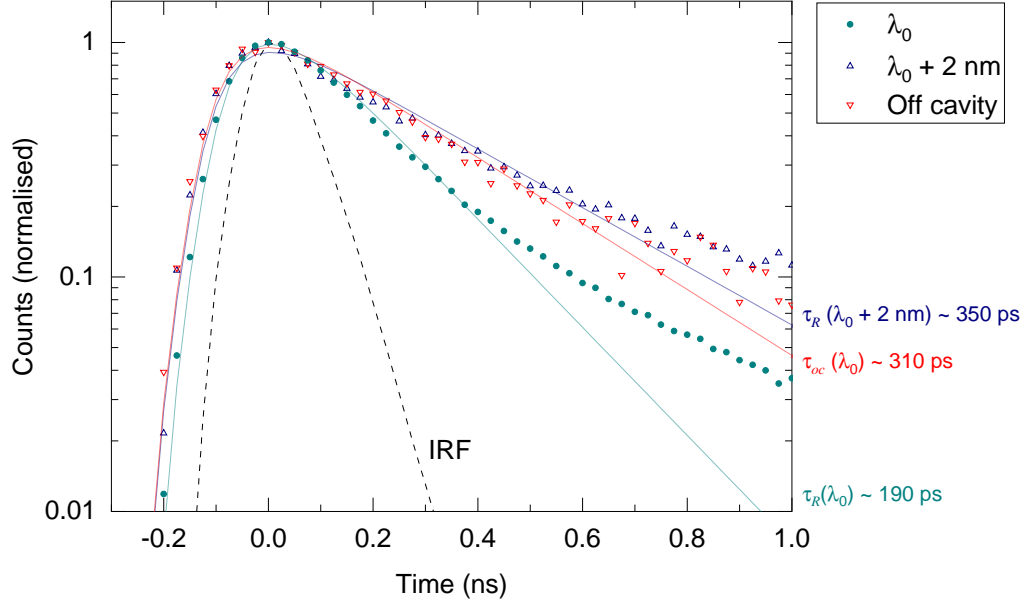


Figure 5.21: TRPL results from an L3 cavity from device B. TRPL traces and fits are shown for collection on resonance with the cavity mode (λ_0), off-resonance with the cavity mode while positioned over the cavity ($\lambda_0 + 2$ nm), and from the QD ensemble at an off-cavity location. The TRPL trace is shown by unconnected symbols, according to the legend; the fits are shown by the corresponding coloured lines, with radiative lifetimes marked by text of the same colour. The IRF of the detector is shown by the dashed black line.

mode, Purcell factors in the range ~ 2 – 5 have been reported in the literature [136, 212, 213, 214]; Purcell factors greater than this have been observed from single QDs weakly coupled to PhC cavity modes [80, 168, 182, 211]. We believe that the value of ~ 1.6 obtained for the Purcell factor here, which is slightly lower than the typical values found in the literature for a QD ensemble, was limited by background emission from uncoupled QDs. The width of the spectral filter window (FWHM ~ 0.7 nm) was considerably wider than the FWHM of the cavity mode ($\lesssim 0.2$ nm), which likely resulted in a significant proportion of light being collected from the uncoupled QD background. This is perhaps evident from the shape of the TRPL trace for $\lambda_c = \lambda_0$ (for either cavity), for which a mono-exponential decay does not provide a complete fit and it is likely that the decay is bi-exponential. We suggest that the longer-lived component of this decay is due to the contribution of the uncoupled QD background. We note that the mono-exponential decay does provide a good fit to the faster component of the decay, so we believe it is sufficient for the purpose of estimating the Purcell factor. If the spectral filter window was made narrower, a shorter radiative lifetime might be observed from QDs on resonance with the cavity mode. However, such a short lifetime may approach the resolution limit of the detector, which has an IRF with a FWHM of ~ 130 ps. Issues concerning the resolution limit could be avoided by studying QDs emitting closer to the

centre of the ensemble (~ 1220 nm) which were found to have a much longer radiative lifetime of ~ 1 ns.

5.3.4 FDTD simulations of a more realistic strip

In order to investigate the effect of subtle differences in the SU-8 strip geometry, FDTD simulations were performed of an SU-8 strip device with a more realistic strip profile. The inverse polynomial fit to the SU-8 strip profile of device B (obtained via AFM techniques), shown in figure 5.10(b), was used as an approximation of the strip cross-section. This shape was extruded along the y -direction of the PhC to produce a more realistic strip than the simplified cuboidal strips used in other simulations in this work. A slice through the simulated structure at $y = 0$ is shown in Fig. 5.22, which visualizes the refractive index. The strip profile is defined by the inverse polynomial peak function given in Eq. 5.1, with parameters $H = 82$ nm, $A_1 = 0.641$, $A_2 = -0.808$, $A_3 = 0.944$ and $w = 1.32$ μm .

Parameters extracted from the fundamental cavity mode are presented in table 5.3, along with simulation results from a simplified cuboidal SU-8 strip cavity for comparison. The geometry of the cuboidal strip was set to $h_{\text{strip}} = 80$ nm and $w_{\text{strip}} = 1.3$ μm to correspond to the height and FWHM of the more realistic strip profile. Both sets of results are presented for simulations performed with mesh resolution parameters $\rho_{xy} = 30$ and $\rho_z = 40$ (defined in section 2.2.4). Convergence testing (following a similar method to that laid out in section 2.5.4) performed on the realistic SU-8 strip cavity suggests that all parameters presented in table 5.3, except for Q_{out} , are accurate to within $\sim 5\%$. The value of Q_{out} is predicted to be accurate within 17%; the poorer convergence is attributed to the high magnitude of Q_{out} , which is more sensitive to the mesh resolution. Similar sensitivity was found for the high Q WMLD cavity in section 2.5.4.

Examining the simulation results in table 5.3, we see that the fundamental mode of the cavity with a more realistic SU-8 strip profile exhibits a higher Q_{total} than the simplified geometry. The results

| Strip type | λ_0 (nm) | Q_{total} | Q_{in} | Q_{out} | $V_0 [(\lambda_0/n)^3]$ |
|------------|------------------|--------------------|-----------------|-------------------|-------------------------|
| Realistic | 1274.0 | 14, 500 | 15, 200 | 3.2×10^5 | 1.44 |
| Cuboid | 1273.1 | 9400 | 10, 800 | 7.4×10^4 | 1.36 |

Table 5.3: Comparison of the simulated parameters of the fundamental cavity mode, extracted from an SU-8 strip defined cavity with a more realistic strip profile (extracted from device B) or a simplified cuboidal strip with $h_{\text{strip}} = 80$ nm and $w_{\text{strip}} = 1.3$ μm .

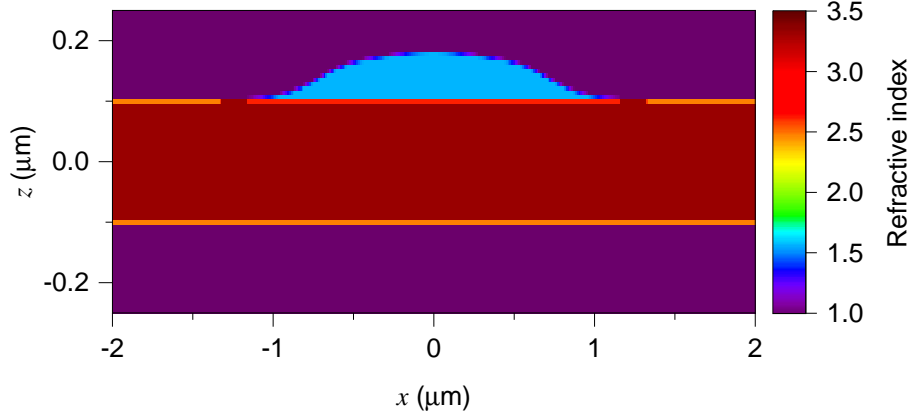


Figure 5.22: Refractive index profile in the $y = 0$ plane of the more realistic simulated SU-8 strip cavity, with a strip geometry obtained from profile averaging of device B.

show that the V_0 of the more realistic strip is larger, likely due to a wider mode gap potential, but the increased Q_{total} results in a higher $Q_{\text{total}}/V_0 = 1.0 \times 10^4 (n/\lambda_0)^3$, $\eta = 1.7 \times 10^{10} \text{ m}^{-1}$ for the realistic cavity compared to $Q_{\text{total}}/V_0 = 6900 (n/\lambda_0)^3$, $\eta = 1.2 \times 10^{10} \text{ m}^{-1}$ for the simplified geometry. The results therefore suggest that a more realistic cavity geometry is better suited for coupling experiments. The subtle differences in the strip geometry responsible for the higher Q_{total} in this example may go towards explaining the higher-than-predicted Q of the fabricated devices in Fig. 5.16.

We note that the $Q = 8300$ measured from the actual cavity of device B does not reach either of the simulated values of Q_{total} presented in table 5.3. We attribute this predominantly to the limitations of the wafer discussed in section 5.3.2, but differences between the theoretical and actual geometry are also expected to play a role. Firstly, the actual PhC had target lattice parameters $a = 320 \text{ nm}$, $r/a = 0.25a$, which differ from the simulated $a = 340 \text{ nm}$, $r/a = 0.27a$. Secondly, the inverse polynomial profile used does not capture the complete geometry of the real strip, shown in Fig. 5.19. Simulating a more detailed strip – which would be much more computationally demanding due to removal of the symmetry planes – might be of interest for subsequent work, but is deemed beyond the scope of this project.

5.4 Varying the strip width: simulation results

Having successfully demonstrated SU-8 strip cavities in section 5.3, we now investigate the effects of altering the strip width. In particular, we focus on increasing the strip width to widen the mode gap confinement potential. This is feasible experimentally either by writing multiple closely spaced

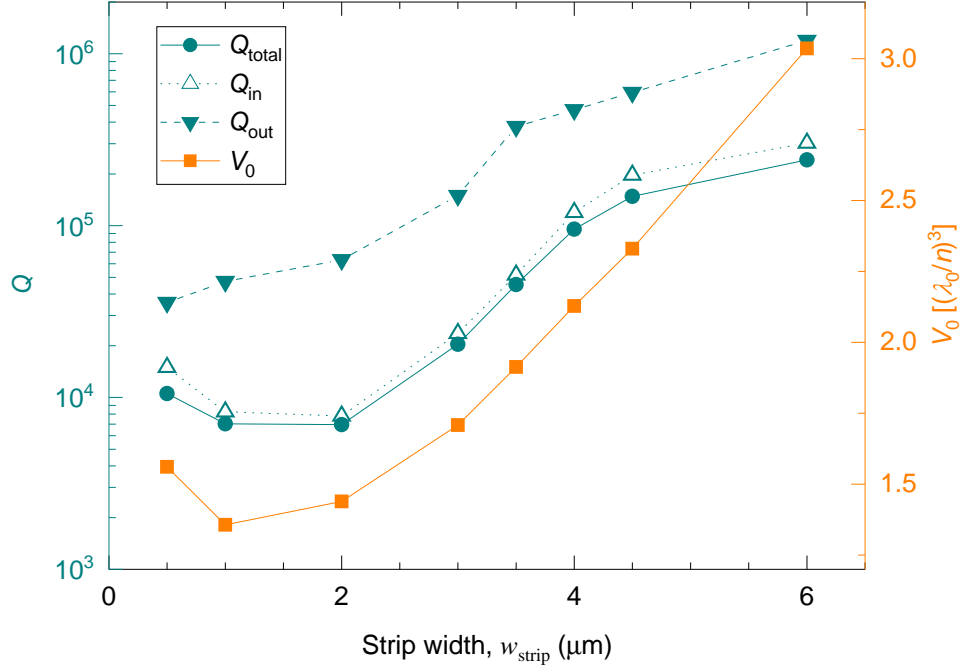


Figure 5.23: FDTD simulation results for SU-8 strip cavities with $h_{\text{strip}} = 100 \text{ nm}$ and variable w_{strip} . Q factor components and the mode volume of the fundamental cavity mode are shown.

strips, as will be shown in section 5.5, or by using a larger laser spot diameter for writing single strips. Increasing the cavity width has been shown to increase the Q factor of comparable mode gap cavity designs [90, 95]; the work presented here aimed to achieve a similar beneficial effect for the SU-8 strip cavity design.

We first consider the effects of varying the strip width, w_{strip} , while keeping the strip height $h_{\text{strip}} = 100 \text{ nm}$ constant. FDTD simulations were performed with w_{strip} ranging from $0.5 \mu\text{m}$ to $6 \mu\text{m}$; the parameters extracted from the fundamental cavity mode are presented in Fig. 5.23. As the strip width is increased beyond $\sim 2 \mu\text{m}$, Q_{total} increases by up to approximately an order of magnitude, while V_0 increases by only a factor of ~ 2 over the range of w_{strip} simulated. This suggests that cavities defined by a wider SU-8 strip could be preferable for QD-cavity coupling applications.

The Q_{total} of the SU-8 strip cavity mode, which is limited by in-plane TE-TM coupling losses (see section 2.6.3), shows an increase with w_{strip} that is reflected by an increase in Q_{in} . This suggests a reduction of the in-plane losses, which is understood by considering how the cavity mode field profile changes with w_{strip} . In Fig. 5.24, the $|\mathbf{E}|^2$ profiles for SU-8 strip cavities with $w_{\text{strip}} = 1 \mu\text{m}$ [Figs. 5.24(a) and 5.24(c)] and $w_{\text{strip}} = 4 \mu\text{m}$ [Figs. 5.24(b) and 5.24(d)] are compared

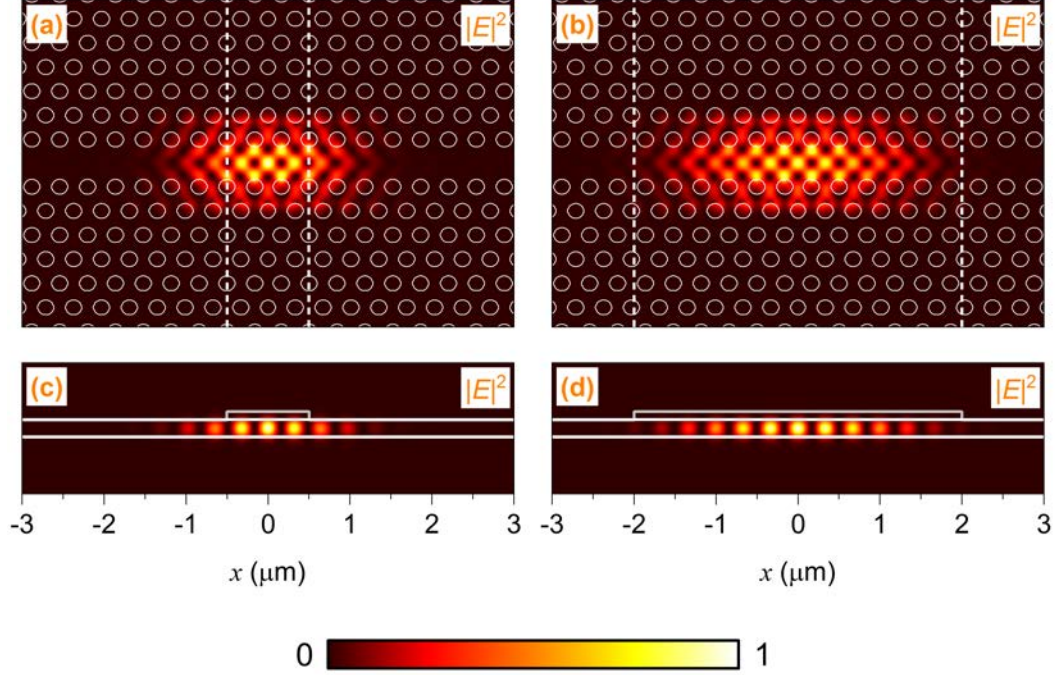


Figure 5.24: $|E|^2$ field profile extracted from FDTD simulations of SU-8 strip-defined PhC cavities with $h_{\text{strip}} = 100$ nm and different strip width, w_{strip} . (a) and (c): SU-8 strip with $w_{\text{strip}} = 1$ μm , shown through the planes $z = 0$ and $y = 0$. (b) and (d): SU-8 strip with $w_{\text{strip}} = 4$ μm , shown through the planes $z = 0$ and $y = 0$, respectively. Each profile shows the normalised intensity – the colour scale used is displayed at the bottom of the figure.

($h_{\text{strip}} = 100$ nm for both). Intuitively, the mode is more delocalized along the waveguide (x -direction) for the cavity defined by a wider strip, due to a wider mode gap confinement potential. This increased spatial delocalization of the mode appears to be responsible for the increased Q_{total} , which becomes apparent from analysis of the spatial Fourier components of the mode.

In Fig. 5.25, we consider the spatial Fourier transform of the main \mathbf{E} field components of the TE-like cavity mode, $|\text{FT}(E_x)| + |\text{FT}(E_y)|$, in the top plane of the slab ($z = z_{\text{slab}}/2$). This is compared for the cavity with $w_{\text{strip}} = 1$ μm [Fig. 5.25(a)] and the cavity with $w_{\text{strip}} = 4$ μm [Fig. 5.25(b)]. As explained in section 2.6.3, the dominant source of losses from the SU-8 strip cavity is due to coupling of the TE-like cavity mode to TM-like slab modes, which occurs along the TM contours marked on the diagrams by the dashed lines. Such coupling is facilitated by the broken z -symmetry of the structure, and is clearly evident for the 1 μm -wide strip by the significant field components along the TM contour. However, for the 4 μm -wide strip, the field components along the TM contours are much weaker. This appears to be due to the increased localization of the Fourier components along k_x , which is a result of the decreased spatial localization of the mode along the waveguide. We propose that this inhibits TE-TM coupling, since the field components of the TE-

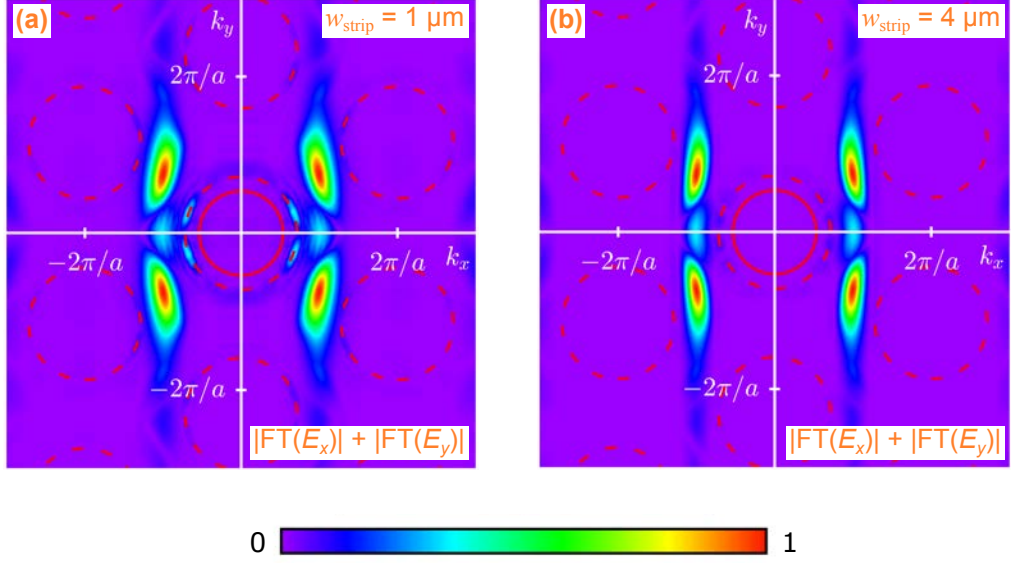


Figure 5.25: Spatial Fourier transform, $|FT(E_x)| + |FT(E_y)|$, extracted from FDTD simulations through the plane $z = z_{\text{slab}}/2$ for a device with (a) $w_{\text{strip}} = 1 \mu\text{m}$ and (b) $w_{\text{strip}} = 4 \mu\text{m}$. Both devices have $h_{\text{strip}} = 100 \text{ nm}$. The light cone is marked on as a solid red circle; contours of the TM-like slab mode are marked by dashed red lines. Each result is normalised.

like cavity mode overlap less with the TM contours. We therefore attribute the increase in Q_{total} with w_{strip} to a reduction in TE-TM coupling losses, resulting from the more localized Fourier components of the mode.

We note that an increase in Q_{total} is also observed as w_{strip} is reduced from $1 \mu\text{m}$ to $0.5 \mu\text{m}$. This is likely due to similar suppression of the TE-TM coupling losses as for wide strips, since it coincides with an increased V_0 (more spatially delocalized mode) and an increase of Q_{in} . This suggests that reducing the strip width may also be a method of increasing the Q/V_0 ratio, but in practice the width is limited by the spot diameter of the writing laser. Note that additional convergence testing was performed for $w_{\text{strip}} = 0.5 \mu\text{m}$ and $w_{\text{strip}} = 4.5 \mu\text{m}$ – good convergence was found in both cases. For the other simulations, convergence was assumed based on testing of the device with $w_{\text{strip}} = 1 \mu\text{m}$ presented in section 2.6.

For coupling applications, the Q_{total}/V_0 ratio and η of the cavity mode should be maximised, as discussed in section 3.3, for the weak coupling regime and strong coupling regime, respectively. These parameters are plotted in Fig. 5.26 for $h_{\text{strip}} = 100 \text{ nm}$ and variable w_{strip} , along with λ_0 , which is also important to control to achieve spectral resonance with a QD. The results confirm that, as long as the strip height is kept constant, it is possible to increase Q_{total}/V_0 and η simply by increasing the width of the SU-8 strip. Increasing the SU-8 strip width also results in a redshift

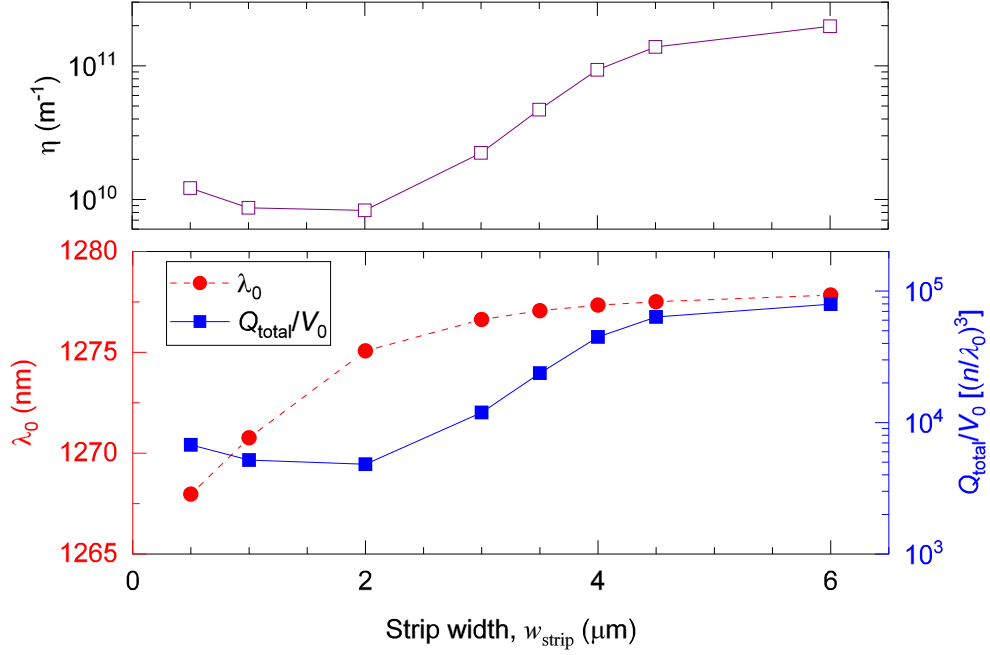


Figure 5.26: λ_0 , Q_{total}/V_0 and η of the fundamental cavity mode extracted from FDTD simulations of SU-8 strip cavities with $h_{\text{strip}} = 100$ nm and variable w_{strip} .

to the cavity mode, which could potentially be utilised as a method of tailoring the cavity mode into spectral resonance with a target QD. We explore this possibility in section 5.5.

The work presented so far on SU-8 disk and SU-8 strip cavities has shown that the height of the SU-8 structure on the PhC waveguide is critical to the Q factor and is challenging to control in practice, due to fluctuations in the SU-8 film thickness. It is therefore important to consider the effects of altering the strip height on a wider SU-8 strip cavity. FDTD simulations of a device with $w_{\text{strip}} = 4 \mu\text{m}$ and variable h_{strip} were performed, which we compare to results from an SU-8 strip cavity with $w_{\text{strip}} = 1 \mu\text{m}$ in Fig. 5.27. As for the $1 \mu\text{m}$ -wide strip, we see that the Q_{total} of the $4 \mu\text{m}$ -wide strip is drastically reduced as it is made thicker. We attribute this to an increase in the same TE-TM coupling loss mechanism as for the $1 \mu\text{m}$ -wide strip, since Q_{total} is again limited by Q_{in} (not shown). In Fig. 5.28 we plot the spatial Fourier components $|\text{FT}(E_x)| + |\text{FT}(E_y)|$ in the top plane of the slab ($z = z_{\text{slab}}/2$) for devices with thick strips ($h_{\text{strip}} = 400$ nm) of width $w_{\text{strip}} = 1 \mu\text{m}$ [5.28(a)] and $w_{\text{strip}} = 4 \mu\text{m}$ [5.28(b)]. In both cases, strong evidence of TE-TM coupling losses is demonstrated by the significant field components along the TM contours. This suggests that the spatial delocalization of the $w_{\text{strip}} = 4 \mu\text{m}$ cavity mode, which appeared to suppress the TE-TM coupling losses for the case of $h_{\text{strip}} = 100$ nm (see Fig. 5.25), is not sufficient to strongly suppress the TE-TM coupling losses as the strip is made thicker. Perhaps this is due to the TE-TM modes coupling more readily, as the z -symmetry is more severely broken by increasing h_{strip} .

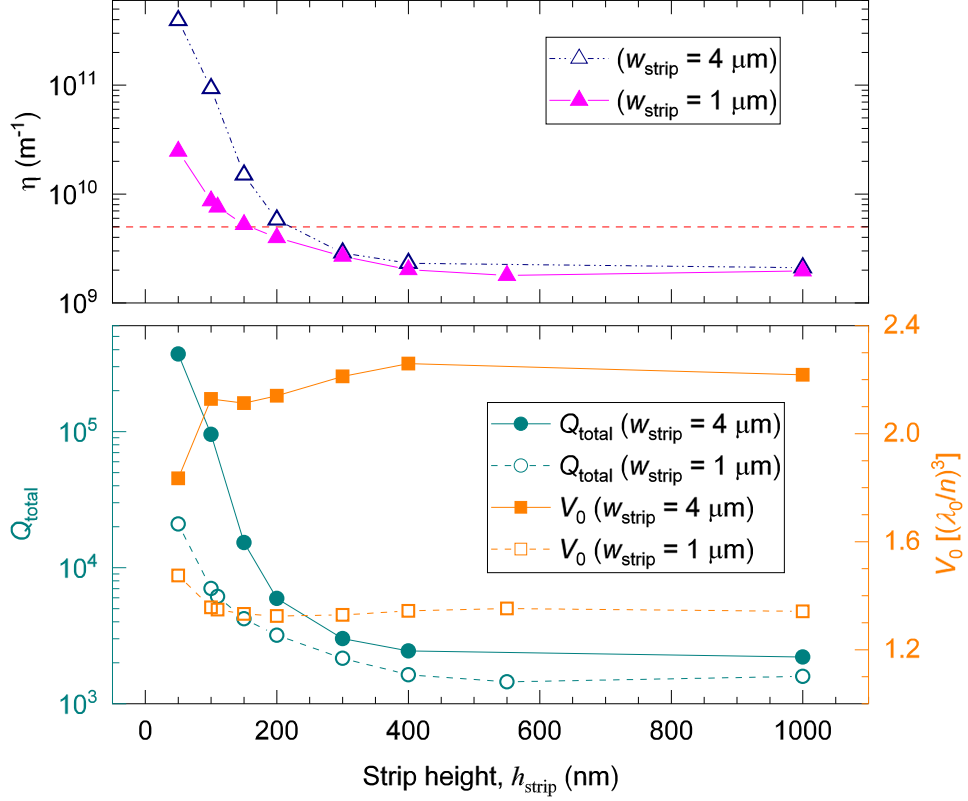


Figure 5.27: Comparison of parameters of the fundamental cavity mode extracted from SU-8 strip cavities with $w_{\text{strip}} = 1 \mu\text{m}$ and $w_{\text{strip}} = 4 \mu\text{m}$ and variable h_{strip} . The bottom half of the figure shows Q_{total} and V_0 ; the top half shows the calculated η . The red dashed line indicates the minimum η theoretically required for strong coupling.

Comparison of Q_{total} for devices with $w_{\text{strip}} = 1 \mu\text{m}$ and $w_{\text{strip}} = 4 \mu\text{m}$ in Fig. 5.27 reveals that the $4 \mu\text{m}$ -wide strip yields a higher Q factor for any h_{strip} in the range simulated. However, the larger V_0 , which is less favourable for coupling, should also be considered. The strong coupling figure of merit, η , which factors this in (Eq. 3.16), calculated for each strip is plotted in the top half of Fig. 5.27. Evidently, using a $4 \mu\text{m}$ -wide strip rather than a $1 \mu\text{m}$ -wide strip to generate the cavity mode only offers a significant benefit to η if $h_{\text{strip}} \lesssim 200 \text{ nm}$. For thicknesses greater than this, η is similar for both strip widths and falls below the minimum theoretical value required for strong coupling (see section 3.6). We therefore choose a target strip height of below $\sim 200 \text{ nm}$ for fabrication of wider strips. Note that a similar trend to η was verified for Q_{total}/V_0 , which is relevant to Purcell enhancement.

Additional FDTD simulations were performed to provide a more complete picture of the dependence of the cavity mode parameters on h_{strip} and w_{strip} . Strip heights of 50 nm , 100 nm , 200 nm and 400 nm were tested for w_{strip} in the range $1\text{--}4 \mu\text{m}$. The extracted λ_0 is shown in Fig. 5.29; Q_{total} and V_0 are shown in Fig. 5.30.

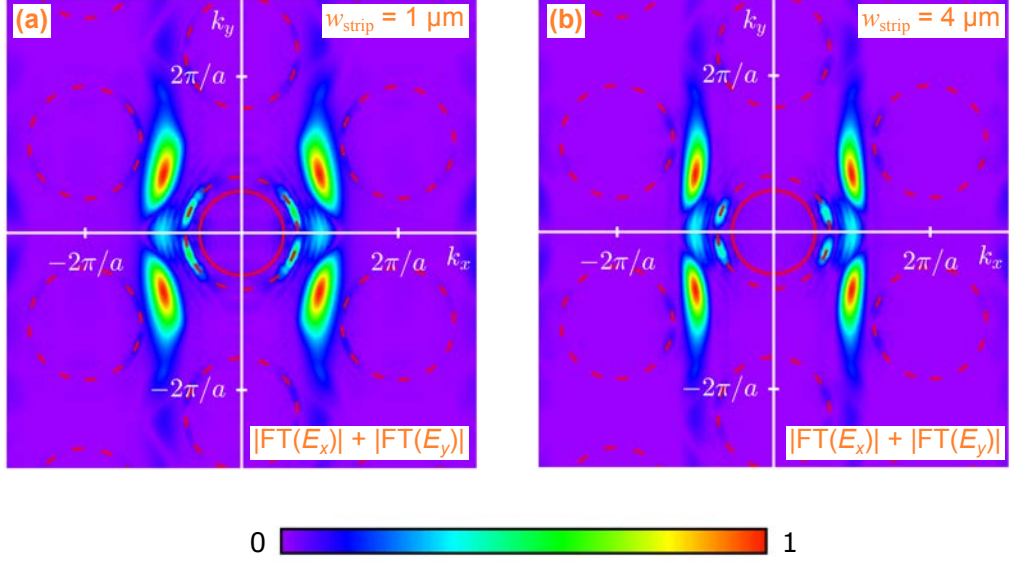


Figure 5.28: Similar spatial Fourier transform analysis to Fig. 5.25, except for SU-8 strips with $h_{\text{strip}} = 400 \text{ nm}$ (instead of $h_{\text{strip}} = 100 \text{ nm}$). $|FT(E_x)| + |FT(E_y)|$, extracted through the plane $z = z_{\text{slab}}/2$, is plotted for devices with strip widths of (a) $w_{\text{strip}} = 1 \mu\text{m}$ and (b) $w_{\text{strip}} = 4 \mu\text{m}$. The light cone is marked on as a solid red circle; contours of the TM-like slab mode are marked by dashed red lines. Each result is normalised.

For a given h_{strip} , λ_0 is found to redshift as w_{strip} is increased (Fig. 5.29), suggesting that for any reasonable strip height the wavelength can be controlled by altering the strip width. A redshift is also predicted as h_{strip} is increased, so good control of the strip thickness will be required in practice if λ_0 is to be tailored by altering w_{strip} . Also marked on Fig. 5.29 for each h_{strip} is the wavelength corresponding to the WM1 photonic band at the edge of first Brillouin zone, $\lambda_{\text{WM1}}(k_x = \pi/a)$, obtained from photonic band structure simulations of the PhC waveguide topped with an SU-8 film of thickness $T_{\text{film}} = h_{\text{strip}}$ (see Fig. 5.7). As discussed in section 5.2, the mode gap generated by this modified WM1 band is believed to be responsible for the generation of a cavity mode by the strip. As w_{strip} is increased, λ_0 appears to converge towards $\lambda_{\text{WM1}}(k_x = \pi/a)$ for the relevant SU-8 thickness. This is expected, since the structure converges towards the situation of a waveguide topped with SU-8 film, as simulated for the photonic band structure. This provides further evidence that the SU-8 strip cavity operates on the principle of mode-gap confinement, proposed in section 2.6.

A general observation from the predicted values of Q_{total} (Fig. 5.30) is that thinner SU-8 strips benefit more from an increase to w_{strip} . The results suggest that for $h_{\text{strip}} \gtrsim 200 \text{ nm}$, little benefit is gained from a wider SU-8 strip, especially considering the larger V_0 . This is consistent with the sub-200 nm thickness target stated previously. For some strip parameters, the theoretical Q_{total}

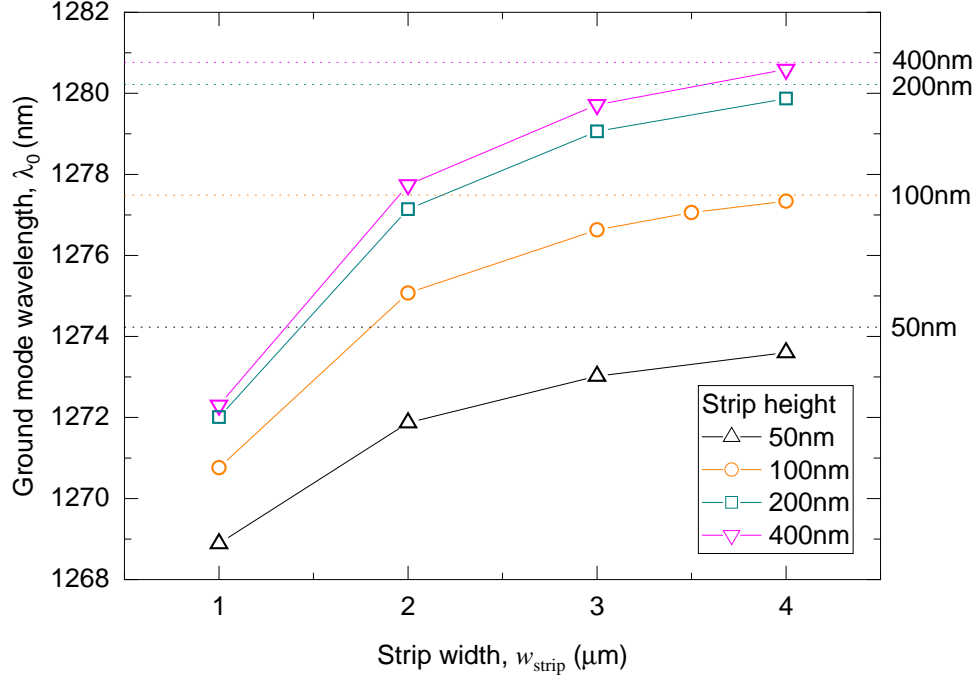


Figure 5.29: Wavelength of the fundamental cavity mode, λ_0 , extracted from FDTD simulations of SU-8 strip cavities with various width and height. Also marked by each horizontal dashed line is the wavelength of the WM1 band at the edge of the first Brillouin zone, $\lambda_{\text{WM1}}(k_x = \pi/a)$, obtained from photonic band structure simulations of the PhC waveguide topped with an SU-8 film with the annotated thickness (displayed at the right hand side).

exceeds 10^5 , which is consistent with the order of magnitude found for polymer strips with slightly different geometries [90] to those simulated here. This magnitude of Q_{total} also approaches the theoretical values for mode gap cavities which do not have broken z -symmetry (and therefore do not have TE-TM coupling losses), such as those defined by selective infiltration of the PhC air holes [95] or sections of the waveguide with altered refractive index [96]. The theoretical performance is even comparable to the frequently-used optimised L3 cavity design, which was simulated in section 2.4.3.4.

5.5 Varying the strip width: experimental results

A run of SU-8 strip cavity devices was fabricated to investigate the effects of altering the width of the SU-8 strip. This experiment was performed with the aim of verifying the trends predicted by the simulation results presented in section 5.4. In particular, the experiment aimed to produce higher Q factor SU-8 strip cavities than those already reported in section 5.3 and to test whether altering the strip width to tailor λ_0 can be performed with sufficient accuracy in practice to benefit

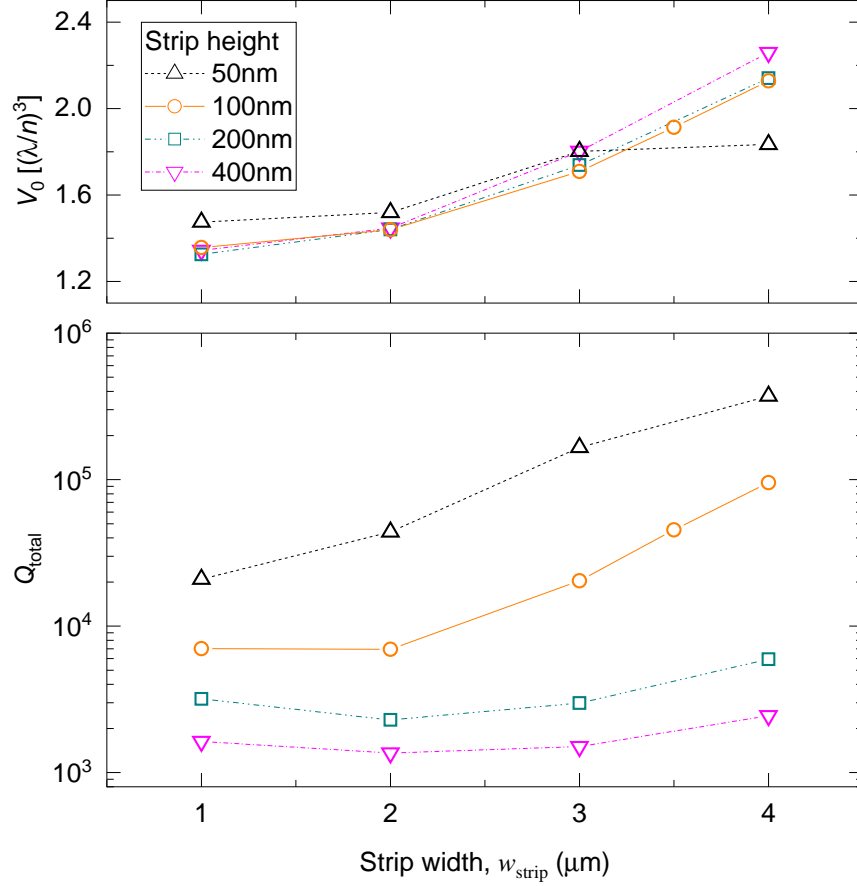


Figure 5.30: Mode volume (top) and Q_{total} (bottom) of the fundamental cavity mode, extracted from FDTD simulations of SU-8 strip cavities with various width and height.

QD-cavity coupling applications.

5.5.1 Fabrication and atomic force microscope characterisation

Experiments were performed on a high density InGaAs/GaAs QD sample, very similar to the one used for the first batch of SU-8 strip cavities in section 5.3.1. A 4 minute HCl treatment was applied to remove the AlGaAs layer in this case. A similar SU-8 spin-coating procedure was applied, but with an 8:1 ratio of cyclopentanone to SU-8 2007. Additionally, the sample was bathed in PGMEA (and rinsed with IPA) before spin coating, to clean the surface.

The applied SU-8 spin-coat generally provided good coverage of the sample surface and coated the vast majority of PhC devices successfully. Areas of coverage that were predicted to have highly uniform film thickness were identified by their consistent colouration under illumination from a white LED, as expected from thickness-dependent interference effects of the film (see section 5.3.1). Large parts of the sample displayed one of two distinct colourations, which are shown in the $500\times$

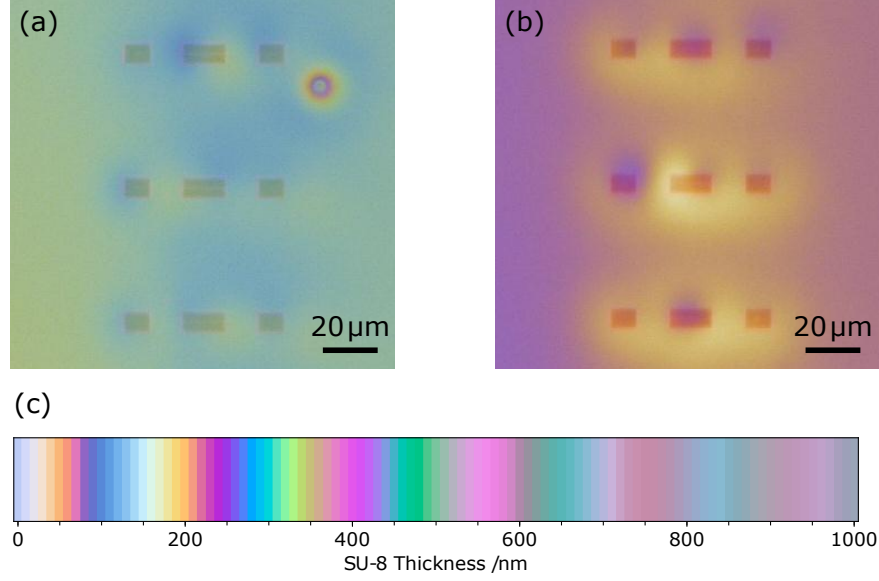


Figure 5.31: Appearance of the SU-8 film under white LED illumination compared to simulated colouration. (a) and (b): 500 \times optical microscope images of three PhC devices, showing two distinct colourations of the SU-8 film. (c) Colour of the SU-8 film predicted as a function of thickness, from simulation results presented by collaborator L. Nuttall [1].

optical microscope images in Figs. 5.31(a) and 5.31(b). Fig. 5.31(a) shows three PhC devices with good SU-8 film coverage, which displays a blue/green appearance; Fig. 5.31(b) shows another three devices, well-covered by SU-8 film which exhibits a yellow/purple colouration. For brevity, these will be referred to as blue film and yellow film, respectively. In Fig. 5.31(c), the expected appearance of the SU-8 film, as a function of thickness (from simulation results by L. Nuttall [1]), is shown for comparison. By comparing the optical microscope images with the simulation results, we can predict with confidence that T_{film} , the SU-8 film thickness, is less than 400 nm. However, the exact T_{film} of the blue and yellow film is hard to predict, due to more than one occurrence of each colouration predicted between 0–400 nm. From the optical microscope images alone, we are only able to infer that the blue film is predicted to be either in the range 90–160 nm or 270–330 nm and the yellow film is predicted to be in the range 30–80 nm or 170–250 nm.

To write the SU-8 strips, a similar technique was applied to the method detailed in section 5.3.1, with some modification to write wider strips. The same 405 nm laser was used, with a power of 17.5 μW after the objective. For this run of experiments, the exposure laser was coupled into the combiner fibre described in section 3.8, to make it co-axial with the excitation laser used for pPL measurements. While this was not necessary for this particular experiment, using this set-up served as a test of the apparatus, which is designed to be used for SU-8 cavity-QD coupling work. The spot of the writing laser was controlled using the piezo stage-mounted objective to expose

| Writing speed ($\mu\text{m/s}$) | Film appearance | Sample size | Yield (%) | Mean strip height (nm) |
|--------------------------------------|--------------------|----------------|--------------|---------------------------|
| 0.5 | Blue | 3 | 0 | - |
| 0.5 | Yellow | 4 | 0 | - |
| 0.25 | Blue | 7 | 43 | 32 ± 1 |
| 0.25 | Yellow | 10 | 0 | - |
| 0.125 | Blue | 4 | 100 | 95 ± 6 |
| 0.125 | Yellow | 5 | 100 | 38 ± 2 |

Table 5.4: Yield summary for single line ($N = 1$) SU-8 strips written with different speeds on PhC waveguide devices, with blue or yellow film covering the PhC. A successful yield indicates a successfully written SU-8 strip and a cavity mode present. Mean strip heights are presented with uncertainty given by the standard error of the mean.

lines of SU-8, perpendicular to the PhC waveguide. Wider SU-8 strips were fabricated by writing multiple parallel lines with the laser spot, with a separation of $0.5\mu\text{m}$ (approximately half the spot diameter) between each parallel line. The number of parallel lines written, N , was between $N = 1$ and $N = 7$, targeting strip widths of approximately $1\mu\text{m}$ to $4\mu\text{m}$, in $0.5\mu\text{m}$ increments. The length of each line was $16\mu\text{m}$; the development process applied after exposure was the same as detailed previously.

5.5.1.1 Single line reference strips

We focus first on the SU-8 strips formed by writing a single line ($N = 1$) with the laser spot, created as reference cavities for comparison with the single strip cavities in section 5.3. Three different writing speeds, v_w were tested: $0.125\mu\text{m/s}$, $0.25\mu\text{m/s}$ and $0.5\mu\text{m/s}$. The results of these tests are summarised in table 5.4, which shows the yields and strip heights for each exposure setting and SU-8 film appearance. For both the blue film and the yellow film, $v_w = 0.5\mu\text{m/s}$ provided too low an exposure dose to successfully produce an SU-8 strip on top of the PhC. At $v_w = 0.25\mu\text{m/s}$, the higher dose resulted in a 43% yield of successful cavities for the blue film, but the dose was still too low to expose strips in the yellow film, which suggests it was thinner than the blue film. This is confirmed by the strips written at the highest dose ($v_w = 0.125\mu\text{m/s}$), which exhibit a larger mean strip height of $(95 \pm 6)\text{nm}$ when written in the blue film, compared to the yellow film $[(38 \pm 2)\text{nm}]$.

Two examples of single lines fabricated using $v_w = 0.125\mu\text{m/s}$ are shown in the SEM images in

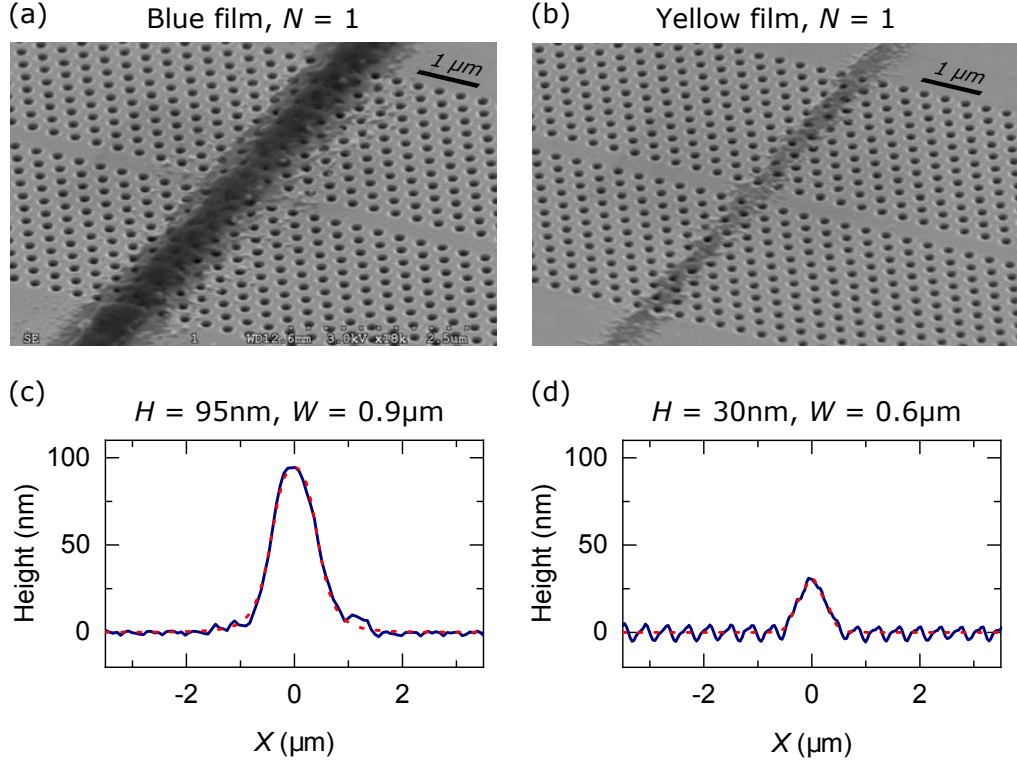


Figure 5.32: Two examples of SU-8 strips on a PhC waveguide fabricated from writing one line ($N = 1$) in either blue or yellow film, with a writing speed of $0.125\mu\text{m/s}$. (a) and (b): SEM images of the strips, written in blue film and yellow film, respectively. (c) and (d): averaged height profiles of the strips, obtained from AFM measurements, corresponding to the strips in (a) and (b), respectively. The height profile is shown in blue; the red dashed line displays an inverse polynomial fit (with parameter constraints) used to extract the height (H) and width (W).

Fig. 5.32: Fig. 5.32(a) shows a strip written on a device covered in blue film, whereas Fig. 5.32(b) shows a device which was covered by yellow film. Evidently, the strip written in the thinner, yellow film appears underexposed compared to the strip written in the thicker, blue film – as one might expect. Profiles of the strip height, obtained by AFM measurements, are presented for the two strips in Figs. 5.32(c) and 5.32(d). These profiles were extracted using the profile averaging techniques applied in section 5.3.1, with height averaging performed over at least a span of 2 rows of PhC holes either side of the waveguide. This was the case for all AFM profile measurements in this experimental run. For the single line written in blue film, we obtain a height of $H = 95\text{nm}$ and for the line written in yellow, we obtain $H = 30\text{nm}$ (to the nearest 5nm). These parameters were extracted using the constrained inverse polynomial fit detailed in section 5.5.1.2. The cavity modes associated with the two example devices presented in Fig. 5.32 were found to have Q factors of over 8000.

5.5.1.2 Varying the strip width

Wider SU-8 strips formed by writing a number of parallel lines (N) in the range 2 to 7 (with $0.5\text{ }\mu\text{m}$ spacing) were fabricated on 52 devices covered by blue film and 60 devices covered by yellow film: at least 8 devices for a given N and film colouration. All of these were written using a speed of $v_w = 0.25\text{ }\mu\text{m/s}$; for the rest of the analysis, SU-8 strips written at this speed only are considered (unless stated otherwise), to allow a fair comparison. For $N = 2$ to $N = 7$, the success rate of writing a strip on a device was 100% for those coated with blue film and 98% (61 devices were attempted) for those coated with yellow film.

Selected examples of wider SU-8 strips written onto PhC waveguides are presented in Fig. 5.33. In Figs. 5.33(a) and 5.33(b), we show SEM images of strips with $N = 4$ (target width $\sim 2.5\text{ }\mu\text{m}$) on devices which were covered by blue film and yellow film, respectively. Successful fabrication of a single, continuous strip is confirmed in both cases, although the strip written in blue film appears overexposed compared to the yellow film. The corresponding height profiles of the strips (obtained as detailed in section 5.5.1.1), presented in Figs. 5.33(c) and 5.33(d) confirm that the strip written in blue film is indeed thicker and wider. Similar behaviour is observed from the two examples given in Figs. 5.33(e) and 5.33(f), which show SEM images of wide SU-8 strips with $N = 7$ (target width $\sim 4\text{ }\mu\text{m}$), which were written on a PhC waveguide with blue film and yellow film, respectively. The strip written in blue SU-8 again appears more exposed compared to yellow film. The height profiles of the strips, presented in Figs. 5.33(g) and 5.33(h), confirm that the $N = 7$ strip written in blue film is thicker, as expected.

In order to extract parameters describing the geometry of the SU-8 strips, we apply fitting techniques to the extracted height profiles. In section 5.3.1, an inverse polynomial fit was applied (see Eq. 5.1) as an arbitrary function which provided an excellent fit to the profile shape, in order to extract the strip height. For this experiment, we wish to also extract the width of the strip. To do this, we modify the inverse polynomial fit, applying constraints so that the parameter w is identical to the FWHM of the peak. By applying the constraint

$$A_1 + A_2 + A_3 = 1, \quad (5.2)$$

the inverse polynomial function has the value $f(x) = c_0 + H/2$ at $x = x_c \pm w/2$, hence w corresponds to the FWHM. We are free to apply this constraint, because the inverse polynomial function was chosen as an arbitrary fit, without physical significance. This constrained function was found

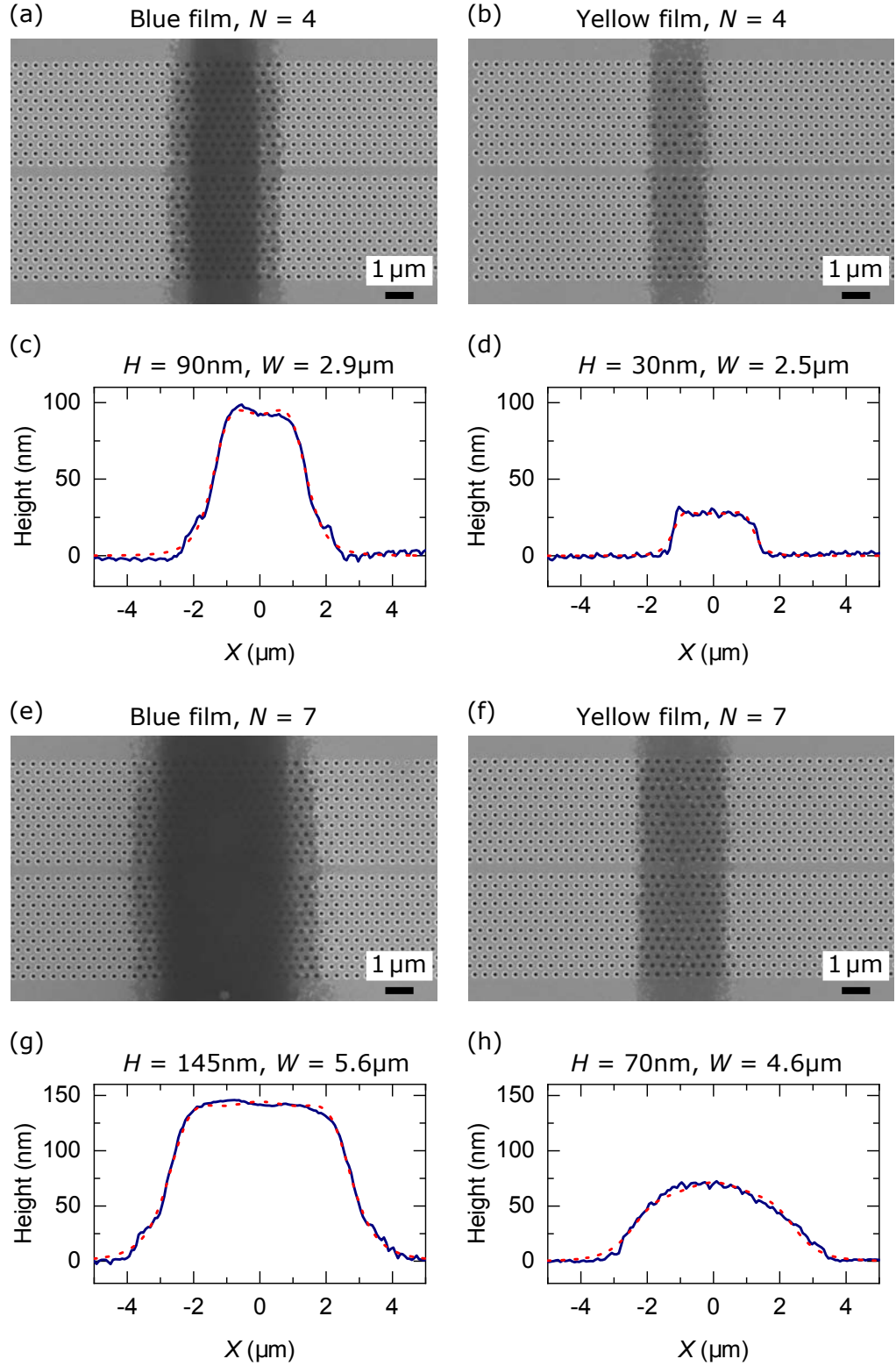


Figure 5.33: Selected examples of SU-8 strips of different widths. SEM images are shown in Figs. (a), (b), (e) and (f); the number of lines written to create the strip, N , and the film colour over the device are shown at the top of each figure. Profiles of each strip, obtained via AFM measurements, are displayed below the corresponding SEM image, in (c), (d), (g) and (h). The profile is shown in blue; the red dashed line displays an inverse polynomial fit (with parameter constraints).

| Film \ N | 1 | 2 | 3 | 4 | 5 | 6 | 7 |
|------------|---|----|----|---|----|----|----|
| Blue | 3 | 6 | 8 | 8 | 7 | 8 | 7 |
| Yellow | 0 | 10 | 11 | 8 | 10 | 10 | 10 |

Table 5.5: Sample size for each film colouration and number of lines written (N).

to still provide an excellent fit to the SU-8 strip height profiles: the fits shown in Figs. 5.32(c) and 5.32(d) for the $N = 1$ strips, in addition to the fits shown in Figs. 5.33(c), 5.33(d), 5.33(g) and 5.33(h) are all inverse polynomial functions with this parameter constraint applied. The strip height, H , and strip width (FWHM), W , extracted from the profiles are noted at the top of each of these figures.

The batch of devices fabricated using a writing speed $v_w = 0.25 \mu\text{m/s}$ was characterised via the described AFM measurements and profile fitting process. A total of 9 devices were excluded from the analysis, either due to damage or contamination of the PhC, which occurred between μPL measurements of the sample (detailed in section 5.5.2) and the subsequent AFM characterisation. The 3 successful devices with $N = 1$ and $v_w = 0.25 \mu\text{m/s}$, which were discussed in section 5.5.1.1, were included in the sample set, giving a total sample size of 106 devices: 47 written in blue film and 59 written in yellow film. The number of devices fabricated for each film colour and N are displayed in table 5.5, for completeness.

The variation of the SU-8 strip geometry parameters, H and W , with N is presented in Fig. 5.34 for each film colouration. The mean value of each parameter, $\overline{H}(N)$ or $\overline{W}(N)$, is shown, with error bars corresponding to one standard deviation, $\sigma_H(N)$ or $\sigma_W(N)$, either side of the mean. It is clear from these results that the thickness of the SU-8 film has a significant influence on the dimensions of the strip: for a given N , SU-8 strips written in the blue film possess a higher \overline{H} and \overline{W} than those written in yellow film. Both of these differences are attributed to the thicker T_{film} estimate for the blue film compared to the yellow SU-8 film. It is also evident that for either film colouration, \overline{H} increases with N , which we propose is due to some overlap between the regions of SU-8 exposed by each parallel line written using the laser spot. Another possible contributing factor is that exposing a larger area of SU-8 is likely to generate a larger proportion of photoacid catalyst, which could lead to a thicker cross-linked strip during the development process.

The mean width of the fabricated strips, \overline{W} , plotted in the lower half of Fig. 5.34, shows a strong, positive, linear correlation with N for a given film colouration. For $N \leq 4$, \overline{W} is reasonably

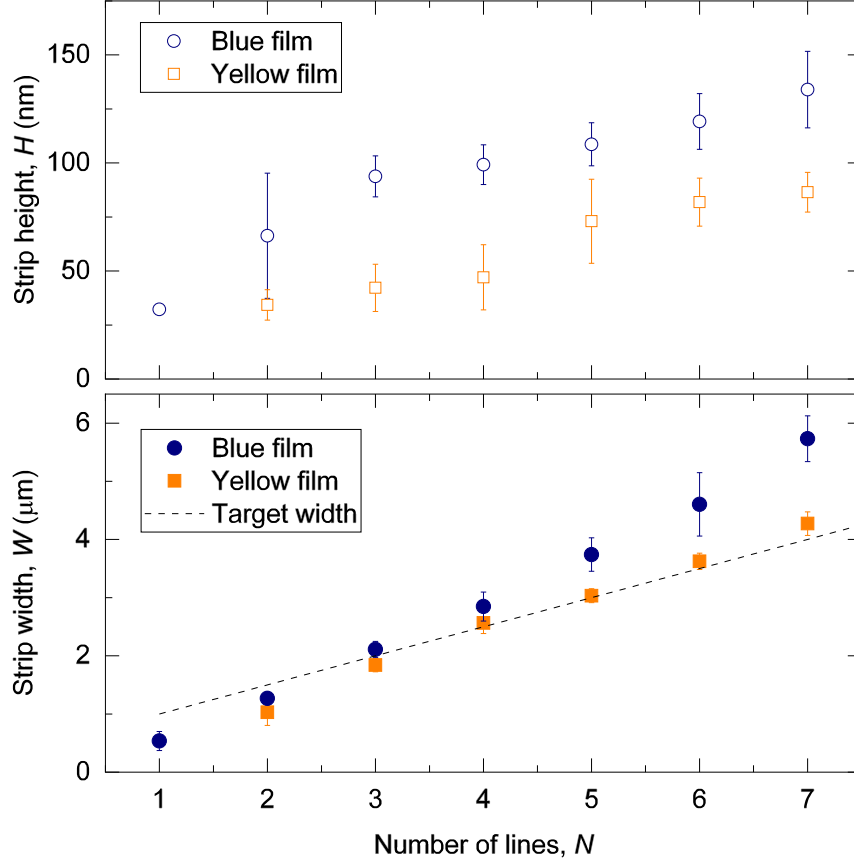


Figure 5.34: Dependence of SU-8 strip geometry on N and the film colouration. The mean values of H and W (\bar{H} and \bar{W}) are shown for each N ; error bars represent one standard deviation either side of the mean value. The target \bar{W} , assuming a laser spot diameter of $\sim 1 \mu\text{m}$, is also shown.

consistent with the target width for either film colouration. However, for $N > 4$, only strips written in yellow film remain consistent with the target width, as those written in the thicker blue film tend to exceed the target width due to the overexposure effects previously mentioned. The broadening of the strip could potentially be avoided by increasing v_w as N is increased, to reduce the exposure dose for each line written. Another approach could be to increase the spacing between the individual lines written by the laser spot, in order to reduce the overlap of exposed regions from each line. However, this risks creating a non-uniform strip, or even distinct single lines, if the line spacing is too wide. Separate lines on the same PhC waveguide could form multiple cavities – a concept which is explored in Ch. 6.

The results presented from this fabrication run show promise for the ability to consistently control the geometry of a sub-200 nm-thick SU-8 strip on a PhC waveguide. For a given N and film colouration, relatively small variations in W and H were observed between devices: the average (mean) values of σ_H or σ_W were 13 nm and $0.2 \mu\text{m}$, respectively. This demonstrates the ability to

reproducibly fabricate SU-8 strips on multiple PhC devices with height consistent within 50 nm and width consistent to better than 1 μm , as long as PhC waveguide devices coated with SU-8 film of similar thickness can be identified in the fabrication stage. A more difficult challenge than achieving consistent (precise) H is to be able to control the exposure parameters to accurately target a specific \overline{H} . The exposure dose calibration data presented in appendix A is intended to help towards this goal.

5.5.2 Micro-photoluminescence characterisation and mapping

All devices from the fabrication run which had a successfully written SU-8 strip on the PhC waveguide were characterised using μPL measurements. For this experiment, comparison of μPL maps before and after writing the SU-8 (to confirm the creation of cavity modes) was not deemed necessary, as high yields found from other SU-8 strip investigations (single strip cavities in section 5.3 and the double-strip cavities in section 6.3) suggest that the majority of devices will successfully support cavity modes.

Excitation of the QD ensemble was provided by the 532 nm CW laser, which was coupled into a combiner fibre with the 405 nm writing laser, as described in section 3.8. A power of $\sim 60 \mu\text{W}$ after the objective was used. Note that a higher power was necessary than for the experiments detailed in section 5.3.2, because the typical mode wavelength was longer and therefore further spectrally from the ensemble emission. μPL mapping measurements were acquired using the same techniques and parameters as for the initial run of single strip ($N = 1$) cavities detailed in section 5.3.2, unless stated otherwise. Measurements of the ground mode Q factor of each cavity were obtained via the method described previously, using the 1200 lines/mm grating (with 20 μm slit width). The acquisition time applied for each spectrum was varied between 10 s and 30 s, depending on the brightness of the cavity mode. All measurements were performed at $\sim 8 \text{ K}$ and were carried out before any of the AFM or SEM characterisation detailed in section 5.5.1.

Selected examples of 1D μPL maps from successful devices with various SU-8 strip dimensions are shown in Fig. 5.35. The measured H and W of the SU-8 strip on the device is shown inset in each sub-figure, in addition to the fabrication parameters (N , v_w and the SU-8 film colouration). Note that the map in Fig. 5.35(a) is a typical single strip map ($N = 1$) obtained from one of the devices from section 5.5.1.1, which was written with $v_w = 0.125 \mu\text{m/s}$. This is intended as a reference device for comparison, with similar SU-8 strip dimensions to the first run of SU-8 strip

cavities in section 5.3. This map shows a highly localized single cavity mode, as expected, although the wavelength of the mode (1303.2 nm) is considerably longer than the cavities from the previous batch. This offset was found to be systematic: all cavities, including the reference L3 cavity modes,

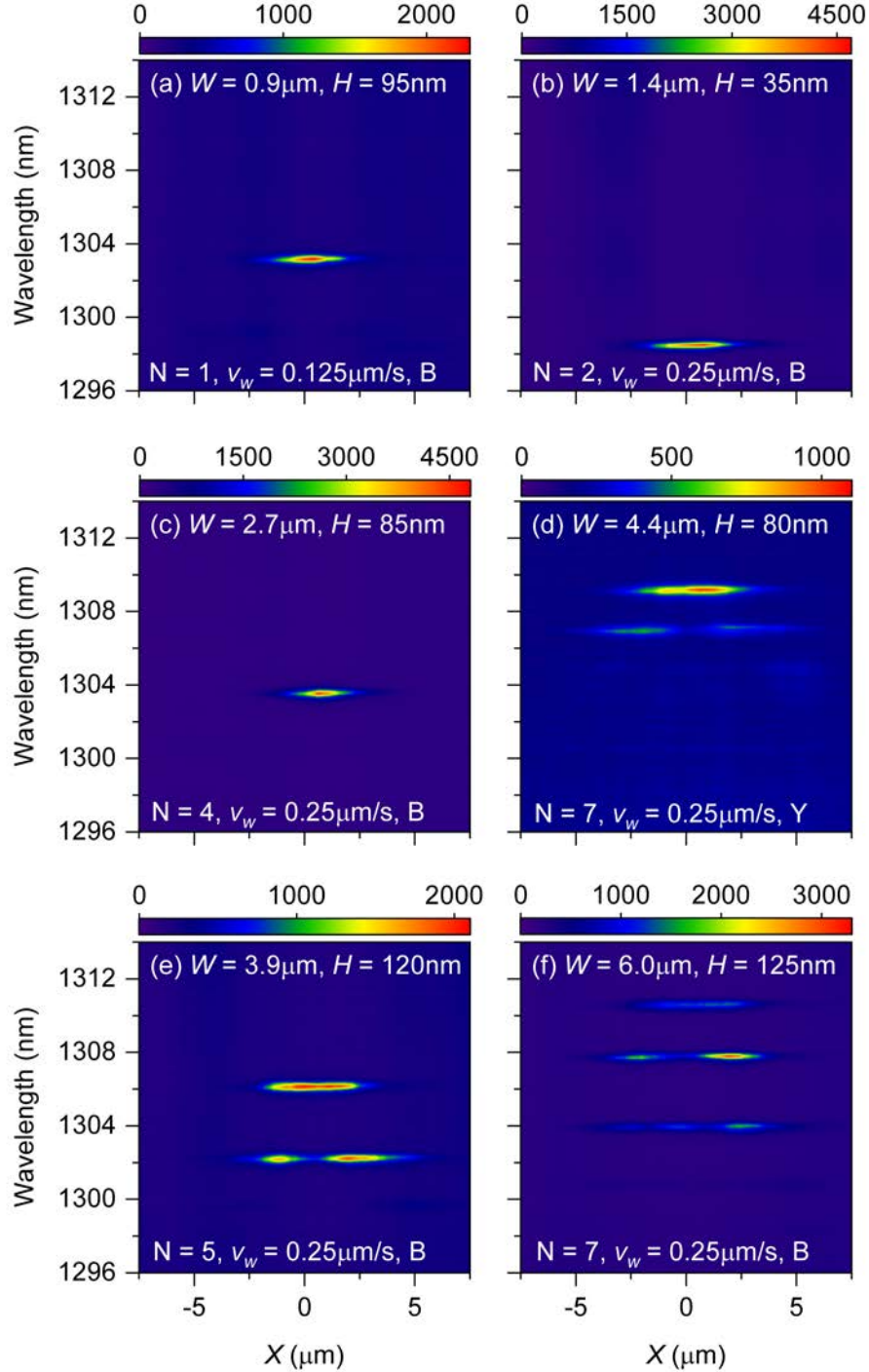


Figure 5.35: Selected examples of 1D μ PL maps taken along the waveguide of successful SU-8 strip cavities. Dimensions of the SU-8 strip (W and H) are provided in the corresponding sub-figure, in addition to fabrication parameters N , v_w and the SU-8 film colouration: blue (B) or yellow (Y). The intensity scale is shown above the corresponding map (in arbitrary units); all maps use the same wavelength and position (X) scale.

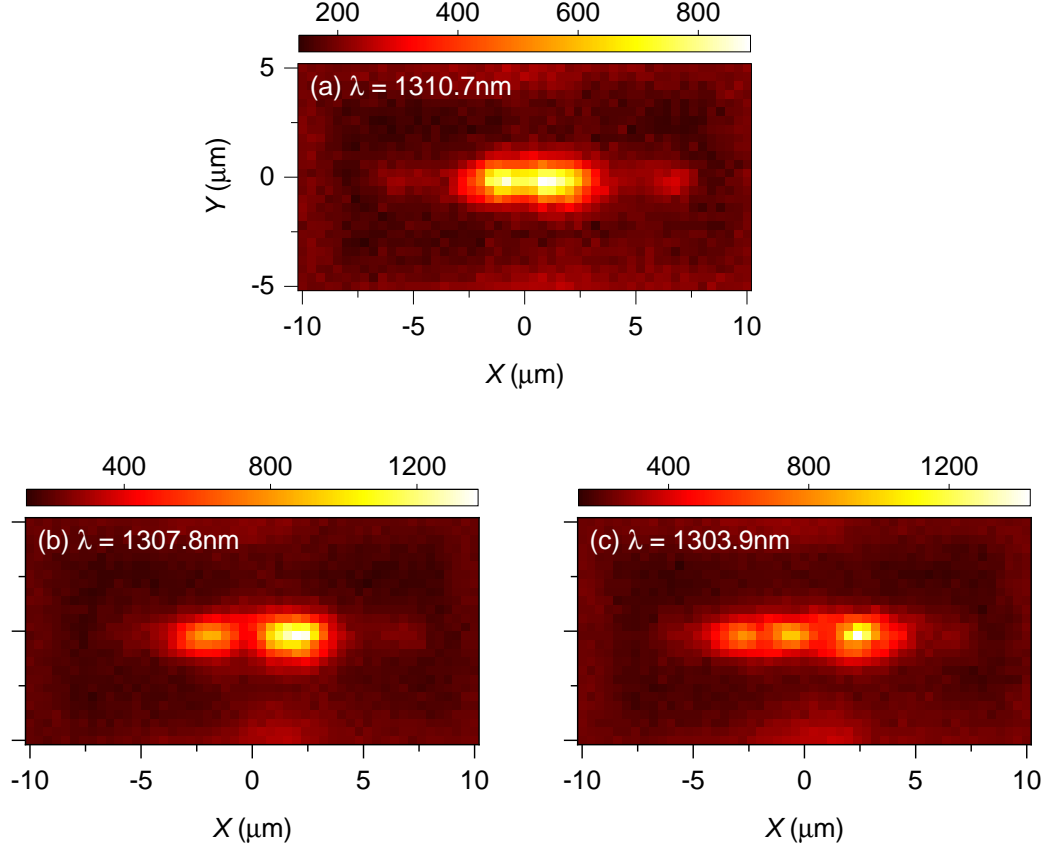


Figure 5.36: 2D μ PL map of an SU-8 strip cavity device with $W = 6.0\mu\text{m}$ and $H = 125\text{nm}$. (a) Ground mode. (b) First excited mode. (c) Second excited mode. The intensity scale is shown above the corresponding map (in arbitrary units); all maps use the same X and Y scale. The wavelength of each mode is noted in each sub-figure.

were of a longer wavelength on this sample. We therefore attribute the discrepancy to differences in the PhC etching, rather than an effect of the SU-8 strips.

All maps in Fig. 5.35 show evidence of a single-peaked, localized ground mode, which intuitively becomes broader as W is increased. Cavities formed from a wider strip also tend to support higher order cavity modes, as seen in Figs. 5.35(d)–(f). Figs. 5.35(d) and 5.35(e) clearly show a double-peaked second mode, which matches that of the WMLD mode gap cavity [56]. Fig. 5.35(f) also shows a triple-peaked third mode exhibited by a very wide ($W = 6.0\mu\text{m}$) SU-8 strip cavity. The three modes of this cavity are mapped in more detail in Fig. 5.36, which displays results of a 2D μ PL map of the device. The map was performed by scanning the objective in steps of $0.4\mu\text{m}$; spectra were acquired for 1 s at each position. In Figs. 5.36(a), 5.36(b) and 5.36(c), the intensity recorded at the wavelength of the ground mode (1310.7 nm), first excited mode (1307.8 nm) and second excited mode (1303.9 nm), respectively, is shown. The maps demonstrate the local antinodes in greater detail than the 1D map and clearly show that the modes are well-localized to the waveguide,

as one would expect from a mode gap cavity.

5.5.3 Batch analysis

The overall trends between cavity mode parameters and SU-8 strip geometry across the batch of 106 devices are now examined. The Q factor and the wavelength of the ground mode, λ_0 , are compared with the extracted strip geometry parameters, W and H . Referring back to the simulation results presented in section 5.4 and making the approximations $h_{\text{strip}} \approx H$ and $w_{\text{strip}} \approx W$, the general trends anticipated are as follows. Firstly, for a given H , a redshift of λ_0 is expected as W is increased, as the cavity mode converges towards the wavelength of its associated WM1 band at the Brillouin zone edge. For thin strips with $H \lesssim 100$ nm (which is true for the majority of cavities fabricated), the Q factor should rise significantly as the strip width is increased beyond $W \gtrsim 2$ μm , due to the decreased localization of the mode and resulting inhibition of TE-TM coupling losses. For a given W , as H is increased, the Q of the cavity mode is expected to decrease (attributed to increased TE-TM coupling losses from stronger breaking of the z -symmetry) and λ_0 is expected to redshift (likely due to the increase in average refractive index).

The potential correlations between W , H , and Q are explored in Fig. 5.37, which plots H against W for each device, with the ground mode Q represented by the colour scale. The positive correlation between W and H is to be expected, due to the overall increase in exposure dose applied when writing a wider strip – as discussed in section 5.5.1.2. Additionally, the majority of devices written in yellow film possess a lower H for a given W than those written in blue film, since the yellow film is thinner. The measured Q values suggest a weak trend: for a given H , the highest possible Q appears more likely for a wider strip. However, the Q factors achieved clearly do not reach the magnitude predicted by the simulation results. For example, a strip with $H \sim 100$ nm and $W \sim 4$ μm would be predicted to have a $Q \sim 10^5$, but the measured values do not exceed 1.1×10^4 . We attribute the restricted Q factors to similar limitations of the GaAs wafer as those discussed in section 5.3.2; we anticipate that a much more significant increase in Q with W (for thin, constant H) would be observed in a more perfectly constructed PhC capable of supporting $Q \gtrsim 10^5$, such as a Si-based wafer [48, 91, 93].

Despite the lack of a strong trend in Q with strip geometry shown by the results, a highly positive outcome of the experiment is that the Q factors achieved were, in general, high, given the limitations of the wafer. Taking all 106 devices, the mean Q was 7900, with a lower and upper quartile

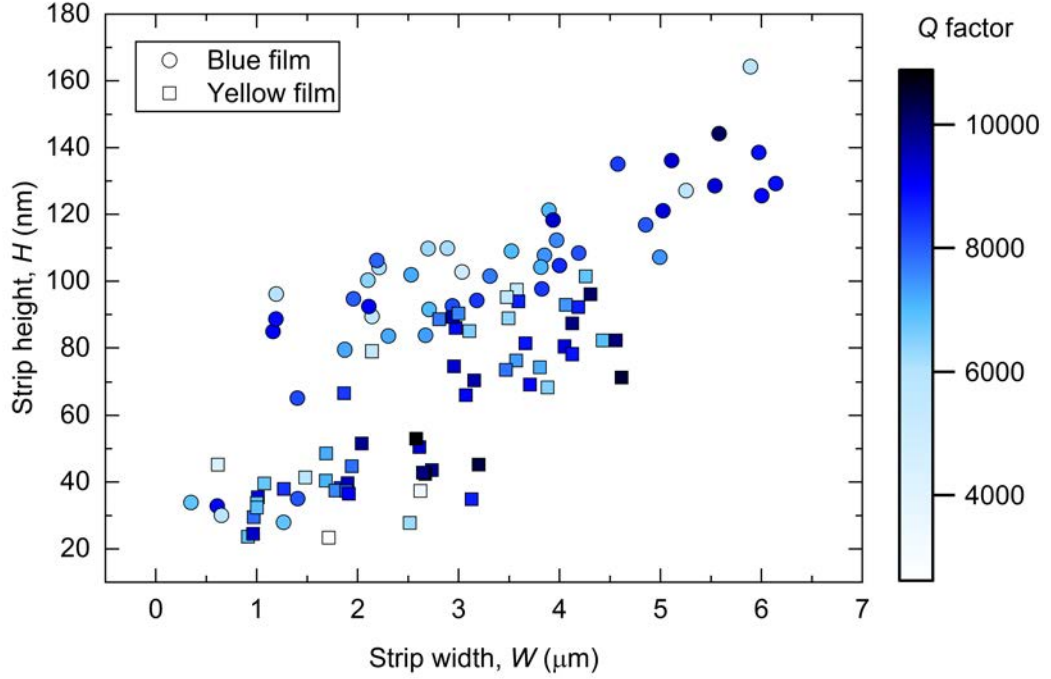


Figure 5.37: Strip geometry parameters and measured Q extracted from each of the 106 devices in the SU-8 strip cavity batch. The colouration of the film covering each device before writing the strip is indicated by the symbol shape: square symbols for yellow colouration and circles for blue colouration. The measured Q is indicated by the symbol colour; the corresponding scale is shown to the right of the figure.

of 6900 and 9000 – demonstrating the ability to consistently produce high Q cavities with the SU-8 writing technique. We also observed the highest Q factors yet from our SU-8 strip-on-PhC cavities: 6 devices (with $N \geq 4$) exhibited a Q factor in excess of 10,000, with a maximum of $Q = 10,900$. Of course, for coupling applications, the mode volume is also important, which will be addressed later in this section. It should also be taken into account that the cavity modes were spectrally further from the QD ensemble than the previously described batch in section 5.3, so it is possible that the Q factor could be increased due to reduced re-absorption by the ensemble [208].

We note that higher Q factors than those measured here have been reported for mode gap cavities fabricated using other non-conventional methods, such as microfluidic infiltration of the PhC holes in a section of a Si PhC waveguide ($Q \sim 57,000$) [97] and refractive index modification of a section of a PhC waveguide made from photosensitive chalcogenide glass ($Q \sim 125,000$) [98]. Both of the cavity designs used in these methods do not break the z -symmetry of the PhC, which may be partly responsible for the higher Q factors achieved (due to the absence of TE-TM coupling losses). However, it is also likely the Q is not as limited by the materials used in these examples (compared to the GaAs wafer used in this work), so we predict that Q factors approaching these

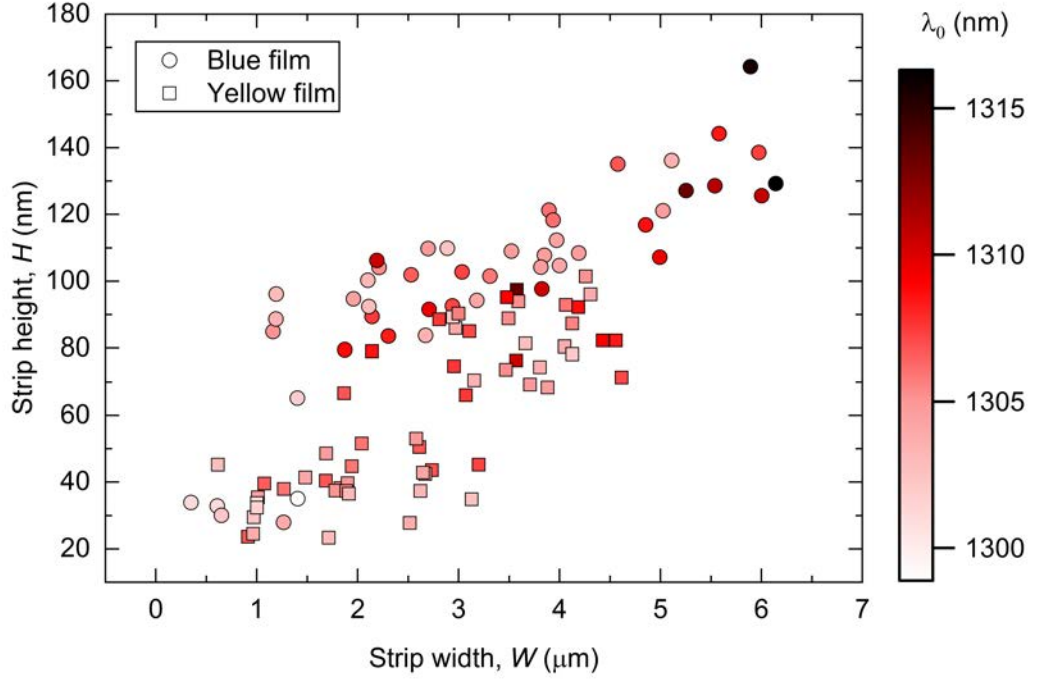


Figure 5.38: Strip geometry parameters and measured ground mode wavelength, λ_0 , extracted from each of the 106 devices in the SU-8 strip cavity batch. The colouration of the film covering each device before writing the strip is indicated by the symbol shape: square symbols for yellow colouration and circles for blue colouration. The measured λ_0 is indicated by the symbol colour; the corresponding scale is shown to the right of the figure.

values might be possible using wide SU-8 strip-defined cavities on a more ideal PhC.

The dependence of λ_0 on the strip geometry is investigated in Fig. 5.38, which is similar to Fig. 5.37, except the colour scale now represents the value of λ_0 . A positive correlation between W , H and λ_0 is suggested: cavities formed from SU-8 strips that are wider and thicker appear more likely to support a ground cavity mode at a longer wavelength. This is consistent with the redshift expected from simulation results as W or H are increased – a trend which, unlike the Q factor, is probably not limited by fabrication imperfections of the GaAs PhCs.

For coupling applications, it would be desirable to have the ability to tailor λ_0 at the SU-8 cavity writing stage, which may be possible by altering the strip width. In practice, this would ideally be controlled by choosing N to attain the desired λ_0 . We therefore consider $\overline{\lambda_0}(N)$, the mean λ_0 as a function of N , which is plotted in Fig. 5.39, categorised by film colouration. A positive correlation is found for either film colouration, demonstrating that it is indeed possible to redshift the average ground mode wavelength of the SU-8 strip cavity by writing more parallel lines. The correlation is attributed to increases of \overline{W} and \overline{H} with N (see Fig. 5.34), which are both predicted to redshift the mode. The strongest redshift is observed for cavities written in blue film, which

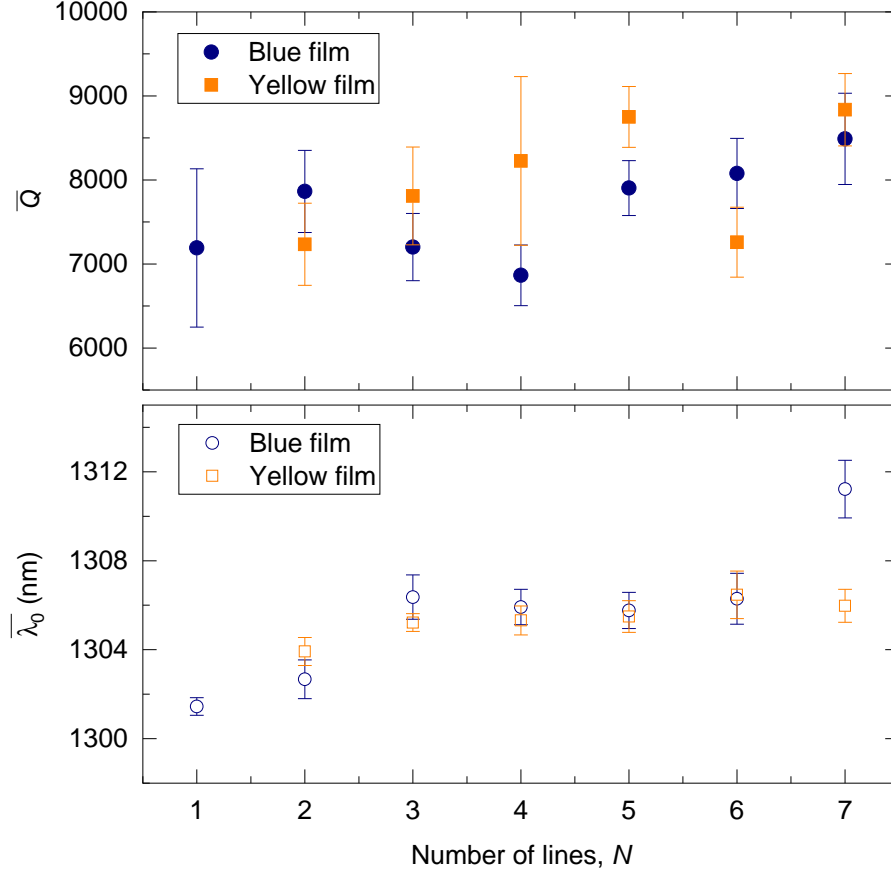


Figure 5.39: Mean quality factor, \bar{Q} and ground mode wavelength, $\bar{\lambda}_0$, as a function of N , the number of parallel SU-8 lines written during the exposure process. The quantities are shown separately for strips written in yellow or blue film - denoted by the symbol used. Error bars show the standard error of the mean.

we attribute to a larger increase in \bar{W} between low and high N than for strips written in yellow film, in addition to a larger \bar{H} for high N (see Fig. 5.34). A redshift of ~ 10 nm to $\bar{\lambda}_0$ is observed between $N = 1$ and $N = 7$ for cavities written in blue film, which is much larger than the ~ 1 nm temperature tuning range of a single QD. Control of N therefore has potential utility for achieving spectral overlap with a target QD over a wider range than achievable using temperature tuning alone. A smaller redshift is observed for cavities written in yellow film, for which $\bar{\lambda}_0$ increases by only ~ 2 nm between $N = 2$ and $N = 7$. We attribute the less pronounced redshift to the less extreme change in \bar{W} over the range of N , which stayed closer to the target value than for blue film; we also expect that a larger redshift over the whole range of N would have been observed if cavities with $N = 1$ had been successful for yellow film.

The effect of N on the mean Q factor, $\bar{Q}(N)$, is displayed in the top half of Fig. 5.39: a very weak correlation is suggested, but no significant ability to control the Q factor by changing N is observed. The Q may partially be limited by the increase of \bar{H} with N , but, as stated previously,

is likely to ultimately be limited by fabrication imperfections of the PhC waveguide. This means that, despite meeting the $H \lesssim 200$ nm target required in theory to benefit the Q/V_0 and η of the cavity mode (see section 5.4), increasing N is actually expected to be detrimental to these figures of merit. Writing wider strips in this manner would therefore not be recommended for coupling experiments, unless one wishes to redshift the cavity mode, or if the limitations could be overcome (such as by using a more ideal PhC and/or perhaps by altering the exposure dose to prevent the positive correlation between \overline{H} and N).

Despite the unfavourable effect of increasing N on Q/V_0 and η , it can be shown that their values are still predicted to be acceptable for coupling. Since the Q factor is similar for all N , we expect the worst-case scenario for the widest strips with the largest V_0 , which are the strips fabricated in blue film with $N = 7$. Considering $\overline{W} \sim 6$ μm for devices fabricated under these conditions, the mode volume is expected to be $V_0 \sim 3(\lambda_0/n)^3$ from FDTD simulation results, which, using $\overline{Q} \approx 8500$ and $\overline{\lambda_0} \approx 1311.2$ nm, gives a maximum theoretical Purcell factor of 215. The strong coupling figure of merit for these parameters is $\eta \sim 7 \times 10^9 \text{ m}^{-1}$, which does not meet the target $\eta \sim 10^{10} \text{ m}^{-1}$ of devices in the literature (see section 3.6), but is still theoretically predicted to be high enough to achieve the strong coupling regime. We therefore conclude that, even taking the limitations into account, increasing the strip width in order to redshift $\overline{\lambda_0}$ still yields an acceptable Q and V_0 of the cavity mode for QD-cavity coupling experiments.

In summary, we have demonstrated that by altering N , it is possible to achieve a redshift of up to ~ 10 nm of $\overline{\lambda_0}$ – which could be beneficial to tailor the cavity wavelength to be closer to resonance with a QD – while still maintaining an acceptable Q/V_0 ratio (and η) for coupling experiments. There are, however, severe limitations to the tuning of the cavity wavelength, which should be considered. Firstly, we note that altering N to tune $\overline{\lambda_0}$ perhaps does not provide the level of precision that one would desire for practical applications. The value of $\overline{\lambda_0}$ can be tuned, but for a given N and film colouration, the standard deviation of λ_0 is typically ~ 2.3 nm, which is larger than would be desired and is, for some N , similar to the targeted redshift. Additionally, for moderate N between 3–6, very little difference is observed in $\overline{\lambda_0}$, preventing its fine control. These limitations, in addition to the challenge of predicting $\overline{\lambda_0}$ based on film thickness, exposure dose and PhC characteristics (which can vary between wafers and devices), will reduce the success rate of setting the cavity wavelength to match a QD in practice.

5.6 Summary

The extensive investigations into the SU-8 strip cavity design performed in this chapter, both using FDTD simulations and μ PL characterisation techniques, have demonstrated its ability to support highly localized cavity modes with a high Q and small V_0 . It has been shown that the SU-8 strip cavity can offer similar performance to the SU-8 disk cavity, but with the inherent advantage that it does not require precise alignment with the PhC waveguide. SU-8 strip cavities fabricated from writing a single line ($N = 1$) were first investigated, for which simulation results suggest that Q factors exceeding 10^4 are possible for sub-100 nm-thick SU-8 strips. A batch of SU-8 strip cavity devices was successfully fabricated with an 82% yield, using the thickness-dependent colouration of the SU-8 film to guide the exposure dose. Successful cavities with SU-8 strips as thin as ~ 60 nm were fabricated, and a maximum Q of 8700 was measured, exceeding that of the SU-8 disk cavities measured in Ch. 4. Ultimately, the Q factor is expected to be limited by fabrication limitations of the wafer.

Variation of the Q factor and cavity mode wavelength with the strip height was verified experimentally and the observed trends were generally consistent with expectations from the simulation results. Analysis of the cavity mode properties suggested that SU-8 strip cavities with a strip height of ~ 100 nm or less are good candidates for achieving strong coupling to a single QD, as the figure of merit, $\eta \sim 10^{10} \text{ m}^{-1}$, is similar to devices for which strong coupling has been achieved in the literature (see section 3.6).

TRPL measurements were performed on a selected high Q device to demonstrate Purcell enhancement of the QD ensemble emission by a factor $F_P \sim 1.6$. The TRPL techniques applied in this chapter would be important to confirm weak coupling of a single QD to the cavity mode, if it can be achieved in subsequent work. Additional FDTD simulations were performed using a more realistic height profile for the SU-8 strip, extracted from a real device. These simulations demonstrated that the Q factor of the cavity mode generated by this strip is actually higher than a simplified cuboidal strip of similar geometry.

Further investigations into the SU-8 strip cavity were performed to explore the effect of altering the width of the SU-8 strip, thus changing the width of the mode gap confinement potential. FDTD simulations showed that increasing w_{strip} can provide a simple method of increasing the Q factor of the cavity mode. This was attributed to a suppression of the in-plane TE-TM mode coupling losses due to the increased spatial delocalization of the mode along the waveguide. For strips of

height $h_{\text{strip}} \lesssim 200$ nm, increasing w_{strip} is predicted to benefit the Q/V_0 ratio and η of the cavity mode, so could be beneficial for coupling applications. Making the strip wider was also identified as a possible convenient method of redshifting the cavity mode, which could help to tailor it into resonance with a target QD.

A batch of SU-8 strip cavities with variable widths was fabricated by using the exposure laser to write multiple, closely spaced lines in the SU-8 film. SU-8 strips with widths up to ~ 6 μm were fabricated with a close to 100% success rate, with strip heights mostly in the 25–150 nm range. For given exposure settings (and film thickness), very good consistency of the SU-8 strip geometry was achieved, demonstrating the reproducibility of the fabrication technique. The highest Q factors yet from fabricated SU-8 strip devices were measured from this dataset, with a lower quartile of 6900 and upper quartile of 9000. Q factors in excess of 10,000 were measured, with a maximum $Q \sim 10,900$. However, these Q factors are believed to be limited by the wafer, so currently higher Q/V_0 ratios (and η) are achievable by writing a narrower, single line to make the cavity. A positive correlation was found between the cavity width and mode wavelength, which could be useful to tailor the cavity mode to a target QD. However, the results suggest that it would be challenging to control the cavity mode wavelength precisely using this technique. Overall, SU-8 strip cavities defined by wider strips do show promise, with the potential for a much higher Q/V_0 ratio and η than the cavities written using a single line, but the limitations of the wafer prevent much of the theoretical advantages from being applicable in practice. Therefore, unless the limitations can be lifted, narrower SU-8 strip cavities defined by writing a single line are likely more favourable for coupling experiments.

6

SU-8 strip photonic molecules

In this chapter, we build on work presented in Ch. 5 on single SU-8 strip cavities to investigate the behaviour of pairs of optically coupled SU-8 strip-defined cavities on the same PhC waveguide. This system of coupled cavities is often referred to as a photonic molecule (PM), owing to the similarity of its modes to the bonding and anti-bonding orbitals of a diatomic molecule [38]. Properties of the PM supermodes, which arise from the interactions of individual cavity modes, are investigated using FDTD simulations and compared to successfully fabricated devices. We characterise the devices using μ PL and AFM measurements and demonstrate varying degrees of coupling between the two cavities according to the separation between the two SU-8 strips. This enables us to observe the transition from independent, uncoupled cavities to strongly coupled PMs with delocalized optical modes. Finally, we explicitly show optical coupling between two cavities of an SU-8 strip PM device using confocal mapping techniques in conjunction with an independently moveable laser spot, enabling independent excitation of and collection from each cavity. Key results from this chapter have been published in Ref. [206].

6.1 Introduction to photonic molecules

6.1.1 Theory of coupled oscillators

Optical coupling between two cavities is typically achieved by placing them in close proximity so that there is some degree of overlap between their evanescent fields. The resulting exchange of energy between the cavities can result in the formation of so-called supermodes, which are highly delocalized across the coupled cavity system. The similarity of these supermodes to the bonding

and antibonding electron orbitals in a diatomic molecule led to the term ‘photonic molecule’ popularised by Bayer *et al.* [38]. This similarity is illustrated in Fig. 6.1. Fig. 6.1(a) is a schematic representation of the lowest order H_2 diatomic orbitals, arising from constructive or destructive interference of the $1s$ orbital associated with the isolated atoms [215]. The σ^*_{1s} antibonding orbital is easily distinguished from the σ_{1s} bonding orbital by its characteristic node between the two atoms. This antibonding orbital is typically at a higher energy and less stable than the bonding orbital, due to the less energetically favourable configuration of the electron wavefunction. We compare the diatomic orbitals to 6.1(b), in which the interaction between two PhC cavities separated by 6 lattice units is considered. We consider the two cavities oscillating in-phase and with π phase difference, which result in constructive and destructive superpositions of the individual E_y profiles, respectively. The resulting symmetric (S) and antisymmetric (AS) supermodes are analogous to the bonding and antibonding orbitals of a diatomic molecule. The E_y field is delocalized across the two cavities, with a more pronounced dip in the AS supermode field envelope at $X = 0$ than the S supermode. This behaviour is comparable to the characteristic node of the σ^*_{1s} orbital that is not present in the σ_{1s} orbital.

A wide variety of nano- and micro-scale photonic structures have been used to realise PMs at visible and infra-red wavelengths. The first demonstration of a PM by Bayer *et al.* [38] utilised a pair of micropillar cavities connected via a channel, as shown in Fig. 6.2(a). Adjustment of the channel width and length enables control of the coupling strength between the two cavities, which allows control over the energy splitting of the PM supermodes. Bayer *et al.* calculated the electric field distributions of the 6 lowest energy supermodes supported by the PM, which are presented in Fig. 6.2(b). The modes are labelled n, P_x, P_y , where n labels the energy ordering of the modes in the uncoupled cavities and P_x, P_y are the parities in x and y . In analogy with a diatomic molecule, the two lowest energy S and AS modes, $0++$ and $0-+$, correspond to σ bonding and antibonding orbitals from s -like atom states. The $1++$ and $1-+$ modes are the next highest in energy, which correspond to σ bonding and antibonding orbitals from p -like atom states oriented along x . The $1+-$ and $1--$ modes are higher still in energy and correspond to π bonding orbitals from p -like atom states oriented along y . Each of the pairs of modes exhibits an energy splitting dependent on the coupling strength between the two cavities.

Following the seminal work by Bayer *et al.*, a wide variety of PM geometries have been explored, including coupled micropillar [154] and microdisk [216, 217] cavities, and coupled microsphere resonators [218]. PhC cavities, with their favourably high Q/V_0 ratio, soon also became a popular

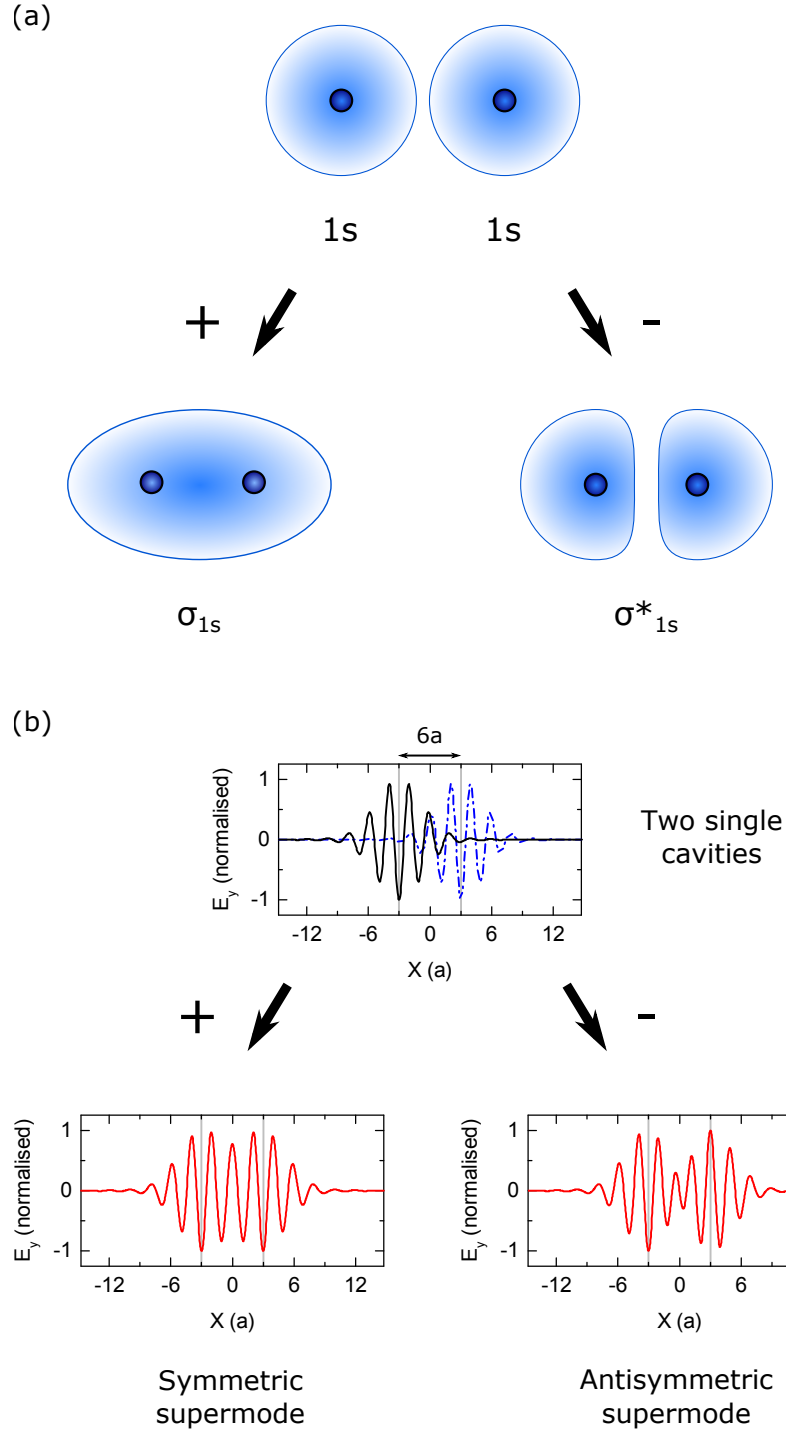


Figure 6.1: Schematic diagram to demonstrate the similarity of diatomic molecular orbitals to PM supermodes. (a) Schematic representation of H_2 diatomic orbitals. The wavefunctions of two independent 1s orbitals constructively or destructively interfere to form the σ_{1s} bonding or σ^*_{1s} antibonding orbitals, respectively. (b) E_y profiles of two identical single cavities (solid black and dashed blue lines) with a separation of 6 lattice units are added/subtracted to predict the symmetric/anti-symmetric supermodes of the resulting PM.

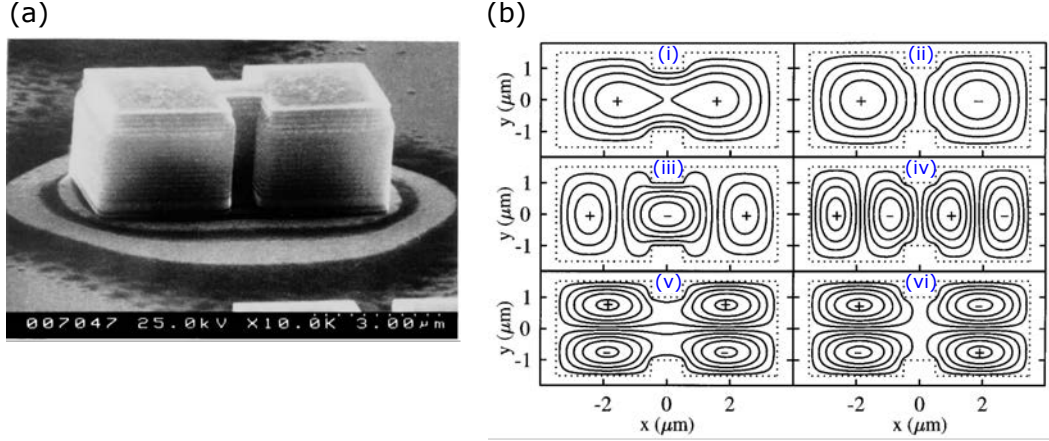


Figure 6.2: The first PM structure, reported in the work by Bayer *et al.* [38], from which these figures are taken. (a) SEM image of the PM. (b) Electric field calculations of the first 6 modes: (i) 0 + +, (ii) 0 - +, (iii) 1 + +, (iv) 1 - +, (v) 1 + - and (vi) 1 - -.

candidate for PMs. Coupled cavity systems utilising the H1 [219, 220], D2 [221, 222, 223, 224], L3 [57, 72, 74, 171, 184, 225, 226, 227, 228, 229, 230], L5 [231] and waveguide [56, 92, 99, 232] cavity geometries have all been investigated. The mode properties of such PM systems, including the coupling-induced mode splitting, are typically adjustable by altering the distance between the two cavities. This allows alteration of the inter-cavity coupling strength via control of the evanescent field overlap. The origins of the coupling-induced mode splitting can be understood by considering the general theory of a coupled system, which we provide an overview of here.

This overview follows the derivation set out by Cohen-Tannoudji *et al.* in Ref. [233] (Ch. 4, pp. 406-415). We first consider a lossless, uncoupled system with two energy eigenstates, $|\psi_1\rangle$ and $|\psi_2\rangle$, of the Hamiltonian H_0 . The eigenvalues of $|\psi_1\rangle$ and $|\psi_2\rangle$ are E_1 and E_2 , respectively. We introduce a time-independent perturbation, W , to the system to represent internal interactions, so that the total Hamiltonian is given by

$$H = H_0 + W. \quad (6.1)$$

In the $\{|\psi_1\rangle, |\psi_2\rangle\}$ basis of eigenstates of the unperturbed Hamiltonian H_0 , W can be represented as a Hermitian matrix:

$$W = \begin{pmatrix} W_{11} & W_{12} \\ W_{21} & W_{22} \end{pmatrix}, \quad (6.2)$$

where W_{11} and W_{22} are real and $W_{12} = W_{21}^*$. The states $|\psi_1\rangle$ and $|\psi_2\rangle$ are no longer eigenstates of the system, because the off-diagonal terms W_{12} and W_{21} induce a coupling between the two

unperturbed states. For simplicity, the diagonal terms that do not govern this coupling will be assumed to be zero: $W_{11} = W_{22} = 0$. The total Hamiltonian for the coupled system can therefore be represented by the matrix

$$H = \begin{pmatrix} E_1 & W_{12} \\ W_{21} & E_2 \end{pmatrix}. \quad (6.3)$$

It can be shown by diagonalising this matrix (see Ch. 4, pp. 420-423 of Ref. [233]) that the new eigenvalues of the system, E_+ and E_- are given by

$$E_{\pm} = \frac{1}{2}(E_1 + E_2) \pm \frac{1}{2}\sqrt{(E_1 - E_2)^2 + 4|W_{12}|^2}. \quad (6.4)$$

The eigenstates of the system, $|\Psi_+\rangle$ and $|\Psi_-\rangle$, corresponding to these eigenvalues are superpositions of the unperturbed states, given by

$$|\Psi_+\rangle = \sin \frac{\theta}{2} e^{i\phi/2} |\psi_2\rangle + \cos \frac{\theta}{2} e^{-i\phi/2} |\psi_1\rangle, \quad (6.5)$$

$$|\Psi_-\rangle = \cos \frac{\theta}{2} e^{i\phi/2} |\psi_2\rangle - \sin \frac{\theta}{2} e^{-i\phi/2} |\psi_1\rangle, \quad (6.6)$$

where the angles θ and ϕ are defined as

$$\tan \theta = \frac{2|W_{12}|}{E_1 - E_2}, \quad 0 \leq \theta < \pi, \quad (6.7)$$

$$W_{21} = |W_{21}| e^{i\phi}. \quad (6.8)$$

The states of the coupled system, $|\Psi_+\rangle$ and $|\Psi_-\rangle$, are therefore positive and negative superpositions of the uncoupled states, weighted by a factor which depends on the ratio of the coupling strength, $|W_{12}|$, to the detuning, $E_1 - E_2$ (and a phase factor). For the case of large coupling strength and small detuning, $|W_{12}| \gg (E_1 - E_2)$, or for finite $|W_{12}|$ with zero detuning ($E_1 = E_2$), the angle $\theta = \pi/2$. Neglecting the phase factor, the states $|\Psi_+\rangle$ and $|\Psi_-\rangle$ are then made up of equal superpositions of $|\psi_1\rangle$ and $|\psi_2\rangle$, in an S or AS combination. In a strongly coupled PM, with a coupling strength much larger than the detuning between the two individual cavity modes, these correspond to the S and AS supermodes. The consequences of a more significant detuning are considered in more detail in section 6.2.5.

We apply the theory of the general coupled system derived here to the lowest order supermodes of a PM, resulting from coupling between the lowest order modes of two individual cavities with frequencies ω_1 and ω_2 . Based on the energy levels of the coupled system expressed in Eq. 6.4, we can expect the frequency splitting, $\Delta\Omega$, between the S and AS supermodes to be given by

$$\Delta\Omega = \sqrt{(\omega_1 - \omega_2)^2 + 4g^2}, \quad (6.9)$$

where g is the coupling strength between the two cavities. An expression for $\Delta\Omega$ in a system with cavity losses can also be obtained by replacing the frequencies of the cavity modes with complex frequencies, in a similar manner to the approach in section 3.3.1. The frequencies ω_1 and ω_2 are replaced with $\omega_1 - i\gamma_1$ and $\omega_2 - i\gamma_2$, respectively, where γ_1 and γ_2 are the field decay rates of the two cavity modes. With these losses, the frequency splitting of the supermodes is given by [225]

$$\Delta\Omega = \text{Re} \left\{ \sqrt{[\omega_1 - \omega_2 - i(\gamma_1 - \gamma_2)]^2 + 4g^2} \right\}, \quad (6.10)$$

where g can also be complex. Evidently, as long as the terms in the square root have a real root, the system exhibits a mode splitting, $\Delta\Omega \neq 0$. As commented on by Lin *et al.* [216], the strong coupling regime for a PM in the case of zero detuning between the cavities ($\omega_1 = \omega_2$) is defined as $\text{Re}(g) > |\gamma_1 - \gamma_2|/2$, for which the root in Eq. 6.10 is real and a mode splitting results. Physically, this corresponds to the regime in which photons can be reversibly exchanged between the two cavities before escaping the system. The weak coupling regime refers to the case in which this reversible exchange of photons is not possible and mathematically corresponds to the case of the terms under the square root of Eq. 6.10 being imaginary. A PM is therefore in the weak coupling regime at zero detuning if $\text{Re}(g) < |\gamma_1 - \gamma_2|/2$ and no energy splitting is present. For cavities with equal linewidths, $2\gamma_1 = 2\gamma_2$, the expression is the same as for the lossless system (eq. 6.9) and a mode splitting is always present as long as $\text{Re}(g) \neq 0$. Interestingly, if the square root of Eq. 6.10 has an imaginary part, the frequencies of the two supermodes have different imaginary components and exhibit a so-called loss splitting [225]. This manifests as a difference in decay rates of the two supermodes of the PM.

In this work, the mode splitting of the PMs studied is measured in units of wavelength, rather than frequency. It is therefore useful to define an equivalent coupling strength to g in units of wavelength. Assuming cavities of equal linewidths, the mode splitting in units of angular frequency is given by Eq. 6.9. We recall that a small angular frequency interval, $\Delta\omega$, can be converted to an equivalent

wavelength interval, $\Delta\lambda$, using the expression

$$|\Delta\lambda| = \left| \frac{\partial\lambda}{\partial\omega} \Delta\omega \right| = \frac{2\pi c}{\omega^2} |\Delta\omega| = \frac{\lambda^2}{2\pi c} |\Delta\omega|, \quad (6.11)$$

where ω and λ are the centre frequency and wavelength of the interval. Applying this to the expression for $\Delta\Omega$ in Eq. 6.9 yields an expression for $\Delta\Lambda$, the mode splitting in units of wavelength [56]:

$$\Delta\Lambda = \sqrt{(\Delta\lambda)^2 + 4J^2}, \quad (6.12)$$

$$\Delta\lambda = \lambda_1 - \lambda_2, \quad (6.13)$$

where $\Delta\lambda$ is the cavity detuning, λ_1 and λ_2 are the wavelengths of the two individual cavity modes (in the absence of coupling) and J is the real part of the coupling strength in units of wavelength. J is related to g by $\text{Re}(g) = (2\pi c/\lambda^2)J$, where λ is the centre wavelength of the splitting.

6.1.2 Photonic crystal cavity photonic molecules

The mode properties of PMs designed to be implemented in photonic devices are largely determined by the device geometry. In theory, it is relatively straightforward to create a PM structure based on existing single cavity technologies, usually by placing two such cavities in close proximity to achieve coupling between them. By making small alterations to the geometry of the PM, the coupling strength can be tailored to engineer the mode splitting and mode profiles of the PM supermodes to suit the application. However, the process of engineering the PM properties – particularly in a coupled PhC cavity system – can be notably complex and computationally demanding, usually relying on FDTD simulations as an invaluable tool. The large variety of factors involved in optimising PhC-based cavities is illustrated in the significant amount of work that has been published on the design of PMs consisting of two coupled L3-type cavities. The simplest way of altering the coupling strength is to change the inter-cavity distance, which generally results in an increase in coupling strength as the cavity separation is reduced. However, the magnitude of the coupling strength, as well as the mode properties, are also strongly influenced by the angle between the coupled cavities [74]. Arranging the cavities at an optimal angle of 30° has been shown experimentally to result in very large mode splittings [227] up to ~ 20 nm (at a centre wavelength of ~ 900 nm), compared to typical splittings of $\lesssim 5$ nm measured for L3 cavities without an offset

angle [171, 225]. Another degree of freedom that can be altered to tune the PM is the hole radius of the PhC lattice: Haddadi *et al.* [228] have demonstrated that the coupling strength between two L3 cavities at 90° can be altered without changing the inter-cavity distance by adjusting the radius of all holes in a single row between them. Through careful engineering of the cavities, it is even possible for the AS supermode to become the ground mode, which has been verified experimentally in L3 cavity PMs by Haddadi *et al.* by imaging the Fourier plane. This phenomenon has also been demonstrated in D2 cavity PMs [223].

PMs based on waveguide heterostructure [92, 232] or local-width-modulated waveguide cavities [56] have been less frequently explored than the L3 PM geometry and could have more potential for novel development and applications as a consequence. A notable application that has been demonstrated is the ability to couple a large chain of these cavities together along a waveguide to engineer slow light propagation with a group velocity less than $0.01c$ [232, 234]. Compared to other methods of achieving slow light [58], the use of coupled resonators offers the potential of a low group velocity dispersion [234]. This would be ideal for CQED applications, which often require the use of pulsed light that would otherwise be unfavourably shaped by a high group velocity dispersion. The coupling strength between two waveguide cavities is commonly tuned either by altering individual PhC holes to engineer the tunnelling barrier between the optical wells of the cavities [56], or by altering the distance between the cavities. The latter of these two methods is applicable to the SU-8 defined cavity PMs studied in this chapter.

A similar concept to writing two SU-8 strips to form a PM has been presented by Brossard *et al.*, in which the cavities are defined by inkjet-printed strips on a PhC waveguide [99]. However, the SU-8 writing method offers novelty over this technique with the major advantage that it can be used at cryogenic temperatures, offering the potential of deterministically coupling PM modes to a QD located using low temperature μ PL measurements.

6.1.3 Effects of photonic molecule detuning

While the use of FDTD methods enables the properties of PhC PM modes to be intricately designed to suit specific applications, in practice it is difficult to precisely achieve the desired properties in fabricated devices. The presence of minor fabrication imperfections, typically arising from inconsistencies in the e-beam patterning and etching process, is well-known to introduce detuning between the cavities [56, 171, 225, 227, 230, 232, 235]. This disorder-induced detuning

has a detrimental effect on the coupling of the PM and results in mode localization towards the individual cavities [56]. A variety of sophisticated tuning methods have been developed to correct for the disorder-induced detuning, which require selective tuning of one cavity relative to the other. One such technique is photo-oxidative tuning [57, 223], in which a focused laser spot can be used to selectively induce oxidation in close proximity to one of the cavities, lowering the local refractive index and causing a blueshift of one cavity only. A disadvantage of this technique, however, is that the photo-oxidation is irreversible and so it cannot be applied as a dynamic tuning process. A notable, reversible tuning process that has been successfully demonstrated is tuning via nanofluidic deposition [221, 235]. In this process, fluid is locally injected into holes of the PhC near one of the cavities, which raises the local refractive index and redshifts the cavity mode. By applying a heating laser, the fluid can be evaporated in a controlled manner to fine-tune the cavity wavelength. A major disadvantage of both the photo-oxidative and nanofluidic deposition tuning methods is that they cannot be used under vacuum and therefore are not suitable for experiments at cryogenic temperatures. As such, they are not suited to devices operating with few or single QDs. A promising alternative is the use of photo-chromic tuning techniques, in which a photo-chromic thin film is spin-coated over the sample [231]. The refractive index of the film can be locally and reversibly modified by laser illumination of different wavelengths, enabling selective tuning of a single cavity, even at cryogenic temperatures. Another similar possibility that has been explored is the application of a chalcogenide glass layer to the top of the PhC, which can be locally photodarkened to tune a cavity [236]. While these techniques have seen success for conventional PhC cavities, it is unlikely that they are compatible with SU-8 strip cavities, since the cavity design already relies on material on top of the PhC. It is not clear whether the cross-linked SU-8 itself could be given photo-chromic properties, but this would be an interesting prospect.

Other known tuning methods also present compatibility problems with our SU-8 PM device and measurement system: thermo-optic (also known as photothermal) tuning [92, 237] via a focused laser spot is possible but the heating effect may not be well-localized enough to selectively heat one cavity, especially if the SU-8 strips scatter or obstruct the heating laser. Local variation of the refractive index to tune cavities is also possible via carrier injection [92, 238], but again may not be well localized enough and will also cause emission from the QDs, which could make single QD measurements (for coupling experiments) difficult. Other reported PhC cavity tuning methods include nano-mechanical tuning using an AFM tip [239], although this would require a highly specialised experimental setup to implement. Similarly, the use of radio frequency surface acoustic

waves to dynamically tune PM cavities in and out of resonance on sub-nanosecond timescales by periodic deformation of the PhC has been demonstrated [230], but requires a highly specialised sample structure and experimental apparatus. Furthermore, this tuning technique appears unable to statically tune the cavities into resonance, so would not be useful for time-integrated μ PL mapping measurements.

A significant advantage of applying a tuning method is that it enables anticrossing of the two cavity modes of a PM to be observed as the detuning is altered to zero. This behaviour proves that the two cavities of the PM are strongly coupled to each other and enables a direct measurement of the coupling strength, equal to half the mode splitting at the zero detuning point [57, 92, 216, 223, 230, 231, 235]. In section 6.3, we present a method of indirectly estimating the coupling strength that does not require tuning of the cavity modes. Using μ PL mapping measurements, the coupling strength and the cavity detuning are extracted from the PM mode splitting and delocalization.

6.1.4 Applications of photonic molecules

PMs have found a number of applications relevant to the fields of quantum optics, as well as quantum information and communication. Perhaps the highest impact application of a PM to date was by Dousse *et al.* [154], who demonstrated an ultrabright source of polarization-entangled photon pairs from a micropillar PM coupled to a single QD. The unique advantage offered by a PM rather than a single cavity was the ability to engineer the mode splitting of the PM modes such that two of the modes coupled simultaneously to two different energy transitions in a biexciton cascade decay. This coupling enabled Purcell enhancement of both steps of the decay, facilitating the brightest source of entangled photons (in terms of photon pair rate per excitation pulse) reported at the time. The work by Dousse *et al.* utilized a novel technique incorporating photoresist to position the micropillars, which the author cites as being influenced by previous work on registration of QDs using SU-8 photoresist markers [192] and is similar to the SU-8 cavity-writing technique employed in this work. Single QDs were identified using μ PL measurements and two disks were exposed in a photoresist to define the PM, which served as masks for etching. The success of such a technique, which enabled deterministic coupling between the PM and QD, is very encouraging for the potential applications of the SU-8 cavities in this work. If a similar coupled QD-PM source of entangled photons could be achieved using our SU-8 PMs, it could benefit from the generally higher Q/V_0 ratio achievable in PhC cavities relative to micropillar cavities, which could potentially

result in an even brighter Purcell-enhanced source.

Currently at the leading-edge of research on PMs is a phenomenon referred to as the unconventional photon blockade [240]. First proposed by Liew *et al.* [241], the coupling between two microcavities can enable a photon blockade to be achieved which suppresses the two-photon emission probability from a system. This was shown by Bamba *et al.* [242] to be applicable to a Jaynes-Cummings system (a coupled cavity structure with a single emitter) and explained in terms of a quantum interference effect. A significant benefit of exploiting the unconventional photon blockade in a QD-PM coupled system would be that a photon blockade can be achieved with a weakly coupled QD, rather than the more challenging requirement of a strongly coupled system for a conventional photon blockade [67, 174]. It has even been predicted that, under certain conditions, counter-polarized single photon emission from the non-pumped cavity of the PM can be achieved [243].

The unconventional photon blockade has been demonstrated in the microwave domain via coupled superconducting resonators [244] and in a coupled QD-micropillar system by Snijders *et al.* [245]. In the work by Snijders *et al.*, a single QD was coupled to orthogonally polarised modes of a single micropillar cavity, which functioned analogously to a coupled cavity system. The unconventional photon blockade was confirmed via the detection of antibunched photons. The potential for deterministic dot-cavity coupling offered by our SU-8 cavity writing method could help facilitate observation of the unconventional photon blockade in a QD-PhC cavity system if PMs can be reliably fabricated. However, there would be some limitations to overcome: most notably, observation of the effect is made easier by exploiting counter-polarized modes, which may not be achievable in an SU-8-defined PM. Furthermore, the unavoidable coupling-induced mode splitting of the PM modes may suppress the quantum interference effect responsible for the unconventional photon blockade, which assumes energy-degenerate modes [242].

Another implementation of PMs has been in the dynamic control of light-matter coupling in CQED experiments. Bose *et al.* [184] have demonstrated the ability to tune a single QD in and out of resonance with a PM mode by applying a cavity-enhanced Stark shift induced by a second PM mode that is not resonant with the QD. Later work [72] then showed that this could be applied on ultrafast timescales with a QD strongly coupled to one PM mode and a pulsed laser used to control the Stark shift induced by the second mode, enabling dynamic control of the emitter-cavity coupling. Another experiment by Jin *et al.* [92] facilitated ultrafast control of Purcell enhancement of QD ensemble emission, utilising a PhC waveguide double heterostructure cavity coupled to a

Fabry-Perot cavity. By tuning the Fabry-Perot modes into resonance with the cavity mode, the Q factor could be altered to control the Purcell factor on ultrafast timescales. Similar applications to these works should be possible using an SU-8-defined PM architecture, with the additional benefit of increased reproducibility due to the potential for deterministic QD-cavity coupling.

A variety of other interesting works on PMs are less inclined to benefit specifically from the advantages offered by SU-8-defined PMs, but are detailed here for completeness. These include the demonstration of cavity coupling over long distances via a PhC waveguide [83], for which the cavity tuning could be turned off via optically-controlled tuning to freeze the photon state, leaving the photons predominantly confined to one cavity. Another method with the potential to controllably trap light is the all-optical analogue to electromagnetically-induced transparency presented by Yang *et al.* [246]. PMs also offer potential as on-chip coherent light sources, with the interesting potential for switchable lasing between the S and AS modes [247]. PM lasers have even been used to experimentally investigate spontaneous mirror-symmetry breaking using two states localized preferentially towards each cavity of the PM [248]. Optical switching of these states was also demonstrated, which could be applicable to optical memories.

Overall, the development of SU-8 PMs shows promise for a number of potential high-impact applications in the control of light-matter coupling and the achievement of single photon sources. The ability to position the two SU-8 strips based on μ PL measurements of single QDs offers the advantage to alter the position, structure and wavelength of the PM supermodes as necessary to suit the application and compensate for variation in the QD position and emission lines. As long as the SU-8 cavity fabrication process can be precisely controlled, coupling between a PM and a QD should be much more reliably achievable than with a random, brute-force approach, paving the way towards scalable devices for practical applications.

6.2 FDTD simulations of SU-8 strip photonic molecules

6.2.1 Initial investigation

The behaviour of two SU-8 strip cavities on the same PhC waveguide was first investigated using FDTD simulations to verify the potential for inter-cavity coupling, predict properties of the system and identify parameters that could be measured experimentally. Simulations were performed to model a PhC waveguide with the same geometry and parameters as the PhC waveguide described

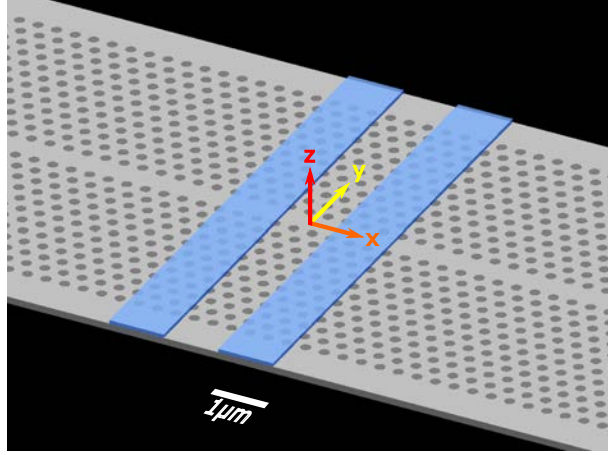


Figure 6.3: 3D render of a typical SU-8 strip PM structure that FDTD simulations were performed for. The GaAs slab is shown in grey, with darker circles representing the hole locations of the PhC lattice. The SU-8 strips are represented in blue, with a $2\ \mu\text{m}$ centre-to-centre separation in this example. Render produced using Lumerical FDTD solutions software [49].

in section 2.6.2. The waveguide is defined parallel to the x -direction, as illustrated in Fig. 6.3, a 3D render of a typical simulated structure. SU-8 strips with height $h_{\text{strip}} = 100\text{ nm}$ and width $w_{\text{strip}} = 1\ \mu\text{m}$ were initially investigated, with a length spanning the extent of the PhC in the y -direction and no infiltration of the PhC holes by the SU-8. As noted in section 5.2.1, the potential for SU-8 infiltration into the PhC holes, not accounted for here, is not expected to have a detrimental effect on the cavity modes. Unless stated otherwise, all simulation results in this chapter are for 100 nm -thick, $1\ \mu\text{m}$ -wide SU-8 strips with no hole infiltration.

The FDTD simulations of the SU-8 strip PMs were performed following the methodology outlined in section 2.4. Simulations were run with resolution parameters $\rho_x = 20$, $\rho_y = 20$ and $\rho_z = 30$. Symmetry conditions were carefully selected to isolate modes of interest: applying a symmetric or anti-symmetric boundary condition at $x = 0$ enabled selection of the S or AS supermodes of the PM, respectively. An anti-symmetric boundary condition was applied at $y = 0$ to reduce the computation time, while no symmetry condition could be enforced at $z = 0$ due to breaking of the z -symmetry by the SU-8 strips.

FDTD simulations were performed for a range of SU-8 strip separations to investigate the effect on the mode structure and coupling-induced mode splitting. The resulting E_y field profiles presented in Fig. 6.4 demonstrate clearly the hybridization of the individual cavity modes into the supermodes expected for a PM. This is perhaps most evident for a strip separation of $2\ \mu\text{m}$, for which the S supermode is highly delocalized over the PM, extending across the two strips and the gap between them. Additionally, the AS supermode possesses a sharp local minimum in intensity in the space

between the strips. As explained with the aid of Fig. 6.1 in section 6.1.1, these characteristics are analogous to the σ_{1s} and σ^*_{1s} orbitals of a diatomic molecule. We observe that as the SU-8 strip separation is increased beyond $2\text{ }\mu\text{m}$, the modes become more localized towards the individual cavities. This indicates a weaker coupling strength between them, which is to be expected from the reduced overlap of the evanescent fields of the individual cavity modes. As the strip separation is reduced below $2\text{ }\mu\text{m}$, the modes approach the S ground mode and AS excited mode expected from a single cavity [56]. A strip separation of $1\text{ }\mu\text{m}$ corresponds to a $2\text{ }\mu\text{m}$ -thick SU-8 strip, for which we observe these single cavity modes.

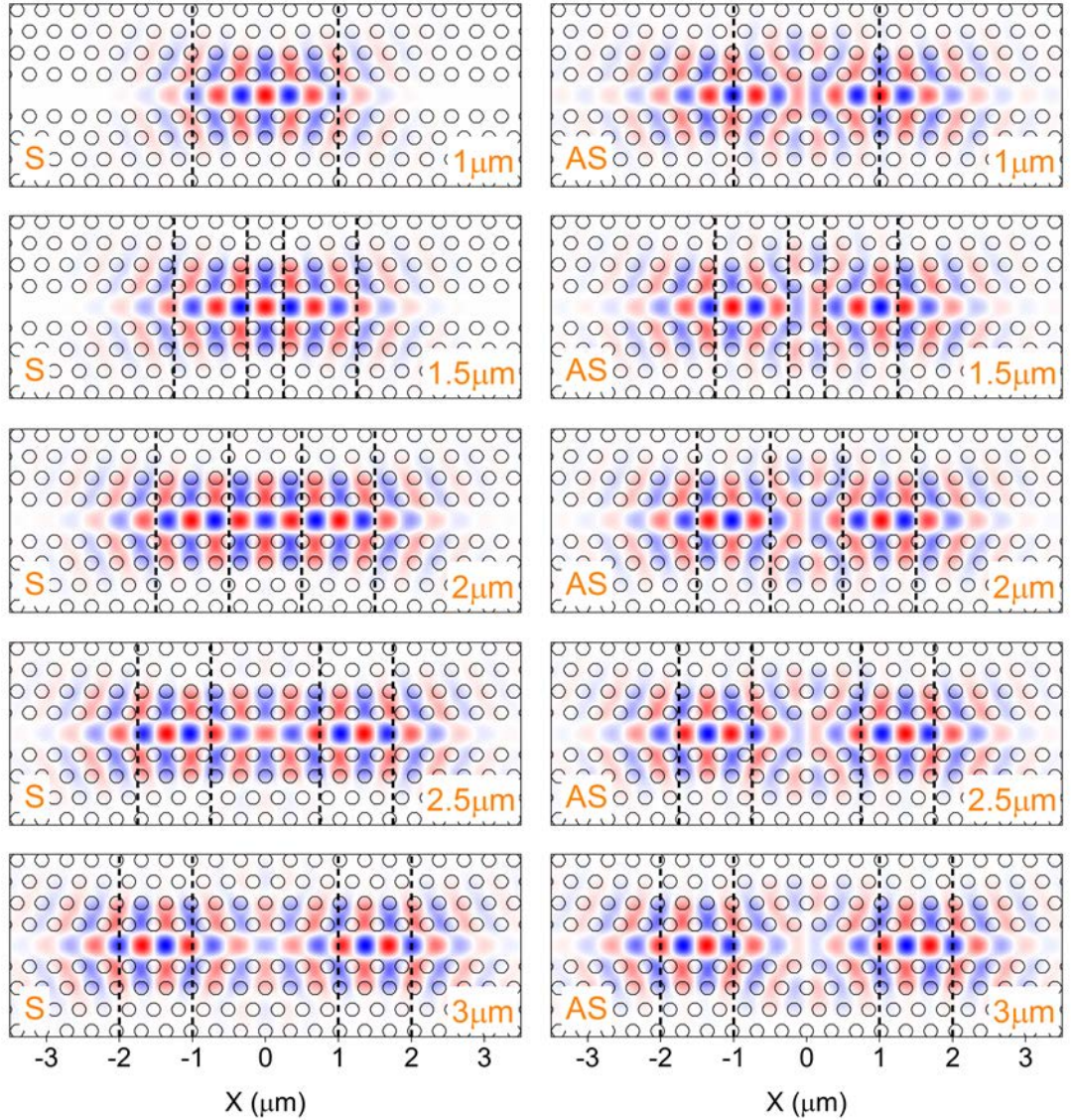


Figure 6.4: Simulated E_y field profiles of the S and AS modes for SU-8 strip PMs of varying separation, with a thickness of 100 nm and strip width of $1\text{ }\mu\text{m}$. Boundaries of the SU-8 strips are indicated by the dashed lines; the mode type and strip separation are labelled in the bottom left and right corner of each diagram, respectively. A separation of $1\text{ }\mu\text{m}$ corresponds to a single strip of $2\text{ }\mu\text{m}$ width. Red and blue correspond to opposite polarities of the field.

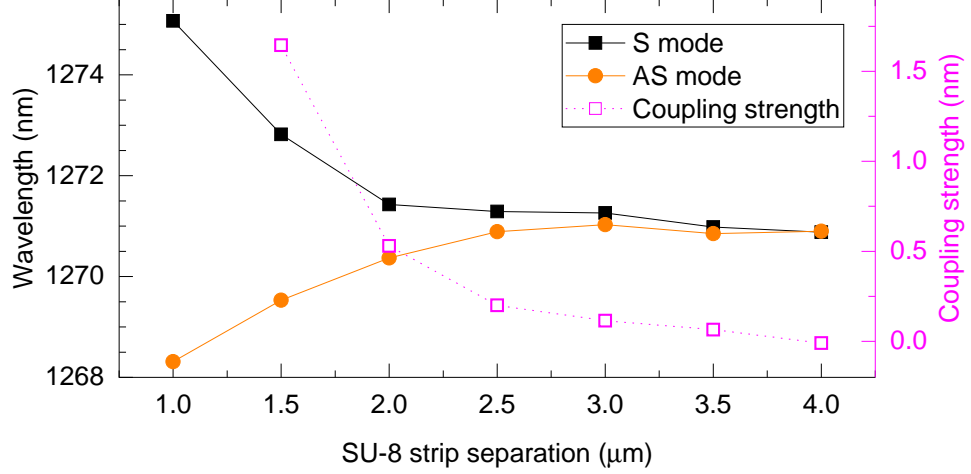


Figure 6.5: Wavelengths of the symmetric (S) and anti-symmetric (AS) modes predicted by FDTD simulations for SU-8 strip PMs of 100 nm thickness (and 1 μm width) with varying strip separation. Also plotted in magenta is the real part of the coupling strength, J , calculated from the simulations. A separation of 1 μm corresponds to a single strip of 2 μm width, for which the coupling strength is not applicable.

In order to quantify the coupling strength, the wavelengths of the S and AS modes were extracted from the simulations. These are plotted in Fig. 6.5 and clearly demonstrate increasing mode splitting as the SU-8 strips are brought closer together, gradually approaching the characteristically large mode splitting expected for a single cavity [56]. We observe that the S supermode is always the ground mode, although in general an AS ground state is possible in PM structures [223, 224, 228]. As shown in section 6.1.1, the predicted mode splitting, $\Delta\lambda$, of a PM formed from cavities with equal linewidths can be related to the coupling strength, J , using Eq. 6.12. This expression can be simplified even further for the PMs simulated, which are composed of two identical cavities and therefore possess zero wavelength detuning ($\Delta\lambda = 0$). Hence, the coupling strength can be extracted from the mode splitting via

$$J = \Delta\lambda/2, \quad (6.14)$$

for which the simulated values are plotted in Fig. 6.5. The trend displayed by the numerical values of the coupling strength match our expectations from the behaviour of the S and AS field profiles in Fig. 6.4.

6.2.2 Q factor and mode volume

The Q factor and mode volumes of the S and AS PM modes were extracted from the FDTD simulations for each SU-8 strip separation. In addition to confirming that a high Q/V_0 ratio is achievable, this revealed some interesting and unexpected behaviour exhibited by the coupled cavity system. The total quality factor, Q_{total} , of the S and AS modes is plotted as a function of strip separation in Fig. 6.6(a). The magnitude of Q_{total} for each mode clearly exhibits an oscillation with strip separation: when one of the S or the AS modes exhibits a local maximum in Q_{total} , the other mode is at a local minimum. The full period of these oscillations is approximately $6a$. Additional simulations were performed with strip separations that were an integer multiple of a , in order to check that finer details in the pattern were not being missed. Data for strip separations of $5a$ ($1.7\text{ }\mu\text{m}$), $6a$ ($2.04\text{ }\mu\text{m}$), $7a$ ($2.38\text{ }\mu\text{m}$) and $8a$ ($2.72\text{ }\mu\text{m}$) are included in Fig. 6.6(a), which do not reveal any additional behaviour.

We propose that the oscillatory behaviour of the Q factor is due to a subtle interference effect between the two cavities, which results in variable cancellation of losses as the separation is altered [74]. Further investigations beyond the scope of this work would be recommended to fully characterise the effect. However, it is not expected to be of major significance for the purposes of this work, as the effect is likely to be destroyed by cavity detuning in a real system due to its significant influence on the mode structure (see section 6.2.5). For this reason, the effect is not examined further here and we expect that the Q factors of real devices will lie towards the lower end of Q_{total} simulated here. More details on the effects of field cancellation on Q factors of single cavity modes can be found in Ch. 8 of the textbook by Joannopoulos *et al.* [39].

The mode volumes extracted from the SU-8 PM simulations are shown in Fig. 6.6(b), which demonstrate behaviour that would be expected for a coupled cavity system. For a single, $2\text{ }\mu\text{m}$ -wide cavity (strip separation $1\text{ }\mu\text{m}$), the double-peaked AS mode has a significantly larger mode volume than the single-peaked S ground mode. As the strip separation is increased, the S mode volume initially increases more sharply than the AS mode volume, as the S mode shape changes more dramatically. For moderate strip separations of $\sim 2\text{ }\mu\text{m}$ – $3\text{ }\mu\text{m}$, the S mode volume is noticeably larger than the AS mode volume. This is due to the constructive interference of the constituent cavity modes for the S mode, versus the destructive interference for the AS mode. As the strip separation becomes wide enough that the coupling strength approaches zero ($\gtrsim 3.5\text{ }\mu\text{m}$), the system tends towards two uncoupled cavities. The mode volumes of the S and AS modes converge to a

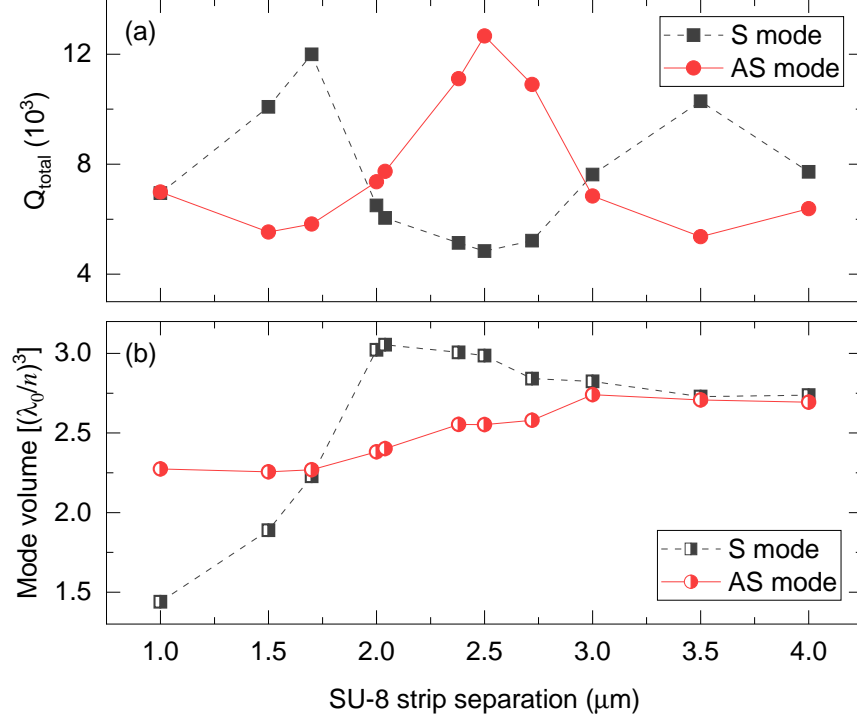


Figure 6.6: Total Q factor (a) and mode volume (b) of the S and AS modes extracted from FDTD simulations of an SU-8 strip PM with varying SU-8 strip separation.

value of $\sim 2.7(\lambda_0/n)^3$ – approximately double the $1.36(\lambda_0/n)^3$ mode volume of the ground mode of a single SU-8 strip cavity with $h_{\text{strip}} = 100 \text{ nm}$ and $w_{\text{strip}} = 1 \mu\text{m}$, which is what would be expected intuitively. As with the Q factors, the mode volume is expected to be significantly affected by the effects of detuning which, as shown in section 6.2.5, can have a dramatic effect on the mode profiles.

6.2.3 Energy transfer between photonic molecule cavities

Additional simulations were performed to confirm coupling between the cavities of the PM, by monitoring the transfer of electromagnetic energy. For these simulations, the symmetry condition at $x = 0$ was removed and the PM was excited asymmetrically by placing a dipole source in the right-hand cavity. This technique, which has been applied in the literature to optimize PM design [83, 225, 229], excites both the S and AS supermodes simultaneously. A magnetic dipole source, polarised along the z -direction, was positioned at an antinode common to the S and AS modes in the right-hand cavity, to excite both modes efficiently. The x position of this antinode was selected as the closest integer multiple of a from the origin to the centre of the SU-8 strip. The electric field was then monitored at equivalent positions in both the left and right cavities.

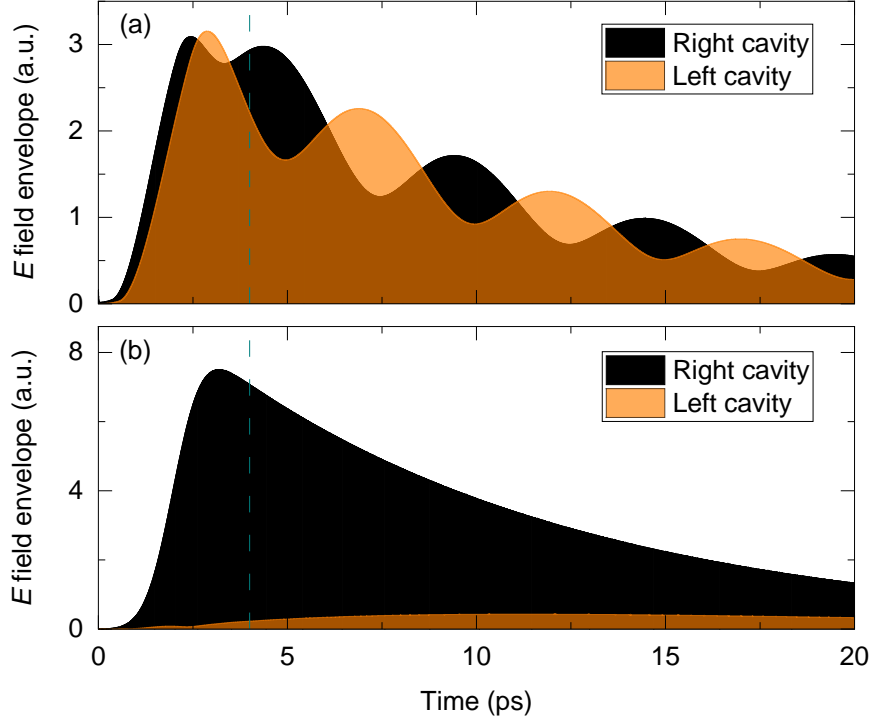


Figure 6.7: Envelope of the electric field magnitude recorded at antinodes of the left and right cavity of SU-8 PMs with different separations, excited at the right hand cavity. (a) SU-8 PM with $2\ \mu\text{m}$ strip separation, showing strong evidence of reversible photon transfer indicative of the strong coupling regime. (b) SU-8 PM with $4\ \mu\text{m}$ strip separation, showing no evidence of reversible photon transfer. The dashed dark cyan line marks a time at which the source has fully decayed.

Results for a PM with a $2\ \mu\text{m}$ strip separation (coupling strength $0.53\ \text{nm}$) in Fig. 6.7(a) clearly demonstrate picosecond-timescale oscillations of the field between the two cavities. This is significantly slower than the oscillating fields of the individual modes, which occur on a fs timescale, hence only the field envelopes are plotted. The oscillations result from beating of the S and AS modes, enabling energy transfer back and forth between the two cavities. We interpret this as the reversible transfer of photons anticipated in the strong coupling regime, discussed in section 6.1.1. The timescale of these oscillations is far too short to be observed experimentally with the equipment available, so unfortunately cannot be used as an indicator of strong coupling for real devices. However, it is interesting to note that by coupling cavities through a waveguide over much longer distances ($\sim 80\ \mu\text{m}$), Sato *et al.* were able to slow the oscillations down sufficiently to measure them experimentally [83].

It is evident from Fig. 6.7(a) that the energy oscillations between the cavities are incomplete – that is, the field at one cavity does not oscillate to zero when the field is at a maximum in the other cavity. This is attributed to a non-zero imaginary part of the coupling strength, $\text{Im}(g)$ [225], which results in a loss splitting of the S and AS supermodes radiative decay rates. This prevents

complete energy transfer between the cavities, but can usually be accounted for by structural optimisation, typically by fine-tuning the geometry of specific holes in the PhC [229]. Complete energy transfer is desirable for potential applications of a PM as an optical switch. Unfortunately such optimisation is not compatible with the SU-8 strip PM system, as requiring specific holes to be tuned relative to the cavity positions would negate the main advantage of the technique, which is the freedom to position the cavity modes at the desired location along the waveguide. Given the variation of the Q factor with cavity separation, shown in Fig. 6.6, it could be possible to tune the loss splitting to zero by choosing the appropriate strip separation. However, this would come at the cost of significantly altering $\text{Re}(g)$. The inability to correct for the loss splitting is therefore an inherent disadvantage of the SU-8 strip technique for fabricating PMs, unless post-fabrication tuning methods can be developed to overcome this issue. Such methods are beyond the scope of this work, but are not believed to be necessary for key applications such as achieving Purcell enhancement of multiple excitonic transitions of a QD [154].

The energy transfer in a PM with negligibly small coupling strength was also investigated by selecting a strip separation of $4\text{ }\mu\text{m}$. The coupling strength for this separation approaches zero (within error) and this is reflected in the results shown in Fig. 6.7(b). We no longer see evidence of reversible photon transfer between the cavities, as in Fig. 6.7(a). Instead, the field in the right hand cavity decays as we would expect a single cavity to, while only a small amount of energy is transferred to the left cavity. This would suggest that the two cavities are very weakly coupled at this separation, which is consistent with the imperceptible mode splitting (since weakly coupled cavities do not exhibit a mode splitting). We note that the definition of the strong coupling regime as $\text{Re}(g) > |\gamma_1 - \gamma_2|/2$ is slightly problematic in this instance, as both the $\text{Re}(g)$ and $|\gamma_1 - \gamma_2|$ tend to zero for this simulation. However, in a physical system, a realistic value of $|\gamma_1 - \gamma_2|$ would result in the system being categorised as weakly coupled.

6.2.4 Predictions for micro-photoluminescence measurements

In order to prove that experimentally realised SU-8 double-strip devices optically couple to form PMs, it was necessary to predict trends in parameters that could be consistently measured by the μPL experimental system. The PM supermode profiles expected from μPL mapping measurements along the PhC waveguide were estimated by convolving the $|\mathbf{E}|^2$ profile along $y = 0$ with a $1\text{ }\mu\text{m}$ FWHM Gaussian to represent the excitation spot. The predicted mode profiles from this

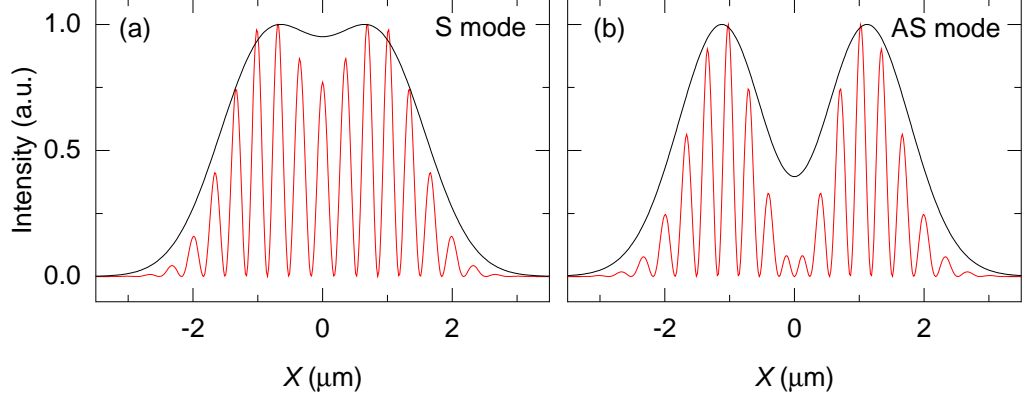


Figure 6.8: Simulated $|E|^2$ profile (red) through $(y, z) = 0$ for the S (a) and AS (b) supermodes of an SU-8 strip PM with $2\ \mu\text{m}$ separation. The convolution of each profile with a $1\ \mu\text{m}$ FWHM Gaussian is shown (black) to represent the mode profile resolved by the μPL system. All profiles are normalised.

method for a PM with $2\ \mu\text{m}$ strip separation displayed in Fig. 6.8 demonstrate a characteristic supermode shape that is analogous to the bonding and antibonding orbitals of a diatomic molecule. The AS supermode [6.8(b)] is easily characterised by its significant antinode, whereas the central dip in intensity of S supermode [6.8(a)] is not easily resolved by the μPL system. As indicated by the field profiles in Fig. 6.4, the spacing of the S mode peaks increases with the SU-8 strip separation, enabling the two peaks to be resolved at larger cavity separations. However, the AS mode can always be resolved as two peaks, regardless of the strip separation. The spatial positions of the AS mode peaks are therefore a useful parameter to quantify and compare the mode behaviour of the PMs.

We define the AS peak separation as the centre-to-centre distance between the two peaks, which is plotted as a function of strip separation in Fig. 6.9, in addition to the S-AS mode splitting predicted by the FDTD simulation results. At large strip separations (around $4\ \mu\text{m}$), the behaviour of the system tends towards what we would expect for weakly coupled or uncoupled cavities, with a negligibly small mode splitting and an AS peak separation that closely matches the strip separation (corresponding to modes highly localized at each cavity position). As the strip separation is reduced, the increase in coupling strength is indicated by an increased mode splitting, in addition to an increase of the AS peak separation beyond the strip separation. For short separations, the system gradually evolves from a PM to a single cavity, which can be distinguished from a PM by its characteristically large mode splitting and significant divergence of the AS peak separation away from the line of equality with strip separation.

Together, the mode splitting and AS peak separation provide a summary of the PM mode behaviour

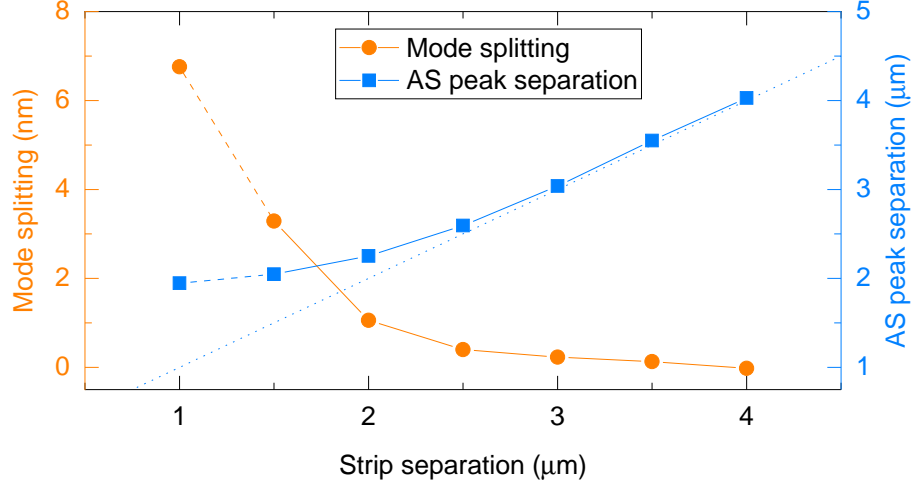


Figure 6.9: Simulated values of the S-AS mode splitting and AS peak separation for 100 nm thick, 1 μm -wide SU-8 strip PMs of varying separations, to be compared with μPL measurements. The dashed blue line is to guide the eye. A separation of 1 μm corresponds to a single strip of 2 μm width.

that can be easily measured experimentally and compared with simulation results to verify successful fabrication of SU-8 PMs. However, the additional effects of cavity detuning, not present in the simulations so far, must be accounted for. This is considered in section 6.2.5.

6.2.5 Theory and modelling of detuned photonic molecules

The effects of cavity detuning, which have not been accounted for so far, are a significant factor to consider in experimentally-realised PhC-defined PM devices. As discussed in section 6.1.3, minor imperfections in the PhC geometry, resulting from e-beam patterning and etching process inconsistencies, introduce random variation to cavities that would otherwise be identical. This commonly results in wavelength variation of up to several nm between cavity modes, even if they are in close proximity on the chip [57, 171, 227]. Without the use of sophisticated tuning techniques, detuning effects in coupled PhC cavity PMs are unavoidable and need to be accounted for. For the SU-8 PM cavity system, we must also make the consideration that inconsistencies and variations in the SU-8 strip geometry may introduce additional detuning effects beyond the anticipated PhC geometry imperfections.

To investigate the effect of detuning on the PM supermodes, FDTD simulations were performed with non-identical coupled cavities. A simple method was applied to tune the wavelength of one of the cavities: by increasing the thickness of the SU-8 strip, the cavity mode is redshifted, as was shown in section 5.2. The symmetry condition at $x = 0$ was removed and the left cavity

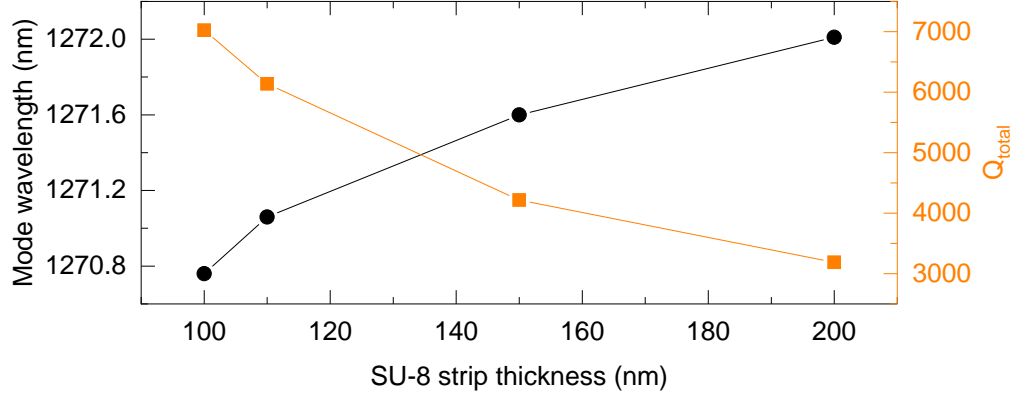


Figure 6.10: FDTD simulation results for a single SU-8 strip cavity of $1\mu\text{m}$ width. The mode wavelength is shown by black circles and Q_{total} is represented by orange squares.

was detuned from the right cavity by altering the thickness of the left SU-8 strip. The magnitude of the wavelength detuning, $\Delta\lambda$, between the two cavities was estimated from separate simulations of single SU-8 strip cavities of the corresponding thickness, the results of which are shown in Fig. 6.10. A strip separation of $6a$ ($2.04\mu\text{m}$) was used so that both strips had the same alignment relative to the PhC lattice as in the single strip simulations, with a local field antinode exactly at the centre of each strip. The right strip thickness was kept as 100 nm and left strip thicknesses of 100 nm , 110 nm , 150 nm and 200 nm were used to simulate estimated detunings of 0 nm , 0.3 nm , 0.8 nm and 1.3 nm , respectively. Both strip widths were kept as $1\mu\text{m}$.

The effects of detuning on the E_y field profiles of the S and AS supermodes are demonstrated in Fig. 6.11. We observe that as the detuning is increased, the modes become more localized towards the individual cavities: the S ground mode is localized towards the lower energy cavity mode defined by the thicker SU-8 strip, whereas the AS excited mode is localized towards the higher energy cavity mode defined by the thinner SU-8 strip. This effect has been characterised for a similar PM system by Brossard *et al.* [56], which explored coupled WMLD cavities in a waveguide generated by hole shifts of the PhC lattice. For the SU-8 PMs, we utilise and extend upon the theory applied by Brossard *et al.*, which is derived from the coupled system theory covered in section 6.1.1. It follows from Eqs. 6.5 and 6.6 that the modes of the coupled system, $\Psi_+(\mathbf{r})$ and $\Psi_-(\mathbf{r})$, are given by linear combinations of the isolated cavity modes, $\psi_1(\mathbf{r})$ and $\psi_2(\mathbf{r})$:

$$\Psi_+(\mathbf{r}) = \left(\sin \frac{\theta}{2} \right) \psi_2(\mathbf{r}) + \left(\cos \frac{\theta}{2} \right) \psi_1(\mathbf{r}), \quad (6.15)$$

$$\Psi_-(\mathbf{r}) = \left(\cos \frac{\theta}{2} \right) \psi_2(\mathbf{r}) - \left(\sin \frac{\theta}{2} \right) \psi_1(\mathbf{r}), \quad (6.16)$$

$$\tan \theta = 2J/\Delta\lambda, \quad (6.17)$$

where θ is a weighting factor. We confirm the validity of this model by applying the semi-analytical approach used by Brossard *et al.* and comparing the results to full FDTD simulations. In the semi-analytical approach, the E_y mode profile of a single, 100 nm-thick, 1 μm -wide SU-8 strip cavity was obtained from FDTD simulations and used to represent $\psi_1(\mathbf{r})$ and $\psi_2(\mathbf{r})$. The S mode and AS mode profiles predicted by the model were then calculated from the expressions for $\Psi_+(\mathbf{r})$ and $\Psi_-(\mathbf{r})$ (Eqs. 6.15 and 6.16), respectively. In Fig. 6.12, the $|E_y|^2$ profiles (along $x = 0$) of the modes calculated using the two approaches are compared for a range of detunings. We choose to compare $|E_y|^2$ as an approximation of the mode intensity, from which the mode profiles observable by μPL

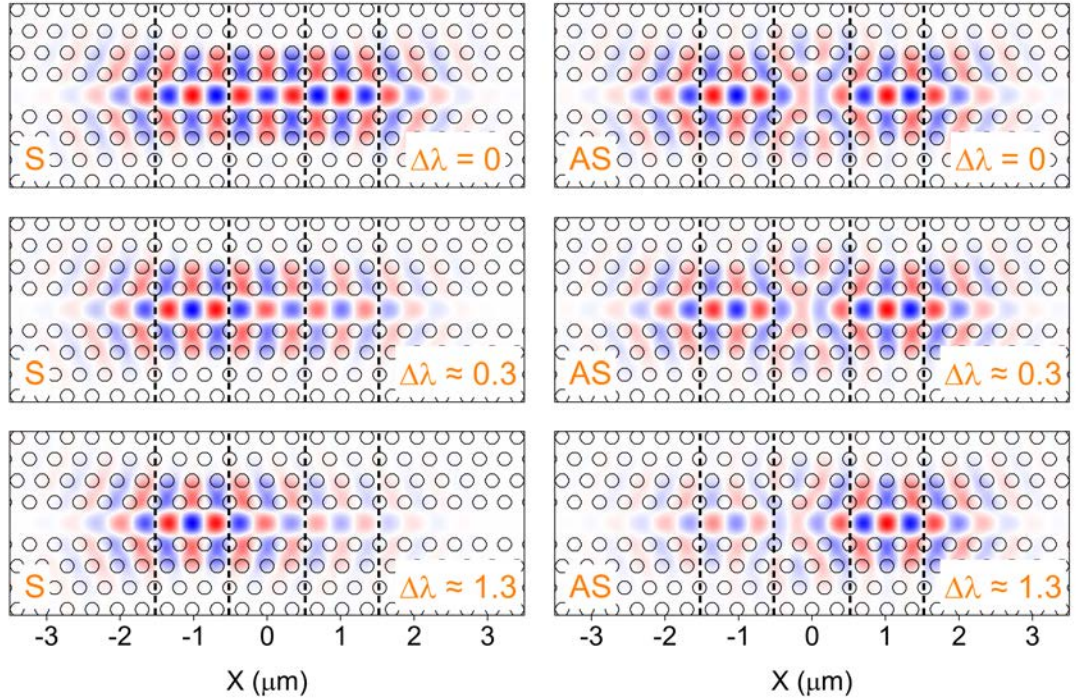


Figure 6.11: Simulated E_y field profiles of the S and AS modes for SU-8 strip PMs of 2 μm separation, with varying degrees of detuning. All detunings, $\Delta\lambda$, are in units of nm. The right strip has a thickness of 100 nm in all simulations; detuning estimates of 0 nm, 0.3 nm and 1.3 nm correspond to thicknesses of 100 nm, 110 nm and 200 nm of the left strip, respectively. Red and blue correspond to opposite polarities of the field.

mapping were predicted by convolving the $|E_y|^2$ profile with a $1\text{ }\mu\text{m}$ FWHM Gaussian. In general, the semi-analytical model is in relatively good agreement with the full FDTD simulation results, which supports the use of coupled mode theory as an approximation to the system. The two approaches offer the closest match for zero detuning and large detunings (such as $\Delta\lambda \approx 1.3\text{ nm}$), with some more significant (but still small) discrepancies arising for small non-zero detunings, as seen for $\Delta\lambda \approx 0.3\text{ nm}$. This is important to consider in the analysis that follows, although it should be noted that this will focus on the AS supermode, which exhibits a smaller discrepancy than the S supermode at small detunings. It is also important to note that the detuning has no significant effect on the AS peak separation, so the values of this in Fig. 6.9 are still applicable for PMs with finite detuning. An additional factor to consider is the significant effect on the Q factor that altering a single strip's thickness has, which is evident from Fig. 6.10. This may also contribute to the discrepancy between the two models, as the semi-analytical approach assumes identical individual cavities and does not account for different linewidths.

In order to characterise the effect of detuning on a physical system, we require a parameter that can be measured via μPL measurements. It is clear from Fig. 6.12 that the relative height of the two AS mode peaks measured by μPL mapping can provide information about the detuning of a PM, as a measure of the mode delocalization. As noted by Brossard *et al.*, it is useful to define the delocalization factor, F , of a given mode as the ratio of the electric field energy at the centres of the two cavities of the PM. It is always defined as the lowest divided by the highest of the two field energies. By considering the field intensities predicted from coupled mode theory, an expression for F can be derived. We consider the AS supermode, with mode intensity represented by $|\Psi_-(\mathbf{r})|^2$. The delocalization factor of the mode is defined as:

$$F = \frac{|\Psi_-(\mathbf{r}_1)|^2}{|\Psi_-(\mathbf{r}_2)|^2}, \quad (6.18)$$

where \mathbf{r}_1 and \mathbf{r}_2 are the positions of the centres of cavities 1 and 2, respectively. Substituting Eq. 6.16 into this expression gives:

$$F = \frac{\left| \left(\cos \frac{\theta}{2} \right) \psi_2(\mathbf{r}_1) - \left(\sin \frac{\theta}{2} \right) \psi_1(\mathbf{r}_1) \right|^2}{\left| \left(\cos \frac{\theta}{2} \right) \psi_2(\mathbf{r}_2) - \left(\sin \frac{\theta}{2} \right) \psi_1(\mathbf{r}_2) \right|^2}. \quad (6.19)$$

Assuming that the isolated cavities have relatively well confined modes, $\psi_1(\mathbf{r}_2)$ and $\psi_2(\mathbf{r}_1)$ are small and cross-terms can be neglected when expanding Eq. 6.19. Considering also that for isolated

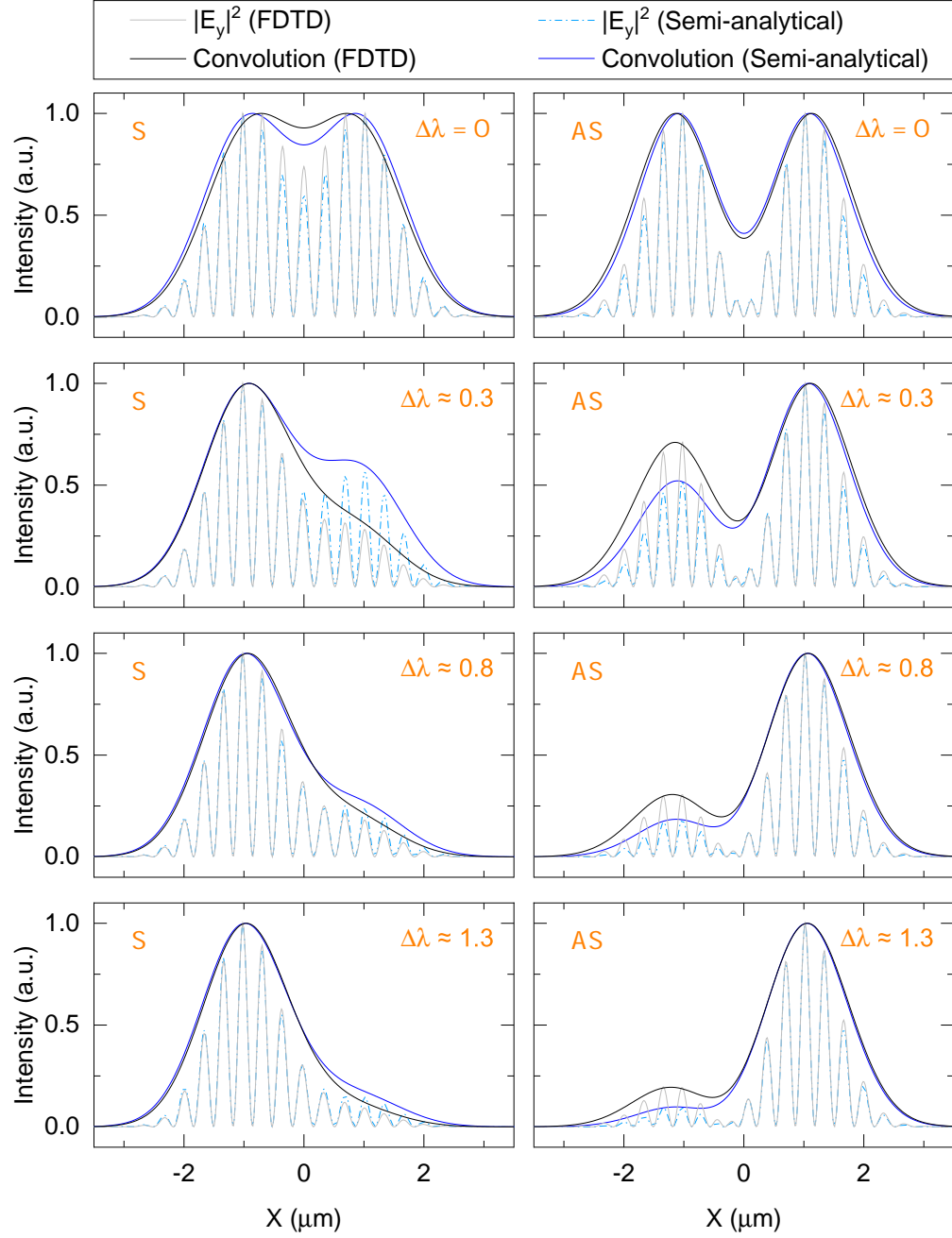


Figure 6.12: Comparison of results from FDTD simulations and the semi-analytical approach for detuned SU-8 strip PMs with $2\ \mu\text{m}$ strip separation. For both methods, the $|E_y|^2$ field profiles of the S and AS modes along $x = 0$ are shown, in addition to the convolution of these with a $1\ \mu\text{m}$ Gaussian to represent the mode profiles resolved by the μPL system. All detunings, $\Delta\lambda$, are in units of nm. The right strip has a thickness of 100 nm in all simulations; detuning estimates of 0 nm, 0.3 nm, 0.8 nm and 1.3 nm correspond to thicknesses of 100 nm, 110 nm, 150 nm and 200 nm of the left strip, respectively. All plots are normalised.

cavities of equal amplitude, $|\psi_1(\mathbf{r}_1)|^2 = |\psi_2(\mathbf{r}_2)|^2$, we obtain

$$F = \frac{\sin^2(\theta/2)}{\cos^2(\theta/2)} = \tan^2(\theta/2). \quad (6.20)$$

Therefore, the delocalization factor is dependent on the ratio $J/\Delta\lambda$, which is related to θ by Eq. 6.17. For an ideal PM with identical cavities and zero detuning, the AS supermode peaks have equal amplitude and therefore F will have its maximum value of 1. For finite detuning, F decreases as the ratio of coupling strength to detuning decreases, which predicts a mode profile increasingly localized towards one of the individual cavities. We now build upon the analysis by Brossard *et al.* [56], and show that it is possible to relate J and $\Delta\lambda$ directly to experimentally measurable properties. Firstly, we show that the $J/\Delta\lambda$ ratio can be obtained from F , which can be estimated for real devices from the fitting of μ PL maps. Rearranging Eq. 6.17 for θ and substituting into Eq. 6.20 yields

$$\frac{J}{\Delta\lambda} = \frac{1}{2} \tan \left[2 \tan^{-1} \left(\sqrt{F} \right) \right], \quad (6.21)$$

which can be simplified using the tangent double angle formula to obtain

$$\frac{J}{\Delta\lambda} = \frac{\sqrt{F}}{1 - F}. \quad (6.22)$$

Using Eq. 6.12, which relates $\Delta\Lambda$ to J and $\Delta\lambda$, individual expressions for the coupling strength and detuning can be derived:

$$J = \left(\frac{\sqrt{F}}{1 - F} \right) \Delta\Lambda, \quad (6.23)$$

$$\Delta\lambda = \left(\frac{1 - F}{1 + F} \right) \Delta\Lambda, \quad (6.24)$$

which enables J and $\Delta\lambda$ to be estimated from experimental measurements of the mode splitting and AS mode delocalization, $\Delta\Lambda$ and F . It should be noted that these expressions only apply for the assumption of similar individual cavities, with equal linewidths ($2\gamma_1 = 2\gamma_2$) and well-localized modes. This is expected to be a reasonable approximation for the SU-8 strip system, as long as the SU-8 strips are uniform (as linewidth correlates with SU-8 thickness) per device and the

cavities are not placed too close together. To our knowledge, this method for calculating J and $\Delta\lambda$ has not been applied in the literature before, and provides a relatively straightforward method of measuring the coupling strength without the need for sophisticated tuning techniques to remove the detuning effects. In section 6.3, this method is applied to experimentally-realised SU-8 strip PMs.

6.3 Fabrication and characterisation of SU-8 strip PMs

6.3.1 Fabrication of SU-8 strip photonic molecules

An experimental investigation was performed with the aim to successfully fabricate and characterise SU-8 strip PMs on PhC waveguide structures. A high density InGaAs/GaAs QD sample was used, as detailed in section 3.7, to enable easy observation of the cavity modes. The sample used was etched with a 4 minute 32% HCl treatment. The spin coating parameters used were the same as listed in section 5.3.1. After an initial coating with an 8:1 ratio of cyclopentanone to SU-8 2007 failed to adhere to the surface uniformly and was removed with PGMEA and an IPA rinse, a thicker coat of 7:1 ratio was chosen which successfully wetted the PhCs. Given the sensitivity of PMs to cavity detuning that could arise from fabrication imperfections in the SU-8 and PhC (see section 6.2.5), the spin-coating and exposure parameters were selected for reliable fabrication rather than the highest Q , thinnest possible strips. As a result, the Q factors were typically in the range 3500-5500.

Fabrication of SU-8 double strips was attempted on 104 clean, undamaged PhC waveguides. Strips were written by piezo-controlled movement of the microscope objective to move the focused 405 nm laser spot (as outlined in section 5.3.1), with target separations in the range 1 μm to 5 μm by 0.5 μm increments. A power of 17.5 μW after the objective (and before the cryostat window) was used and the writing speed was selected between 0.25 $\mu\text{m/s}$ and 0.50 $\mu\text{m/s}$ to control the dose. The dose was selected based on the desired SU-8 strip thickness and predictions of the SU-8 film thickness over each PhC device, estimated from the thickness-dependent appearance of the film (see section 5.3.1). SU-8 strips were successfully written on all but 1 of the 104 attempted devices - a yield greater than 99%. However, this does not represent the yield of successful coupled cavity modes, which is analysed in more detail in section 6.3.2.

An example of a successfully fabricated double SU-8 strip structure with a target separation

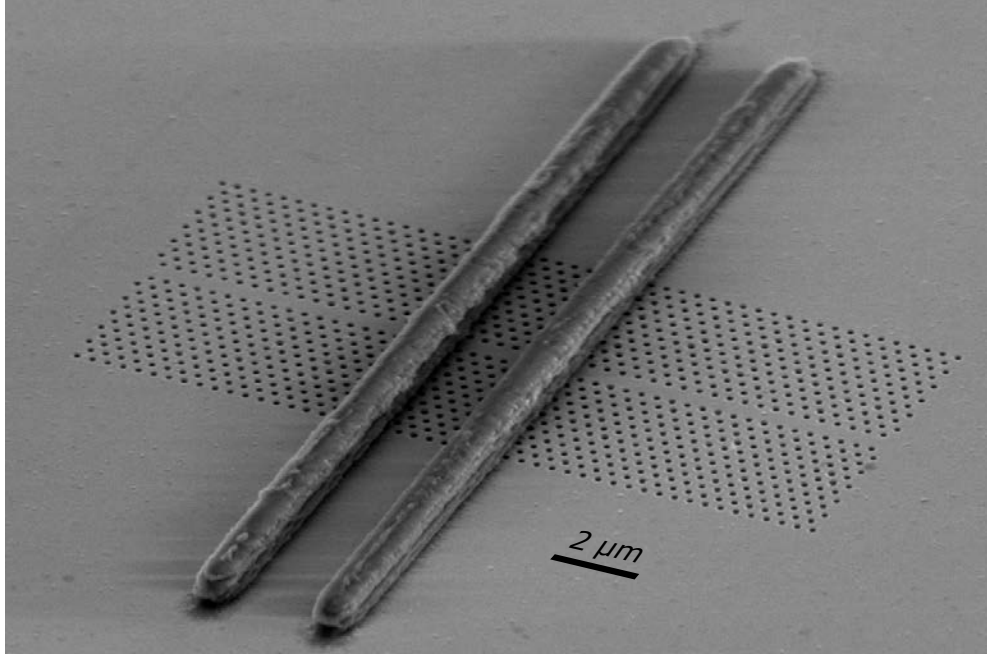


Figure 6.13: SEM image of two SU-8 strips written on a PhC waveguide at a separation of $2.5\ \mu\text{m}$. The mean thickness of the strips was determined from AFM measurements to be $0.55\ \mu\text{m}$, obtained by averaging the thickness of the strips over the width of the PhC.

of $2.5\ \mu\text{m}$ is shown in the SEM image in Fig. 6.13, which clearly shows well-defined, uniform SU-8 strips. The average thickness of the strips was determined to be $0.55\ \mu\text{m}$ from profile averaging of AFM measurements - the averaging was performed across the y -extent of the PhC. The SU-8 strips of this selected device were thicker than average for the sample (see section 6.3.4 for more details of the thickness distribution), but the majority of strips on other devices were similarly well-defined for target separations of $2\ \mu\text{m}$ or larger. As the separation approached $1\ \mu\text{m}$, we observed the SU-8 strips merging together to form a single strip. This is demonstrated in Fig. 6.14, which shows SEM images and profiles from AFM measurements of devices with target strip separations from $1\ \mu\text{m}$ to $2\ \mu\text{m}$. For a separation of $2\ \mu\text{m}$ [Figs. 6.14(c) and 6.14(f)], two clear, distinct strips are written, whereas for a separation of $1.5\ \mu\text{m}$ [Figs. 6.14(b) and 6.14(e)], the strips partially merge together. As the separation is reduced to $1\ \mu\text{m}$ [Figs. 6.14(a) and 6.14(d)], the geometry approaches that of a single strip. This merging of the SU-8 strips places a lower limit of approximately $2\ \mu\text{m}$ on the separation of two individual strips and is an important consideration for narrower separations than this. However, as explored in section 6.2, the system is expected to converge towards the behaviour of a single strip cavity for separations approaching $1\ \mu\text{m}$. This means that hybrid single cavity-PM behaviour (with some characteristics of both systems) would be expected for such small separations even if the two strips were distinct, so the merging of the strips is not a cause of great concern.

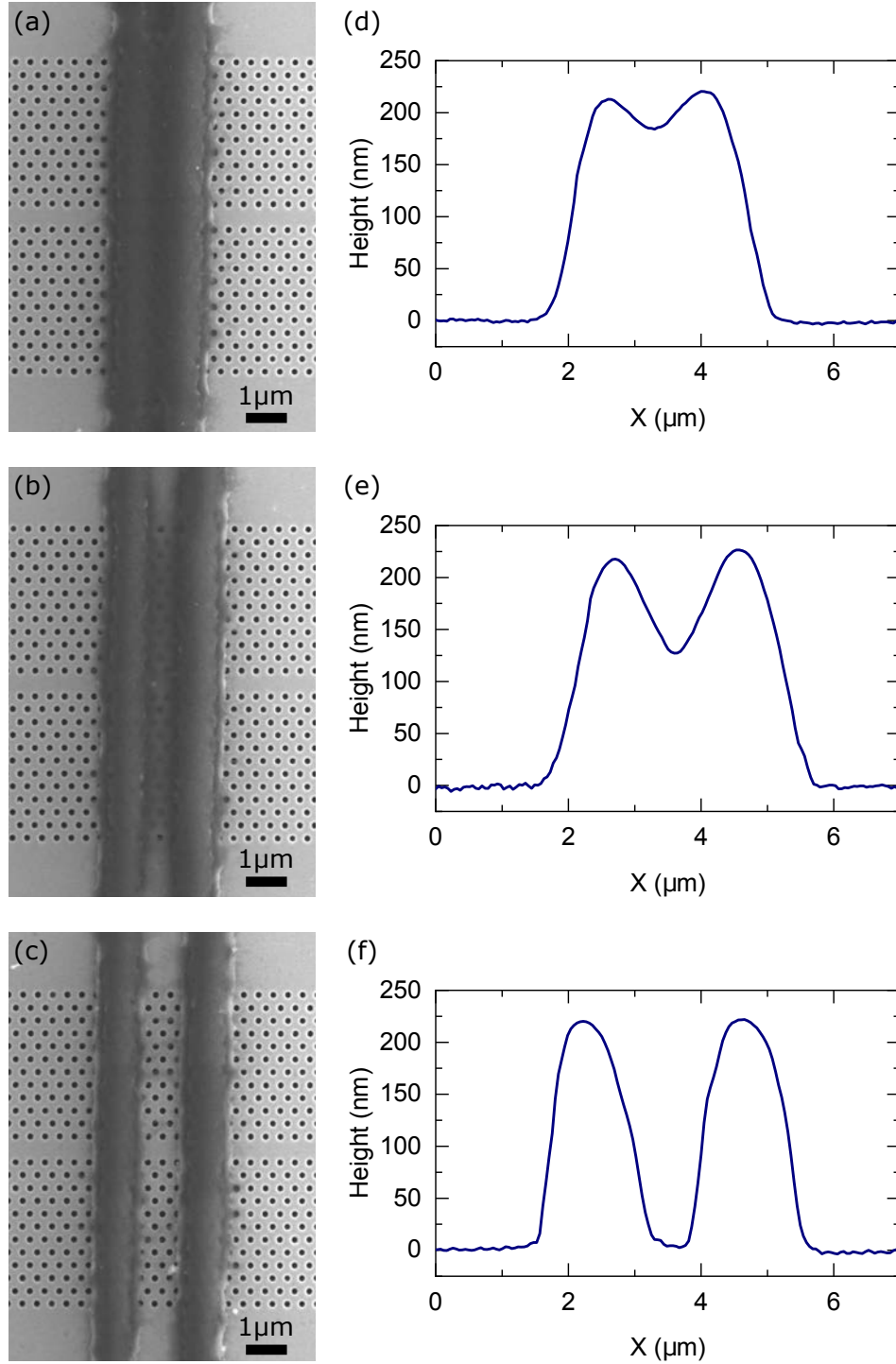


Figure 6.14: (a)–(c) SEM images of two SU-8 strips written on PhC waveguides with target separations of 1 μm (a), 1.5 μm (b) and 2 μm (c). (d)–(f) Height profiles of the respective devices, obtained from profile averaging performed on AFM measurements. AFM profiles were averaged over approximately a 4 μm extent perpendicular to the waveguide. The two strips are fully distinct for a separation of 2 μm .

It should be noted that all AFM and SEM measurements presented in this section were performed after the μ PL measurements taken in subsequent sections, to avoid any potential damage to the sample.

6.3.2 Micro-photoluminescence mapping of SU-8 strip photonic molecules

The modes of the fabricated double SU-8 strip cavities were characterised using μ PL measurements and mapping techniques. To verify the creation of new cavity modes, 1D μ PL maps were performed by scanning the objective along the waveguide before and after the placement of the SU-8 strips, as was carried out for the single cavities in chapters 4 and 5. Maps were performed at ~ 8 K, using a HeNe CW laser (632.8 nm) focused to a ~ 1 μ m diameter laser spot to provide an excitation power of ~ 50 μ W, measured after the objective. This relatively high excitation power was necessary due to the large spectral separation between the centre of the QD ensemble and the cavity modes, which were situated at wavelengths of approximately 1220 nm and 1280 nm, respectively, at ~ 8 K. The mapping step size was 0.2 μ m with an integration time of 0.5 s. The 600 lines/mm spectrometer grating was used, with a slit width of 50 μ m. Unless stated otherwise, the parameters detailed here were used for all μ PL mapping measurements in this chapter.

Some typical examples of 1D maps taken before and after the fabrication of the SU-8 strips are presented in Fig. 6.15. In all cases shown, two new lower energy modes are clearly created by the SU-8 strips [Figs. 6.15(b), 6.15(d) and 6.15(f)] that are distinct to the waveguide modes observed from the corresponding blank PhC waveguide [Figs. 6.15(a), 6.15(c) and 6.15(e)]. We label the lowest energy mode created as M1 and the second-lowest energy mode created as M2. For the device with 1 μ m strip separation (which forms a single SU-8 strip) in Fig. 6.15(b), modes M1 and M2 correspond to ground and first excited states of a single cavity, characterised by the large mode splitting and large spacing of the M2 peaks relative to the strip separation. The map in Fig. 6.15(d) shows evidence of strongly coupled cavities with a small detuning ($J > \Delta\lambda$): the M1 and M2 modes match the expected profiles of detuned PM S and AS supermodes, with peaks corresponding closely to the positions of the 2.5 μ m-separated SU-8 strips. For larger strip separations approaching 5 μ m, it was typical to see behaviour similar to Fig. 6.15(f), which shows evidence of uncoupled cavity modes. In this case, M1 and M2 appear to be single cavity modes localized at the individual cavity positions, suggesting that $\Delta\lambda \gg J$ and the effects of coupling are lost at this separation.

Selected examples of μ PL maps from successful devices with a range of strip separations are

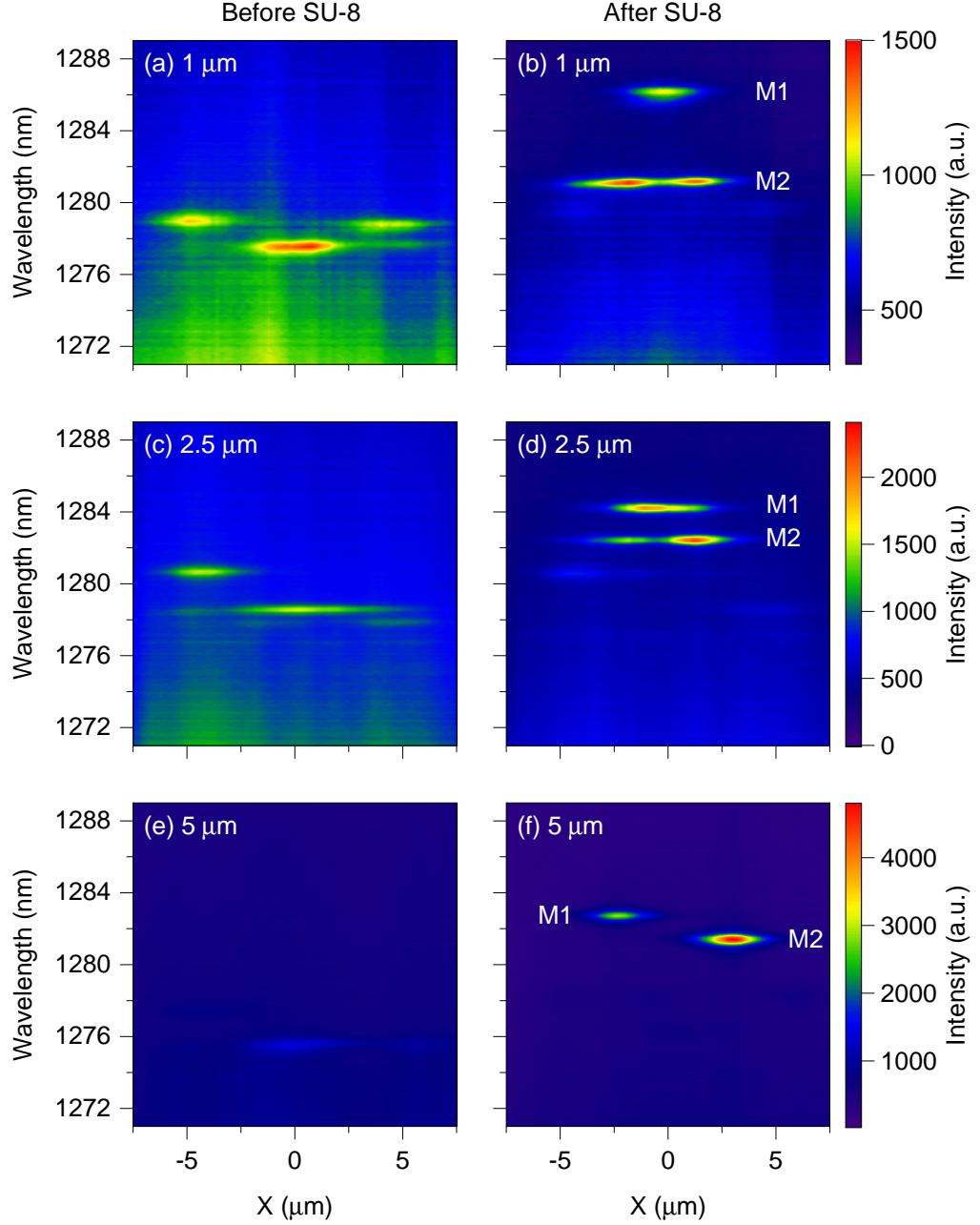


Figure 6.15: Typical 1D μ PL maps taken before and after writing SU-8 strips on PhC waveguides, showing creation of new cavity modes. (a) Before and (b) after strips were written with a separation of $1\ \mu\text{m}$, resulting in a single strip with characteristic single cavity modes. (c) Before and (d) after strips were written with a separation of $2.5\ \mu\text{m}$, showing evidence of (detuned) coupled cavity supermodes. (e) Before and (f) after strips were written with a separation of $5\ \mu\text{m}$, showing evidence of two independent single cavity modes.

shown in Fig. 6.16, which demonstrate evidence of increased coupling as the distance between the cavities is reduced. At a large separation of $4.5\text{ }\mu\text{m}$ [Fig. 6.16(a), device D1], M1 and M2 are two independent, highly-localized cavity modes corresponding to two uncoupled cavities. In this case, the wavelength splitting between the two modes is dominated by the cavity detuning. As was discussed in sections 6.1.3 and 6.2.5, the most likely source of this detuning is from fabrication imperfections in the PhC and variation in the SU-8 strip geometry. The effects of detuning are also evident for device D2 in Fig. 6.16(b), with a $3.5\text{ }\mu\text{m}$ strip separation. This device exhibits coupled PM modes which are moderately localized towards either cavity, as expected for a PM with $\Delta\lambda$ of similar magnitude to J . The device D3 in Fig. 6.16(c) displays clear signatures of a strongly coupled PM, with M1 and M2 taking the form of highly delocalized S and AS supermodes. The modes are nearly symmetric about $X = 0$, indicating a high $J/\Delta\lambda$ ratio. An AFM image of this device is also included in Fig. 6.16(d).

The devices were further characterised by estimating the delocalization factor, F (as defined in section 6.2.5), of the M2 mode from the μPL maps. The M2 mode was chosen here, as it corresponds to the AS supermode for strongly coupled PMs, which consists of two easily resolvable peaks to compare. The value of F was estimated from the amplitude ratio of the two peaks of the M2 mode, with the calculation method as follows: the X positions of the M2 mode peaks were identified by applying a double Gaussian fit to the spatial profile of the mode and using the centres of the two Gaussians, X_{GA} and X_{GB} . For each X_{G} position, the spectrum obtained at the nearest X position of the map was fitted with a Lorentzian plus a straight line, to fit the peak of the mode on an ensemble background (approximated by the straight line). Note that in some cases, a double Lorentzian (plus straight line) fit was instead applied, if the M1 and M2 modes were close spectrally. The ratio of the amplitudes of the Lorentzian fits to M2 at X_{GA} and X_{GB} was then taken as an estimate of F , such that $F \leq 1$. For cases such as device D1 in Fig. 6.16(a), for which the M2 mode is spatially localized in one cavity and a double Gaussian fit is not possible, the X position of the second cavity was approximated as the X position of the centre of the M1 mode (from a single Gaussian fit to the spatial profile) instead.

The values of F estimated for the coupled cavity devices D2 and D3 were 0.33 and 0.77 respectively, while the uncoupled cavities of D1 yielded an F of less than 0.01. These measurements of F not only provide a convenient indicator of the degree of mode delocalization in the devices, but also enable us to estimate the coupling strength and detuning of the devices: estimates of J and $\Delta\lambda$ can be obtained from F and $\Delta\lambda$ through Eqs. 6.23 and 6.24. Applying this analysis, we estimate

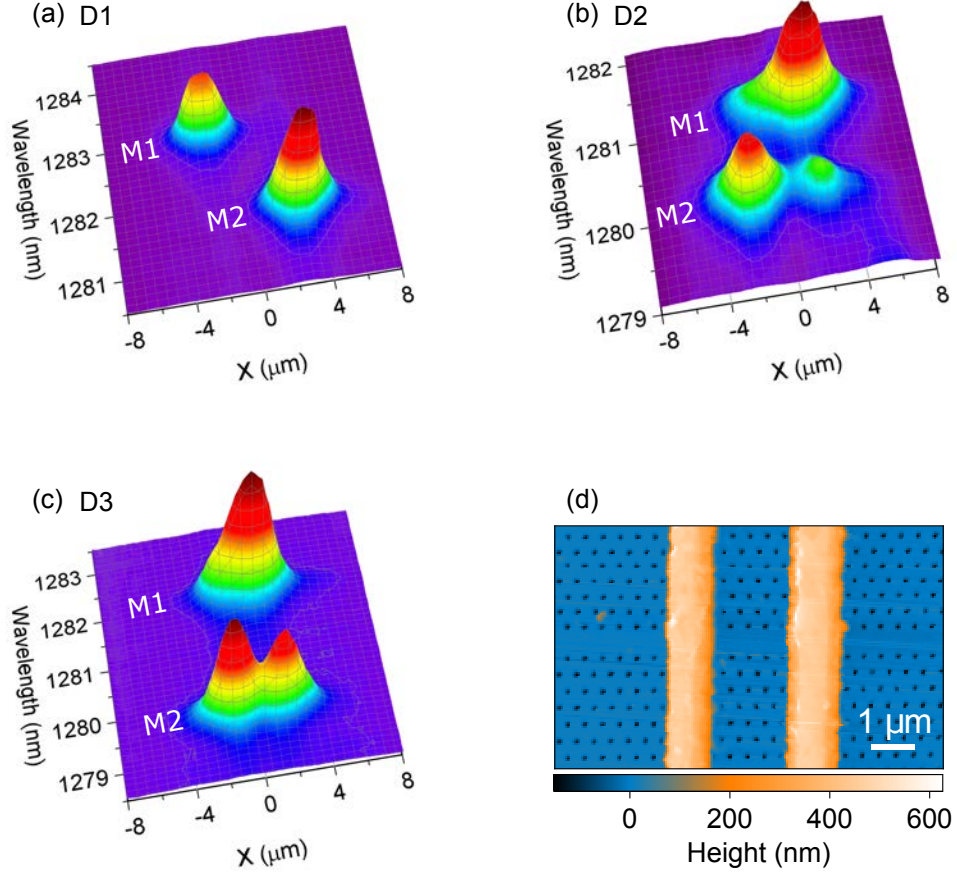


Figure 6.16: (a)–(c) μ PL maps from selected SU-8 double strip devices, showing increasing coupling as the strip separation is reduced. (a) Device D1, separation $4.5\ \mu\text{m}$. (b) Device D2, separation $3.5\ \mu\text{m}$. (c) Device D3, separation $2.5\ \mu\text{m}$. Device D1 shows uncoupled cavity modes, whilst D2 and D3 show coupled cavity modes with moderate and small detuning, respectively. (d) AFM image of device D3. Note that the full size of the holes in the PhC is not resolved by the AFM tip, so they appear smaller than their true size.

coupling strengths of $J_{D2} \sim 0.4\ \text{nm}$ and $J_{D3} \sim 1.1\ \text{nm}$ for devices D2 and D3, from mode splittings of $\Delta\Lambda_{D2} = 0.97\ \text{nm}$ and $\Delta\Lambda_{D3} = 2.33\ \text{nm}$. Detunings of $\Delta\lambda_{D2} \sim 0.5\ \text{nm}$ and $\Delta\lambda_{D3} \sim 0.3\ \text{nm}$ are estimated for these devices. We find that D3 yields a particularly high $J/\Delta\lambda$ ratio, which correlates with its highly delocalized mode profiles, whereas the detuning of D2 is of similar magnitude to the coupling strength, resulting in the slightly more localized modes. For device D1, J tends to zero and we estimate a detuning of $\Delta\lambda_{D1} = 1.27\ \text{nm}$ from the mode splitting of the uncoupled cavities. The differences in the detuning magnitudes are anticipated to result predominantly from random variation of the disorder-induced detuning caused by e-beam fabrication imperfections, although minor fluctuations of the SU-8 strip thickness may also contribute.

6.3.3 SU-8 photonic molecule batch analysis

Comparative μ PL maps before and after the SU-8 strip fabrication were acquired for all 103 devices with successfully written SU-8 strips. In all cases, changes to the observed modes were confirmed. In 87 of the devices, clear M1 and M2 modes could be identified. In this section, analysis is performed on these 87 devices. The most common reason for excluding devices from the analysis was due to the creation of only a single mode, M1, by the SU-8 strips. This was more frequent for small strip separations (less than $2\text{ }\mu\text{m}$), for which the SU-8 strips begin to merge and approach the behaviour of a single cavity. In some instances, as with single SU-8 strips, the resulting single cavity only supported the ground mode and not the first excited mode. Despite the exclusion of some devices, a reasonable number of cavities were still examined for each strip separation: an average of 10 cavities was sampled at each separation, with a minimum sample size of 7 devices (for a $1\text{ }\mu\text{m}$ separation).

Several parameters were extracted from the μ PL mapping data for each device, in order to characterise their modes. The mode splitting, peak spacing and delocalization factor were obtained for every device and their mean value at each strip separation was calculated. The results of the analysis, plotted in Fig. 6.17, display trends that provide further evidence of the successful creation of SU-8 PMs, with coupling strength tunable by altering the strip separation. The mean mode splitting between the M1 and M2 mode, presented in Fig. 6.17(a), decreases (as we would expect) as the strips are brought further apart. The trend observed is in good agreement with predictions from FDTD results (Fig. 6.9), except for the additional effects of fabrication imperfection-induced cavity detuning not accounted for in the simulation. Instead of converging to zero as in the zero detuning case, we expect from Eq. 6.12 that the mean mode splitting should converge towards the mean value of $\Delta\lambda$ (which is expected to be independent of the strip separation) as the strip separation is increased and J tends to zero. At large separations, the cavity detuning is expected to be the sole source of the mode splitting. Therefore, we estimate a mean cavity detuning of $\overline{\Delta\lambda} = (1.15 \pm 0.13)\text{ nm}$ from the mode splitting of the PMs with a strip separation of $4\text{ }\mu\text{m}$ or more. The magnitude of this detuning is comparable to e-beam defined PhC PMs reported in the literature [56, 171, 227, 230], which supports this novel SU-8 writing technique as a reliable method for creating PMs and suggests that the additional optical cavity fabrication step is not a significant source of cavity detuning beyond the PhC fabrication imperfections.

The spacing between the peaks of the PM modes was also recorded, defined as follows. If possible,

the peak spacing was measured as the spatial separation of the two peaks of the M2 mode. However, if the M2 mode did not have two clearly defined peaks, such as in the case of a large detuning, the peak spacing was instead measured as the separation of the M1 and M2 peaks. The mean values of the measured peak spacing are plotted in Fig. 6.17(b) as a function of SU-8 strip separation. The observed trend is consistent with the predicted behaviour of the AS peak separation obtained from simulation results [Fig. 6.9], which the peak spacing is intended as an analogue to. At a large strip separation, for which the inter-cavity coupling is weak, the modes are well-localized at the cavity positions. As the strip separation is reduced and the coupling strength increases, the

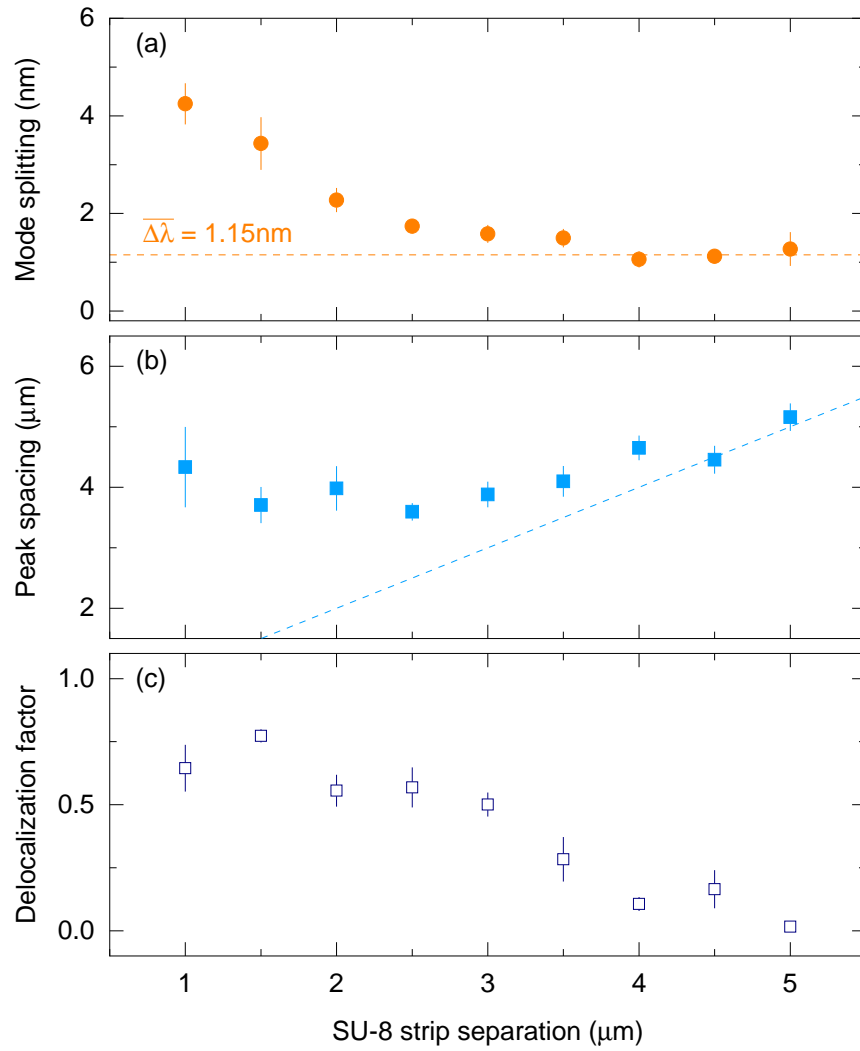


Figure 6.17: Mean values of the (a) mode splitting, (b) peak spacing and (c) delocalization factor obtained for each SU-8 strip separation in a batch of successful devices. Error bars represent estimates of the standard error of the mean at each separation. The dashed orange line in (a) represents the estimated mean detuning, $\overline{\Delta\lambda} = 1.15 \text{ nm}$ from strip separations of 4 μm or more. The dashed blue line in (b) is included to guide the eye, showing equality of strip separation to peak spacing.

peak spacing diverges from the strip separation, approaching the behaviour of a single cavity with characteristically larger peak spacing than the width of the SU-8.

Delocalization factors were estimated for every device using the method outlined in section 6.3.2. The mean delocalization factor for each strip separation is shown in Fig. 6.17(c). At large separations, the modes are highly localized to the individual cavities, indicating a low $J/\Delta\lambda$ ratio. For intermediate separations of $\sim 2\text{--}3\,\mu\text{m}$, moderate to highly delocalized PM modes were observed, providing a clear indication of strongly coupled PMs. However, due to the significant average detuning, it was not common to observe near-symmetric ($F \sim 1$) PM supermodes, hence the mean F of ~ 0.5 for these strip separations. For short separations, the system approaches a single cavity and F is less relevant as the coupled cavity model somewhat breaks down. In this case, F can be seen as a measure of the symmetry of the M2 mode corresponding to the first excited single cavity mode, which is still likely to be affected by fabrication non-uniformities so does not converge to 1.

In combination, the trends displayed by the three parameters in Fig. 6.17 provide substantial evidence that we have successfully created double SU-8 strip cavities of variable (and controllable) inter-cavity coupling strength. At large strip separations of $\gtrsim 4\,\mu\text{m}$, the cavities are typically uncoupled or minimally coupled, with a detuning-dominated mode splitting and highly localized cavity modes indicated by a low F and peak spacing close to the strip separation. The measured parameters are all consistent with a low $J/\Delta\lambda$ ratio. To create strongly coupled PMs, a target range of $\sim 2\text{--}3.5\,\mu\text{m}$ strip separation would be recommended for which, on average, the mode splitting typically exceeds the detuning and the modes exhibit moderate delocalization. The peak spacing begins to increase above the strip separation, indicating significant overlap and interaction of the modes of the constituent cavities. For these separations, all parameters are consistent with a moderate to high $J/\Delta\lambda$ ratio. For separations less than $2\,\mu\text{m}$, the results suggest that the system approaches a single cavity, with its characteristically large mode splitting and peak spacing of the double-peaked excited mode. This is especially anticipated considering the merging of the SU-8 strips reported in section 6.3.1. For CQED applications, the convergence of the system to single cavity behaviour for short separations is not necessarily an issue. As an example, the experimental implementation of the unconventional photon blockade by Snijders *et al.* [245] was achieved using two modes of a single micropillar cavity, rather than strongly-coupled PM modes.

Q factors of the PM modes were measured for each device using the 1200 lines/mm spectrometer grating (slit width $20\,\mu\text{m}$) and an integration time of 10 s. The Q factors of both the M1 and M2

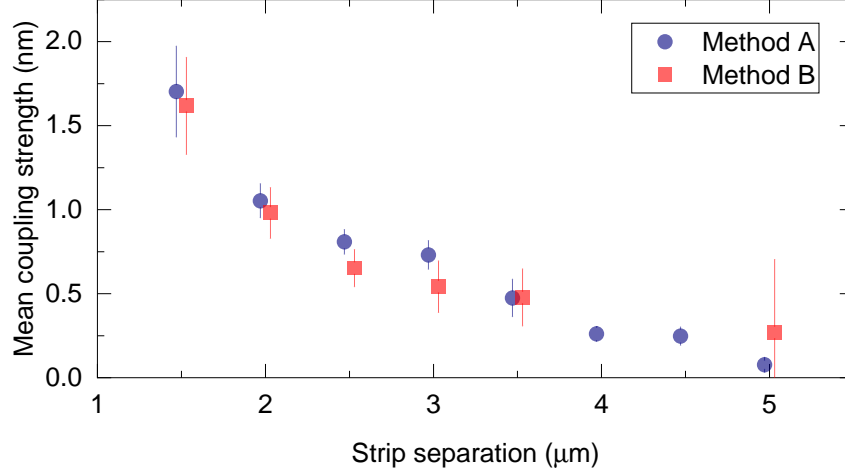


Figure 6.18: Estimated mean coupling strength for each SU-8 strip separation, calculated using methods A and B. The data points have a small artificial horizontal offset either side of the true strip separation for ease of reading. The mean coupling strength could not be calculated using method B for the case of $\overline{\Delta\Lambda} < \overline{\Delta\lambda}$, which is the reason for the missing data points. Error bars for method A represent the standard error of the mean and the errors for method B were propagated appropriately from the parameters used in the calculation.

modes were typically in the range 3500-5500. No evidence of the Q factor oscillations with strip separation, observed in simulation results in section 6.2.2, was found, which we attribute to the presence of random cavity detuning that was not accounted for in those simulations.

We next sought to estimate the magnitude of the coupling strength for different SU-8 strip separations, which was obtained using two different methods. In method A, J was calculated separately for each of the 87 devices from the measured values of $\Delta\Lambda$ and F , using Eq. 6.23. The mean coupling strength at each separation was then extracted from these results, which is plotted in Fig. 6.18. As a consistency check, the mean coupling strength was also calculated using method B. For this method, Eq. 6.12 was rearranged to estimate the mean coupling strength, \overline{J} , at each separation using the mean mode splitting, $\overline{\Delta\Lambda}$ and mean detuning, $\overline{\Delta\lambda}$ from Fig. 6.17(a):

$$\overline{J} \approx \frac{1}{2} \sqrt{(\overline{\Delta\Lambda})^2 - (\overline{\Delta\lambda})^2}. \quad (6.25)$$

Making the assumption that the average detuning is independent of strip separation, a value of $\overline{\Delta\lambda} = (1.15 \pm 0.13)$ nm was used for all separations (calculated from the mode splitting of devices with a strip separation of 4 μm or more). The values of $\overline{\Delta\Lambda}$ used for each separation were the same as those presented in Fig. 6.17(a). The results of this method are also plotted in Fig. 6.18. It is important to note that method B cannot be used to calculate J for individual devices, since the disorder-induced detuning per device can vary significantly from this estimate. The method is

only valid to calculate the mean, \bar{J} , at each separation.

The estimates of the coupling strength from methods A and B (Fig. 6.18) are in good agreement, within error. Both methods confirm the expected trend of decreasing J with increasing strip separation. We note that method B is not as effective at larger strip separations, for which $\overline{\Delta\Lambda}$ and $\overline{\Delta\lambda}$ are similar. When this is the case, uncertainty in these two quantities is propagated to a large uncertainty in \bar{J} , as is evident for the value calculated for a strip separation of 5 μm . Additionally, $\overline{\Delta\Lambda}$ was marginally smaller than $\Delta\lambda$ for strip separations of 4 μm and 4.5 μm , meaning that method B could not be applied as the root in Eq. 6.25 became negative. Fortunately, method A can be used to estimate the coupling strength in these cases and yields sensibly small values. Devices with a strip separation of 1 μm gave excellent agreement between methods A and B, but were excluded from the presented results as the system forms a single strip cavity, hence J is not relevant.

It is evident that the estimated mean values of J that have been obtained for the fabricated devices are generally larger than those predicted by the simulation results for 0.1 μm -thick, 1 μm -wide SU-8 strips in Fig. 6.5 of section 6.2.1. The reason for this is not clear, but may be due to differences in the SU-8 geometry between the simulated structure and the fabricated devices. This could include the strip width and thickness (the typical thickness was 0.25 μm , as detailed in section 6.3.4), in addition to filling of the PhC holes by the SU-8, which was not accounted for in the model. These differences in the real devices may have resulted in altered mode behaviour with increased coupling strength, for example if the modes had an increased evanescent field overlap. For a given strip separation, the magnitude of the estimated mean coupling strength is comparable to similarly spaced PhC-based PMs in the literature [171, 225, 230], especially those operating at a similar wavelength to the SU-8 PMs presented here [56, 57]. This supports the validity of the results despite their discrepancy with the simulated values, and confirms that the PM devices perform as they would be expected to.

We note that the accuracy of method A could potentially be improved by implementing confocal light collection in the μPL mapping system. The reduced light collection area may enable the M2 mode profiles to be more accurately determined and therefore be beneficial for the estimation of F . However, since method B was used to predict the mean coupling strength independently of the measured values of F , the close agreement between the two methods supports the effectiveness of the measurements of F obtained using the non-confocal collection area. Still, it is worth considering

that there may be a small systematic error, as method A appears to slightly overestimate the mean coupling strength relative to method B. We identify two potential contributing factors to this: firstly, the non-confocal light collection area may result in an overestimate of F , which results in an overestimate of J through Eq. 6.23. Secondly, limitations of the coupled mode theory model applied as an approximation to the physical system may apply: in section 6.2.5, a small discrepancy between the semi-analytical implementation of coupled mode theory and full FDTD results of detuned PMs was identified. A consequence of this is that applying the coupled mode theory model may be liable to over-estimate the value of F and, by extension, the estimated value of J . In the worst-case scenario, for a strip separation of $3\text{ }\mu\text{m}$, the mean coupling strength estimated from method B is 26% smaller than estimated from method A. Therefore, we estimate that the coupling strength extracted from a device using Eq. 6.23 should differ from the true value by no more than this factor, in the majority of cases.

6.3.4 AFM characterisation of SU-8 strip photonic molecules

AFM characterisation measurements were performed on a selected sample of the fabricated devices to check the thickness of the SU-8 strips. A selection criterion was applied to select for devices with two distinct cavities and modes corresponding closely to the SU-8 strip locations. Devices were chosen that had a measured peak spacing within $\pm 1\text{ }\mu\text{m}$ of the target strip separation, as expected from FDTD simulation results in section 6.2.4. AFM profiling was performed on the 37 devices which met this requirement (all with a strip separation larger than $1.5\text{ }\mu\text{m}$), and the SU-8 strip thicknesses were extracted using profile averaging with inverse polynomial fits, as was performed for single strip cavities in section 5.3.1. The average thickness of the two strips per device, plotted in Fig. 6.19, demonstrates relatively good repeatability of the technique. The majority of strip thicknesses are tightly distributed about a median thickness of $0.25\text{ }\mu\text{m}$, with an upper and lower quartile of $0.32\text{ }\mu\text{m}$ and $0.25\text{ }\mu\text{m}$ (rounded to the nearest $0.01\text{ }\mu\text{m}$), respectively.

The moderate thickness of the SU-8 strips is a consequence of the optimisation of the fabrication process for reliability rather than the thinnest possible, highest Q cavities. The extreme values of thickness observed for some devices are predominantly due to variation in the thickness of the applied SU-8 thin film – the exposure dose was adjusted for each device to attempt to correct for this, but cannot compensate completely for the thickness fluctuations. It is important to note that the SU-8 film does not vary significantly over the length scale of a single PhC device, which is

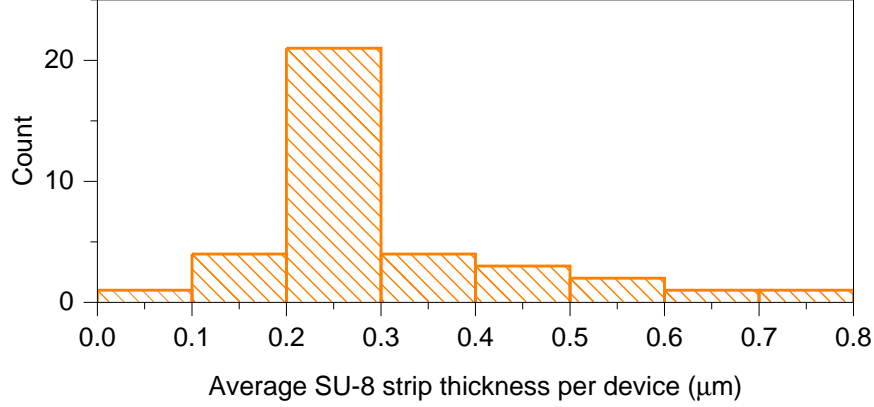


Figure 6.19: Distribution of average SU-8 strip thickness per device, as measured from AFM profiling of a selected sample of devices.

proven by the uniformity of the strips on a per device basis: we found on average only 5% variation in thickness between the two SU-8 strips of a device. The high uniformity of the pairs of strips suggests that the individual cavities of the coupled cavity devices would have approximately equal Q factors in the absence of coupling, since the Q factor of a single strip cavity highly correlates with the SU-8 strip thickness. This supports an assumption that is vital to the theory developed and applied in this chapter, which is that the two cavity modes would have equal linewidths in the absence of coupling: $2\gamma_1 = 2\gamma_2$. Most pertinently, this assumption is necessary for the calculation of J and $\Delta\lambda$ from Eqs. 6.23 and 6.24 to be valid, in addition to the validity of methods A and B to calculate the mean coupling strength. These AFM measurements therefore support the validity of these results, as it is implied from the strip uniformity per device that this assumption is approximated well by the system.

6.4 Confocal measurements of SU-8 strip PMs

In this section, confocal techniques are applied to facilitate improved mapping of the SU-8 PM devices. We show that the smaller light collection area achieved by confocal methods enables finer details of the cavity modes to be resolved and compare the results to measurements obtained using a non-confocal collection area. Combined with piezo-controlled movement of the microscope objective and a scanning mirror, the confocal technique allows individual cavities of the PM to be probed and we apply this to explicitly demonstrate coupling between the two cavities of an SU-8 PM. Details of the scanning methods used are provided in section 3.8.3.

6.4.1 Comparison of mapping with and without confocal techniques

Confocal light collection from the sample was achieved by focusing the light collected by the $100\times$ microscope objective into a multi-mode optical fibre with a core diameter of $25\text{ }\mu\text{m}$. A $5\times$ microscope objective was selected to focus light into the fibre core, targeting a collection area on the sample of similar size to the diffraction-limited laser spot. The confocal collection was characterised by performing μPL mapping measurements on a reference L3 cavity, which we approximate as a point source on the sample surface (relative to the size of the laser spot and collection area). Measurements in this section were performed on the same high density QD sample as other work in this chapter, mounted in the cryostat at 8 K. A HeNe excitation laser was used, with a power of $\sim 50\text{ }\mu\text{W}$ after the objective. Figs. 6.20(a) and 6.20(b) show the result of a 1D objective map performed over the L3 cavity mode. As the excitation spot and collection are moved simultaneously when moving the objective, we expect this map to yield approximately the convolution of the Gaussian spatial profile of the laser spot with the spatial profile of the L3 cavity mode. Since the L3 cavity mode is approximately a point source in this instance, the profile observed is predicted to be approximately that of the HeNe laser spot. Indeed, the profile is very well fitted by a Gaussian with a FWHM of $1.4\text{ }\mu\text{m}$ [Fig. 6.20(a)], which is close to the diffraction-limited spot size of $1.2\text{ }\mu\text{m}$ expected for this 0.5 NA objective. The discrepancy between the two may be due to effects of the cryostat window or because the L3 cavity is not an exact point source.

Collection maps were performed to estimate the size of the confocal collection area achieved, shown in Figs. 6.20(c) and 6.20(d). In a collection map, the objective and scanning mirror are moved in combination so that the excitation spot remains at a fixed (X, Y) position on the sample surface and the collection area is moved. The laser spot was kept fixed over the L3 cavity and the collection area was scanned along a line, passing over the cavity mode. Since the L3 cavity is approximately a point source, the obtained map is expected to be an estimate of the confocal collection spatial profile. We approximate that the confocal collection achieves a $\sim 2.2\text{ }\mu\text{m}$ collection area in the plane of the sample surface, obtained from the FWHM of a Gaussian fit to the profile in Fig. 6.20(c). This collection area should be sufficiently narrow to selectively collect from individual cavities of an SU-8 PM – especially those with strip separations larger than $2\text{ }\mu\text{m}$ – in addition to improving the spatial resolution of μPL mapping.

The improvement to the spatial resolution granted by confocal mapping is demonstrated by the μPL maps of an SU-8 strip PM shown in Fig. 6.21. 1D objective maps (excitation and collection moved

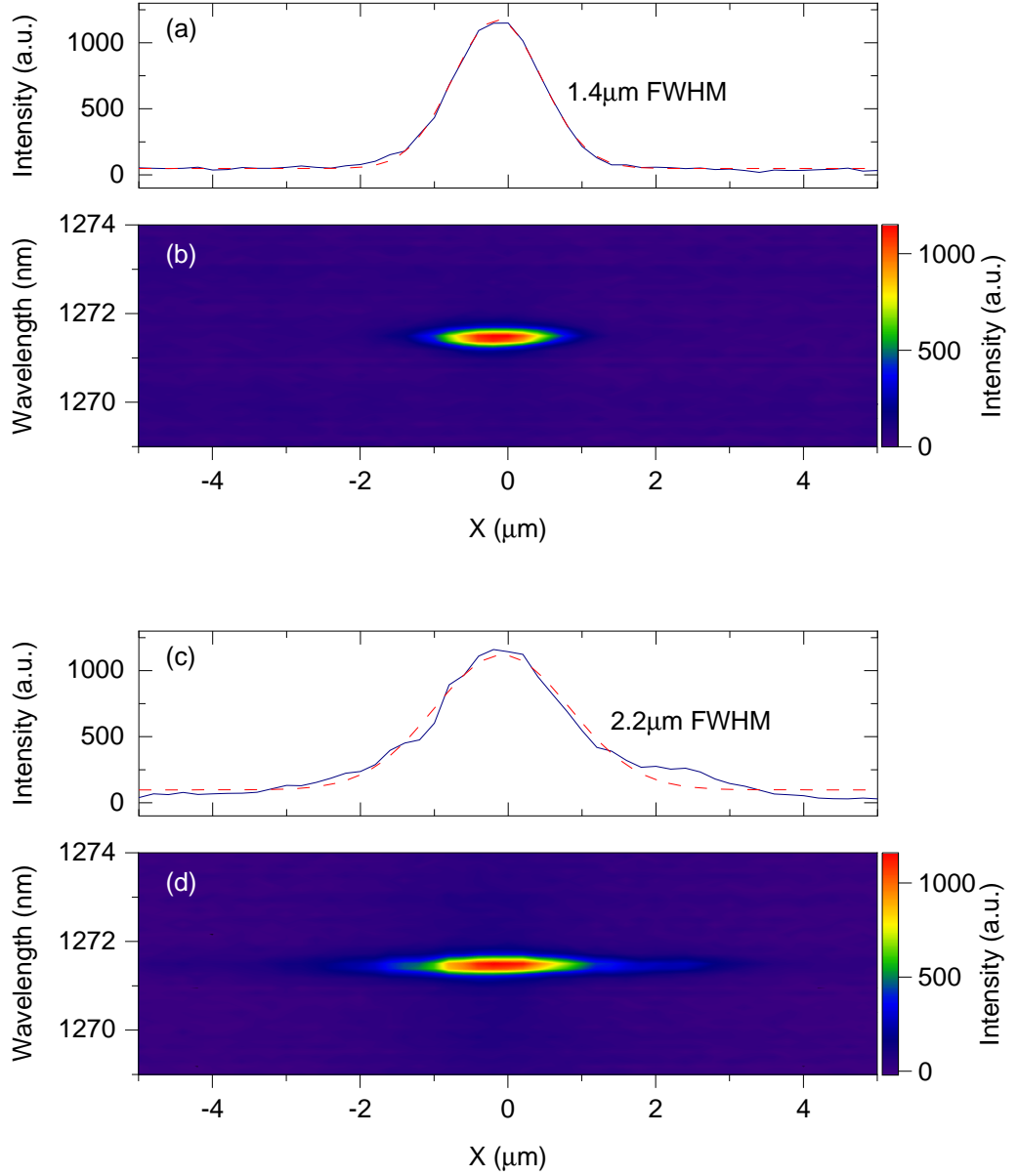


Figure 6.20: μ PL mapping measurements taken of an L3 cavity to characterise the confocal collection area. (a)–(b) Intensity profile recorded from an objective map, which moves the overlapping excitation spot and collection area simultaneously. (b) shows a 1D scan, passing over the single cavity mode, and (a) shows a cross-section through this map at a wavelength of 1271.50 nm. The cross-section is fitted by a Gaussian with a FWHM of 1.4 μ m, corresponding approximately to the size of the laser spot. (c)–(d) Intensity profile recorded from a collection map, which keeps the laser spot fixed over the L3 cavity, while moving the collection area. (d) shows a 1D scan of the collection area and (c) shows a cross-section through this map at the same wavelength as (a). The cross-section is fitted by a Gaussian with a FWHM of 2.2 μ m, corresponding approximately to the size of the confocal collection area. A step size of 0.2 μ m was used for mapping, with an integration time of 0.5 s at each step.

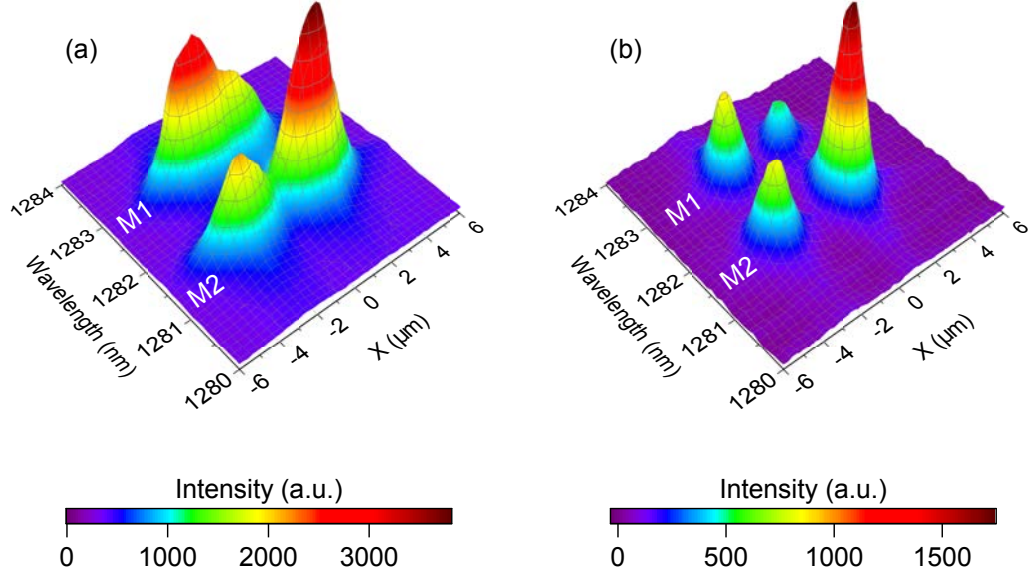


Figure 6.21: 1D μ PL objective maps obtained along the waveguide for the same SU-8 PM device with a strip separation of $3\text{ }\mu\text{m}$ using (a) non-confocal and (b) confocal light collection. The confocal light collection enables finer details in the M1 and M2 mode profiles to be resolved, including the ability to resolve the two peaks of the M1 mode. A step size of $0.2\text{ }\mu\text{m}$ was used for mapping, with an integration time of 0.5 s at each step for (a) and 1 s at each step for (b).

simultaneously) performed along the waveguide of the same device either without or with confocal light collection are displayed in Figs. 6.21(a) and 6.21(b) respectively. The M1 and M2 modes are mapped in both cases, which correspond to detuned S and AS PM supermodes. It is immediately clear that the spatial width of the peaks is narrower as a result of the narrower collection area for confocal mapping in Fig. 6.21(b). Additionally, the improved resolution enables the two peaks of the M1 mode to be resolved, which were otherwise observed as a single peak in Fig. 6.21(a) due to the large collection area when not using confocal techniques. It follows from the FDTD simulations in section 6.2 that these two peaks of the M1 mode are expected when the strip separation is sufficiently large and the spatial resolution is sufficient to resolve them.

We can compare the delocalization factor, F , and coupling strength, J , from the confocal measurements of the device in Fig. 6.21(b) to the non-confocal measurements of the same device in 6.21(a) to investigate the significance of the light collection as a source of error. We find a value of $F = 0.45$ for confocal measurement, compared to a value of $F = 0.50$ without confocal techniques, which suggests that a large collection area may result in an overestimate of F (as would be expected intuitively). This discrepancy has little effect on the calculation of J , which was estimated to be $J \sim 0.6\text{ nm}$ for both light collection methods. This supports the validity of the coupling strength estimates performed in section 6.3 without the use of confocal techniques. It is also possible for

this particular device to estimate F from the M1 mode, since the two peaks are resolved in the confocal map. Applying the same calculation method as for the M2 mode, this yields a higher value of $F = 0.74$, suggesting a coupling strength of $J \sim 0.7$ nm. The differences in the parameters obtained for the two different modes is not surprising given the number of approximations made in the coupled mode theory model (section 6.2.5), which is an incomplete description of the physical system. However, it is reassuring that the calculated coupling strength is reasonably consistent for all methods applied to this device. It should be noted that the estimate of the detuning, $\Delta\lambda$, is more strongly affected by the deviation in F , yielding values of $\Delta\lambda \sim 0.2$ nm and $\Delta\lambda \sim 0.5$ nm from confocal mapping of the M1 and M2 modes respectively. This is compared to a value of $\Delta\lambda \sim 0.4$ nm estimated from M2 without confocal techniques. As the values obtained from the M2 mode using both collection methods still agree well, the discrepancy from the M1 mode is likely to be due to limitations of the model.

The results for confocal and non-confocal mapping were compared for 8 selected devices (including the example in Fig. 6.21) with 2.5 μm and 3 μm strip separations (4 of each separation), which all had moderate delocalization of $F > 0.4$ when measured initially without confocal techniques. Devices were selected with relatively narrow strip separation and moderate F as this is the regime for which the resolution of the light collection technique is likely to have the most influence. Parameters measured and estimated using confocal maps will be denoted with the subscript C, while those from non-confocal maps will be denoted by NC. The change in delocalization factor, $\Delta F = F_{\text{NC}} - F_{\text{C}}$ observed when switching to confocal mapping was a mean of -0.1 ± 0.3 , with uncertainty represented by the sample standard deviation. Theoretically, we would typically expect a slight decrease in the value of F (and therefore a negative ΔF) when the light collection area is reduced, as a large collection area can artificially increase the measured F . While on average this was the case, ΔF exhibited significant variation between devices and was positive in some cases. This may suggest that some devices experienced physical changes between the initial non-confocal measurements and the confocal mapping, causing a physical change to F . Such a change is possible, as the sample was cooled down to 8 K and warmed up to room temperature multiple times (while stored under vacuum) between the sets of measurements. The expansion and contraction of the sample resulting from this could have introduced additional random detuning of the PM devices, which we would observe the effects of here, in addition to the effect of the reduced confocal light collection area. Given the good agreement of parameters estimated from the confocal and non-confocal maps of the device in Fig. 6.21, which supports good consistency between the confocal and

non-confocal method, this is a plausible possibility. Indeed, the change in the estimated detuning between the methods, $\Delta\lambda_{C-NC} = \Delta\lambda_{NC} - \Delta\lambda_C$ was found to have a mean of (0.3 ± 0.5) nm, which exhibits very large variation between devices. The mean change in the estimated coupling strength going to the confocal method, $\Delta J = J_{NC} - J_C$, was $(-3 \pm 20)\%$ relative to the estimate without confocal techniques.

Overall, while clear benefits of the increased spatial resolution granted by confocal techniques have been shown for the device in Fig. 6.21, in general it is difficult to quantify the influence that confocal techniques have on the estimates of the parameters F , J and $\Delta\lambda$ due to the possibility of additional detuning effects introduced in other devices studied by cooling and heating processes. If the example given in Fig. 6.21 is in fact representative of the differences between confocal and non-confocal techniques, then we would expect similar accuracy from both methods. More work would be recommended to quantify ΔF , $\Delta\lambda_{C-NC}$ and ΔJ , with measures taken to eliminate the possibility of physical changes to the sample between the measurements. This may require the ability to easily switch between confocal and non-confocal light collection, which is experimentally challenging due to the stringent requirements of the confocal alignment (and limits our ability to perform these tests).

6.4.2 Independent probing of photonic molecule cavities with confocal techniques

A significant advantage of using confocal techniques is the potential to collect selectively from one of two closely spaced cavities of a PM. We demonstrate that this is possible from confocal mapping of the double SU-8 strip device shown in Fig. 6.22 with a large strip separation of 4 μm . The 1D objective map in Fig. 6.22(a) shows the profile of the modes along the waveguide, which consist of two highly localized peaks corresponding to the constituent cavities, A and B. This suggests that these two cavities are uncoupled; it follows that when one cavity is pumped we do not expect to observe emission from the other cavity of device. This is confirmed by the 1D mirror maps in Figs. 6.22(b) and 6.22(c), which show mapping of the laser spot along the waveguide with the confocal collection fixed at either cavity A or B, respectively. In the discussion that follows, we refer to the cavity that the confocal collection is centred on as the primary cavity and the other cavity of the device as the secondary cavity. In both Figs. 6.22(b) and 6.22(c), we observe that light collected from the secondary cavity is heavily suppressed by the confocal collection. The majority

of (non-background) light is collected from the primary cavity, which allows it to be investigated individually. We see that emission is not observed from the primary cavity mode when the laser spot is positioned at the secondary cavity, which confirms that the two cavities are uncoupled.

2D confocal mapping (with a step size of $0.5\ \mu\text{m}$) of a strongly coupled SU-8 strip PM was performed to explicitly demonstrate optical coupling between the two cavities. We focus on the M2 mode (a detuned AS supermode) of a device with a strip separation of $3\ \mu\text{m}$ and a peak spacing of $3.3\ \mu\text{m}$ – sufficiently far apart to enable independent probing of the cavities. The objective map in Fig. 6.23(a) shows the mode profile, which has a brighter peak at cavity B than cavity A due

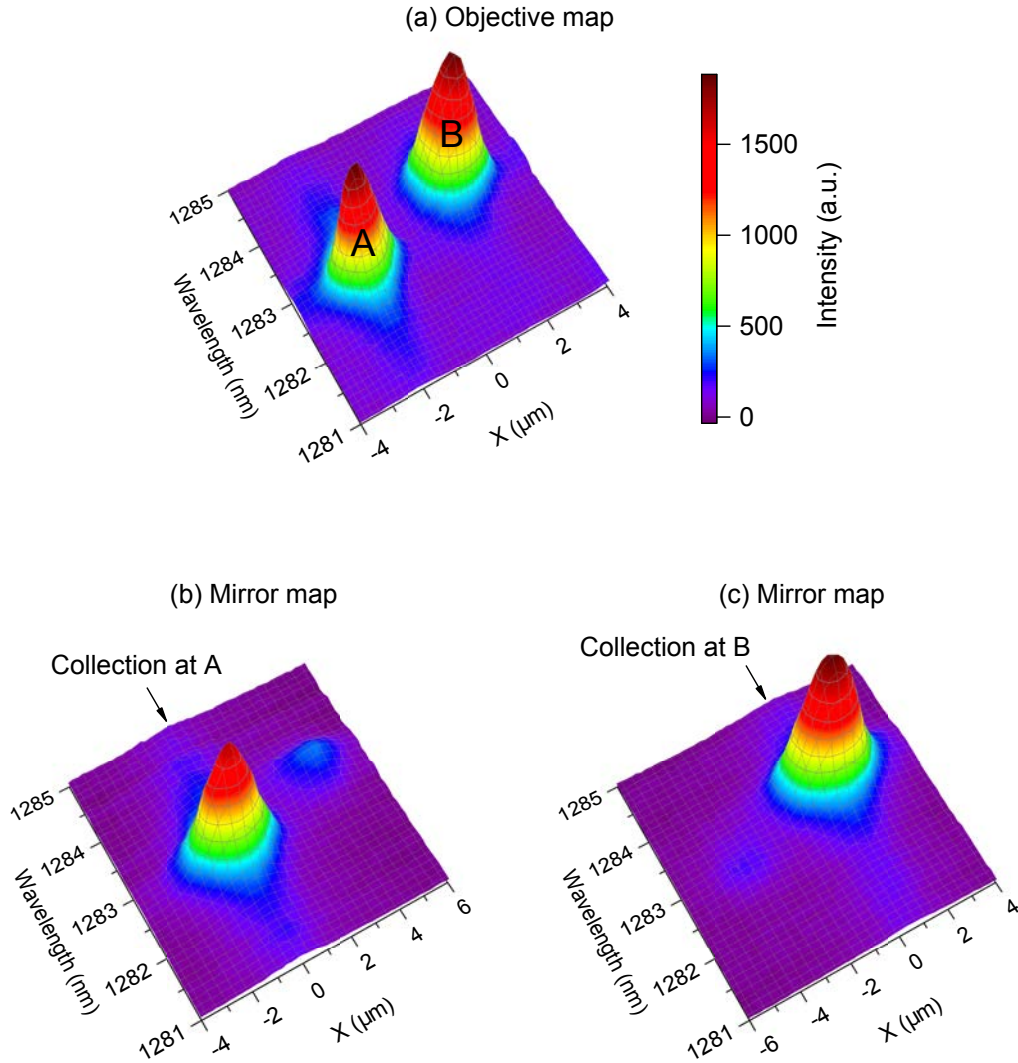


Figure 6.22: 1D confocal μPL maps obtained along the waveguide for a double SU-8 strip device (separation $4\ \mu\text{m}$) with uncoupled cavities. (a) Objective map (collection and excitation scanned simultaneously along the waveguide) showing two highly localized modes corresponding to cavities A and B. (b) and (c): mirror maps with collection fixed at A or B, respectively. The excitation spot is moved independently of the collection; its X position is presented relative to the collection. All maps use the same colour scale displayed in (a). An integration time of 1 s was used.

to the effects of detuning. From this map we estimate a coupling strength $J \sim 0.5$ nm and cavity detuning $\Delta\lambda \sim 0.5$ nm from a measured mode splitting of 1.14 nm and $F = 0.36$. Mirror maps of the device are plotted in Figs. 6.23(b) and 6.23(c), with the confocal collection positioned at cavity A or B respectively. Again we refer to the cavity at which the collection is centred as the primary cavity and the other cavity of the device as the secondary cavity. The observations from these maps clearly demonstrate coupling between the cavities: emission is observed from the primary cavity when the laser spot is positioned at the secondary cavity in either case. Additionally, the intensity collected from the primary cavity is approximately equal whether the primary or secondary cavity is pumped, with a dip in intensity clearly visible when neither cavity is strongly pumped. The appearance of two peaks with a pronounced dip in intensity between them demonstrates that the excitation spot and the effects of carrier diffusion are sufficiently small to not strongly pump either cavity when the spot is positioned between them. This is important, as it provides reassurance that the cavities can be pumped independently. In both Figs. 6.23(b) and 6.23(c), the maximum intensity collected from the primary cavity correlates well with the peak of the corresponding cavity measured in the objective map, Fig. 6.23(a). This correlation provides strong evidence that the confocal technique adequately excludes light from the secondary cavity and therefore the technique is sufficiently successful at selectively collecting light from the primary cavity.

Collection maps were also performed on the strongly coupled device, for which the laser spot was fixed at cavity A [Fig. 6.23(d)] or B [Fig. 6.23(e)] and the collection was scanned over a 2D area, using a combination of mirror and objective movement. The maps observed are approximately equivalent, with only a translational shift between them due to the definition of the co-ordinate system relative to the pumped cavity. It follows that the emission from the device is largely independent of which cavity is pumped, as would intuitively be expected for a well-coupled system for which light can easily pass between the two cavities. Therefore, the collection maps provide further evidence of the coupling between the cavities of the SU-8 strip PM.

6.5 Summary

The work of this chapter has demonstrated the successful application of the SU-8 cavity-writing technique to PMs. First, an overview of the field was given, with a focus on identifying what benefits the SU-8 method can offer for the fabrication of PMs. Perhaps the most promising aspect of the ability to position the PM cavities after e-beam fabrication steps is the potential to tune the

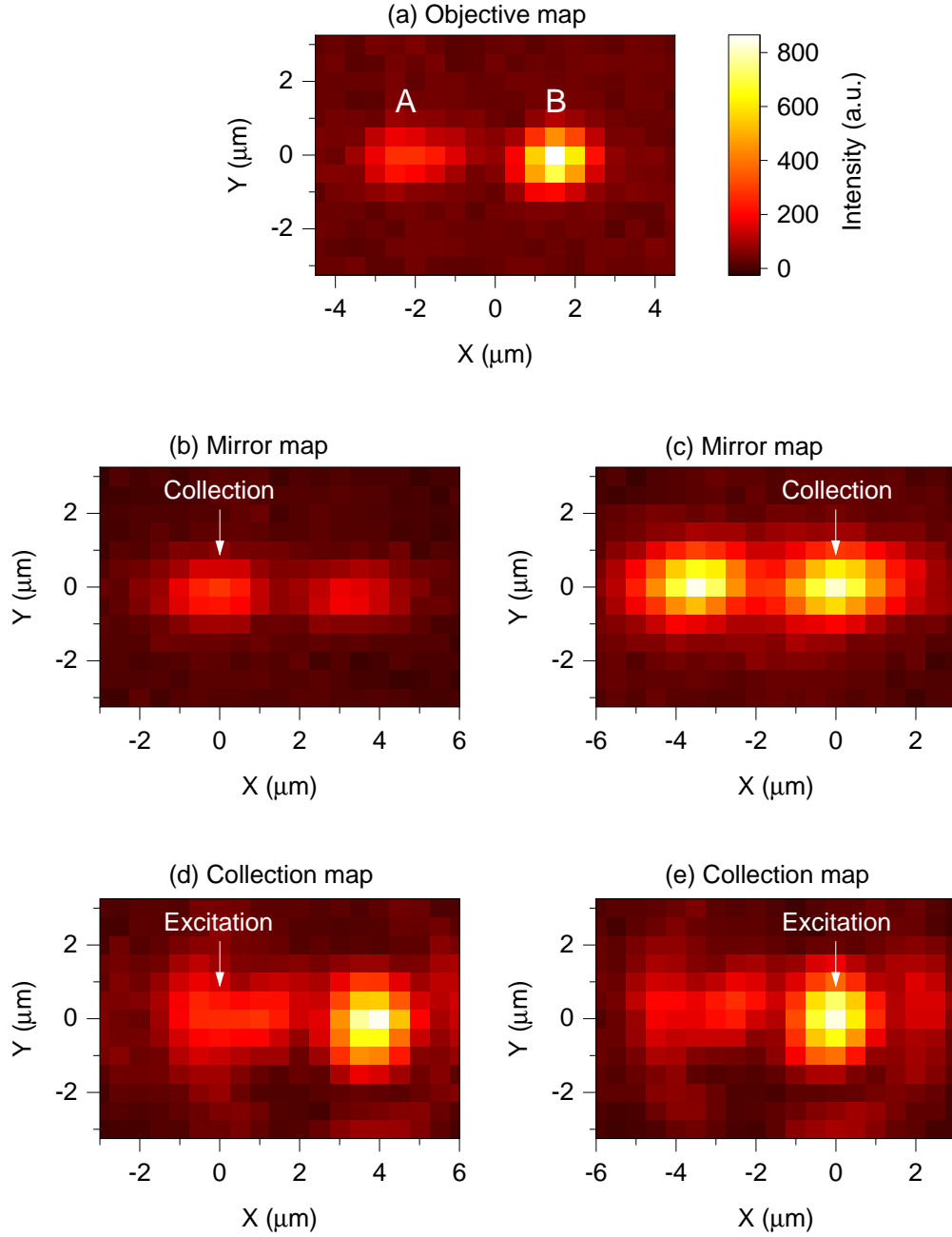


Figure 6.23: Confocal 2D μPL maps of the M2 mode of a strongly coupled SU-8 PM with a strip separation of $3\mu\text{m}$, recorded at a wavelength of 1281.3nm . All maps use the same colour scale for intensity. (a) Objective map showing local maxima of the mode labelled as A and B, which correspond to the two cavities of the PM. (b) and (c): scanning mirror maps with the confocal collection fixed at A or B, respectively. The laser spot is scanned independently of the collection area; its (X, Y) coordinate is defined relative to the collection position. (d) and (e): collection maps with the excitation fixed at A or B, respectively. The excitation remains fixed over one cavity and the confocal collection is scanned independently. The (X, Y) position corresponds to the position of the collection relative to the excitation spot.

PM mode splitting and structure to match multiple excitonic transitions of a QD located using μ PL measurements. This could facilitate the realisation of a PhC PM-based source of entangled photons similar to the micropillar PM device reported by Dousse *et al.* [154]. The potential for deterministic QD-PM coupling could also help achieve the unconventional photon blockade in a QD-PhC cavity system, which allows a photon blockade with only a weakly-coupled emitter [242].

FDTD simulations were performed to characterise the modes of double SU-8 strip devices, which clearly demonstrated their viability as a coupled two-cavity system. Simulations of detuned PMs were performed and coupled mode theory was applied from work by Brossard *et al.* [56] to explain the supermode behaviour. This theory was developed further to enable the coupling strength and detuning of devices to be estimated from their mode splitting and the delocalization factor of the modes. This enables the coupling strength and detuning to be estimated from a μ PL map of a PM device – a simple and convenient method that does not require the detuning to be reduced to zero in order to measure the coupling strength. Therefore, the sophisticated tuning techniques discussed in section 6.1.3, often applied to other systems, were not required in order to estimate the coupling strength using this method.

A large batch of double SU-8 strip devices was fabricated with a close to 100% rate of successful strip writing and an 84% yield of devices with modes that could be attributed to a coupled cavity system (including its convergence to a single cavity for small strip separations). The devices were characterised using μ PL mapping measurements; trends in the mode splitting, peak spacing and delocalization factor with strip separation were found to be consistent with trends predicted by FDTD simulations and from coupled mode theory, providing strong evidence of the successful creation of PMs. A trend of decreasing coupling strength as the separation between the cavities is increased was observed, evident from the decreasing trend in mode splitting and delocalization factor with increasing strip separation. This trend is attributed to a reduced evanescent field overlap as the cavity separation is increased and enables moderate control over the mode splitting by altering the strip separation, although this is somewhat limited by random variation due to fabrication imperfections. The mean coupling strength for a given strip separation was approximated using two methods, which gave consistent results and showed the expected trend of decreasing coupling strength with increasing strip separation. The estimation of the coupling strength from method A relied on measurements of the delocalization factor for each device, the determination of which could potentially be made more accurate by implementing confocal techniques with a reduced light collection area. This would be recommended for subsequent investigations. The

magnitude of the coupling strength was found to be consistent with similar devices from the literature [56, 57, 171, 225, 230].

Further investigations were conducted, implementing confocal techniques to reduce the light collection area. Improved mapping resolution was demonstrated, including the ability to resolve the two peaks of a detuned S supermode of a PM device. The effect of confocal collection on the estimates of parameters such as the coupling strength and delocalization factor was investigated for a selected sample of devices, but results were inconsistent. The possibility of physical changes to the sample (resulting in changes to the cavity detuning) between sets of non-confocal and confocal measurements was proposed as a contributing factor to this inconsistency. The difference made by switching to confocal collection could therefore not be quantified with certainty and further investigation would be recommended. Finally, confocal techniques were applied to explicitly show optical coupling between two cavities of a strongly coupled PM, using decoupled collection and excitation. This technique possesses the capability for applications in which different cavities of the device are pumped and collected from, such as an implementation of the unconventional photon blockade in which single photons are generated from the secondary (non-pumped) cavity [243].

Overall, the SU-8 strip PM technique is promising for novel applications and has relatively good reliability considering the level of technical challenge involved in consistently achieving strongly coupled PMs [56]. The method could benefit further from more refined SU-8 spinning processes to allow for more reliable fabrication of thin ($\lesssim 100$ nm) SU-8 strips, which would result in higher Q factors and likely larger coupling strength for a given strip separation due to an increased mode volume for very thin strips. The strips investigated in this work were instead optimised for reliable fabrication, with a median thickness of $0.25\text{ }\mu\text{m}$ determined from a selected sample. It would also be highly recommended to implement a method of independently tuning the cavities of the SU-8 PM, so that the detuning could be manually altered. This would require further investigation: perhaps the SU-8 could be altered to give it photo-chromic properties [231] or a method of tuning via localized photo-thermal heating could be applied [92, 237].

Conclusion

If quantum technologies based on single photons are to be utilised in real world applications, a challenge which needs to be addressed is the ability to fabricate SPSs on a larger scale. SPSs based on single self-assembled In(Ga)As/GaAs QDs coupled to microcavity modes can offer excellent performance, with high efficiencies, single photon purity and indistinguishability [14], but the limited yield of conventional brute-force fabrication methods (which rely on coupling by chance) has driven the need for more deterministic methods of achieving QD-cavity coupling. The SU-8 cavity writing method has been designed with this in mind, which, through the theoretical and experimental work presented in this thesis, is now sufficiently developed to be applied to attempts at achieving coupling.

The FDTD simulation investigations presented in Ch. 2 laid the groundwork required to understand the physics of the 2D PhC slab devices that the SU-8 cavity is based upon. The photonic band structure calculations and simulations of mode gap cavities [33, 34] performed were crucial to understanding the mechanisms by which the SU-8 cavity confines light. A proof-of-concept simulation of a 100 nm-thick SU-8 strip defined PhC waveguide cavity was performed, which supports a cavity mode with $Q_{\text{total}} = 7000$ and $V_0 = 1.36(\lambda_0/n)^3$. The generated cavity mode is attributed to a local alteration of the mode gap in the section of the PhC waveguide covered by SU-8, due to the local increase in refractive index contrast. Fourier analysis of the cavity mode revealed that the Q factor is limited by in-plane TE-TM mode coupling losses due to the broken z -symmetry of the structure, which is an important factor to consider in optimising the cavity design.

The first successful experimental demonstration of SU-8-defined cavities was by writing a disk of SU-8 photoresist on a PhC waveguide, which was covered in Ch. 4. It was shown via μ PL mapping

of the PhC waveguide, before and after writing the SU-8 disk, that cavity modes were created by the presence of the disk, with a 90% yield. FDTD simulation results suggested that the Q factor of the mode strongly depends on the height of the disk, with $h_{\text{disk}} \lesssim 100$ nm yielding a much higher Q . The fabricated disks had heights in the range 60-400 nm and the cavity modes exhibited a Q in the range 2300-7400. A negative correlation between height and Q was verified, as predicted by the FDTD simulations. From these results, it was evident that thin SU-8 structures are necessary to achieve a high Q for a laser spot-sized disk (~ 1 μm diameter); however, increasing the disk radius was also shown as a method of increasing the Q .

The technique for writing single cavities using SU-8 was refined in Ch. 5. The SU-8 strip cavity design was favoured because it supports a mode with a similar Q and V_0 to the SU-8 disk mode, but offers less stringent alignment requirements. A method of predicting the SU-8 film thickness via evaluation of its thickness-dependent colouration was introduced, which is a valuable tool for adjusting the exposure dose (via the writing speed) to achieve the desired SU-8 strip thickness. A large batch of SU-8 strip cavities was fabricated; 84% of the devices were confirmed via μPL mapping to support new cavity modes. Strips as thin as ~ 60 nm were achieved and higher Q factors were measured than for disk cavities, up to a maximum of 8700. The targeted cavity figure of merit for strong coupling, $\eta \sim 10^{10}\text{m}^{-1}$, derived in Ch. 3, was met by some of the devices, suggesting that these cavities would be suitable for the observation of strong coupling if sufficiently well-coupled to a QD. A cavity mode wavelength variation of ~ 5 nm was observed, which is larger than desired for coupling experiments (we ideally target $\lesssim 1$ nm), but is not considered unfeasibly large and could potentially be improved with more consistent fabrication. TRPL measurements on a high Q example demonstrated Purcell enhancement of the QD ensemble emission, with an estimated $F_{\text{P}} \sim 1.6$.

SU-8 cavities defined by wider strips were also investigated, which were shown theoretically to have a significantly higher Q/V_0 ratio and η . Increasing the width of a 100 nm-thick strip by just a few μm is theoretically predicted to increase the Q by an order of magnitude, while V_0 increases by only a factor of ~ 2 or less. The increased Q was attributed to a suppression of TE-TM coupling losses due to increased localization of the mode in Fourier space. Altering the strip width was also proposed as a method of controlling the cavity wavelength.

SU-8 strips with a variety of widths were fabricated on PhC waveguides, with thicknesses mostly in the 25-150 nm range. Strips were successfully written with close to 100% yield; however, the

yield of cavity modes was not explicitly measured (a high yield was assumed based on the previous experiments). The highest Q factors from an SU-8 cavity were recorded from these devices: the lower and upper quartiles were 6900 and 9000 respectively and the maximum Q was 10,900. However, it is expected that the Q factors were fabrication-limited due to imperfections in the PhC waveguides, which prevented the higher Q factors predicted by FDTD simulations from being achieved. Due to these limitations, writing wider SU-8 strips on the current wafers is unlikely to increase the Q/V_0 ratio or η , as a result of the increased V_0 for wider strips. Therefore, narrow SU-8 strip cavities are likely preferable for QD-cavity coupling experiments.

In Ch. 6, PMs formed from two SU-8 strip cavities on the same PhC waveguide were theoretically and experimentally investigated as an application of the SU-8 cavity technique. It was shown that the coupling strength between the two evanescently-coupled cavities can be adjusted by controlling the separation between the two strips, which alters the splitting between the supermodes of the PM. Fabricated devices, which exhibited modes with an 84% yield, were characterised using μ PPL techniques, principally to measure the mode splitting and the delocalization factor of the supermodes. This allowed estimation of the coupling strength and cavity detuning. Confocal mapping measurements with an independently movable collection area and laser excitation spot were used to explicitly demonstrate optical coupling between two cavities of a PM.

Going forwards, the obvious next step would be to attempt the proposed SU-8 cavity-QD coupling technique, which the SU-8 strip cavity design has proven to be well-suited for. This would require a low density QD sample with PhC waveguide devices on the surface, which was not available during this project. If a cavity mode can be placed with sufficient spatial overlap and spectral proximity to a single QD, then we could test for the strong coupling regime by looking for the signature anticrossing as the QD is temperature tuned into resonance with the mode. If anticrossing is not observed, the weak coupling regime could be tested for by using TRPL measurements to search for Purcell enhancement of the QD emission. If a coupled system is achieved at the target wavelength of 1.3 μm , its performance as a telecommunications wavelength SPS could be tested. The first step would be to perform an HBT experiment and look for the characteristic $g^{(2)}(0) < 1$.

If coupling is successful with the SU-8 cavity technique, it could also be desirable to couple a QD to an SU-8 PM. This could potentially enable some interesting configurations, such as the Purcell enhancement of two exciton lines from the same QD, which has been used in another PM system to generate a Purcell-enhanced source of entangled photons [154]. Another interesting prospect is

the unconventional photon blockade, which could allow a photon blockade with a QD only weakly coupled to the PM [242, 245].

Another avenue would be to further improve the SU-8 cavity design and performance. According to FDTD results, cavities formed from wide SU-8 strips could potentially reach a much higher Q/V_0 and η than the devices fabricated for this thesis. If cavities were created on a less fabrication-limited PhC capable of reaching higher Q , such as a Si wafer [48], much higher Q factors might be observed. Additionally, a stronger trend between strip width and Q might be observed than the weak trend observed in Ch. 5. The Q factors of the thinner strips ($\lesssim 100$ nm) presented in this work may have also been limited by the wafer, so would benefit from PhCs capable of a higher Q . Further optimisation of the SU-8 writing process would be desirable, to achieve higher consistency SU-8 structures. This could help to reduce the variation of the cavity mode wavelength, which would be preferable for coupling techniques. More uniform coverage of the PhCs would help to improve the process, which could perhaps be achieved with surface treatment to improve adhesion of SU-8 to the PhC membranes or by using larger chips, which may spin-coat more uniformly. An interesting prospect might also be to alter the properties of the SU-8 itself. For example, if the SU-8 could be given photochromic properties [188, 231], the cavity mode wavelength could be tuned by exposing it to certain colours of laser light. Another attractive prospect might be to dope the SU-8 with emitters, which could then potentially couple to the cavity mode.

Overall, the SU-8 cavity writing technique has shown reproducible success and considerable promise for future applications. The technology is ready to be applied towards the goal of deterministic fabrication of telecoms wavelength QD-cavity coupled SPSs and perhaps beyond.

Appendix A

Exposure dose calibration summary

This appendix summarises the yield data from 3 runs of SU-8 strip fabrication, in order to provide a tool for calibrating the exposure dosage. Run 1 refers to the first batch of fabricated SU-8 strips, reported in section 5.3. Run 2 refers to the reference ($N = 1$) SU-8 strips of the fabrication run detailed in section 5.5. Run 3 refers to double SU-8 strip devices reported in section 6.3: for the purposes of this analysis, devices with a strip separation of $2.5\text{ }\mu\text{m}$ or more were analysed (for which the SU-8 strips are distinct – see section 6.3.1) and each individual strip was recorded separately.

For each run, AFM profiling measurements were performed (as detailed in section 5.3.1) on devices to obtain the mean SU-8 strip height, \overline{H} , for given exposure settings. In Fig. A.1, data are plotted from all three runs, grouped by run number, SU-8 film thickness (T_{film}) estimated from its thickness-dependent colouration (see section 5.3.1) and ratio of cyclopentanone to SU-8 2007 used in the spin-coating mixture. \overline{H} is plotted against v_w , the writing speed, which determines the exposure dose, as all strips were written with the same 405 nm laser, with a power of $17.5\text{ }\mu\text{W}$ after the objective. Each data point is annotated with a yield (and sample size) for those settings. Fig. A.1(a) shows the full range of the data, whereas Fig. A.1(b) shows the thinner strips in more detail. The figures are intended to guide choice of v_w used for SU-8 strip exposures, based on the T_{film} estimate and spin-coating parameters, in addition to the target \overline{H} and yield.

It should be noted that all SU-8 exposures were performed at room temperature, with the sample mounted inside the cryostat (so that the effects of the window are accounted for), but not under vacuum. Based on previous studies, the SU-8 writing technique is expected to work at cryogenic temperatures [1, 192], but the required exposure dose may require some adjustment to those detailed here.

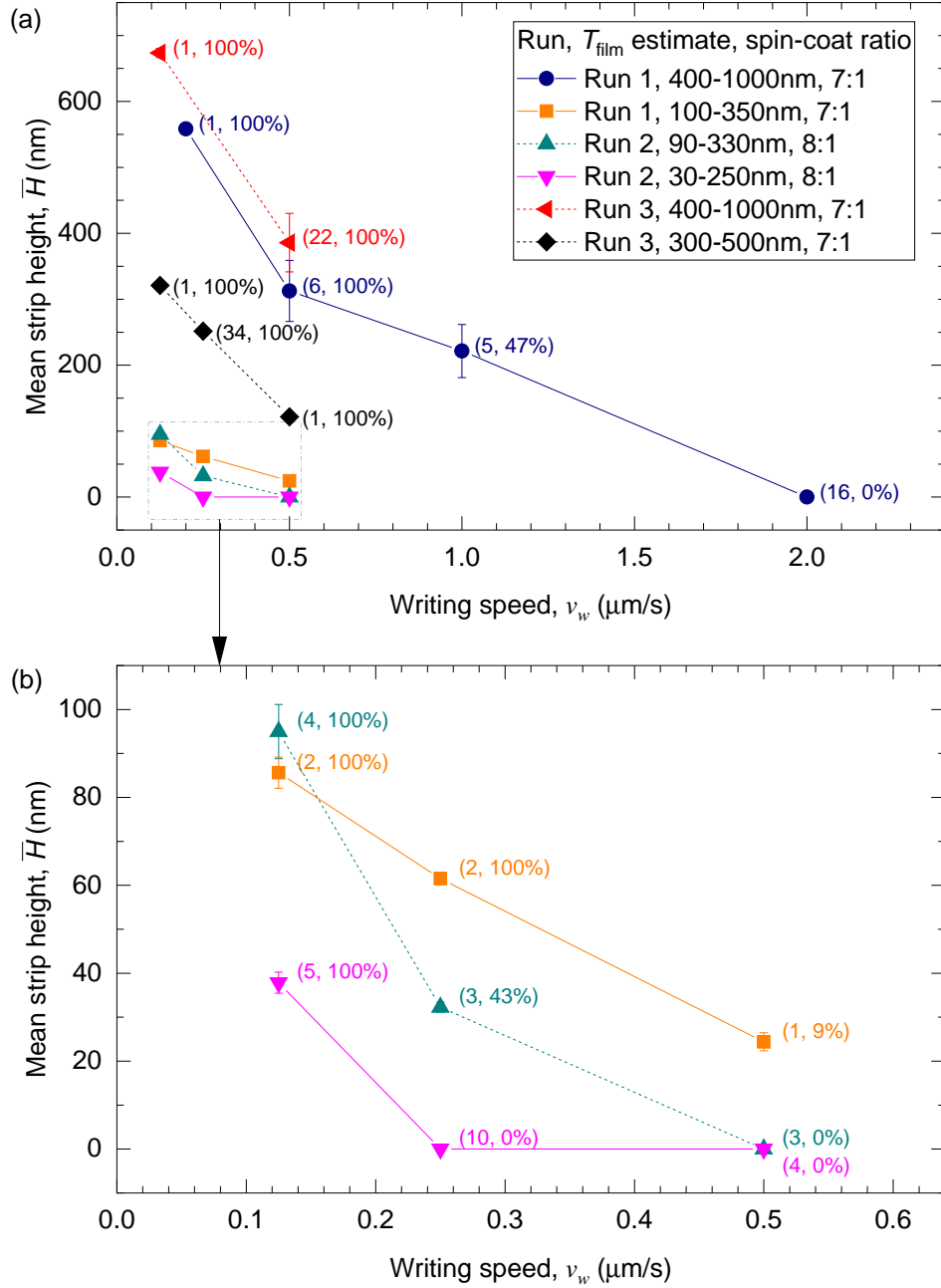


Figure A.1: Charts summarising data from 3 SU-8 strip fabrication runs, to be used as a guide to calibrate the required exposure dose for SU-8 strip writing. For each data series, the run number, T_{film} estimate and spin-coat ratio of cyclopentanone to SU-8 2007 is shown in the legend. For each writing speed, v_w , the mean strip height, \bar{H} , obtained from AFM profiling is shown. The full range is shown in (a); Fig. (b) displays the thinner strips in more detail. Each data point is labelled in the format (N_{AFM}, Y) , where N_{AFM} is the number of devices measured by AFM techniques and Y is the yield of successfully written strips for those parameters. Error bars show the standard error of the mean, where applicable.

Bibliography

- [1] L. P. Nuttall, “Scanning Micro-Photoluminescence Studies of GaAs Photonic Crystals and Perovskite Structures,” D.Phil thesis, University of Oxford (2019). iv, 23, 39, 86, 88, 99, 102, 103, 105, 120, 128, 129, 134, 154, 225
- [2] P. W. Shor, “Algorithms for quantum computation: discrete logarithms and factoring,” in “Proceedings 35th Annual Symposium on Foundations of Computer Science,” (1994), pp. 124–134. 1
- [3] C. H. Bennett and G. Brassard, “Quantum Cryptography: Public Key Distribution and Coin Tossing,” in “Proc. IEEE International Conference on Computers Systems and Signal Processing,” (IEEE, New York, 1984), pp. 175–179. 1, 63
- [4] P. W. Shor and J. Preskill, “Simple Proof of Security of the BB84 Quantum Key Distribution Protocol,” *Physical Review Letters* **85**, 441–444 (2000). 1, 63
- [5] T. D. Ladd, F. Jelezko, R. Laflamme, Y. Nakamura, C. Monroe, and J. L. O’Brien, “Quantum computers.” *Nature* **464**, 45–53 (2010). 1, 62
- [6] J. L. O’Brien, G. J. Pryde, A. G. White, T. C. Ralph, and D. Branning, “Demonstration of an all-optical quantum controlled-NOT gate,” *Nature* **426**, 264–267 (2003). 1, 62, 64
- [7] P. Kok, W. J. Munro, K. Nemoto, T. C. Ralph, J. P. Dowling, and G. J. Milburn, “Linear optical quantum computing with photonic qubits,” *Reviews of Modern Physics* **79**, 135–174 (2007). 1, 62
- [8] A. Politi, M. J. Cryan, J. G. Rarity, S. Yu, and J. L. O’Brien, “Silica-on-Silicon Waveguide Quantum Circuits,” *Science* **320**, 646–649 (2008). 1, 62, 64
- [9] A. Politi, J. C. F. Matthews, and J. L. O’Brien, “Shor’s Quantum Factoring Algorithm on a Photonic Chip,” *Science* **325**, 1221–1221 (2009). 1, 62, 64
- [10] A. Beveratos, R. Brouri, T. Gacoin, A. Villing, J.-P. Poizat, and P. Grangier, “Single Photon Quantum Cryptography,” *Physical Review Letters* **89**, 187901 (2002). 1
- [11] E. Waks, K. Inoue, C. Santori, D. Fattal, J. Vučković, G. S. Solomon, and Y. Yamamoto, “Secure communication: Quantum cryptography with a photon turnstile,” *Nature* **420**, 762 (2002). 1, 63
- [12] C. Gobby, Z. L. Yuan, and A. J. Shields, “Quantum key distribution over 122 km of standard telecom fiber,” *Applied Physics Letters* **84**, 3762–3764 (2004). 1
- [13] K. Takemoto, Y. Nambu, T. Miyazawa, Y. Sakuma, T. Yamamoto, S. Yoroazu, and Y. Arakawa, “Quantum key distribution over 120 km using ultrahigh purity single-photon source and superconducting single-photon detectors,” *Scientific Reports* **5**, 14383 (2015). 1, 82
- [14] P. Senellart, G. Solomon, and A. White, “High-performance semiconductor quantum-dot single-photon sources,” *Nature Nanotechnology* **12**, 1026 (2017). 1, 63, 64, 65, 78, 82, 93, 221

- [15] P. Michler, A. Kiraz, C. Becher, W. V. Schoenfeld, P. M. Petroff, L. Zhang, E. Hu, and A. Imamoglu, “A Quantum Dot Single-Photon Turnstile Device,” *Science* **290**, 2282–2285 (2000). 1, 63, 66, 71, 79, 80
- [16] O. Gazzano, S. Michaelis de Vasconcellos, C. Arnold, A. Nowak, E. Galopin, I. Sagnes, L. Lanco, A. Lemaître, and P. Senellart, “Bright solid-state sources of indistinguishable single photons,” *Nature Communications* **4**, 1425 (2013). 1, 81
- [17] K. H. Madsen, S. Ates, J. Liu, A. Javadi, S. M. Albrecht, I. Yeo, S. Stobbe, and P. Lodahl, “Efficient out-coupling of high-purity single photons from a coherent quantum dot in a photonic-crystal cavity,” *Physical Review B* **90**, 155303 (2014). 1, 81
- [18] E. M. Purcell, “Spontaneous emission probabilities at radio frequencies,” in “Confined electrons and photons,” (Springer, 1995), p. 839. 1, 72
- [19] T. Yoshie, A. Scherer, J. Hendrickson, G. Khitrova, H. M. Gibbs, G. Rupper, C. Ell, O. B. Shchekin, and D. G. Deppe, “Vacuum Rabi splitting with a single quantum dot in a photonic crystal nanocavity,” *Nature* **432**, 200–203 (2004). 2, 5, 17, 20, 24, 76, 80, 82, 83, 91, 138, 139
- [20] K. Hennessy, A. Badolato, M. Winger, D. Gerace, M. Atature, S. Gulde, S. Falt, E. L. Hu, and A. Imamoglu, “Quantum nature of a strongly coupled single quantum dot-cavity system,” *Nature* **445**, 896–899 (2007). 2, 24, 42, 81, 84, 85, 88, 91, 138, 139
- [21] D. Leonard, “Structural and optical properties of self-assembled InGaAs quantum dots,” *Journal of Vacuum Science & Technology B: Microelectronics and Nanometer Structures* **12**, 2516 (1994). 2
- [22] J. Y. Marzin, J. M. Gérard, A. Izraël, D. Barrier, and G. Bastard, “Photoluminescence of Single InAs Quantum Dots Obtained by Self-Organized Growth on GaAs,” *Physical Review Letters* **73**, 716–719 (1994). 2, 66
- [23] A. Badolato, K. Hennessy, M. Atatüre, J. Dreiser, E. Hu, P. M. Petroff, and A. Imamoglu, “Deterministic Coupling of Single Quantum Dots to Single Nanocavity Modes,” *Science* **308**, 1158–1161 (2005). 2, 79, 84
- [24] A. Dousse, L. Lanco, J. Suffczyński, E. Semenova, A. Miard, A. Lemaître, I. Sagnes, C. Roblin, J. Bloch, and P. Senellart, “Controlled Light-Matter Coupling for a Single Quantum Dot Embedded in a Pillar Microcavity Using Far-Field Optical Lithography,” *Physical Review Letters* **101**, 267404 (2008). 2, 84
- [25] S. M. Thon, M. T. Rakher, H. Kim, J. Gudat, W. T. M. Irvine, P. M. Petroff, and D. Bouwmeester, “Strong coupling through optical positioning of a quantum dot in a photonic crystal cavity,” *Applied Physics Letters* **94**, 111115 (2009). 2, 81, 84
- [26] A. K. Nowak, S. L. Portalupi, V. Giesz, O. Gazzano, C. Dal Savio, P.-F. Braun, K. Karrai, C. Arnold, L. Lanco, I. Sagnes, A. Lemaître, and P. Senellart, “Deterministic and electrically tunable bright single-photon source,” *Nature Communications* **5**, 3240 (2014). 2, 84
- [27] M. Gschrey, A. Thoma, P. Schnauber, M. Seifried, R. Schmidt, B. Wohlfeil, L. Krüger, J. H. Schulze, T. Heindel, S. Burger, F. Schmidt, A. Strittmatter, S. Rodt, and S. Reitzenstein, “Highly indistinguishable photons from deterministic quantum-dot microlenses utilizing three-dimensional in situ electron-beam lithography,” *Nature Communications* **6**, 7662 (2015). 2
- [28] M. Sartison, S. L. Portalupi, T. Gissibl, M. Jetter, H. Giessen, and P. Michler, “Combining in-situ lithography with 3D printed solid immersion lenses for single quantum dot spectroscopy,” *Scientific Reports* **7**, 39916 (2017). 2

- [29] B. Alloing, C. Zinoni, V. Zwiller, L. H. Li, C. Monat, M. Gobet, G. Buchs, A. Fiore, E. Pelucchi, and E. Kapon, “Growth and characterization of single quantum dots emitting at 1300 nm,” *Applied Physics Letters* **86**, 101908 (2005). 2, 66, 67, 79
- [30] E. C. Le Ru, P. Howe, T. S. Jones, and R. Murray, “Strain-engineered InAs/GaAs quantum dots for long-wavelength emission,” *Physical Review B* **67**, 165303 (2003). 2, 67, 69
- [31] E. M. Clarke and R. Murray, “Optical Properties of In(Ga)As/GaAs Quantum Dots for Optoelectronic Devices,” in “Handbook of Self Assembled Semiconductor Nanostructures for Novel Devices in Photonics and Electronics,” , M. B. T. Henini, ed. (Elsevier, Amsterdam, 2008), chap. 3, pp. 84–131. 2, 66, 67
- [32] Y. Akahane, T. Asano, B.-S. Song, and S. Noda, “High-Q photonic nanocavity in a two-dimensional photonic crystal,” *Nature* **425**, 944–947 (2003). 2, 5, 20, 24, 27, 33, 35, 59, 61, 80, 113
- [33] B.-S. Song, S. Noda, T. Asano, and Y. Akahane, “Ultra-high-Q photonic double-heterostructure nanocavity,” *Nat Mater* **4**, 207–210 (2005). 2, 5, 20, 39, 40, 41, 45, 61, 80, 138, 221
- [34] E. Kuramochi, M. Notomi, S. Mitsugi, A. Shinya, T. Tanabe, and T. Watanabe, “Ultrahigh-Q photonic crystal nanocavities realized by the local width modulation of a line defect,” *Applied Physics Letters* **88**, 041112 (2006). 2, 5, 17, 37, 42, 44, 45, 61, 82, 99, 221
- [35] H. Lorenz, M. Despont, N. Fahrni, N. LaBianca, P. Renaud, and P. Vettiger, “SU-8: a low-cost negative resist for MEMS,” *Journal of Micromechanics and Microengineering* **7**, 121–124 (1997). 2, 86
- [36] M. Notomi, K. Yamada, A. Shinya, J. Takahashi, C. Takahashi, and I. Yokohama, “Extremely Large Group-Velocity Dispersion of Line-Defect Waveguides in Photonic Crystal Slabs,” *Physical Review Letters* **87**, 253902 (2001). 2, 36, 39
- [37] M. Notomi, A. Shinya, S. Mitsugi, E. Kuramochi, and H.-Y. Ryu, “Waveguides, resonators and their coupled elements in photonic crystal slabs,” *Optics Express* **12**, 1551–1561 (2004). 2, 36
- [38] M. Bayer, T. Gutbrod, J. P. Reithmaier, A. Forchel, T. L. Reinecke, P. A. Knipp, A. A. Dremin, and V. D. Kulakovskii, “Optical Modes in Photonic Molecules,” *Physical Review Letters* **81**, 2582–2585 (1998). 3, 85, 171, 172, 174
- [39] J. D. Joannopoulos, S. G. Johnson, J. N. Winn, and R. D. Meade, *Photonic Crystals: Molding the Flow of Light* (Princeton University Press, Princeton, 2007), 2nd ed. 4, 9, 10, 15, 20, 23, 35, 39, 186
- [40] R. D. Meade, A. Devenyi, J. D. Joannopoulos, O. L. Alerhand, D. A. Smith, and K. Kash, “Novel applications of photonic band gap materials: Low-loss bends and high Q cavities,” *Journal of Applied Physics* **75**, 4753 (1994). 5
- [41] T. F. Krauss, R. M. D. L. Rue, and S. Brand, “Two-dimensional photonic-bandgap structures operating at near-infrared wavelengths,” *Nature* **383**, 699–702 (1996). 5
- [42] E. Yablonovitch, “Inhibited Spontaneous Emission in Solid-State Physics and Electronics,” *Physical Review Letters* **58**, 2059–2062 (1987). 5
- [43] S. Y. Lin, J. G. Fleming, D. L. Hetherington, B. K. Smith, R. Biswas, K. M. Ho, M. M. Sigalas, W. Zubrzycki, S. R. Kurtz, and J. Bur, “A three-dimensional photonic crystal operating at infrared wavelengths,” *Nature* **394**, 251–253 (1998). 5
- [44] O. Painter, R. K. Lee, A. Scherer, A. Yariv, J. D. O’Brien, P. D. Dapkus, and I. Kim, “Two-Dimensional Photonic Band-Gap Defect Mode Laser,” *Science* **284**, 1819–1821 (1999). 5

- [45] S. Noda, A. Chutinan, and M. Imada, “Trapping and emission of photons by a single defect in a photonic bandgap structure,” *Nature* **407**, 608–610 (2000). 5, 23, 36
- [46] J. Vučković, M. Lončar, H. Mabuchi, and A. Scherer, “Design of photonic crystal microcavities for cavity QED,” *Physical Review E* **65**, 016608 (2001). 5, 23
- [47] S. Ogawa, M. Imada, S. Yoshimoto, M. Okano, and S. Noda, “Control of Light Emission by 3D Photonic Crystals,” *Science* **305**, 227–229 (2004). 5
- [48] H. Sekoguchi, Y. Takahashi, T. Asano, and S. Noda, “Photonic crystal nanocavity with a Q-factor of ~ 9 million,” *Optics Express* **22**, 916–24 (2014). 5, 42, 45, 138, 164, 224
- [49] Lumerical Inc., “Lumerical FDTD Solutions,” <https://www.lumerical.com/products/fdtd-solutions/>. 6, 103, 183
- [50] K. Yee, “Numerical solution of initial boundary value problems involving Maxwell’s equations in isotropic media,” *IEEE Transactions on antennas and propagation* **14**, 302–307 (1966). 6
- [51] A. Taflov and S. C. Hagness, *Computational electrodynamics: the finite-difference time-domain method* (Artech house, 2005). 8
- [52] J.-P. Berenger, “A perfectly matched layer for the absorption of electromagnetic waves,” *Journal of Computational Physics* **114**, 185–200 (1994). 10, 11
- [53] Lumerical Inc., “Conformal FDTD Mesh Technology Delivers Subcell Accuracy,” <https://www.lumerical.com/learn/whitepapers/conformal-fdtd-mesh-technology-delivers-subcell-accuracy/>. 12
- [54] M. N. O. Sadiku, *Numerical techniques in electromagnetics* (CRC press, Boca Raton, 2000). 13
- [55] D. C. Reynolds, K. K. Bajaj, C. W. Litton, G. Peters, P. W. Yu, and J. D. Parsons, “Refractive index, n , and dispersion, $dn/d\lambda$, of GaAs at 2 K determined from FabryPerot cavity oscillations,” *Journal of Applied Physics* **61**, 342 (1987). 17
- [56] F. S. F. Brossard, B. P. L. Reid, C. C. S. Chan, X. L. Xu, J. P. Griffiths, D. A. Williams, R. Murray, and R. A. Taylor, “Confocal microphotoluminescence mapping of coupled and detuned states in photonic molecules,” *Optics Express* **21**, 16934–16945 (2013). 17, 66, 163, 174, 177, 178, 179, 184, 185, 192, 196, 204, 208, 219, 220
- [57] A. Y. Piggott, K. G. Lagoudakis, T. Sarmiento, M. Bajcsy, G. Shambat, and J. Vučković, “Photo-oxidative tuning of individual and coupled GaAs photonic crystal cavities,” *Optics Express* **22**, 15017–15023 (2014). 17, 20, 174, 179, 180, 191, 208, 220
- [58] Y. A. Vlasov, M. O’Boyle, H. F. Hamann, and S. J. McNab, “Active control of slow light on a chip with photonic crystal waveguides,” *Nature* **438**, 65 (2005). 20, 36, 39, 178
- [59] A. R. A. Chalcraft, S. Lam, D. O’Brien, T. F. Krauss, M. Sahin, D. Szymanski, D. Sanvitto, R. Oulton, M. S. Skolnick, A. M. Fox, D. M. Whittaker, H.-Y. Liu, and M. Hopkinson, “Mode structure of the L3 photonic crystal cavity,” *Applied Physics Letters* **90**, 241117 (2007). 20, 24, 32
- [60] J. Vučković, “Quantum optics and cavity QED with quantum dots in photonic crystals,” *arXiv* **1402.2541** (2014). 23, 31, 72, 73, 75
- [61] D. Englund, I. Fushman, and J. Vučković, “General recipe for designing photonic crystal cavities,” *Optics Express* **13**, 5961–5975 (2005). 23, 29
- [62] A. F. Oskooi, D. Roundy, M. Ibanescu, P. Bermel, J. D. Joannopoulos, and S. G. Johnson, “Meep: A flexible free-software package for electromagnetic simulations by the FDTD method,” *Computer Physics Communications* **181**, 687–702 (2010). 23, 103

- [63] H.-Y. Ryu, M. Notomi, and Y.-H. Lee, “High-quality-factor and small-mode-volume hexapole modes in photonic-crystal-slab nanocavities,” *Applied Physics Letters* **83**, 4294 (2003). 23
- [64] L. C. Andreani, D. Gerace, and M. Agio, “Gap maps, diffraction losses, and exciton-polaritons in photonic crystal slabs,” *Photonics and Nanostructures - Fundamentals and Applications* **2**, 103–110 (2004). 24, 32
- [65] S. L. Portalupi, M. Galli, C. Reardon, T. F. Krauss, L. O’Faolain, L. C. Andreani, and D. Gerace, “Planar photonic crystal cavities with far-field optimization for high coupling efficiency and quality factor,” *Optics Express* **18**, 16064–16073 (2010). 24, 32, 72, 79
- [66] D. Englund, A. Faraon, I. Fushman, N. Stoltz, P. Petroff, and J. Vucković, “Controlling cavity reflectivity with a single quantum dot,” *Nature* **450**, 857–61 (2007). 24, 91, 138, 139
- [67] A. Faraon, I. Fushman, D. Englund, N. Stoltz, P. Petroff, and J. Vučković, “Coherent generation of non-classical light on a chip via photon-induced tunnelling and blockade,” *Nature Physics* **4**, 859–863 (2008). 24, 81, 83, 88, 181
- [68] A. Faraon, I. Fushman, D. Englund, N. Stoltz, P. Petroff, and J. Vučković, “Dipole induced transparency in waveguide coupled photonic crystal cavities,” *Optics Express* **16**, 12154–12162 (2008). 24, 36
- [69] I. Fushman, D. Englund, A. Faraon, N. Stoltz, P. Petroff, and J. Vuckovic, “Controlled phase shifts with a single quantum dot,” *Science* **320**, 769–772 (2008). 24, 91, 138
- [70] M. Nomura, N. Kumagai, S. Iwamoto, Y. Ota, and Y. Arakawa, “Laser oscillation in a strongly coupled single-quantum-dot-nanocavity system,” *Nat Phys* **6**, 279–283 (2010). 24, 91
- [71] F. Pagliano, Y. Cho, T. Xia, F. van Otten, R. Johne, and A. Fiore, “Dynamically controlling the emission of single excitons in photonic crystal cavities,” *Nature Communications* **5**, 5786 (2014). 24, 80, 83
- [72] R. Bose, T. Cai, K. R. Choudhury, G. S. Solomon, and E. Waks, “All-optical coherent control of vacuum Rabi oscillations,” *Nat Photon* **8**, 858–864 (2014). 24, 81, 83, 91, 174, 181
- [73] C. Bonato, J. Hagemeier, D. Gerace, S. M. Thon, H. Kim, L. C. Andreani, P. M. Petroff, M. P. van Exter, and D. Bouwmeester, “Far-field emission profiles from L3 photonic crystal cavity modes,” *Photonics and Nanostructures - Fundamentals and Applications* **11**, 37–47 (2013). 27, 32
- [74] A. R. A. Chalcraft, S. Lam, B. D. Jones, D. Szymanski, R. Oulton, A. C. T. Thijssen, M. S. Skolnick, D. M. Whittaker, T. F. Krauss, and A. M. Fox, “Mode structure of coupled L3 photonic crystal cavities,” *Optics Express* **19**, 5670–5675 (2011). 27, 174, 177, 186
- [75] Y. Tanaka, T. Asano, R. Hatsuta, and S. Noda, “Investigation of point-defect cavity formed in two-dimensional photonic crystal slab with one-sided dielectric cladding,” *Applied Physics Letters* **88**, 11112 (2006). 32, 53, 54, 56, 57, 59
- [76] A. Chutinan and S. Noda, “Waveguides and waveguide bends in two-dimensional photonic crystal slabs,” *Physical Review B* **62**, 4488–4492 (2000). 36, 39
- [77] M. Notomi, “Manipulating light with strongly modulated photonic crystals,” *Reports on Progress in Physics* **73**, 96501 (2010). 36
- [78] T. Tanabe, M. Notomi, E. Kuramochi, A. Shinya, and H. Taniyama, “Trapping and delaying photons for one nanosecond in an ultrasmall high-Q photonic-crystal nanocavity,” *Nat Photon* **1**, 49–52 (2007). 36, 43, 45

- [79] M. Notomi, T. Tanabe, A. Shinya, E. Kuramochi, H. Taniyama, S. Mitsugi, and M. Morita, “Nonlinear and adiabatic control of high-Q photonic crystal nanocavities,” *Optics Express* **15**, 17458–17481 (2007). 36
- [80] F. Liu, A. J. Brash, J. O’Hara, L. M. P. P. Martins, C. L. Phillips, R. J. Coles, B. Royall, E. Clarke, C. Bentham, N. Prtljaga, I. E. Itskevich, L. R. Wilson, M. S. Skolnick, and A. M. Fox, “High Purcell factor generation of indistinguishable on-chip single photons,” *Nature Nanotechnology* **13**, 835–840 (2018). 36, 143
- [81] R. Bose, D. Sridharan, G. S. Solomon, and E. Waks, “Observation of strong coupling through transmission modification of a cavity-coupled photonic crystal waveguide,” *Optics Express* **19**, 5398–5409 (2011). 36, 81, 91
- [82] M. Arcari, I. Söllner, A. Javadi, S. Lindskov Hansen, S. Mahmoodian, J. Liu, H. Thyrrestrup, E. H. Lee, J. D. Song, S. Stobbe, and P. Lodahl, “Near-Unity Coupling Efficiency of a Quantum Emitter to a Photonic Crystal Waveguide,” *Physical Review Letters* **113**, 93603 (2014). 36
- [83] Y. Sato, Y. Tanaka, J. Upham, Y. Takahashi, T. Asano, and S. Noda, “Strong coupling between distant photonic nanocavities and its dynamic control,” *Nat Photon* **6**, 56–61 (2012). 36, 182, 187, 188
- [84] J. T. Mok and B. J. Eggleton, “Expect more delays,” *Nature* **433**, 811 (2005). 36
- [85] A. Javadi, I. Sollner, M. Arcari, S. L. Hansen, L. Midolo, S. Mahmoodian, G. Kirsanske, T. Pregnolato, E. H. Lee, J. D. Song, S. Stobbe, and P. Lodahl, “Single-photon non-linear optics with a quantum dot in a waveguide,” *Nat Commun* **6**, 8655 (2015). 36
- [86] F. S. F. Brossard, X. L. Xu, D. A. Williams, M. Hadjipanayi, M. Hugues, M. Hopkinson, X. Wang, and R. A. Taylor, “Strongly coupled single quantum dot in a photonic crystal waveguide cavity,” *Applied Physics Letters* **97**, 111101 (2010). 37, 42, 43, 44, 69, 81, 82, 83, 88, 91, 135, 138
- [87] M. Notomi and H. Taniyama, “On-demand ultrahigh-Q cavity formation and photon pinning via dynamic waveguide tuning,” *Optics Express* **16**, 18657–18666 (2008). 37, 39, 46
- [88] M.-K. Seo, J.-H. Kang, M.-K. Kim, B.-H. Ahn, J.-Y. Kim, K.-Y. Jeong, H.-G. Park, and Y.-H. Lee, “Wavelength-scale photonic-crystal laser formed by electron-beam-induced nanoblock deposition,” *Optics Express* **17**, 6790–8 (2009). 39, 47, 85, 137
- [89] S. Gardin, F. Bordas, X. Letartre, C. Seassal, A. Rahmani, R. Bozio, and P. Viktorovitch, “Microlasers based on effective index confined slow light modes in photonic crystal waveguides,” *Optics Express* **16**, 6331–9 (2008). 39, 47, 53, 85, 137
- [90] S. Tomljenovic-Hanic, C. M. de Sterke, M. J. Steel, B. J. Eggleton, Y. Tanaka, and S. Noda, “High-Q cavities in multilayer photonic crystal slabs,” *Optics Express* **15**, 17248–17253 (2007). 39, 47, 53, 85, 126, 146, 152
- [91] T. Asano, Y. Ochi, Y. Takahashi, K. Kishimoto, and S. Noda, “Photonic crystal nanocavity with a Q factor exceeding eleven million,” *Optics Express* **25**, 1769–1777 (2017). 42, 45, 79, 138, 164
- [92] C.-Y. Jin, R. Johne, M. Y. Swinkels, T. B. Hoang, L. Midolo, P. J. van Veldhoven, and A. Fiore, “Ultrafast non-local control of spontaneous emission,” *Nature nanotechnology* **9**, 886–890 (2014). 43, 174, 178, 179, 180, 181, 220
- [93] T. Asano, B.-S. Song, and S. Noda, “Analysis of the experimental Q factors (~ 1 million) of photonic crystal nanocavities,” *Optics Express* **14**, 1996–2002 (2006). 45, 164

-
- [94] S.-H. Kwon, T. Sünner, M. Kamp, and A. Forchel, “Ultrahigh-Q photonic crystal cavity created by modulating air hole radius of a waveguide,” *Optics Express* **16**, 4605–4614 (2008). 45
 - [95] S. Tomljenovic-Hanic, C. M. de Sterke, and M. J. Steel, “Design of high-Q cavities in photonic crystal slab heterostructures by air-holes infiltration,” *Optics Express* **14**, 12451–12456 (2006). 46, 85, 146, 152
 - [96] S. Tomljenovic-Hanic, M. J. Steel, C. Martijn de Sterke, and D. J. Moss, “High-Q cavities in photosensitive photonic crystals,” *Optics Letters* **32**, 542–544 (2007). 46, 85, 152
 - [97] U. Bog, C. L. C. Smith, M. W. Lee, S. Tomljenovic-Hanic, C. Grillet, C. Monat, L. O’Faolain, C. Karnutsch, T. F. Krauss, R. C. McPhedran, and B. J. Eggleton, “High-Q microfluidic cavities in silicon-based two-dimensional photonic crystal structures,” *Optics Letters* **33**, 2206–2208 (2008). 46, 85, 165
 - [98] M. W. Lee, C. Grillet, S. Tomljenovic-Hanic, E. C. Mägi, D. J. Moss, B. J. Eggleton, X. Gai, S. Madden, D.-Y. Choi, D. A. P. Bulla, and B. Luther-Davies, “Photowritten high-Q cavities in two-dimensional chalcogenide glass photonic crystals,” *Optics Letters* **34**, 3671–3673 (2009). 46, 85, 165
 - [99] F. S. F. Brossard, P. Vincenzo, A. J. Ramsay, J. P. Griffiths, H. Maxime, and S. Henning, “Inkjet-Printed Nanocavities on a Photonic Crystal Template,” *Advanced Materials* **29**, 1704425 (2017). 47, 85, 137, 174, 178
 - [100] T. C. Sum, A. A. Bettiol, J. A. van Kan, F. Watt, E. Y. B. Pun, and K. K. Tung, “Proton beam writing of low-loss polymer optical waveguides,” *Applied Physics Letters* **83**, 1707–1709 (2003). 48, 126
 - [101] E. Knill, R. Laflamme, and G. J. Milburn, “A scheme for efficient quantum computation with linear optics,” *Nature* **409**, 46–52 (2001). 62, 64
 - [102] A. J. Shields, “Semiconductor quantum light sources,” *Nat Photon* **1**, 215–223 (2007). 62, 63, 66, 67, 78
 - [103] G. Brassard, N. Lütkenhaus, T. Mor, and B. C. Sanders, “Limitations on Practical Quantum Cryptography,” *Physical Review Letters* **85**, 1330–1333 (2000). 63
 - [104] R. Hanbury Brown and R. Q. Twiss, “A Test of a New Type of Stellar Interferometer on Sirius,” *Nature* **178**, 1046–1048 (1956). 63
 - [105] M. Fox, *Quantum Optics : An Introduction*, Oxford Master Series in Physics (Oxford University Press, Oxford, 2006). 63, 78
 - [106] H. J. Kimble, M. Dagenais, and L. Mandel, “Photon Antibunching in Resonance Fluorescence,” *Physical Review Letters* **39**, 691–695 (1977). 63, 65
 - [107] F. Diedrich and H. Walther, “Nonclassical radiation of a single stored ion,” *Physical Review Letters* **58**, 203–206 (1987). 63, 65
 - [108] T. Basché, W. E. Moerner, M. Orrit, and H. Talon, “Photon antibunching in the fluorescence of a single dye molecule trapped in a solid,” *Physical Review Letters* **69**, 1516–1519 (1992). 63, 65
 - [109] C. K. Hong, Z. Y. Ou, and L. Mandel, “Measurement of subpicosecond time intervals between two photons by interference,” *Physical Review Letters* **59**, 2044–2046 (1987). 64
 - [110] S. Fasel, O. Alibart, S. Tanzilli, P. Baldi, A. Beveratos, N. Gisin, and H. Zbinden, “High-quality asynchronous heralded single-photon source at telecom wavelength,” *New Journal of Physics* **6**, 163 (2004). 64

- [111] M. Barbieri, T. J. Weinhold, B. P. Lanyon, A. Gilchrist, K. J. Resch, M. P. Almeida, and A. G. White, “Parametric downconversion and optical quantum gates: two’s company, four’s a crowd,” *Journal of Modern Optics* **56**, 209–214 (2009). 64
- [112] B. Lounis and W. E. Moerner, “Single photons on demand from a single molecule at room temperature,” *Nature* **407**, 491–493 (2000). 65
- [113] R. Brouri, A. Beveratos, J.-P. Poizat, and P. Grangier, “Photon antibunching in the fluorescence of individual color centers in diamond,” *Optics Letters* **25**, 1294–1296 (2000). 65
- [114] C. Kurtsiefer, S. Mayer, P. Zarda, and H. Weinfurter, “Stable Solid-State Source of Single Photons,” *Physical Review Letters* **85**, 290–293 (2000). 65
- [115] D. Leonard, K. Pond, and P. M. Petroff, “Critical layer thickness for self-assembled InAs islands on GaAs,” *Physical Review B* **50**, 11687–11692 (1994). 65
- [116] J. Tatebayashi, M. Nishioka, and Y. Arakawa, “Over 1.5 μm light emission from InAs quantum dots embedded in InGaAs strain-reducing layer grown by metalorganic chemical vapor deposition,” *Applied Physics Letters* **78**, 3469 (2001). 65, 67
- [117] I. N. Stranski and L. Krastanow, “Zur Theorie der orientierten Ausscheidung von Ionenkristallen aufeinander,” *Akad. Wiss. Lit. Mainz Math. -Natur. Kl.IIb* **146**, 797–810 (1938). 65
- [118] K.-i. Shiramine, T. Itoh, S. Muto, T. Kozaki, and S. Sato, “Adatom migration in Stranski-Krastanow growth of InAs quantum dots,” *Journal of Crystal Growth* **242**, 332–338 (2002). 66
- [119] J. M. Moison, F. Houzay, F. Barthe, L. Leprince, E. André, and O. Vatel, “Self-organized growth of regular nanometer-scale InAs dots on GaAs,” *Applied Physics Letters* **64**, 196–198 (1994). 66
- [120] R. M. Thompson, R. M. Stevenson, A. J. Shields, I. Farrer, C. J. Lobo, D. A. Ritchie, M. L. Leadbeater, and M. Pepper, “Single-photon emission from exciton complexes in individual quantum dots,” *Physical Review B* **64**, 201302 (2001). 66, 71
- [121] H. Saito, K. Nishi, and S. Sugou, “Influence of GaAs capping on the optical properties of InGaAs/GaAs surface quantum dots with 1.5 μm emission,” *Applied Physics Letters* **73**, 2742–2744 (1998). 66
- [122] J. M. García, G. Medeiros-Ribeiro, K. Schmidt, T. Ngo, J. L. Feng, A. Lorke, J. Kotthaus, and P. M. Petroff, “Intermixing and shape changes during the formation of InAs self-assembled quantum dots,” *Applied Physics Letters* **71**, 1014 (1997). 66
- [123] C. Santori, D. Fattal, J. Vučković, G. S. Solomon, and Y. Yamamoto, “Indistinguishable photons from a single-photon device,” *Nature* **419**, 594–597 (2002). 66, 81
- [124] R. Murray, D. Childs, S. Malik, P. Sivers, C. Roberts, J.-M. Hartmann, and P. Stavrinou, “1.3 μm Room Temperature Emission from InAs/GaAs Self-Assembled Quantum Dots,” *Japanese Journal of Applied Physics* **38**, 528–530 (1999). 66
- [125] D. L. Huffaker, G. Park, Z. Zou, O. B. Shchekin, and D. G. Deppe, “1.3 μm room-temperature GaAs-based quantum-dot laser,” *Applied Physics Letters* **73**, 2564 (1998). 66
- [126] K. Nishi, H. Saito, S. Sugou, and J.-S. Lee, “A narrow photoluminescence linewidth of 21 meV at 1.35 μm from strain-reduced InAs quantum dots covered by $\text{In}_{0.2}\text{Ga}_{0.8}\text{As}$ grown on GaAs substrates,” *Applied Physics Letters* **74**, 1111 (1999). 66
- [127] A. Löffler, J.-P. Reithmaier, A. Forchel, A. Sauerwald, D. Peskes, T. Kümmell, and G. Bacher, “Influence of the strain on the formation of GaInAs/GaAs quantum structures,” *Journal of Crystal Growth* **286**, 6–10 (2006). 67

- [128] E. Clarke, P. Spencer, E. Harbord, P. Howe, and R. Murray, “Growth, optical properties and device characterisation of InAs/GaAs quantum dot bilayers,” *Journal of Physics: Conference Series* **107**, 12003 (2008). 67
- [129] J. Johansen, S. Stobbe, I. S. Nikolaev, T. Lund-Hansen, P. T. Kristensen, J. M. Hvam, W. L. Vos, and P. Lodahl, “Size dependence of the wavefunction of self-assembled InAs quantum dots from time-resolved optical measurements,” *Physical Review B* **77**, 73303 (2008). 67
- [130] M. Grundmann, O. Stier, and D. Bimberg, “InAs/GaAs pyramidal quantum dots: Strain distribution, optical phonons, and electronic structure,” *Physical Review B* **52**, 11969–11981 (1995). 67
- [131] S. Kako, C. Santori, K. Hoshino, S. Gotzinger, Y. Yamamoto, and Y. Arakawa, “A gallium nitride single-photon source operating at 200 K,” *Nat Mater* **5**, 887–892 (2006). 67
- [132] M. J. Holmes, K. Choi, S. Kako, M. Arita, and Y. Arakawa, “Room-Temperature Triggered Single Photon Emission from a III-Nitride Site-Controlled Nanowire Quantum Dot,” *Nano Letters* **14**, 982–986 (2014). 67
- [133] T. Aichele, V. Zwiller, and O. Benson, “Visible single-photon generation from semiconductor quantum dots,” *New Journal of Physics* **6**, 90 (2004). 67
- [134] T. Miyazawa, K. Takemoto, Y. Sakuma, S. Hirose, T. Usuki, N. Yokoyama, M. Takatsu, and Y. Arakawa, “Single-Photon Generation in the 1.55- μm Optical-Fiber Band from an InAs/InP Quantum Dot,” *Japanese Journal of Applied Physics* **44**, L620–L622 (2005). 67, 82
- [135] S. Marcinkevicius and R. Leon, “Photoexcited carrier transfer in InGaAs quantum dot structures: Dependence on the dot density,” *Applied Physics Letters* **76**, 2406–2408 (2000). 68
- [136] J. Gérard, B. Sermage, B. Gayral, B. Legrand, E. Costard, and V. Thierry-Mieg, “Enhanced Spontaneous Emission by Quantum Boxes in a Monolithic Optical Microcavity,” *Physical Review Letters* **81**, 1110–1113 (1998). 68, 79, 143
- [137] C. Zinoni, B. Alloing, C. Monat, V. Zwiller, L. H. Li, A. Fiore, L. Lunghi, A. Gerardino, H. de Riedmatten, H. Zbinden, and N. Gisin, “Time-resolved and antibunching experiments on single quantum dots at 1300 nm,” *Applied Physics Letters* **88**, 131102 (2006). 68, 69, 71, 82
- [138] X. Xu, F. Brossard, K. Hammura, D. A. Williams, B. Alloing, L. H. Li, and A. Fiore, “Plug and Play single photons at 1.3 μm approaching gigahertz operation,” *Applied Physics Letters* **93**, 021124 (2008). 68, 82
- [139] I. E. Itskevich, M. S. Skolnick, D. J. Mowbray, I. A. Trojan, S. G. Lyapin, L. R. Wilson, M. J. Steer, M. Hopkinson, L. Eaves, and P. C. Main, “Excited states and selection rules in self-assembled InAs/GaAs quantum dots,” *Physical Review B* **60**, R2185–R2188 (1999). 69
- [140] J.-H. Kim, T. Cai, C. J. K. Richardson, R. P. Leavitt, and E. Waks, “Two-photon interference from a bright single-photon source at telecom wavelengths,” *Optica* **3**, 577–584 (2016). 69, 82
- [141] E. C. Le Ru, J. Fack, and R. Murray, “Temperature and excitation density dependence of the photoluminescence from annealed InAs/GaAs quantum dots,” *Physical Review B* **67**, 245318 (2003). 69
- [142] K. Mukai, N. Ohtsuka, and M. Sugawara, “High photoluminescence efficiency of InGaAs/GaAs quantum dots self-formed by atomic layer epitaxy technique,” *Applied Physics Letters* **70**, 2416–2418 (1997). 69

- [143] M. Bayer and A. Forchel, “Temperature dependence of the exciton homogeneous linewidth in $\text{In}_{0.60}\text{Ga}_{0.40}\text{As}/\text{GaAs}$ self-assembled quantum dots,” *Physical Review B* **65**, 41308 (2002). 69
- [144] P. Lodahl, S. Mahmoodian, and S. Stobbe, “Interfacing single photons and single quantum dots with photonic nanostructures,” *Reviews of Modern Physics* **87**, 347–400 (2015). 69, 78
- [145] M. Bayer, G. Ortner, O. Stern, A. Kuther, A. A. Gorbunov, A. Forchel, P. Hawrylak, S. Fafard, K. Hinzer, T. L. Reinecke, S. N. Walck, J. P. Reithmaier, F. Kloppe, and F. Schäfer, “Fine structure of neutral and charged excitons in self-assembled $\text{In}(\text{Ga})\text{As}/(\text{Al})\text{GaAs}$ quantum dots,” *Physical Review B* **65**, 195315 (2002). 69
- [146] D. Gammon, E. S. Snow, B. V. Shanabrook, D. S. Katzer, and D. Park, “Fine Structure Splitting in the Optical Spectra of Single GaAs Quantum Dots,” *Physical Review Letters* **76**, 3005–3008 (1996). 70
- [147] A. J. Bennett, M. A. Pooley, R. M. Stevenson, M. B. Ward, R. B. Patel, A. B. de la Giroday, N. Sköld, I. Farrer, C. A. Nicoll, D. A. Ritchie, and A. J. Shields, “Electric-field-induced coherent coupling of the exciton states in a single quantum dot,” *Nature Physics* **6**, 947 (2010). 70, 71, 83
- [148] R. Seguin, A. Schliwa, S. Rodt, K. Pötschke, U. W. Pohl, and D. Bimberg, “Size-Dependent Fine-Structure Splitting in Self-Organized InAs/GaAs Quantum Dots,” *Physical Review Letters* **95**, 257402 (2005). 70
- [149] N. Akopian, N. H. Lindner, E. Poem, Y. Berlatzky, J. Avron, D. Gershoni, B. D. Gerardot, and P. M. Petroff, “Entangled Photon Pairs from Semiconductor Quantum Dots,” *Physical Review Letters* **96**, 130501 (2006). 71
- [150] E. Moreau, I. Robert, L. Manin, V. Thierry-Mieg, J. M. Gérard, and I. Abram, “Quantum Cascade of Photons in Semiconductor Quantum Dots,” *Physical Review Letters* **87**, 183601 (2001). 71
- [151] R. M. Stevenson, R. J. Young, P. Atkinson, K. Cooper, D. A. Ritchie, and A. J. Shields, “A semiconductor source of triggered entangled photon pairs,” *Nature* **439**, 179–182 (2006). 71
- [152] J. Zhang, J. S. Wildmann, F. Ding, R. Trotta, Y. Huo, E. Zallo, D. Huber, A. Rastelli, and O. G. Schmidt, “High yield and ultrafast sources of electrically triggered entangled-photon pairs based on strain-tunable quantum dots,” *Nature Communications* **6**, 10067 (2015). 71
- [153] R. J. Young, R. M. Stevenson, P. Atkinson, K. Cooper, D. A. Ritchie, and A. J. Shields, “Improved fidelity of triggered entangled photons from single quantum dots,” *New Journal of Physics* **8**, 29 (2006). 71
- [154] A. Dousse, J. Suffczynski, A. Beveratos, O. Krebs, A. Lemaitre, I. Sagnes, J. Bloch, P. Voisin, and P. Senellart, “Ultrabright source of entangled photon pairs,” *Nature* **466**, 217–220 (2010). 71, 85, 172, 180, 189, 219, 223
- [155] M. Pelton, C. Santori, J. Vučković, B. Zhang, G. S. Solomon, J. Plant, and Y. Yamamoto, “Efficient Source of Single Photons: A Single Quantum Dot in a Micropost Microcavity,” *Physical Review Letters* **89**, 233602 (2002). 72, 79
- [156] A. Muller, E. B. Flagg, M. Metcalfe, J. Lawall, and G. S. Solomon, “Coupling an epitaxial quantum dot to a fiber-based external-mirror microcavity,” *Applied Physics Letters* **95**, 173101 (2009). 72
- [157] A. Schwagmann, S. Kalliakos, D. J. P. Ellis, I. Farrer, J. P. Griffiths, G. A. C. Jones, D. A. Ritchie, and A. J. Shields, “In-plane single-photon emission from a L3 cavity coupled to a photonic crystal waveguide,” *Optics Express* **20**, 28614–28624 (2012). 72, 79

- [158] S. Varoutsis, S. Laurent, P. Kramper, A. Lemaître, I. Sagnes, I. Robert-Philip, and I. Abram, “Restoration of photon indistinguishability in the emission of a semiconductor quantum dot,” *Physical Review B* **72**, 41303 (2005). 72, 81
- [159] J. P. Reithmaier, G. Sek, A. Löffler, C. Hofmann, S. Kuhn, S. Reitzenstein, L. V. Keldysh, V. D. Kulakovskii, T. L. Reinecke, and A. Forchel, “Strong coupling in a single quantum dot-semiconductor microcavity system,” *Nature* **432**, 197–200 (2004). 76, 79, 80, 81, 82, 83
- [160] C. Schneider, P. Gold, S. Reitzenstein, S. Höfling, and M. Kamp, “Quantum dot micropillar cavities with quality factors exceeding 250,000,” *Applied Physics B* **122**, 19 (2016). 79
- [161] C. Arnold, V. Loo, A. Lemaître, I. Sagnes, O. Krebs, P. Voisin, P. Senellart, and L. Lanco, “Optical bistability in a quantum dots/micropillar device with a quality factor exceeding 200 000,” *Applied Physics Letters* **100**, 111111 (2012). 79
- [162] G. S. Solomon, M. Pelton, and Y. Yamamoto, “Single-mode Spontaneous Emission from a Single Quantum Dot in a Three-Dimensional Microcavity,” *Physical Review Letters* **86**, 3903–3906 (2001). 79
- [163] E. Moreau, I. Robert, J. M. Gerard, I. Abram, L. Manin, and V. Thierry-Mieg, “Single-mode solid-state single photon source based on isolated quantum dots in pillar microcavities,” *Applied Physics Letters* **79**, 2865 (2001). 79
- [164] J. Vučković, D. Fattal, C. Santori, G. S. Solomon, and Y. Yamamoto, “Enhanced single-photon emission from a quantum dot in a micropost microcavity,” *Applied Physics Letters* **82**, 3596–3598 (2003). 79
- [165] A. J. Bennett, D. C. Unitt, P. Atkinson, D. A. Ritchie, and A. J. Shields, “High performance single photon sources from photolithographically defined pillar microcavities,” *Optics Express* **13**, 50–55 (2005). 79
- [166] Z. Yuan, B. E. Kardynal, R. M. Stevenson, A. J. Shields, C. J. Lobo, K. Cooper, N. S. Beattie, D. A. Ritchie, and M. Pepper, “Electrically Driven Single-Photon Source,” *Science* **295**, 102–105 (2002). 79
- [167] A. J. Bennett, D. C. Unitt, P. See, A. J. Shields, P. Atkinson, K. Cooper, and D. A. Ritchie, “Microcavity single-photon-emitting diode,” *Applied Physics Letters* **86**, 181102 (2005). 79
- [168] D. Englund, D. Fattal, E. Waks, G. Solomon, B. Zhang, T. Nakaoka, Y. Arakawa, Y. Yamamoto, and J. Vučković, “Controlling the Spontaneous Emission Rate of Single Quantum Dots in a Two-Dimensional Photonic Crystal,” *Physical Review Letters* **95**, 13904 (2005). 79, 143
- [169] S. Laurent, S. Varoutsis, L. Le Gratiet, A. Lematre, I. Sagnes, F. Raineri, A. Levenson, I. Robert-Philip, and I. Abram, “Indistinguishable single photons from a single-quantum dot in a two-dimensional photonic crystal cavity,” *Applied Physics Letters* **87**, 163107 (2005). 79, 81
- [170] E. Peter, P. Senellart, D. Martrou, A. Lemaître, J. Hours, J. M. Gérard, and J. Bloch, “Exciton-Photon Strong-Coupling Regime for a Single Quantum Dot Embedded in a Microcavity,” *Physical Review Letters* **95**, 67401 (2005). 81
- [171] A. Majumdar, A. Rundquist, M. Bajcsy, and J. Vučković, “Cavity quantum electrodynamics with a single quantum dot coupled to a photonic molecule,” *Physical Review B* **86**, 045315 (2012). 81, 83, 91, 174, 178, 191, 204, 208, 220
- [172] D. Press, S. Götzinger, S. Reitzenstein, C. Hofmann, A. Löffler, M. Kamp, A. Forchel, and Y. Yamamoto, “Photon Antibunching from a Single Quantum-Dot-Microcavity System in the Strong Coupling Regime,” *Physical Review Letters* **98**, 117402 (2007). 81

- [173] A. Imamoglu, H. Schmidt, G. Woods, and M. Deutsch, “Strongly Interacting Photons in a Nonlinear Cavity,” *Physical Review Letters* **79**, 1467–1470 (1997). 81
- [174] K. M. Birnbaum, A. Boca, R. Miller, A. D. Boozer, T. E. Northup, and H. J. Kimble, “Photon blockade in an optical cavity with one trapped atom,” *Nature* **436**, 87–90 (2005). 81, 181
- [175] Y.-M. He, Y. He, Y.-J. Wei, D. Wu, M. Atatüre, C. Schneider, S. Höfling, M. Kamp, C.-Y. Lu, and J.-W. Pan, “On-demand semiconductor single-photon source with near-unity indistinguishability,” *Nature nanotechnology* **8**, 213–7 (2013). 81
- [176] A. J. Bennett, D. C. Unitt, A. J. Shields, P. Atkinson, and D. A. Ritchie, “Influence of exciton dynamics on the interference of two photons from a microcavity single-photon source,” *Optics Express* **13**, 7772–7778 (2005). 81
- [177] J. C. Loredó, N. A. Zakaria, N. Somaschi, C. Anton, L. de Santis, V. Giesz, T. Grange, M. A. Broome, O. Gazzano, G. Coppola, I. Sagnes, A. Lemaitre, A. Auffeves, P. Senellart, M. P. Almeida, and A. G. White, “Scalable performance in solid-state single-photon sources,” *Optica* **3**, 433–440 (2016). 81
- [178] R. B. Patel, A. J. Bennett, I. Farrer, C. A. Nicoll, D. A. Ritchie, and A. J. Shields, “Two-photon interference of the emission from electrically tunable remote quantum dots,” *Nature Photonics* **4**, 632 (2010). 81
- [179] M. B. Ward, O. Z. Karimov, D. C. Unitt, Z. L. Yuan, P. See, D. G. Gevaux, A. J. Shields, P. Atkinson, and D. A. Ritchie, “On-demand single-photon source for 1.3 μm telecom fiber,” *Applied Physics Letters* **86**, 201111 (2005). 82
- [180] M. B. Ward, T. Farrow, P. See, Z. L. Yuan, O. Z. Karimov, A. J. Bennett, A. J. Shields, P. Atkinson, K. Cooper, and D. A. Ritchie, “Electrically driven telecommunication wavelength single-photon source,” *Applied Physics Letters* **90**, 063512 (2007). 82
- [181] M. D. Birowosuto, H. Sumikura, S. Matsuo, H. Taniyama, P. J. van Veldhoven, R. Nötzel, and M. Notomi, “Fast Purcell-enhanced single photon source in 1,550-nm telecom band from a resonant quantum dot-cavity coupling,” *Scientific Reports* **2**, 321 (2012). 82
- [182] M. Petruzzella, T. Xia, F. Pagliano, S. Birindelli, L. Midolo, Z. Zobenica, L. H. Li, E. H. Linfield, and A. Fiore, “Fully tuneable, Purcell-enhanced solid-state quantum emitters,” *Applied Physics Letters* **107**, 141109 (2015). 83, 143
- [183] A. Laucht, F. Hofbauer, N. Hauke, J. Angele, S. Stobbe, M. Kaniber, G. Böhm, P. Lodahl, M.-C. Amann, and J. J. Finley, “Electrical control of spontaneous emission and strong coupling for a single quantum dot,” *New Journal of Physics* **11**, 23034 (2009). 83
- [184] R. Bose, T. Cai, G. S. Solomon, and E. Waks, “All-optical tuning of a quantum dot in a coupled cavity system,” *Applied Physics Letters* **100**, 231107 (2012). 83, 91, 174, 181
- [185] E. B. Flagg, A. Muller, S. V. Polyakov, A. Ling, A. Migdall, and G. S. Solomon, “Interference of Single Photons from Two Separate Semiconductor Quantum Dots,” *Physical Review Letters* **104**, 137401 (2010). 83
- [186] R. Trotta, J. Martín-Sánchez, J. S. Wildmann, G. Piredda, M. Reindl, C. Schimpf, E. Zallo, S. Stroj, J. Edlinger, and A. Rastelli, “Wavelength-tunable sources of entangled photons interfaced with atomic vapours,” *Nature Communications* **7**, 10375 (2016). 83
- [187] S. Mosor, J. Hendrickson, B. C. Richards, J. Sweet, G. Khitrova, H. M. Gibbs, T. Yoshie, A. Scherer, O. B. Shchekin, and D. G. Deppe, “Scanning a photonic crystal slab nanocavity by condensation of xenon,” *Applied Physics Letters* **87**, 141105 (2005). 83
- [188] D. Sridharan, E. Waks, G. Solomon, and J. T. Fourkas, “Reversible tuning of photonic crystal cavities using photochromic thin films,” *Applied Physics Letters* **96**, 153303 (2010). 83, 224

-
- [189] C. Schneider, M. Strauß, T. Sünner, A. Huggenberger, D. Wiener, S. Reitzenstein, M. Kamp, S. Höfling, and A. Forchel, “Lithographic alignment to site-controlled quantum dots for device integration,” *Applied Physics Letters* **92**, 183101 (2008). 83
 - [190] C. Schneider, A. Huggenberger, T. Sünner, T. Heindel, M. Strauss, S. Göpfert, P. Weinmann, S. Reitzenstein, L. Worschech, M. Kamp, S. Höfling, and A. Forchel, “Single site-controlled In(Ga)As/GaAs quantum dots: growth, properties and device integration.” *Nanotechnology* **20**, 434012 (2009). 83
 - [191] C. Schneider, T. Heindel, A. Huggenberger, T. A. Niederstrasser, S. Reitzenstein, A. Forchel, S. Höfling, and M. Kamp, “Microcavity enhanced single photon emission from an electrically driven site-controlled quantum dot,” *Applied Physics Letters* **100**, 91108 (2012). 83
 - [192] K. H. Lee, A. M. Green, R. A. Taylor, D. N. Sharp, J. Scrimgeour, O. M. Roche, J. H. Na, A. F. Jarjour, A. J. Turberfield, F. S. F. Brossard, D. A. Williams, and G. A. D. Briggs, “Registration of single quantum dots using cryogenic laser photolithography,” *Applied Physics Letters* **88**, 193106 (2006). 84, 87, 88, 105, 180, 225
 - [193] A. Dousse, J. Suffczyński, R. Braive, A. Miard, A. Lemaître, I. Sagnes, L. Lanco, J. Bloch, P. Voisin, and P. Senellart, “Scalable implementation of strongly coupled cavity-quantum dot devices,” *Applied Physics Letters* **94**, 121102 (2009). 84, 85
 - [194] A. del Campo and C. Greiner, “SU-8: a photoresist for high-aspect-ratio and 3D submicron lithography,” *Journal of Micromechanics and Microengineering* **17**, R81–R95 (2007). 86
 - [195] B. Yang, L. Yang, R. Hu, Z. Sheng, D. Dai, Q. Liu, and S. He, “Fabrication and Characterization of Small Optical Ridge Waveguides Based on SU-8 Polymer,” *Journal of Lightwave Technology* **27**, 4091–4096 (2009). 86
 - [196] B. S. Schmidt, A. H. J. Yang, D. Erickson, and M. Lipson, “Optofluidic trapping and transport on solid core waveguides within a microfluidic device,” *Optics Express* **15**, 14322–14334 (2007). 86
 - [197] M. Deubel, G. von Freymann, M. Wegener, S. Pereira, K. Busch, and C. M. Soukoulis, “Direct laser writing of three-dimensional photonic-crystal templates for telecommunications,” *Nature Materials* **3**, 444–447 (2004). 86
 - [198] A. Sundaramurthy, P. J. Schuck, N. R. Conley, D. P. Fromm, G. S. Kino, and W. E. Moerner, “Toward Nanometer-Scale Optical Photolithography: Utilizing the Near-Field of Bowtie Optical Nanoantennas,” *Nano Letters* **6**, 355–360 (2006). 87
 - [199] I. S. Amiri, V. J. Sorger, M. M. Ariannejad, X. Ling, M. Ghasemi, and P. Yupapin, “Channel resolution enhancement through scalability of nano/micro-scale thickness and width of SU-8 polymer based optical channels using UV lithography,” *Microsystem Technologies* **24**, 1673–1681 (2018). 87
 - [200] R. J. Warburton, C. S. Dürr, K. Karrai, J. P. Kotthaus, G. Medeiros-Ribeiro, and P. M. Petroff, “Charged Excitons in Self-Assembled Semiconductor Quantum Dots,” *Physical Review Letters* **79**, 5282–5285 (1997). 88, 91
 - [201] R. Bose, D. Sridharan, H. Kim, G. S. Solomon, and E. Waks, “Low-Photon-Number Optical Switching with a Single Quantum Dot Coupled to a Photonic Crystal Cavity,” *Physical Review Letters* **108**, 227402 (2012). 88, 91
 - [202] P. G. Eliseev, H. Li, A. Stintz, G. T. Liu, T. C. Newell, K. J. Malloy, and L. F. Lester, “Transition dipole moment of InAs/InGaAs quantum dots from experiments on ultralow-threshold laser diodes,” *Applied Physics Letters* **77**, 262–264 (2000). 92

- [203] L. P. Nuttall, F. S. F. Brossard, S. A. Lennon, B. P. L. Reid, J. Wu, J. Griffiths, and R. A. Taylor, “Optical fabrication and characterisation of SU-8 disk photonic waveguide heterostructure cavities,” *Optics Express* **25**, 24615–24622 (2017). 102, 105, 116
- [204] X. Letartre, C. Seassal, C. Grillet, P. Rojo-Romeo, P. Viktorovitch, M. Le Vassor d’Yerville, D. Cassagne, and C. Jouanin, “Group velocity and propagation losses measurement in a single-line photonic-crystal waveguide on InP membranes,” *Applied Physics Letters* **79**, 2312–2314 (2001). 107
- [205] D. W. Marquardt, “An Algorithm for Least-Squares Estimation of Nonlinear Parameters,” *Journal of the Society for Industrial and Applied Mathematics* **11**, 431–441 (1963). 109
- [206] S. A. Lennon, F. S. F. Brossard, L. P. Nuttall, J. Wu, J. Griffiths, and R. A. Taylor, “Photonic molecules defined by SU-8 photoresist strips on a photonic crystal waveguide,” *Optics Express* **26**, 32332–32345 (2018). 117, 171
- [207] D. Nečas and K. Petr, “Gwyddion: an open-source software for SPM data analysis,” *Open Physics* **10**, 181 (2012). 130
- [208] J. Hendrickson, B. C. Richards, J. Sweet, S. Mosor, C. Christenson, D. Lam, G. Khitrova, H. M. Gibbs, T. Yoshie, A. Scherer, O. B. Shchekin, and D. G. Deppe, “Quantum dot photonic-crystal-slab nanocavities: Quality factors and lasing,” *Physical Review B* **72**, 193303 (2005). 137, 165
- [209] S. Combr  , A. De Rossi, Q. V. Tran, and H. Benisty, “GaAs photonic crystal cavity with ultrahigh Q: microwatt nonlinearity at 1.55 μm ,” *Optics Letters* **33**, 1908–1910 (2008). 138
- [210] W.-H. Chang, W.-Y. Chen, H.-S. Chang, T.-P. Hsieh, J.-I. Chyi, and T.-M. Hsu, “Efficient Single-Photon Sources Based on Low-Density Quantum Dots in Photonic-Crystal Nanocavities,” *Physical Review Letters* **96**, 117401 (2006). 141
- [211] L. Balet, M. Francardi, A. Gerardino, N. Chauvin, B. Alloing, C. Zinoni, C. Monat, L. H. Li, N. Le Thomas, R. Houdr  , and A. Fiore, “Enhanced spontaneous emission rate from single InAs quantum dots in a photonic crystal nanocavity at telecom wavelengths,” *Applied Physics Letters* **91**, 123115 (2007). 141, 143
- [212] N. Chauvin, L. Balet, B. Alloing, C. Zinoni, L. Li, A. Fiore, L. Grenouillet, P. Gilet, N. Olivier, A. Tchebnokov, M. Terrier, and J.-M. G  rard, “Enhanced spontaneous emission from InAs/GaAs quantum dots in pillar microcavities emitting at telecom wavelengths,” *Optics Letters* **32**, 2747–2749 (2007). 142, 143
- [213] R. Hostein, R. Braive, M. Larqu  , K.-H. Lee, A. Talneau, L. Le Gratiet, I. Robert-Philip, I. Sagnes, and A. Beveratos, “Room temperature spontaneous emission enhancement from quantum dots in photonic crystal slab cavities in the telecommunications C band,” *Applied Physics Letters* **94**, 123101 (2009). 143
- [214] A. Kress, F. Hofbauer, N. Reinelt, M. Kaniber, H. J. Krenner, R. Meyer, G. B  hm, and J. J. Finley, “Manipulation of the spontaneous emission dynamics of quantum dots in two-dimensional photonic crystals,” *Physical Review B* **71**, 241304 (2005). 143
- [215] I. Fleming, *Molecular Orbitals and Organic Chemical Reactions* (Wiley, Chichester, 2011), reference ed. 172
- [216] H. Lin, J.-H. Chen, S.-S. Chao, M.-C. Lo, S.-D. Lin, and W.-H. Chang, “Strong coupling of different cavity modes in photonic molecules formed by two adjacent microdisk microcavities,” *Optics Express* **18**, 23948–23956 (2010). 172, 176, 180
- [217] A. Nakagawa, S. Ishii, and T. Baba, “Photonic molecule laser composed of GaInAsP microdisks,” *Applied Physics Letters* **86**, 41112 (2005). 172

- [218] T. Mukaiyama, K. Takeda, H. Miyazaki, Y. Jimba, and M. Kuwata-Gonokami, “Tight-Binding Photonic Molecule Modes of Resonant Bispheres,” *Physical Review Letters* **82**, 4623–4626 (1999). 172
- [219] T. D. Happ, M. Kamp, A. Forchel, A. V. Bazhenov, I. I. Tartakovskii, A. Gorbunov, and V. D. Kulakovskii, “Coupling of point-defect microcavities in two-dimensional photonic-crystal slabs,” *Journal of the Optical Society of America B* **20**, 373–378 (2003). 174
- [220] S. I. Baba, K. Nozaki, and Toshihiko, “Photonic Molecules in Photonic Crystals,” *Japanese Journal of Applied Physics* **45**, 6108 (2006). 174
- [221] S. Vignolini, F. Riboli, F. Intonti, D. S. Wiersma, L. Balet, L. H. Li, M. Francardi, A. Gerardino, A. Fiore, and M. Gurioli, “Mode hybridization in photonic crystal molecules,” *Applied Physics Letters* **97**, 63101 (2010). 174, 179
- [222] F. Intonti, F. Riboli, N. Caselli, M. Abbarchi, S. Vignolini, D. S. Wiersma, A. Vinattieri, D. Gerace, L. Balet, L. H. Li, M. Francardi, A. Gerardino, A. Fiore, and M. Gurioli, “Young’s Type Interference for Probing the Mode Symmetry in Photonic Structures,” *Physical Review Letters* **106**, 143901 (2011). 174
- [223] N. Caselli, F. Intonti, F. Riboli, A. Vinattieri, D. Gerace, L. Balet, L. H. Li, M. Francardi, A. Gerardino, A. Fiore, and M. Gurioli, “Antibonding ground state in photonic crystal molecules,” *Physical Review B* **86**, 35133 (2012). 174, 178, 179, 180, 185
- [224] N. Caselli, F. Intonti, F. Riboli, and M. Gurioli, “Engineering the mode parity of the ground state in photonic crystal molecules,” *Optics Express* **22**, 4953–4959 (2014). 174, 185
- [225] K. A. Atlasov, K. F. Karlsson, A. Rudra, B. Dwir, and E. Kapon, “Wavelength and loss splitting in directly coupled photonic-crystal defect microcavities,” *Optics Express* **16**, 16255–16264 (2008). 174, 176, 178, 187, 188, 208, 220
- [226] M. Brunstein, T. J. Karle, I. Sagnes, F. Raineri, J. Bloch, Y. Halioua, G. Beaudoin, L. Le Gratiet, J. A. Levenson, and A. M. Yacomotti, “Radiation patterns from coupled photonic crystal nanocavities,” *Applied Physics Letters* **99**, 111101 (2011). 174
- [227] K. A. Atlasov, A. Rudra, B. Dwir, and E. Kapon, “Large mode splitting and lasing in optimally coupled photonic-crystal microcavities,” *Optics Express* **19**, 2619–2625 (2011). 174, 177, 178, 191, 204
- [228] S. Haddadi, P. Hamel, G. Beaudoin, I. Sagnes, C. Sauvan, P. Lalanne, J. A. Levenson, and A. M. Yacomotti, “Photonic molecules: tailoring the coupling strength and sign,” *Optics Express* **22**, 12359–68 (2014). 174, 178, 185
- [229] Y. Zhao, C. Qian, K. Qiu, Y. Gao, and X. Xu, “Ultrafast optical switching using photonic molecules in photonic crystal waveguides,” *Optics Express* **23**, 9211–9220 (2015). 174, 187, 189
- [230] S. Kapfinger, T. Reichert, S. Lichtmannecker, K. Muller, J. J. Finley, A. Wixforth, M. Kaniber, and H. J. Krenner, “Dynamic acousto-optic control of a strongly coupled photonic molecule,” *Nat Commun* **6**, 8540 (2015). 174, 178, 180, 204, 208, 220
- [231] T. Cai, R. Bose, G. S. Solomon, and E. Waks, “Controlled coupling of photonic crystal cavities using photochromic tuning,” *Applied Physics Letters* **102**, 141118 (2013). 174, 179, 180, 220, 224
- [232] D. O’Brien, M. D. Settle, T. Karle, A. Michaeli, M. Salib, and T. F. Krauss, “Coupled photonic crystal heterostructure nanocavities,” *Optics Express* **15**, 1228–1233 (2007). 174, 178
- [233] C. Cohen-Tannoudji, B. Diu, and F. Laloë, *Quantum mechanics*, Quantum Mechanics (Wiley, Paris, 1977). 174, 175

- [234] M. Notomi, E. Kuramochi, and T. Tanabe, “Large-scale arrays of ultrahigh-Q coupled nanocavities,” *Nature Photonics* **2**, 741–747 (2008). 178
- [235] S. Vignolini, F. Riboli, D. S. Wiersma, L. Balet, L. H. Li, M. Francardi, A. Gerardino, A. Fiore, M. Gurioli, and F. Intonti, “Nanofluidic control of coupled photonic crystal resonators,” *Applied Physics Letters* **96**, 141114 (2010). 178, 179, 180
- [236] A. Faraon, D. Englund, D. Bulla, B. Luther-Davies, B. J. Eggleton, N. Stoltz, P. Petroff, and J. Vučković, “Local tuning of photonic crystal cavities using chalcogenide glasses,” *Applied Physics Letters* **92**, 43123 (2008). 179
- [237] M. A. Dündar, J. A. M. Voorbraak, R. Nötzel, A. Fiore, and R. W. van der Heijden, “Multimodal strong coupling of photonic crystal cavities of dissimilar size,” *Applied Physics Letters* **100**, 81107 (2012). 179, 220
- [238] I. Fushman, E. Waks, D. Englund, N. Stoltz, P. Petroff, and J. Vučković, “Ultrafast nonlinear optical tuning of photonic crystal cavities,” *Applied Physics Letters* **90**, 91118 (2007). 179
- [239] W. C. L. Hopman, A. J. F. Hollink, R. M. de Ridder, K. O. van der Werf, V. Subramaniam, and W. Bogaerts, “Nano-mechanical tuning and imaging of a photonic crystal micro-cavity resonance,” *Optics Express* **14**, 8745–8752 (2006). 179
- [240] H. Flayac and V. Savona, “Unconventional photon blockade,” *Physical Review A* **96**, 53810 (2017). 181
- [241] T. C. H. Liew and V. Savona, “Single Photons from Coupled Quantum Modes,” *Physical Review Letters* **104**, 183601 (2010). 181
- [242] M. Bamba, A. Imamoğlu, I. Carusotto, and C. Ciuti, “Origin of strong photon antibunching in weakly nonlinear photonic molecules,” *Physical Review A* **83**, 21802 (2011). 181, 219, 224
- [243] M. Bamba and C. Ciuti, “Counter-polarized single-photon generation from the auxiliary cavity of a weakly nonlinear photonic molecule,” *Applied Physics Letters* **99**, 171111 (2011). 181, 220
- [244] C. Vaneph, A. Morvan, G. Aiello, M. Féchant, M. Aprili, J. Gabelli, and J. Estève, “Observation of the Unconventional Photon Blockade in the Microwave Domain,” *Physical Review Letters* **121**, 43602 (2018). 181
- [245] H. J. Snijders, J. A. Frey, J. Norman, H. Flayac, V. Savona, A. C. Gossard, J. E. Bowers, M. P. van Exter, D. Bouwmeester, and W. Löffler, “Observation of the Unconventional Photon Blockade,” *Physical Review Letters* **121**, 43601 (2018). 181, 206, 224
- [246] X. Yang, M. Yu, D.-L. Kwong, and C. W. Wong, “All-Optical Analog to Electromagnetically Induced Transparency in Multiple Coupled Photonic Crystal Cavities,” *Physical Review Letters* **102**, 173902 (2009). 182
- [247] S. V. Zhukovsky, D. N. Chigrin, A. V. Lavrinenko, and J. Kroha, “Switchable Lasing in Multimode Microcavities,” *Physical Review Letters* **99**, 73902 (2007). 182
- [248] P. Hamel, S. Haddadi, F. Raineri, P. Monnier, G. Beaudoin, I. Sagnes, A. Levenson, and A. M. Yacomotti, “Spontaneous mirror-symmetry breaking in coupled photonic-crystal nanolasers,” *Nature Photonics* **9**, 311 (2015). 182